SCUOLA DI DOTTORATO

UNIVERSITÀ DEGLI STUDI DI MILANO-BICOCCA

Department of Materials Science

PhD program in Materials Science and Nanotechnology

Cycle XXXIII

QUANTUM MECHANICAL MODELING OF CHEMICAL ACTIVATED 2D-MATERIALS FOR ELECTROCATALYSIS AND SENSING

Daniele Perilli

Registration number 748030

Supervisor: Prof. Cristiana Di Valentin

Coordinator: Prof. Marco Bernasconi

ACADEMIC YEAR 2019/2020

Abstract

Two-dimensional materials have aroused great interest among the scientific community thanks to their exceptional properties and promising applications in many technological fields. Nevertheless, over the last years, the frontline of research has moved from the study of basic properties of pure 2D crystals to chemical modified forms, i.e. doped 2D materials, and their interaction with other systems, such as nanoparticles, or surfaces.

Within this frame, metal substrates are often employed as heterogeneous catalysts for the growth of 2D materials, although their role is often relegated to mere supporting materials, with a little attention to the potential that these hybrid interfaces (two-dimensional materials/metal surfaces) offer.

This work investigates complex interfaces between two-dimensional materials and metal surfaces, both from the point of view of basic understanding of such systems and application in electrocatalysis and sensing. In particular, the thesis is mainly addressed to the understanding of the synergistic role of the underlying metal substrate and defects like vacancies or dopants on the chemical and physical properties of the two-dimensional adlayer.

We employed state-of-the-art computational methods to model systems that are as realistic as possible. All calculations have been performed through density functional theory (DFT), using dispersion-corrected functionals.

The first part of the work (Chapters 3, 4, and 5) was focused on the study of the interface between a hexagonal boron nitride monolayer and the Cu (111) surface (h-BN/Cu). The atomic structure of the pristine, defective (containing mono- and pluri-atomic vacancies), and doped (Cu, Ni, Co, and Fe) interface, together with its electronic structure and chemical reactivity, was systematically investigated by DFT calculations. In particular, we explore the possibility to trap metal atoms that pop up from the metal bulk or the gas-phase, or already present on the surface as adatom, into the 2D layer to form a metal-trapped h-BN. Such trapped metal atoms, in the form of single atoms or even small clusters, could be interesting active sites in many catalytic or electrocatalytic

processes, as widely investigated in the case of the oxygen and hydrogen evolution reaction (Chapter 4 and 5, respectively).

In the second part of the work (Chapters 6 and 7), we investigated the graphene/Ni(111) interface and the role of N dopants on its chemical reactivity. Such a system may be interesting in the field of electrocatalysis and sensing. This part of the work has been carried out in collaboration with the laboratory of CNR-IOM in Trieste, which was responsible for the synthesis and characterization of the samples.

In Chapter 6, we performed an extensive set of DFT simulations to support and corroborate the experimental evidence on the atomic structure of N dopants in graphene. Our experimental colleagues developed a novel method to produce N-Gr layers and the produced N-Gr layers were thoroughly characterized at the atomic level by STM and XPS in combination with our DFT simulations in order to identify and fully characterize the N dopants.

In Chapter 7, based on the synergic contribution of DFT calculations and experiments, we unraveled the mechanism of CO intercalation at the Gr/Ni interface, which is highly facilitated by the presence of N-dopants, Similar mechanisms are likely to apply to other cases of molecular intercalation at the Gr/M interface, where the process has been observed but not yet explained. A clear solution to this puzzle is a crucial step towards engineering the Gr/M interface in order to design and realize systems with tailored properties.

In conclusion, the main idea of this work is to exploit the high surface area of two-dimensional materials to trap objects that can be atoms or metal clusters, as well as molecules. Such objects can be used as catalytic sites for many reactions of great interest or induce some modification in the 2D material, making it suitable as a sensor.

Contents

1. Introduction

In the last decade, two-dimensional (2D) materials are emerging as new potential candidates for applications in several fields such as electronics, photonics, sensing, energy storage, and catalysis.[1,2,3,4,5,6,7]

Nonetheless, compared to many theoretical proposed 2D crystals, only a few of them have been experimentally produced to date. For example, starting from 100,423 experimentally known materials, high-throughput calculations have been employed to predict possible two-dimensional structures.[8] Such computational screening allowed the identification of 1,835 compounds that are either easily or potentially exfoliable, showing that only a very small fraction of possible 2D materials has been considered up to now.

It is worth highlighting how such materials are characterized by very high flexibility in terms of chemical composition and structure. As shown in **Figure 1-1**, different chemical elements can be combined to form elemental or binary compounds, presenting different geometrical structures. Due to this, different properties can be achieved by varying composition and structure, allowing for different areas of application.

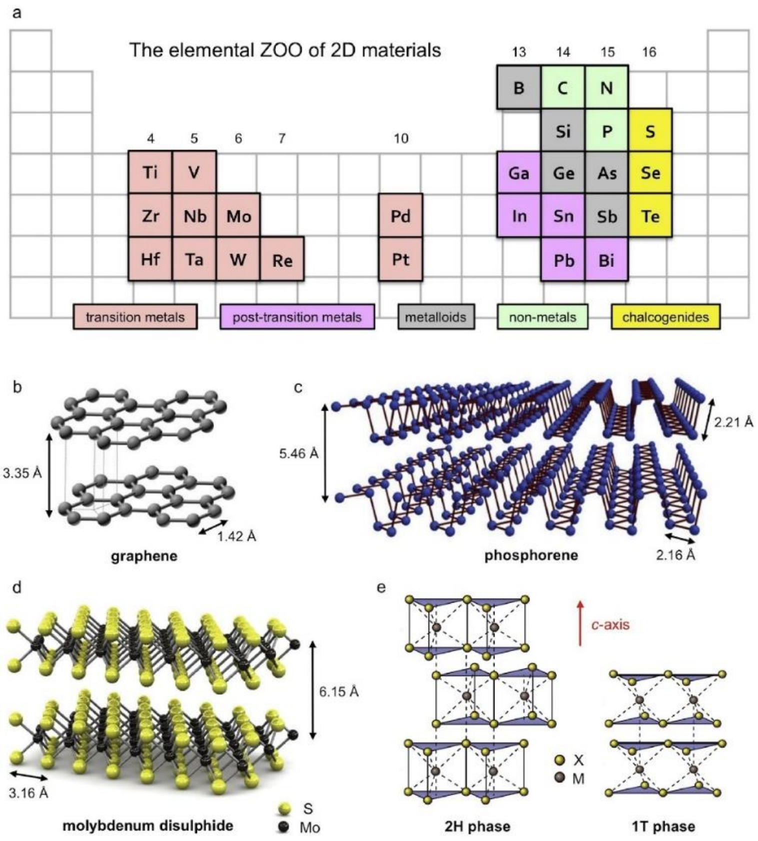

Figure 1-1: (a) Chemical elements present in the most common two-dimensional materials. Ball-and-stick models of (a) graphene, (b) phosphorene, and (c) MoS_2. (e) Schematic representation of the two most common transition metal dichalcogenides (TMDCs) phases: 2H and 1T. The lattice parameters in b, c, and d are taken from Ref. 9,Ref. 10, and Ref. 11, respectively. Figures adapted with permission from: b, Ref. 12. c, Ref. 13. d, Ref. 14. e, Ref. 15. The overall image was taken with permission from Ref. 16.

1.1. Chemical activation of two-dimensional materials

Nowadays, the frontline of research has moved from the study of basic properties of pure 2D crystals to chemical modified forms, i.e. doped 2D materials, and their interaction with other nano-objects, such as nanoparticles, or complex molecules, to form reactive nanocomposites, in contrast to the chemical inertia of pure systems.[4,17,18]
Furthermore, if on the one hand, the chemical activation makes them suitable for chemical applications such as catalysis and sensing,[19] on the other hand, this also allows the tuning of specific physical properties, which can further improve their technological impact.

Therefore, in the following, different strategies to chemically activate 2D materials will be presented, and we will focus on two of the most known 2D crystals: graphene (Chapter 1.1.1) and hexagonal boron nitride (Chapter 1.1.2).

1.1.1. Graphene

Graphene (Gr) is a material consisting of a single layer of C atoms arranged in a honeycomb lattice (**Figure 1-2b**), which was experimentally isolated for the first time in 2004.[20] Although this material was known, at least from a theoretical point of view, several decades earlier, it has always been considered only as a “theoretical model toy”, since it was believed that perfect 2D crystals were not thermodynamically stable, and therefore cannot exist as an isolated monolayer.[21]

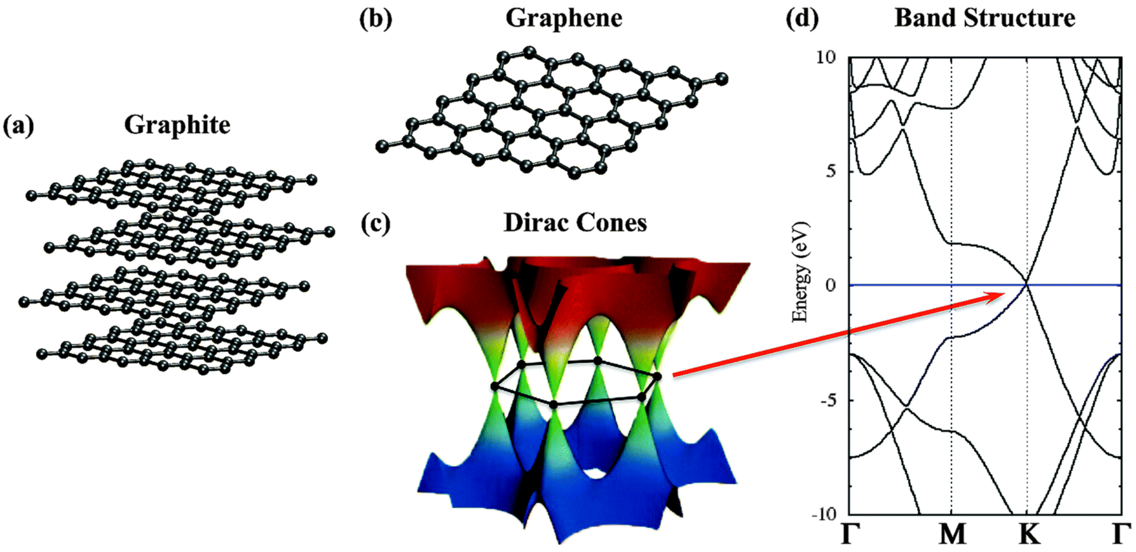

Figure 1-2: (a) 5×5×2 supercell of graphite. (b) 5×5 supercell of graphene. (c) Dirac cones of graphene in the reciprocal space (adopted from Ref. 22). Calculated band structure of graphene along the Γ→M→K→Γ high symmetry path. All energies have been shifted with respect to the Fermi energy, which is indicated by a blue horizontal line. Reprinted with permission from Ref. 23.

The great interest aroused by graphene is due to its unique physical properties. Graphene is a semi-metal: as shown in **Figure 1-2c**, the valence and the conduction bands touch each other in six points of the Brillouin zone (called Dirac points), at which the graphene bands are characterized by a linear dispersion (see band structure in **Figure 1-2d**). Its electronic structure is a consequence of the symmetry, consisting of two triangular sub-lattices of C atoms that interpenetrate in the plane. Due to this, electrons in graphene obey to the Dirac equation, which is the relativistic equivalent of the Schrödinger equation: although they do not move as if they were photons (massless particles and at a speed light velocity), their behavior is well described by the Dirac equation, and they can be called as “massless Dirac fermions”.[21] Therefore, graphene shows a high charge carrier mobility, which makes it a promising material in the field of electronics.[3]

Despite many other attractive physical properties, such as mechanical strength, transparency, and thermal conductivity, graphene shows a very poor chemical reactivity. For example, defect-free Gr is stable in the air up to 500 °C[24] and is also impermeable to any atomic or molecule species in the gas or liquid phase.[25] Due to this, graphene shows great potential for application in anticorrosive coatings as a barrier material.[26]

However, one of the biggest challenges related to potential large-scale use of graphene is how to produce it in a cost-effective way and a huge amount. Obviously, a method for the graphene mass-production must meet the cost and quality criteria, which depend on the application required (**Figure 1-3**).[2]

The first attempts to isolate graphene were carried out through mechanical exfoliation techniques such as the so-called scotch-and-tape method and employing graphite (**Figure 1-2a**) as a starting material. The interaction between C layers is weak and is mainly due to the Van der Waals forces, therefore, their delamination may occur thanks to simple mechanical stress.

Based on this concept, several protocols have been further developed for the chemical exfoliation of graphite, exploiting the interposition of atoms or molecules between carbon layers to weaken their adhesion. Then, graphite splits into graphene sheets through a simple sonication process, and the formed graphene nanosheets can be separated from the other species intercalated by a simple centrifugation procedure.

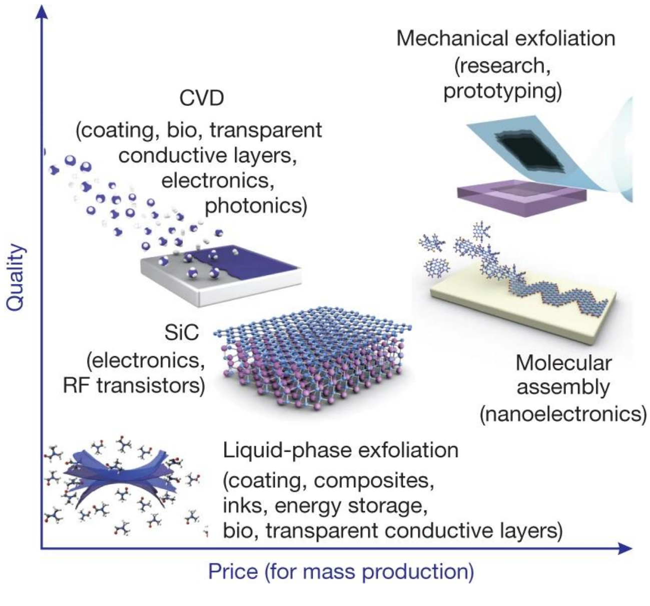

Figure 1-3: Scheme for methods of mass-production of graphene as a function of crystalline quality and price. Reprinted with permission from Ref. 2.

Another method to obtain graphene is the thermal decomposition of silicon carbides (SiC). It has been observed that graphitic layers can be grown by the sublimation of Si atoms (from the SiC surface), leaving a graphitized surface. The first C layer (called buffer layer) is strongly interacting with the underneath SiC surface and shows properties quite far from those of a sheet of graphene.[27] However, when the number of graphene layers increases (which their growth can be controlled), the top layers show higher quality, resembling the unique graphene's properties. One of the main advantages of using this technique is the possibility to obtain graphene directly integrated with SiC, which is a common material used for high-power electronics. But on the other hand, the two major drawbacks for large-scale production are the high cost of the SiC wafers and the high temperatures (above 1000 °C) used.

Among different strategies to the large-scale production of graphene, the chemical vapour deposition (CVD) is considered the most promising. This method involves the decomposition (usually thermally activated) of a molecular precursor, i.e. ethylene, on top of a metal substrate, which acts as a catalyst for the hetero-nucleation of C atoms to form graphene. Among different metal catalysts, Cu and Ni have aroused great interest in the possibility to obtain large-area and high-quality graphene.[28,29] However, the main drawback is the fact that the complete process usually requires the transfer from the metal support to a dielectric surface or other substrate of interest, which can drastically reduce the quality of graphene.

It is clear how the high quality of graphene, i.e. a low number of defects, is an important condition that must be fulfilled for certain kinds of applications but may not be desirable for others: graphene is chemically inert, and defects or interaction with other objects can open a route towards new technological fields.

Therefore, in recent years the scientific community began to chemically activate graphene-based materials, as shown in **Figure 1-4**.[4]

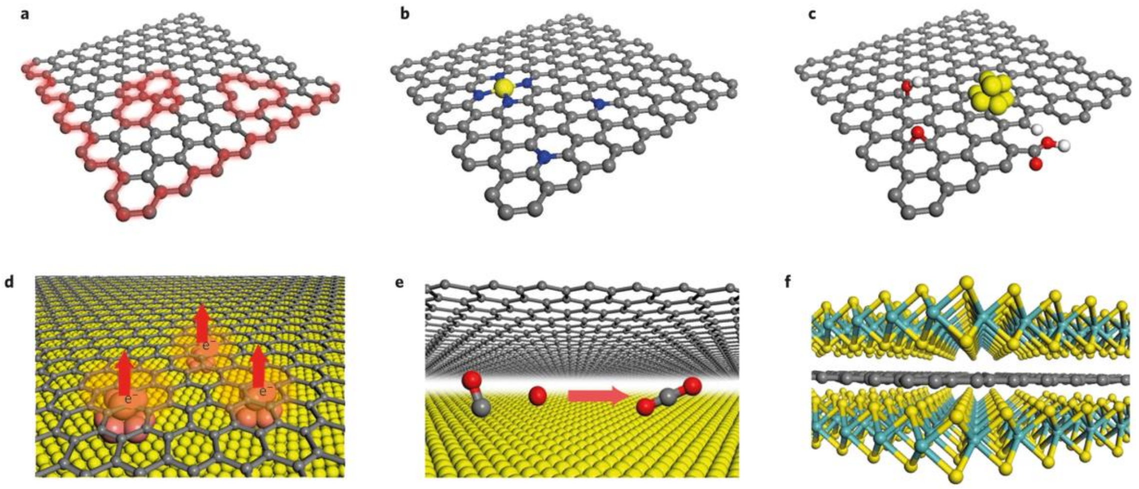

Figure 1-4: Schematic representation for various chemically activated graphene structures: (a) point and extended defects in graphene, (b) graphene doped with metal and non-metal heteroatoms, (c) graphene with oxygen functional groups and small metal clusters, (d) graphene interacting with an underlying metal substrate, (e) catalytic nano space at the interface between graphene and the metal surface, and (f) sandwich structure based on 2D materials, like graphene embedded between two MoS_2 layers. Reprinted with permission from Ref. 4.

The different strategies can be summarized as follows:

1) Point and extended defects (**Figure 1-4a**): from a thermodynamic point of view structural defects are always present in graphene, but their abundance and nature depend on how the material is prepared and treated. For example, the number of vacancies or topological defects (i.e. Stone-Wales defects) can be significantly increased by sputtering treatment followed by thermal annealing,[30,31] as well as the presence of edges can be tailor by the control of the temperature during the CVD growth.[32] Such defects have a huge impact on the properties of graphene,[33,34] often acting as active sites for chemical reactions.
2) Doping with heteroatoms (**Figure 1-4b**): this strategy is arousing great interest based on the possibility to control, in a very precise way, the number and type of dopants. Doping with no-metal heteroatoms, especially N and B, has been successfully achieved employing the arc discharge method, using as a precursor NH_3 or B_2H_6.[35] CVD methods also allow a direct synthesis of doped graphene by exposing the catalytic substrate to dopant- and C-containing precursors that dissociate on the surface, leading to the formation of high-quality doped graphene layers.[36,37] Also doping with metal atoms (M) is generating great interest according to the possibility to exploit precious and non-precious metals, while simultaneously reducing their content.[38] However, the biggest challenge on metal doping is finding a way to stabilize the metal atom into the carbon matrix, which can be overcome by interposing N atoms between C and M atoms (co-doping), forming a C-N-M bond.[39] Unfortunately, this procedure is not trivial to date.
3) Functionalization (**Figure 1-4c**): due to the strong C-C bonds, graphene reactivity is quite poor. However, it can be oxidized under harsh conditions to form graphene oxide (GO),[40] which is commonly used as an intermediate during the chemical exfoliation of graphite though water intercalation (GO is more hydrophilic than graphene). Then GO can be reduced to form reduced graphene oxide (RGO),

which is a chemical modified graphene-based material. Both GO (more) and RGO (less) present many oxygen-containing functional groups, showing a chemical reactivity related to the peculiar group considered (-OH, -CHO, -COOH, and -O). Another functionalization strategy is the deposition on the graphene surface of adsorbates, such as metal adatoms and clusters, which must be properly stabilized to prevent their coalescence.

4) Interaction with an underlying substrate (Figure **1-4d** and **e**): as was previously said, graphene is usually grown or deposited on different substrates, such as metals (mainly), dielectrics, or insulators, depending on the purpose of the device. In this way, graphene may be modified through the interaction with the supporting material, for example by donating or receiving electrons by a charge transfer mechanism (**Figure 1-4d**).[41] Usually, the underlying substrate is used as mere support, but recently the possibility to work with atom-thick 2D layers has opened to a newly emerging approach to catalysis under a graphenic cover, generally referred to as catalysis under cover (**Figure 1-4e**), i.e. at the confined space between the carbon layer and the support.[17] This can be reached through preferential channels represented by graphene defects, such as vacancies, island edges, grain boundaries, or wrinkles, and can extremely boost the usual "free-standing" catalytic efficiency of this material.
5) Out-of-plane heterostructures (**Figure 1-4f**): another strategy to chemically modify graphene is based on the possibility to combine it with different two-dimensional materials to form a sandwich-like structure. Through the combination of confinement effects, charge transfers, and hybridization between the layers, the tuning of the properties of the graphene sheet is possible.

1.1.2. Hexagonal Boron Nitride

Boron nitride is a chemical compound made by boron and nitrogen atoms with the chemical formula BN. It exists in various crystalline allotropes that are similar to carbon analogous structures (**Figure 1-5a**): a hexagonal and rhombohedral form (h-BN and r-BN, analogous to graphite), a cubic form (c-BN, analogous to diamond), and a wurtzite form (w-BN, analogous to lonsdaleite).

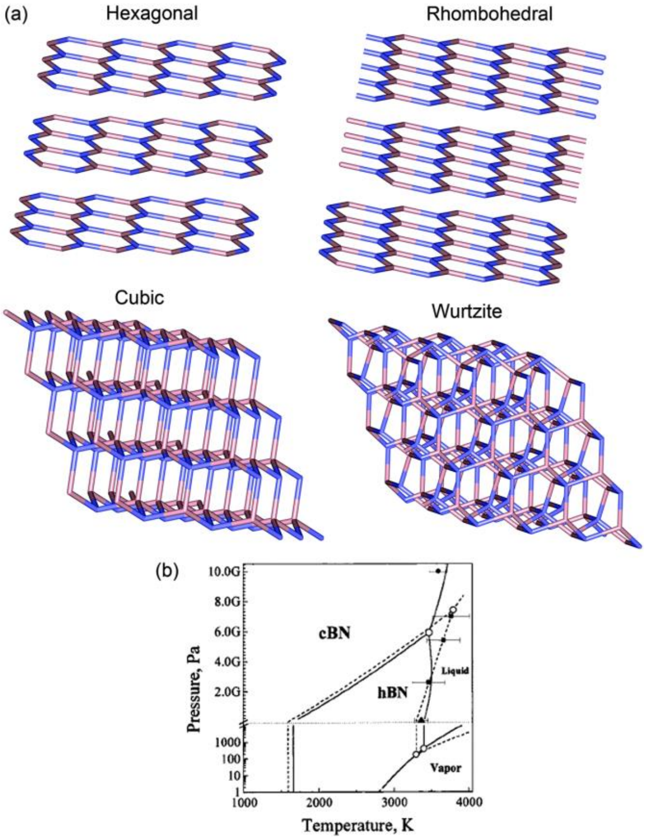

Figure 1-5: (a) Boron nitride crystalline allotropes: B atoms in pink, N atoms in blue. (b) Phase diagram of boron nitride at different temperature and pressure conditions.[42] Reprinted with permission from Ref. 43.

Among the different polymorphs, the most stable is hexagonal boron nitride (h-BN), which is characterized by weakly interacting layers that can be easily exfoliated in two-dimensional sheets (to which we refer from now on simply as h-BN).

H-BN is isostructural with graphene, presenting also a similar lattice parameter: 2.51 vs 2.47 Å, respectively. However, the two materials are characterized by different electronic properties since graphene is a semimetal, whereas h-BN is an insulating material. This intrinsic difference is a consequence of the different nature of the B–N bond (polar covalent bond) with respect to the C–C bond (apolar covalent bond).

Due to the large bandgap ($\approx$ 6 eV),[44] charge carriers mobility is quite low, making h-BN not suitable in applications in which a good electrical conductivity is required. On the other hand, h-BN shows excellent thermal and chemical stability and is thus used as part of high-temperature equipment or in coating applications.[45]

Like graphene, h-BN is considered as the archetype of various BN nanostructures: 1D systems such as nanoribbons and nanotubes, or 0D systems such as fullerenes (**Figure 1-6**).

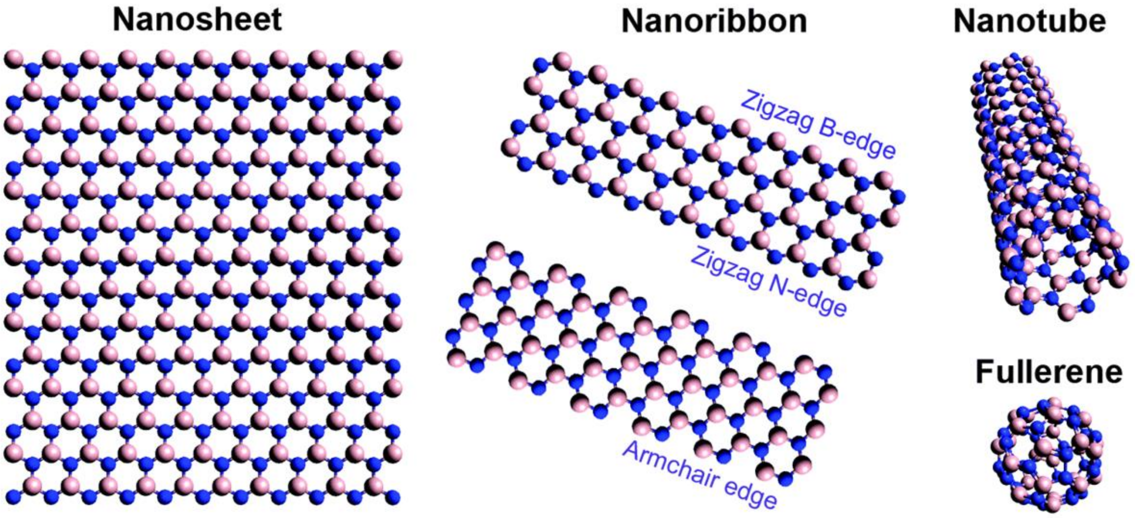

Figure 1-6: Ball-and-stick models for various BN nanostructures. In the case of BN nanoribbon, the edge can be either zigzag or armchair. Reprinted with permission from Ref. 43.

The synthesis of large-area and high-quality h-BN is still challenging. In a similar way to graphene, its production can be divided into top-down and bottom-up approaches. In the latter case, h-BN is grown on a metal surface by chemical vapour deposition (**Figure 1-7a**), using as a precursor borazine ($B_3N_3H_6$), or ammonia borane (H_3NBH_3), or a mixture of BX_3/NH_3 (where X could be F or Cl). Among the possible metal catalysts, Cu and Ni are quite popular choices for CVD growth thanks to their relative low cost and to the possibility to obtain well-aligned h-BN domains (especially in the case of 111 surfaces).[46] Often, for certain applications, it is desirable to transfer h-BN on a different substrate, usually silicon-based support (**Figure 1-7b**). These methods often damage or contaminate the film, reducing its quality. Despite this, h-BN films have been also directly grown on Si,[47] SiO_2/Si,[47] and sapphire[48] substrates.

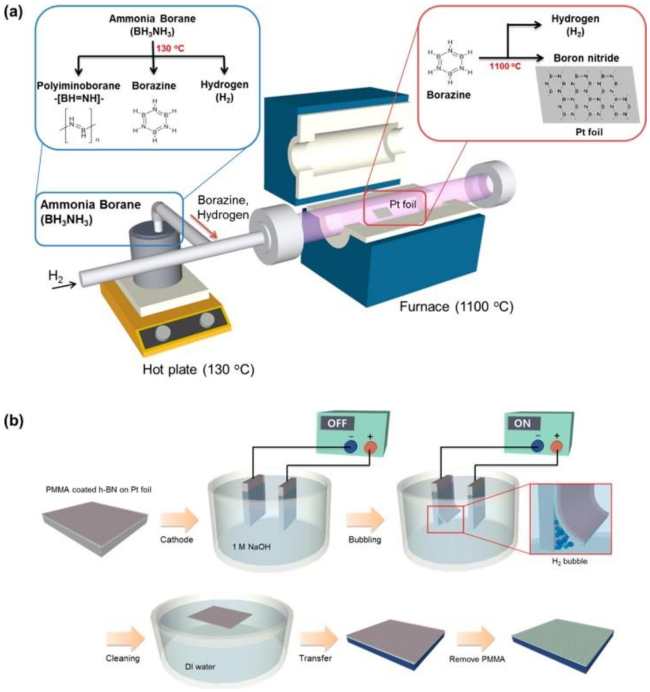

Figure 1-7: (a) Schematic representation of the experimental setup used for the h-BN growth by liquid-phase chemical vapour deposition (LPCVD). (b) Electrochemical bubbling transfer method of h-BN. Reprinted with permission from Ref. 49.

Instead, top-down approaches, such as mechanical and chemical exfoliation protocols, have been successfully developed. These methods are simple ways to produce h-BN sheets, but their yield is quite small (a little bit higher in the case of chemical protocols), and the crystal size is also quite limited. However, the main advantage of mechanical methods with respect to the chemical approaches is the higher quality of the sheets produced, i.e. a low number of defects.[50]

To date, one of the most promising uses of h-BN is in combination with transition metal dichalcogenides (TMDs) or graphene to form Van der Waals heterostructures (**Figure 1-4f**). In such systems, the role of h-BN is relegated only as a platform for the high-quality epitaxial growth of the other 2D materials. This is because h-BN has a commensurate lattice with the top layer, and also a wide bandgap, which ensures a weak interaction.

However, if on the one hand h-BN is mainly used as a mere support thanks to its chemical inertia and symmetry/size, on the other hand, several strategies are being developed to chemically activated it. For example, the presence of an underlying metal support can affect the topography and properties of the h-BN adlayer. Through the different chemical composition, electronic structure, and symmetry of the substrate it is possible to get different chemically nanostructured h-BN/M interfaces (**Figure 1-8**).[51]

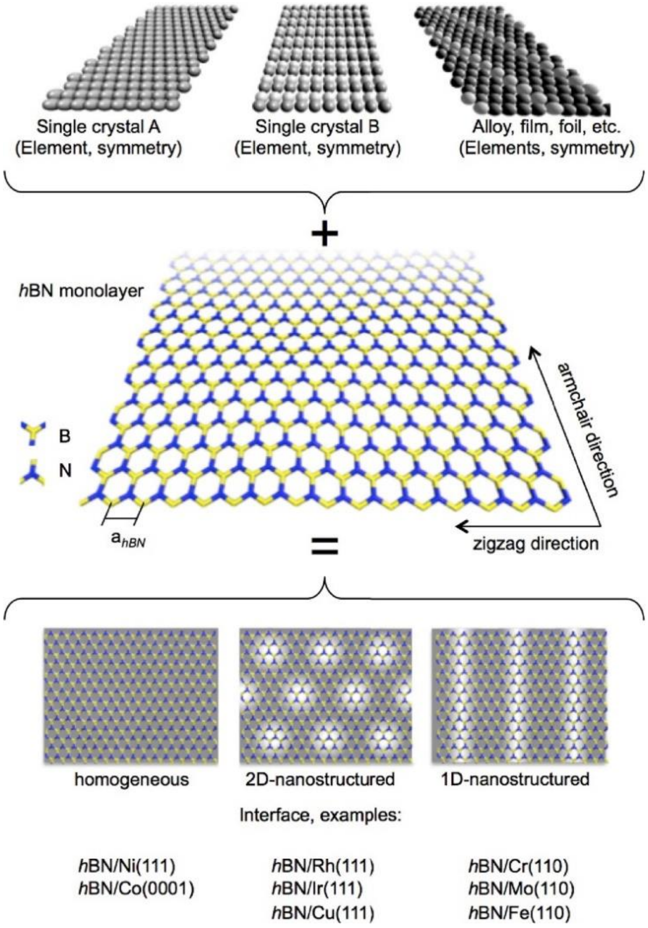

Figure 1-8: Scheme showing the formation of different h-BN/metal interfaces according to the different symmetry and chemical composition of the underlying metal substrate. Reprinted with permission from Ref. 51.

In some cases, h-BN is still a flat monolayer, perfectly aligned to the substrate (h-BN/Ni(111)), while in other cases it forms a corrugated layer (h-BN/Rh(111), h-BN/Ir(111)). In the former case, due to the lattice mismatch, h-BN undergoes a mechanical strain, that could be both negative or positive, depending on the metal considered: for example, we have a compressive strain of -0.4 % in the presence of Ni(111) surface, since the lattice parameter of h-BN is higher than Ni. Such distortion can affect its electronic properties, as well as any possible hybridization and/or charge transfer with a strongly interacting underlying metal (i.e. Ni).

Noteworthy is the case of the Cu(111) substrate, which is arousing a keen interest in the synthesis of large-area and high-quality h-BN layers.[46,51] When h-BN is grown on Cu(111), one should mention that several moiré superstructures appear, as a consequence of the lattice mismatch and the rotational misalignment between the two materials.[52] As shown in **Figure 1-9**, the most common ones are characterized by a periodicity ranging from 5 nm (**Figure 1-9e**) to nearly 14 nm (**Figure 1-9c**) and a small misalignment angle (less than 3°).

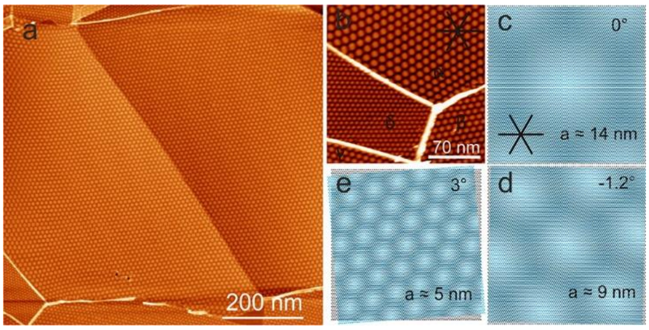

Figure 1-9: (a) STM image showing coexisting BN domains comprising different Moiré superstructures ($V_b = 4$ V, I = 40 pA). (b) Enlarged image highlighting four Moiré phases (labeled α, β, γ, and δ, respectively) separated by domain boundaries ($V_b = 4$ V, I = 0.6 nA). (c-e) Moiré models based on an overlay of two grid patters representing the Cu(111) lattice (black) and a slightly stretched BN overlayer (1.8% mismatch, blue). Minute misalignment angles up to 3° reproduce the full range of periodicities and orientations observed in the experiments. Reprinted with permissions from Ref. 52.

Such moiré superstructures are displayed through scanning tunneling microscopy (STM) measurements, appearing as a 2D lattice made by bright and dark spots. Their origin, in the case of Cu, is still debated. On the one hand, it may be due to a geometrical corrugation of the h-BN layer, as proved by combining noncontact atomic force microscopy and X-ray standing waves methods.[53] On the other hand, such an effect could be due to an "electronic corrugation", namely the different position of N/B atoms with respect to the underlying metal atoms generates a variation of the local work function of about 300 meV, as proved by scanning tunneling spectroscopy measurements.[52]

Finally, as seen in the case of graphene, defects always form during the synthesis of a material, and h-BN is not an exception. However, their number may not be enough to be macroscopic relevant, but it is possible to treat the material to increase the desired defect.

For example, sputtering with an electron beam has been successfully employed to form vacancies in quasi free-standing h-BN monolayers (**Figure 1-10**).[54,55,56]

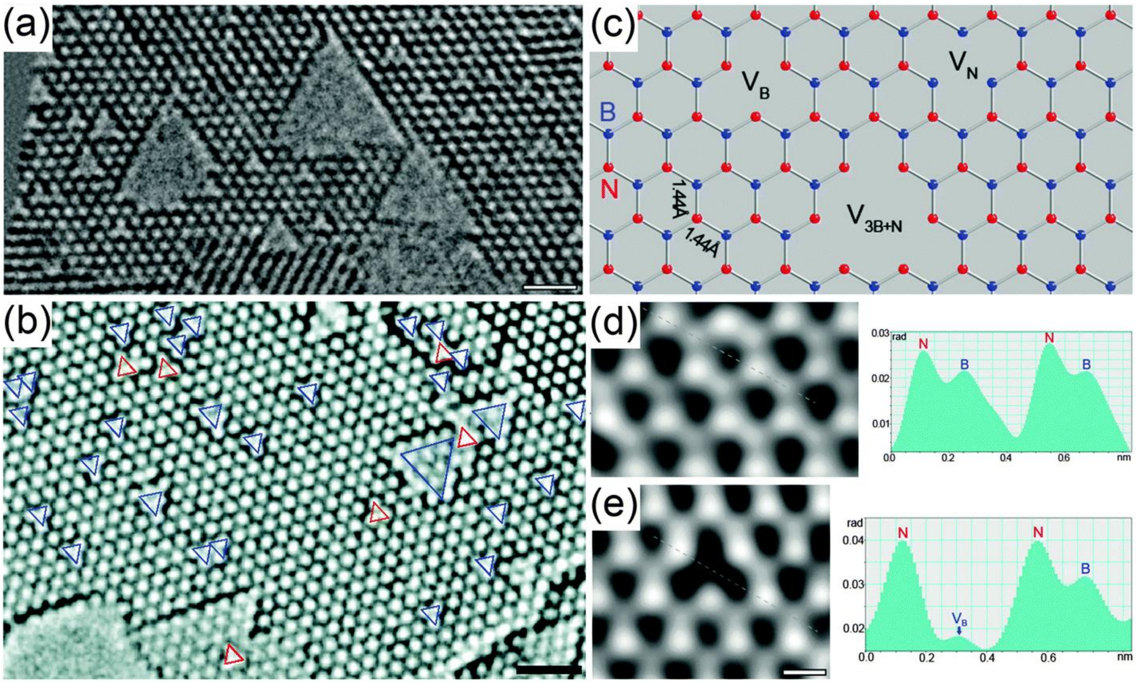

Figure 1-10: (a) HRTEM image presenting vacancy defects in a BN monolayer with the same orientation. (b) An h-BN bilayer, in which red and blue triangles with opposite directions are vacancies in monolayered and bilayered regions, respectively. (c) Ball-and-stick model for the atomic defects in h-BN. (d-e) Reconstructed phase images of pristine and defective regions in a BN monolayer, in which the individual boron and nitrogen atoms are discriminated through their line profiles. Reprinted with permission from Ref. 55.

As observed by high-resolution transmission electron microscopy (HRTEM), the defects appear as triangular holes, which have been assigned as mono- and tetra-atomic vacancies (**Figure 1-10c**). Clearly, these defects present undercoordinated B/N atoms, which can make h-BN reactive.

1.2. State of the art of computational studies on two-dimensional materials

In this section, the state-of-the-art in the field of computational modeling of 2D materials will be discussed, with a special focus on density functional theory (DFT) calculations of pristine and defective metal-supported graphene and h-BN systems.

1.2.1. Graphene

Graphene is no doubt the most studied two-dimensional material both experimentally and computationally.
For example, considering graphene/metal interfaces (Gr/M), many theoretical investigations have been published in the last decade.[41,57,58] Such works have mainly addressed the geometrical and electronic structure understanding of graphene when it is supported on a metal surface. However, the theoretical description of the Gr/M interface is not a simple task. For example, in the case of Cu(111)-supported graphene, Moiré superstructures appear experimentally as a consequence of the lattice mismatch between the two materials. The most common one is characterized by a periodicity of about 6.6 nm and a rotational angle of 0°, and its computational simulation would require a very large supercell model (at least 3800 atoms with four metal atomic layers). This size is clearly not feasible for calculations at the DFT level. However, a possible approach to circumvent this issue is the use of a commensurate model, usually imposing the lattice parameter of graphene. The rationale behind this strategy is based upon the fact that graphene grows on Cu(111) without any structural distortion and the lattice mismatch between the two materials is quite small (≈ 3 %). That such a strategy, although approximate, produces reasonable results, as shown in many theoretical works, and it is so far the most common model to study Gr/Cu interface.

Fortunately, in other cases, like graphene on Ni(111), the choice of a structural model is quite more simple: a commensurate model is well representative of the real system since in the experiments graphene is epitaxially grown on the Ni(111) surface.[59]

The proper choice of a model is not the only problem faced when performing theoretical calculations on such hybrid systems. Since the aim of many studies is the understanding of the interactions between the two components of the interface, a proper description of such effects is also highly desired.
The interaction between graphene and metals can be of different nature and strength according to the substrate on which graphene is placed. In the case of Ni, Co, Pd, and Ru, graphene is strongly interacting through a chemisorbed state and its electronic properties are completely different to those of the free-standing graphene, whereas, in the case of Cu, Pt, Ag, and Au, graphene is weakly interacting though a physisorbed state and its

electronic properties are only slightly changed. It is then clear how in the latter case, the G-M interaction is dominated by van-der-Waals dispersion forces, and it is, therefore, necessary to include them for a proper description. For example, using pure GGA functionals would give a binding of only -2 meV,[57] while including dispersion interactions, through the vdW-DF2^{C09x} functional, increases the binding up to -62 meV.[60]

Besides metal-supported graphene, many other chemically activated graphene-based materials have been extensively studied from a computational point of view.

For example, pure graphene is a zero-gap semiconductor (or semimetal), but for certain purposes, it would be desirable to make it n- or p-type doped.[61] This is possible when graphene is supported on a metal surface, but also when a dopant is introduced into the carbon matrix. In particular, a charge transfer involving the dopant could occur, shifting the position of the Dirac point with respect to the Fermi energy at positive or negative values, making graphene p- or n-type doped, respectively. These effects have been observed in experiments and rationalized through DFT calculations, as seen in the case of N- and B-doped graphene.[62] For instance, the effect coming from the introduction of boron atoms in substitutional position was understood on the basis that B has one less electron than C, and therefore an electron-hole is created in the π system of graphene. The opposite is the case of substitutional N atom since nitrogen has one more electron than C atom, and therefore such an electron is injected into the conduction band, making graphene n-type doped.

Theoretical simulations can also help to distinguish between different dopant configurations.[63] For example, differently from what has been seen for the substitutional N (also called as graphitic N defect), when N is in a pyridinic form, graphene is p-doped.[64] Calculations allow us to understand why the situation here is reversed: a pyridinic N is usually accompanied by the presence of a C vacancy, forming an electron-hole in the valence band, which is not compensated by the extra electron of N. In this case, the extra electron of N is localized in a lone pair (sp^2 state) and does not contribute to the conduction band states.

1.2.2. Hexagonal Boron Nitride

h-BN is an insulating material with a wide band-gap of ≈ 6 eV. Defects can bind excitons and act as recombination centers, leading to a strong luminescence, as experimentally observed.[65,66,67,68,69,70,71,72]

Most of the computational works in literature are based on the gradient corrected approximation (GGA) within the DFT framework, which systematically underestimates the electronic band-gap of insulators. For example, in most cases, the band-gap is calculated within the range of 3-5 eV,[73] clearly at variance with the experimental data. Such discrepancy is significant when the modeling is aimed at the prediction of optical properties. Some attempts exist of going beyond standard density functional theory. In one case,[74] some exact exchange has been introduced in the exchange-correlation functional (hybrid functional) to improve the description of the band-gap and the position of the defect states. In the other case,[75] the Bethe-Salpeter equation (BSE) approach has been used to compute the excitation of defective h-BN layers in order to investigate the role of defects (vacancies and impurities) on the optical properties. However, these approaches usually are limited to model sizes that are unsatisfactory for describing defects involving vast atomic relaxation and typically present in low concentration in real samples.

Fortunately, in many applications an accurate description of the h-BN band-gap is not necessary. For instance, usually, we do not have a band-gap when h-BN is placed on top of a metal substrate, due to the hybridization with the electronic metal states.[76] Such systems are studied as promising catalysts or electrocatalysts: free-standing h-BN is a bad electrical conductor, but when is interacting with underlying metal support, some states appear in the gap, making possible the electron transfer between the two materials.[77]

From a computational point of view, one of the biggest challenges in the modeling of h-BN/M interfaces is when h-BN forms moiré superstructures, like in the Cu(111)-supported case. Their computational simulation would require a very large supercell model which is not feasible for calculations at the DFT level. Despite this, the simulation of one Moiré superstructure has been investigated previously at the DFT level (**Figure 1-11a**) and proved to provide similar results to the commensurated model.[78] For example, in **Figure 1-12**, we can see the perfect agreement between the density of states projected onto N, B, and Cu states for a Moiré superstructure and the commensurated model.

Therefore, the supercells used in most of the theoretical works are based on a commensurated model.

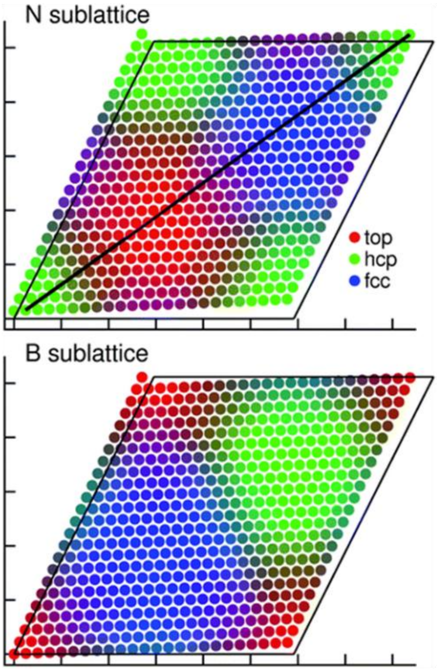

Figure 1-11: Registry of the N and B atoms in the corresponding sublattices relative to the metal substrate. The top, hcp, and fcc registries are shown in red, green, respectively. Mixed colors indicate intermediate and bridging positions. The frame shows the unit cell of the metal substrate for reference. Axis ticks at intervals of 10 Å. Reprinted with permission from Ref. 78.

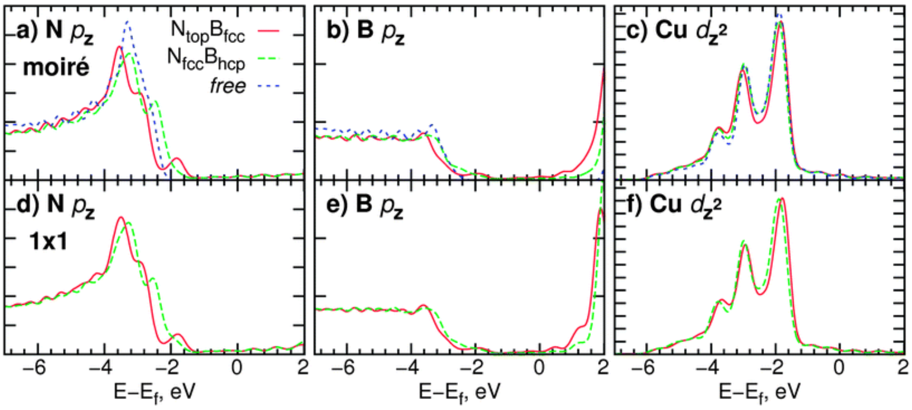

Figure 1-12: (a–c) Projected density of states (PDOS) for N, B, and Cu (surface layer) atoms on the diagonal of the moiré supercell (in the N_{top} and N_{fcc} regions, see Figure 1-11a). The corresponding PDOS for the free-standing h-BN and bare Cu surface is plotted for comparison. (d–f) PDOS for corresponding atoms in the commensurate model in $N_{top}B_{fcc}$ and $N_{fcc}B_{hcp}$ registries (bottom row). Reprinted with permission from Ref. 78.

Another crucial aspect to consider is how to properly describe the dispersion forces: the interaction between h-BN and Cu(111) is rather weak, and most of the energy contributions come from the van der Waals interactions between the two components of the interface. Standard DFT functionals are not sufficient since the electronic correlation they describe is local (local density approximation), or at most semi-local (gradient generalized approximation). Empirical corrections such as Grimme's method (DFT-D2)[79] can improve the description of the systems, giving an adhesion energy per BN pair in the range of -0.25/-0.27 eV and a vertical distance between h-BN and Cu(111) of ≈ 2.92 Å.[80] A direct comparison with experimental data is difficult, both because experimentally h-BN is not commensurated Cu and it is not yet clear if it is flat or corrugated. Nevertheless, some experimental works have provided experimental data to be compared: 57.9 meV/unit cell for the adhesion energy[52] (the value has been estimated by means the empiric rule postulated by Ziroff et al.[81]) and a vertical distance within the range of 3/3.38 Å.[52,53,82] Clearly, PBE-D2 tends to overestimate the interaction between h-BN and the metal surface: lower vertical distance and higher adhesion energy.

Finally, it is worth mentioning that a good number of theoretical publications were addressed to the understanding of simple defects in free-standing h-BN, like vacancies and heteroatom doping (especially C doping).[74,75,83,84] On the contrary, for what concerns metal-supported systems, only a few works have been addressed to the study of defects. In a recent work,[85] different h-BN defective models have been proposed and computationally characterized, both from a structural and electronic point of view (**Figure 1-13**). It is interesting to notice how the presence of a vacancy is able to make the interaction between h-BN and the metal much stronger, forming strong interfacial B/N-Cu bonds.

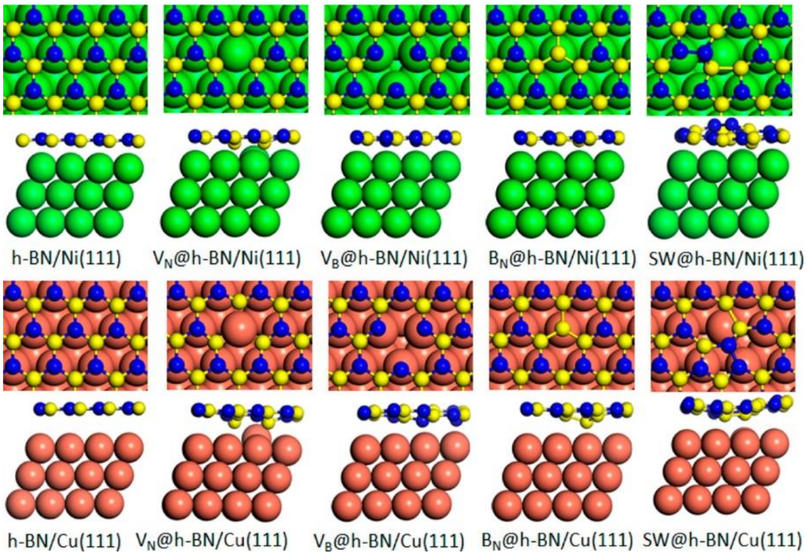

Figure 1-13: Ball-and-stick models for various Ni(111)- and Cu(111)-supported defective h-BN systems. Color scheme: B in yellow, N in blue, Ni in green, and Cu in orange. Reprinted with permission from Ref. 85.

1.3. Experimental methods for the direct comparison with theoretical results

The accuracy of computational simulations achieved today allows us to study increasingly complex systems and a greater comparison with the experimental data (in both a qualitative and quantitative way). However, to date simulations not only allow to corroborate and rationalize experimental results but even to suggest novel experiments. Thanks to this, many combined experimental and theoretical works have been successfully published in the last decade.

Therefore, in the following subsections, the widely used experimental techniques to characterize two-dimensional materials will be detailed, both for what concerns their physical principles and comparison with simulations.

1.3.1. Scanning Tunneling Microscopy (STM) and Spectroscopy (STS)

The scanning tunneling microscopy (STM) is one of the most popular atomic resolution techniques used with surface sensitivity. Through this microscopy it is possible to get information such as the topography of a surface as well as the presence of defects at an extremely small scale, down to single atom resolution.[86]

STM works by scanning a sharp metal tip over a surface and by applying an electrical voltage (called bias voltage), we can detect an electric current flowing between the sample and the tip. Such current occurs by the quantum mechanical effect of tunneling since electrons move through a barrier that they classically should not be able to move through: between the sample and the tip, there is a gap, like a vacuum, air, or liquid. Such current is the signal that is detected during an STM experiment, and its intensity is related to the surface: in particular, atomic height (i.e. the surface may be corrugated) and density of states.

There are two modes to perform STM: i) a constant current mode and ii) a constant height mode. In the former case, when the tip is moved across the sample in the x-y plane, the height of the tip changes keeping fixed the current intensity, and therefore, the measured signal is the change of the height of the tip. Instead, in the constant height mode, the height of the tip is kept fixed during the scanning, and the signal is the change in current intensity. In both cases, all images (topographic maps) obtained by STM are color scale, whose contrast depends on the sample (**Figure 1-14**). However, as we often do not know in detail the surface structure and composition, it is necessary to compare the experimental image with a simulated one, whose exact structure and composition is known. To date, several theoretical techniques (see Chapter 2.6.2) have been developed to simulate STM images with an accuracy that allows comparison with the experiments.[87]

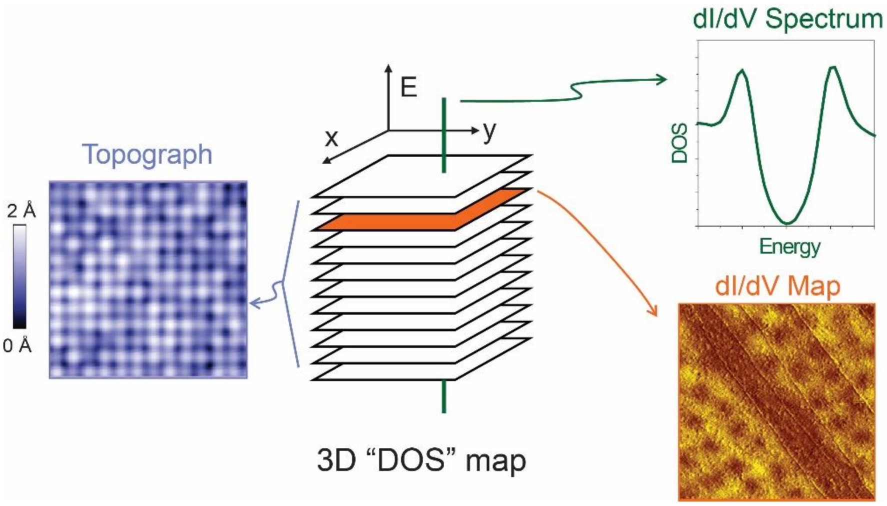

Figure 1-14: Scheme of 3-dimensional data sets obtained on a pixel grid and main types of STM measurements: topographic maps, dI/dV spectrum, and dI/dV maps. Reprinted from Ref. 88.

For example, as shown in **Figure 1-15**, STM simulations allowed to clarify the structure of nitrogen defects in graphene. In one case (**Figure 1-15a** and **b**), the experimental defect appears in the STM image as three bright spots, which have been assigned to three carbon atoms close to two graphitic nitrogen atoms. In another case (**Figure 1-15c** and **d**), the experimental bright triangular spot has been assigned to an isolated graphitic nitrogen dopant. Just considering these two examples, it is clear how the theoretical simulations are essential tools for the rationalization of STM experiments.

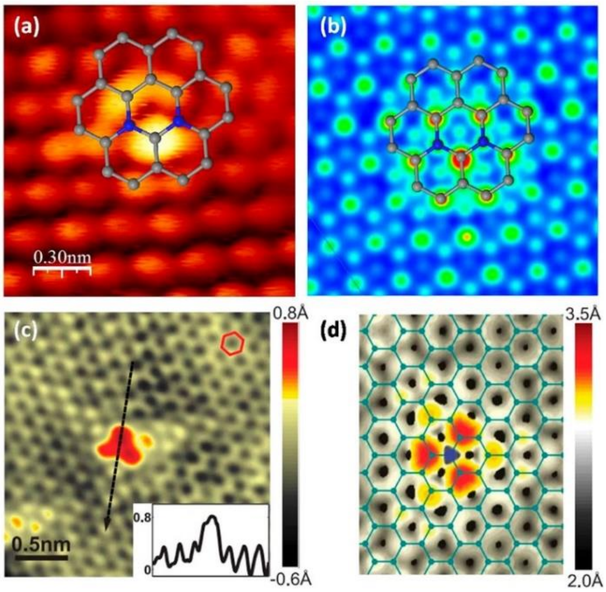

Figure 1-15: (a and c) Experimental and (b and d) simulated STM images of two different N configurations in N-doped graphene. Reprinted with permission from: a and b, Ref. 89; c and e, Ref. 90.

Another experimental technique tied to STM is the scanning tunneling spectroscopy (STS), which can be used in two different ways (see the right side of **Figure 1-14**). However, in both cases, STS probes the local density of states (LDOS) of the surface, but in one case, as shown in **Figure 1-14** (bottom right), the tip-sample bias is kept fixed during the scanning, producing a topographic image (dI/dV map), whereas in the other mode (in the top right of **Figure 1-14**), the position of the tip on the sample is kept fixed by varying the tip-sample bias, producing a spectrum of the local density of states as a function of the energy. Through the dI/dV spectrum it is possible to probe even the band-gap of surfaces, since the measured tunneling currents are really small, allowing the characterization of band-gap materials (whose electronic conductivity is very low).

1.3.2. X-ray Photoelectron Spectroscopy (XPS)

X-ray photoelectron spectroscopy (XPS) is an experimental surface technique based on the photoelectron effect: the sample is irradiated with a monochromatic X-ray source and core electrons are emitted because of the interaction with incident photons. The emitted electrons are collected and their kinetic energy is thus measured in order to determine their binding energy in the sample, according to the following equation:

$$E_K = h\nu - E_B - \Phi$$

where E_K is the kinetic energy of emitted electrons, $h\nu$ is the energy of the incident photons, E_B is the binding of the emitted core electrons, and Φ is the work function of the spectrophotometer (a parameter known).

Since the number of photo emitted electrons depend on the number of atoms in the sample to which they were bound, the peak height (or peak area) in the XPS spectrum will give us information about the concentration of a certain chemical element in the sample. However, besides the concentration of a chemical species, the most interesting information that we can get is the peak energy position.

For example, the core electron binding energy can change as the chemical environment in which the atom is located varies. Such chemical shift could be due to different atomic coordination, or a different oxidation state, or a different hybridization, and thanks to it, we can discriminate different chemical configurations (like in the case of Li element in Li_2O or metallic Li[91]).[92]

Such a technique has been widely used to characterize two-dimensional samples, as shown in **Figure 1-16** for N-doped graphene.[93]

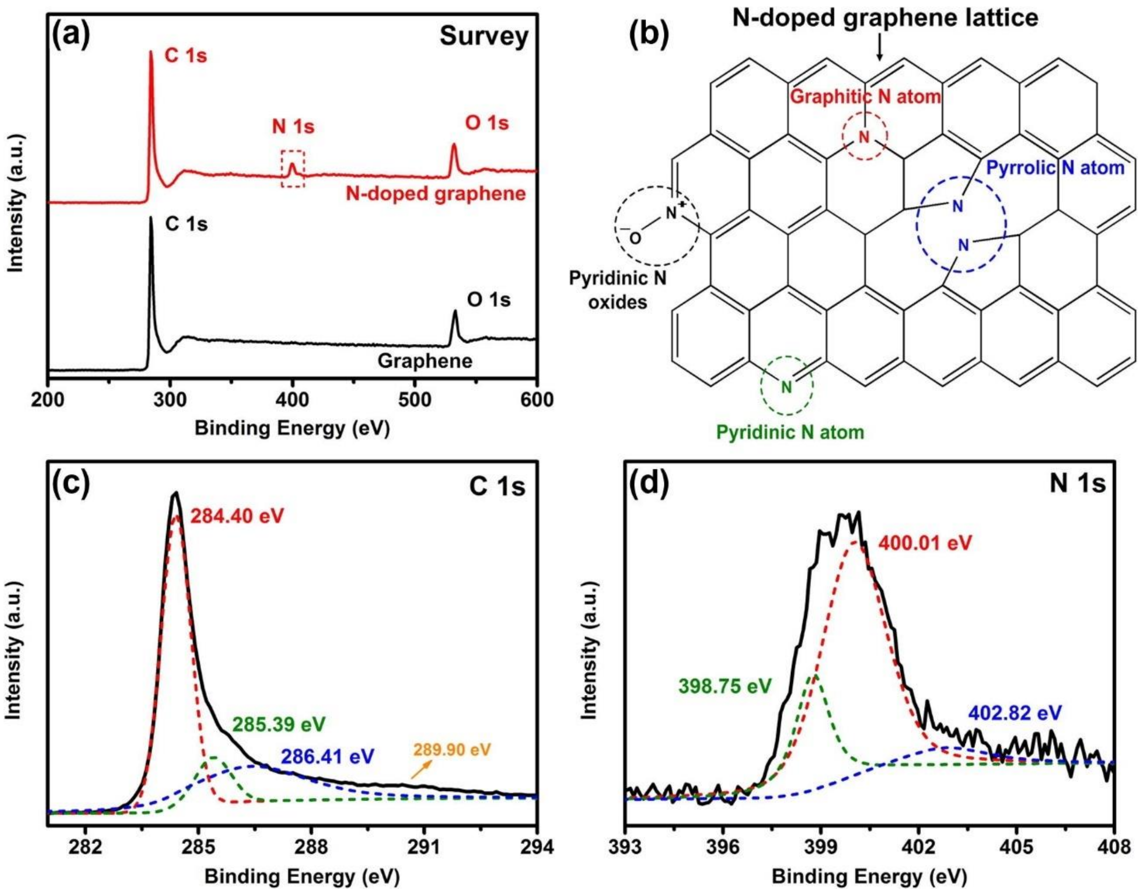

Figure 1-16: (a) XPS spectra of pristine graphene and N-doped graphene samples. (b) Schematic representation for different N dopants in graphene lattice. XPS spectra of (c) C 1s and (d) N 1s for the N-doped graphene. Reprinted with permission from Ref. 93.

Nevertheless, as previously seen for STM, also here theoretical calculations are useful tools to clarify experimental data. Usually, as shown in **Figure 1-16c** and **d**, what you get from an XPS spectrum is a large and asymmetric peak (black curve), which can be deconvoluted in several sub-peaks (red, green, blue, and yellow curves). The assignment of each sub-peak to a specific N or C configuration is often based on what is previously reported in the literature on similar systems. It is however possible to calculate through computational simulations the spectral separation in binding energy between two different configurations of N dopants, like in the case of graphitic and pyridinic N atom. Through this example, it should be evident how simulations can help in the rationalization of experimental XPS spectra.

1.3.3. Angle-Resolved Photoelectron Spectroscopy (ARPES)

Another spectroscopic technique tied to XPS is the angle-resolved photoelectron spectroscopy (ARPES). Both techniques are based on the photoelectron effect, however in this case, not only the kinetic energy of emitted electrons is analyzed, but also their angular distribution (ϑ) relative to the surface normal. From an ARPES experiment one can get an electron emission intensity map $I(E_K,\vartheta)$, where the intensity, i.e. number of emitted electrons, is a function of the electron kinetic energy E_K and the emission angle ϑ. Such maps are linked to the intrinsic distribution of the electrons in the solid, which is expressed as a function of their binding energy (E_B) and the Bloch wave vector (**k**). Through this relationship, the ARPES maps show the band structure of the surface under investigation which can be easily compared with the calculated band structure.

Such technique is particularly suited for the electronic characterization of two-dimensional materials,[94] as shown in the case of G/Ni(111) interface in **Figure 1-17**.[95] When graphene is coupled with the Ni(111) surface (**Figure 1-17a**), graphene bands appear completely different from those of the ideal free-standing case, but after intercalation of Ge atoms, G decouples from the metal surface, and one can see clearly the graphene fingerprint, which is the well-known Dirac Cone feature (**Figure 1-17b** and **c**).

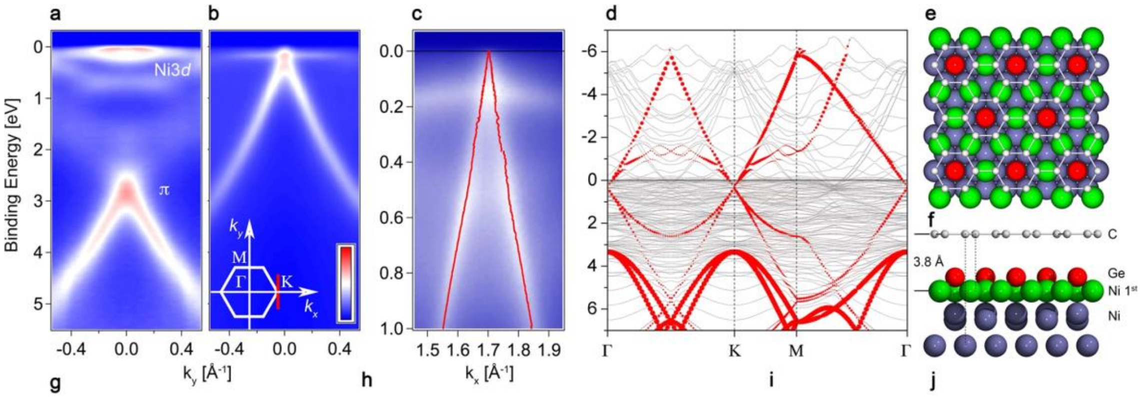

Fig. 1-17: ARPES spectra of (a) Gr/Ni(111) and (**b**) Gr/Ge/Ni(111) systems. (c) High-resolution ARPES spectrum of Gr/Ge/Ni(111). (d) Calculated Gr p_z-projected band structure of Gr/1ML Ge/Ni(111). (e) Top and (f) side view of the optimized model of G/1ML Ge/Ni(111) system. Coloro coding: C atoms in gray, Ni atoms in purple, Ge in red, and topmost Ni in green. Reprinted with permission from Ref. 95.

Theoretical calculations can help to support these experimental results, as shown in **Figure 1-17d**, **e**, and **f**. In the latter, the optimized model shows a graphene layer placed on top of a Ni (111) surface in the presence of a full monolayer of intercalated Ge atoms. From a geometrical point of view, G is flat and quite far from the surface, appearing as a non-interacting system. This is also confirmed by the calculated band structure (**Figure 1-17d**), where at point K the Dirac cone is clearly visible, in perfect agreement with the experimental results.

1.4. Implications for the electrochemical energy conversion

Starting from the end of the 18th century, the world energy consumption has undergone a drastic increase, which was satisfied by the extensive use of fossil fuels, initially coal, then oil and natural gas. Despite numerous advantages, such as high energy density, relatively low cost, transportability, and easy storage, fossil fuels have several drawbacks: first of all, they are not renewable sources; secondly, their combustion releases numerous pollutants in the air, such as CO, CO_2, SO_2, and NO_x. For these reasons, alternative energy, sustainable and with a lower environmental impact, are needed.[96]

In this scenario, molecular hydrogen (H_2) is arousing great interest as fuel for the energy transition.[97] However, despite many advantages, it is not directly available on earth. Nowadays, most of H_2 is produced from petroleum products, that does not make it sustainable from an energy perspective. For this reason, the scientific community is continuously working on sustainable methods for its production, and among several strategies, the electrochemical water splitting using directly or indirectly sunlight may be one of the solutions to the problem.[98] Unfortunately, the bottleneck of the process is the cathodic half-reaction (oxygen evolution reaction, OER), which requires efficient electrocatalysts to lower the overpotential needed. And it is here that two-dimensional materials are arousing interest, namely as efficient, stable, and cheap electrocatalysts both for the anodic and cathodic reaction in water electrolysis.[99] Further details on the OER mechanism will be discussed in Chapter 4.3.

Furthermore, their potential is not only limited to water electrolysis but they are considered as more general electrocatalysts for other electrochemical reactions, like the oxygen reduction reaction (ORR) in fuel cells or the carbon dioxide reduction reaction (CRR).[100,101]

1.4.1. Two-dimensional materials for electrocatalysis

Chemical activation of 2D materials is paving the way for their application in electrocatalysis. Materials like Gr, MoS_2, and h-BN are inert, but become reactive in the presence of defects,[100,101] dopants, or when they are interacting with other “objects”, such as metal surfaces.

Noteworthy is the case of MoS_2, which is one of the most promising materials for the hydrogen evolution reaction (HER), which is the reduction half-reaction of water electrolysis.[102] Interestingly, the active sites involved in the reaction are the metallic Mo-edges, as proved both experimentally and theoretically.[102,103] From **Figure 1-18a**, it is clear how the exchange current density, which is an indicator of the electrochemical activity, does not correlate with the surface area of MoS_2, whereas, with the MoS_2 edge length, the correlation is perfect (**Figure 1-18b**). Such results indicate how HER does not take place on the MoS_2 basal plane, which is therefore inert, but at the edges of the material. Unfortunately, MoS_2 crystals with many exposed edges are difficult to produce since they are not stable. However, through appropriate synthetic strategies, the number of edges can be improved, making MoS_2 a more efficient electrocatalyst.[104]

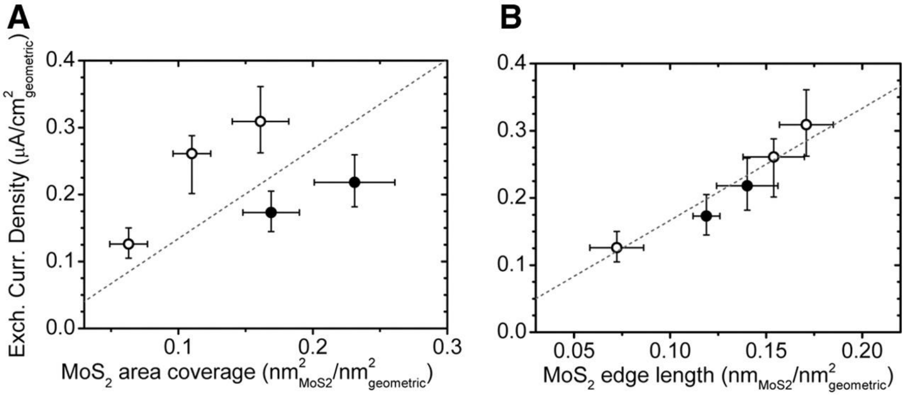

Figure 1-18: Exchange current density versus (**a**) MoS_2 area coverage and **(b)** MoS_2 edge length. In both figures, open circles are samples annealed to 400 °C, filled circles are samples annealed to 550 °C. The edge length was measured on all imaged particles and normalized by the imaged area. Reprinted with permission from Ref. 103.

Promising results have also been obtained for graphene-based materials. As mentioned several times, pure graphene is inert, but it can be made reactive, for instance, by doping.[105] Heteroatom doping makes graphene a promising cathodic electrocatalyst in fuel cells for oxygen reduction reaction (ORR), as shown in **Figure 1-19**.[106] From the Tafel plot, we can see how N- and B-doped cases are promising in terms of electrocatalytic activity, producing, compared to the other doped systems, less overpotential at the same current density.

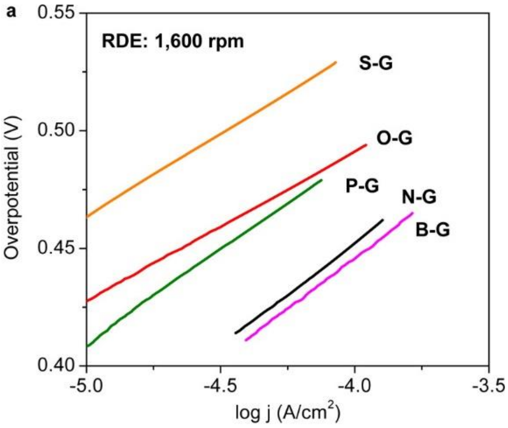

Figure 1-19: Tafel plots for different graphene doped systems: S-, O-, P-, N-, and B-doped. Reprinted from Ref. 106.

Promising results were also seen for the hydrogen evolution reaction, where nitrogen-doped graphene has been interfaced with another 2D material: graphitic carbon nitride (g-C_3N_4).[107] By an electronic coupling between the two materials, it possible to promote the proton adsorption and the subsequent evolution of H_2, with results comparable to some of the well-developed metallic catalysts (**Figure 1-20**).

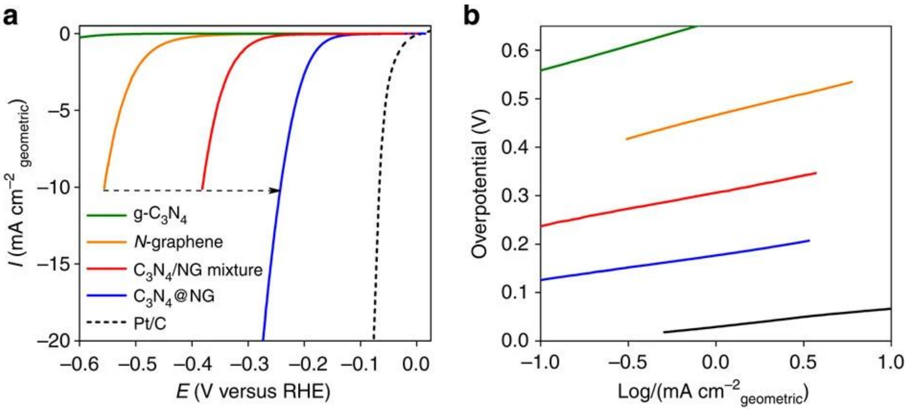

Figure 1-20: (a) HER polarization curves and (b) Tafel plots for four metal-free electrocatalysts (as indicated in the legend) and 20% Pt/C (electrolyte: 0.5 M H_2SO_4, scan rate: 5 mV s^{-1}). Reprinted with permission from Ref. 107.

Another successful strategy for the chemical activation of 2D materials is interfacing them with a metal support. Such an approach was applied to hexagonal boron nitride, which is an intrinsic insulator, but when it is interacting with an underlying metal, it becomes metallic.[77,108]

A notable example is offered when h-BN is supported on Au(111) surface: from **Figure 1-21**, the ORR activity of Au-supported h-BN (BNNS/Au, ii) is significantly higher than just the metal support, whereas h-BN alone (which is comparable to BNNS/GC, iv) shows no electrochemical activity.[109] The active sites involved in the reaction are the edges between h-BN and Au(111) since undercoordinated atoms are prompt to bind oxygen intermediates, resulting in higher activity.

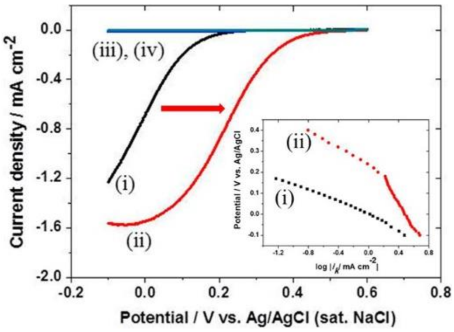

Figure 1-21: Linear sweep voltammetry (LSV) of (i) bare Au, (ii) BNNS/Au, (iii) bare GC, and (iv) BNNS/GC in O_2 saturated 0.5 M H_2SO_4. Inset: Tafel plot of kinetic currents at (i) bare Au and (ii) BNNS/Au obtained by using K–L plot. Reprinted with permission from Ref. 109.

In addition, the chemical composition of the underlying metal plays a key role in tuning the h-BN electrochemical reactivity, as deeply analyzed in a recent work by Liu et al.[77] Comparing Au- and Cu-supported h-BN sheets for the hydrogen evolution reaction, different scenarios have emerged: in the case of the h-BN/Au interface, the performance is higher than h-BN/Cu and close to Au(111) substrate. The different behavior can be rationalized in terms of different interaction with the supporting material, opening a new route towards better electrocatalysts. Of course, also defects may be present into the supported h-BN layer, making the scenario more complex but also possibly more interesting.

1.4.2. Single metal atom catalysis

In heterogenous catalysis, supported metal catalysts are widely used in many important reactions.[110] The size of metal particles is a key factor in determining the performance of such catalysts. In particular, since low-coordinated metal atoms are the most catalytically active sites, the activity per metal atom increases with decreasing the size of the metal particles (see **Figure 1-22**). However, the surface free energy of metals increases significantly with decreasing particle size (**Figure 1-22**). One possibility to overcome this problem is the use of an appropriate supporting material that strongly interacts with the metal species.

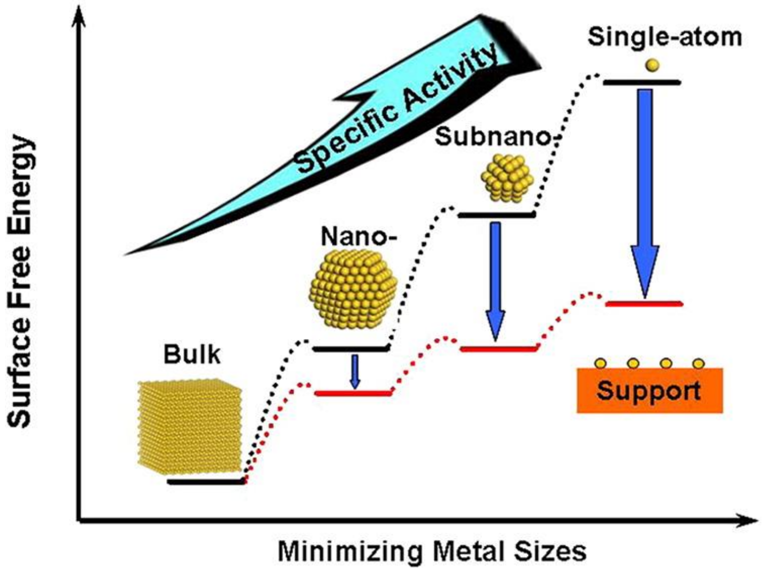

Figure 1-22: Surface free energy as a function of the metal catalyst size (black). The surface free energy may be reduced by supporting the metal catalyst (red). Reprinted with permission from Ref. 111.

The ultimate small-size limit for metal particles is the single-atom catalyst (SAC).[112,113,114] With well-defined and uniform single-atom dispersion, these systems offer great potential for achieving high activity and selectivity, usually larger than corresponding nanoparticles. In this regard, 2D materials are an interesting platform to support isolated metal atoms, due to their large surface area.

In the case of graphene, metal atoms are commonly stabilized by interposing N atoms into the C lattice (forming MN_4 motif). These systems mimic metal porphyrins, which are also excellent single-atom catalysts for crucial processes. However, the interposing of nitrogen atoms between carbon and metal atoms is quite tricky from a synthetic point of view and is still one of the open challenges in this field. One possibility to overcome this problem is that of using 2D materials that intrinsically contain nitrogen atoms, which can act as trapping sites for metal atoms: one example is hexagonal boron nitride, as shown in Chapters 3-4.

Recently, graphene-based carbon materials have been adopted to embed single atoms to obtain novel electrocatalysts. In particular, graphene-confined metal atoms were found to be efficient electrocatalysts for both the oxygen reduction reaction (ORR)[115,116,117] and the hydrogen evolution reaction (HER).[118] Interesting results were also observed for the oxygen evolution reaction (OER), where confined Ni atoms into the N-doped graphene lattice (directly bounded to pyridinic N atoms) enhance the electrochemical activity.[119]

1.4.3. Molecule permeation as a relevant aspect in graphene-based electrochemistry and sensing

Molecule intercalation at the interface between 2D materials (like Gr) and metal surfaces (M) is a crucial step for several applications, such as the catalysis under cover, the graphene-based electrochemistry, and sensing.

The catalysis under cover is an emerging field of research, focusing on the chemical reactivity taking place in the confined zone between two interfacing materials. Typically, at least one of materials is 2D. Still very little is known on the mechanism of this special type of catalysis and on the true role played by the two surfaces. Is the space confinement effect a sufficient reason for the enhanced reaction rate or are surface atoms involved in the reaction steps? Are defects and impurities also active in the promotion of chemical reactions?

Another field in which the molecule permeation is promising is that of sensors. In this case, the 2D material must selectively detect a specific molecule. In this regard, the ability to selectively pass a molecule at the interface between a 2D material and a metal could provide an interesting approach for the development of new sensors, whose signal is linked to the variation of interaction between the two interfacing materials.

Although several experimental proofs exist of the fact that gases succeed in reaching the confined zone beneath Gr, gas or molecule intercalation still remains mostly an empirical observation since the mechanism is not yet understood. It is even not yet established whether it is a general mechanism, or it is molecule dependent.

A deeper knowledge of the intercalation mechanism at the molecular level would allow for the rational design of these interfaces with selective permeation of a specific molecule/gas passing underneath and blocking other not desirable species.

1.5. Outline of the PhD Thesis

The aim of the work described in this thesis is the study of complex interfaces between two-dimensional materials (Gr and h-BN) and metal surfaces. In particular, Cu(111) and Ni(111) were considered as metal substrates, since they are cheap and promising catalysts for the large-scale CVD growth of both of G and h-BN (in particular, it is possible to use large Cu foils). The study is mainly addressed to the understanding of the synergistic role of the underlying metal substrate and defects like vacancies or dopants on the chemical and physical properties of the two-dimensional adlayer. Also, for both interfaces considered (h-BN/Cu(111) and Gr/Ni(111)), we studied possible applications as active materials in electrocatalysis and gas-sensing.

In this study, we employed state-of-the-art computational methods to model systems that are as realistic as possible. All calculations have been performed through density functional theory (DFT), using dispersion-corrected functionals and a plane-wave basis set, which is a well-suited approach to the study of metallic systems. The theoretical methodologies employed in this work are discussed in Chapter 2.

The first part of the work (Chapter 3) was focused on the study of structural and electronic properties of a **pristine and defective (B and N vacancies) free-standing h-BN monolayer**. Then, we considered the effect of an **underlying Cu(111)** substrate, exploring the possibility to **trap Cu atoms**, coming out from the metal bulk, into the 2D layer to form a Cu-trapped h-BN. Such trapped metal atoms, in the form of single atoms or even small clusters, could be interesting active sites in many catalytic or electrocatalytic processes.

Consequently, in Chapter 4, starting from the **Cu-doped models** developed, we systematically investigated them as electrocatalysts for the **oxygen evolution reaction** (OER), employing the computational hydrogen electrode (CHE) model (Chapter 2.).

As a further step (Chapter 5), the idea of metal trapping has not been limited to the case of Cu, but we also generalized such concept considering the possibility to encapsulate **different metal atoms (Ni, Co, and Fe)**, which they can be provide experimentally as vapour during the CVD growth on Cu(111). Such metal-trapped structures have been extensively studied for the hydrogen evolution reaction (HER), the cathodic half-reaction of water electrolysis.

In the second part of the thesis, we moved to a different chemically activated 2D/metal interface: **nitrogen-doped G supported on the Ni(111) surface**. This work was carried out in collaboration with the experimental group led by C. Africh (CNR-IOM in Trieste), with the valuable contribution of S. Fiori.

In Chapter 6, we deeply investigated, both from a **structural and electronic** point of view, the **N-dopant configurations into the graphene matrix**, validating our models through the comparison between **simulated and experimental STM and STS images**.

Finally, in Chapter 7, we studied the **intercalation mechanism of CO molecules** at the interface between **Gr and Ni(111)**, explaining why the process is favorable when graphene is doped with N atoms, as observed by our experimental collaborators. Such a result may open to the possibility of using these interfaces as a sequestration system or a sensor for CO.

2. Theoretical Background

In this chapter, some fundamental aspects of electronic structure theory and its applications in electrocatalysis and surface science will be introduced. In particular, the density functional theory (DFT) will be first presented in its fundamental aspects (which is the method used for all calculations of this thesis work), followed by the presentation of all relevant properties in electrocatalysis and surface science that can be calculated from it.

2.1. The Schrödinger equation

A system consisting of interacting nuclei and electrons can be described by the many-body wavefunction Ψ, which depends on the time and the position of each electron and each nucleus in the system. In the case of N electrons with coordinates $\mathbf{r}_1,\mathbf{r}_2, \ldots,\mathbf{r}_N$ and M nuclei with coordinates $\mathbf{R}_1,\mathbf{R}_2, \ldots ,\mathbf{R}_M$, the wavefunction Ψ can be written as:

$$\Psi = \Psi(\boldsymbol{r}_1, \boldsymbol{r}_2, \ldots, \boldsymbol{r}_N; \boldsymbol{R}_1, \boldsymbol{R}_2, \ldots, \boldsymbol{R}_M; t) \qquad (2\text{-}1)$$

Applying the Hamiltonian operator (H) to Ψ, we obtain the time-dependent Schrödinger equation (SE):

$$H\Psi = \mathrm{i}\hbar\left(\frac{\partial\Psi}{\partial t}\right) \qquad (2\text{-}2)$$

which is the quantum-mechanical equivalent of the Newton's second law of motion.

Unfortunately, its analytical solution is possible only for monoelectronic systems, making the SE not useful for real problems. However, approximate solutions can be obtained by applying approximations to both the Hamiltonian operator (H) and the wave-function (Ψ), which are to discuss next.

If the Hamiltonian operator is time-independent:

$$H(\mathbf{r}, \mathbf{R}, \mathrm{t}) = H(\mathbf{r}, \mathbf{R}) \qquad (2\text{-}3)$$

that the system is in a stationary state, the wavefunction can be written as follows:

$$\Psi(\mathbf{r},\mathbf{R},\mathrm{t}) = \psi(\mathbf{r},\mathbf{R})\, e^{\frac{-iEt}{\hbar}} \qquad (2\text{-}4)$$

and SE takes the following form:

$$H(\boldsymbol{r},\boldsymbol{R})\, \psi(\boldsymbol{r},\boldsymbol{R}) = \mathrm{E}\, \psi(\boldsymbol{r},\boldsymbol{R}) \qquad (2\text{-}5)$$

At a second level, relativistic effects and magnetic couplings (spin-spin, spin-orbit, etc.) are neglected. This leads to an electrostatic non-relativistic Hamiltonian (in atomic unit):

$$H(\boldsymbol{r},\boldsymbol{R}) = T_N + T_e + V_{e-N} + V_{N-N} + V_{e-e} = -\sum_{A=1}^{M} \frac{1}{2M_A} \nabla_A^2 - \sum_{i=1}^{N} \frac{1}{2} \nabla_i^2 - \sum_{A=1}^{M} \sum_{i=1}^{N} \frac{Z_A}{|R_A - r_i|} + \sum_{i=1}^{N} \sum_{j>i}^{N} \frac{1}{|r_i - r_j|} + \sum_{A=1}^{M} \sum_{B>1}^{M} \frac{Z_A Z_B}{|R_A - R_B|} \qquad (2\text{-}6)$$

where Z_A (Z_B) and R_A (R_B) are the charge and the position of the nucleus A (B), respectively; r_i and r_j is the position of the electron i and j, respectively. The first two terms in eq. 2-6 are the kinetic energy operators for each nucleus (T_N) and electron (T_e) in the system, where ∇_A^2 and ∇_i^2 are the Laplace operators, defined as follows:

$$\nabla_A^2 = \left(\frac{\partial^2}{\partial x_A^2} + \frac{\partial^2}{\partial y_A^2} + \frac{\partial^2}{\partial z_A^2} \right) \qquad (2\text{-}7)$$

$$\nabla_i^2 = \left(\frac{\partial^2}{\partial x_i^2} + \frac{\partial^2}{\partial y_i^2} + \frac{\partial^2}{\partial z_i^2} \right) \qquad (2\text{-}8)$$

The next approximation to be introduced is the Born-Oppenheimer (BO) approximation, thanks to which it is possible to separate, or better uncouple, the nuclear motion from electronic one.

The BO approximation allows us to rewrite the Hamiltonian operator of eq. (2-6) as the sum of two operators:

$$H(\boldsymbol{r},\boldsymbol{R}) = H_N(\boldsymbol{R}) + H_e(\boldsymbol{r};\boldsymbol{R}) \qquad (2\text{-}9)$$

where $H_N(\boldsymbol{R})$ is a function only of the nuclear coordinates, while the operator $H_e(\boldsymbol{r};\boldsymbol{R})$ is a function of the electronic coordinates but it depends on the fixed nuclear coordinates $\boldsymbol{R}$ (i.e. nuclear coordinates are parameters). In other words, fixing the molecular geometry, the term related to the nucleus-nucleus repulsion (V_{N-N}) becomes a constant.

Therefore, applying the BO approximation, eq. (2-5) splits into two equations, one for electrons and one for nuclei:

$$H_{el}(\boldsymbol{r};\boldsymbol{R})\psi_{el}(\boldsymbol{r},\boldsymbol{s}) = E_{el}\psi_{el}(\boldsymbol{r},\boldsymbol{s}) \qquad \text{(2-10)}$$

$$[H_N(\boldsymbol{R}) + E_{el} + V_{N-N}(\boldsymbol{R})]\phi_N(\boldsymbol{R}) = E\phi_N(\boldsymbol{R}) \qquad \text{(2-11)}$$

Once the approximations on the Hamiltonian are defined, we move on how to define the wavefunction ψ. A convenient way to simplify the wavefunction of a polyelectronic system is the orbital approximation, which is an independent particle model. In other words, the motion of n electrons is independent and the wavefunction ψ can be written as a product of n functions, each dependent on the coordinates of one electron only: i.e. monoelectronic functions called as spin-orbitals $\phi_i(r_i, s_i)$. The polyelectronic wavefunction ψ is defined as follows:

$$\psi(\boldsymbol{r}_1, \boldsymbol{s}_1, \boldsymbol{r}_2, \boldsymbol{s}_2, \dots, \boldsymbol{r}_n, \boldsymbol{s}_n) = \Phi_1(\boldsymbol{r}_1, \boldsymbol{s}_1)\Phi_2(\boldsymbol{r}_2, \boldsymbol{s}_2) \dots \dots . \Phi_n(\boldsymbol{r}_n, \boldsymbol{s}_n) \qquad \text{(2-12)}$$

where the electron 1 is described by the spin-orbital Φ_1, electron 2 by the spin-orbital Φ_2, and so on.

Suppose now that the spin-orbitals ϕ_i were obtained as the solutions of the single electron Schrödinger equations (we omit for simplicity the spin):

$$H_0(\boldsymbol{r}_i)\Phi_i(\boldsymbol{r}_i) = \varepsilon_i\Phi_i(\boldsymbol{r}_i) \qquad \text{(2-13)}$$

with ε_1 the smallest eigenvalue and $\varepsilon_1 < \varepsilon_2 < \dots < \varepsilon_n$.

Therefore, replacing the trial solution of eq. (2.12) in eq. (2.13) we find:

$$E = \varepsilon_1 + \varepsilon_2 + \dots + \varepsilon_n \qquad \text{(2-14)}$$

the lowest-energy configuration of the system is obtained when we fill the lowest-energy eigenstates of the single-particle equation (2.13) with one electron in each state, starting from the lowest eigenvalue.

However, the orbital approximation, as written in eq. (2.12), carries some important drawbacks. The most important relates to the fact that the wavefunction does not obey Pauli’s exclusion principle.

However, it is possible to overcome such a problem by expressing the wavefunction through a Slater determinant, which satisfies antisymmetry requirements, and consequently the Pauli principle:

$$\psi(\boldsymbol{r}_1, \boldsymbol{r}_2) = \frac{1}{\sqrt{2}} \begin{vmatrix} \phi_1(\boldsymbol{r}_1) & \phi_1(\boldsymbol{r}_2) \\ \phi_2(\boldsymbol{r}_1) & \phi_2(\boldsymbol{r}_2) \end{vmatrix} \qquad (2\text{-}15)$$

The Slater determinant is at the basis of the Hartree-Fock method, which will be discussed in the next paragraphs.

2.2.The Hartree-Fock Approximation

Let us consider the wavefunction ψ with the lowest energy. The energy (E) of this state is obtained by multiplying both sides of eq. (2.10) by ψ^* and integrating over all the variables:

$$E = \int d\boldsymbol{r}_1 \ldots d\boldsymbol{r}_N \, \psi \, \hat{H} \, \psi^* \qquad (2\text{-}16)$$

if we minimize the energy E with respect to variations of the functions $\phi_i(\boldsymbol{r})$ in the Slater determinant of eq. (2-15), and we require that these functions are orthonormal:

$$\frac{\delta E}{\delta \phi_i^*} = 0 \qquad (2\text{-}17)$$

$$\int d\mathbf{r} \phi_i^*(\mathbf{r}) \phi_j^*(\mathbf{r}) = \delta_{ij} \qquad (2\text{-}18)$$

where δ_{ij} is the Kronecker delta and is equal to 1 if $i = j$, 0 if $i \neq j$, then we obtain the Hartree–Fock equations:

$$\left[- \frac{\nabla^2}{2} + V_n(\mathbf{r}) + V_{\mathrm{H}}(\mathbf{r}) \right] \phi_i(\mathbf{r}) + \int d\mathbf{r}' V_x(\mathbf{r}, \mathbf{r}') \, \phi_i(\mathbf{r}') = \varepsilon_i \phi_i(\mathbf{r}) \qquad (2\text{-}19)$$

An additional potential, V_x, called Fock exchange potential has been introduced. The explicit expression of this potential is:

$$V_x(\mathbf{r}, \mathbf{r}') = - \sum_j \frac{\phi_j^*(\mathbf{r}') \phi_i(\mathbf{r})}{|\mathbf{r} - \mathbf{r}'|} \qquad (2\text{-}20)$$

the sum runs over the occupied single-particle states. The $V_x(\mathbf{r}, \mathbf{r}')$ is a non-local exchange potential in single-particle equations. Its evaluation involves an integration over the additional variable $\mathbf{r}'$ that complicates enormously the solution of the Hartree–Fock equations. V_x arises from Pauli's exclusion principle and prevents that two electrons occupy the same quantum state.

So, the Hartree-Fock energy is:

$$E^{HF} = T + E_{V_n} + E_H + E_x + E_{ii} \qquad (2\text{-}21)$$

The first term in eq. (2-21) is the kinetic energy (T), and the second term is the expectation value of the external potential V_n. The third term is the Hartee energy (E_H), followed by the energy involving the exchange operator (E_x), and finally the repulsion between the nuclei (E_{ii}).

The only remaining element left out of the picture is the correlation between electrons. Owing to the Coulomb repulsion, the probability of finding an electron somewhere will decrease if there is another electron nearby. Therefore, it is possible to add in the single-particle equations an additional potential V_c(r), where 'c' stands for correlation.

The exact correlation energy (E_c) is defined, in terms of the exact energy (E_{exact}) and the Hartree-Fock energy (E_{HF}), as follows:

$$E_c = E_{exact} - E_{HF} \qquad (2\text{-}22)$$

In the following section, we will present the density functional theory, which is an independent particle approach that incorporates the effect of interactions and correlation among the particles.

2.3. The Density Functional Theory

The Density Functional Theory (DFT) is a quantum mechanical method originally proposed by P. Hohenberg and W. Kohn in 1964.[120] Over the following years, it has been further developed, becoming today one of the most used computational methods. The main concepts behind the theory will be discussed in the following sections.

2.3.1. The Hohenberg-Kohn theorems

The density functional theory is based on the following two theorems:

- **Theorem 1.** The ground state of a multi-electronic system is a functional of the electronic charge density $\rho(\mathbf{r})$. The functional (f) exists and is unique: E = f[$\rho(\mathbf{r})$].

- **Theorem 2.** The ground state of a multi-electron system can be obtained variationally. The electron charge density ($\rho(\mathbf{r})$) that minimizes the total energy is the exact ground-state density.

It is clear how such theory has significant advantages over the Hartree-Fock based methods: while in HF the ground state energy is obtained from the wave function (ψ), which depends on 4N variables (where N is the number of the electrons), in DFT formalism the ground-state energy depends only on the 3 variables (x, y, z), regardless of the extent of the system studied.

2.3.2. The Kohn-Sham equations

Although the two previous theorems assure the existence and uniqueness of such functional, they say nothing about what form this functional should take nor how the calculation of the ground state should proceed.

In 1965, W. Kohn and L. J. Sham introduced the formalism to make the theory operational.[121] They decomposed the total energy into various contributions and for each of them defined the functional form:

$$E[\rho(\mathbf{r})] = T[\rho(\mathbf{r})] + V_{Ne}[\rho(\mathbf{r})] + J_{ee}[\rho(\mathbf{r})] + E_{xc}[\rho(\mathbf{r})] \qquad (2\text{-}23)$$

where T, V_{Ne}, J_{ee}, and E_{xc} are the functionals for the electron kinetic energy, electron-nucleus attractive potential, electron-electron repulsive potential, and exchange-correlation potential, respectively.

The analytical form of these functionals, with the exception of E_{xc}, has been precisely defined. Instead, the exchange-correlation functional is not yet known exactly. However, E_{xc} may be further decomposed into the following contributions (as will be discussed in the following section):

$$E_{xc}[\rho(\mathbf{r})] = E_x[\rho(\mathbf{r})] + E_c[\rho(\mathbf{r})] \qquad (2\text{-}24)$$

where E_x and E_c are the exchange and correlation functionals, respectively.

Once defined the shape of the functional E[$\rho(\mathbf{r})$], the analytical form of the charge density ($\rho(\mathbf{r})$) remains to be defined. According to the Kohn-Sham scheme, the ground-state charge density of N electrons is defined as:

$$\rho(\mathbf{r}) = \sum_u |\varphi_{u,KS}(\mathbf{r})|^2 \qquad (2\text{-}25)$$

where $\varphi_{u,KS}$ (u=1,….,n) are monoelectronic functions called as Kohn-Sham orbitals, which can be obtained by iterative resolution of monoelectronic equations called as Kohn-Sham equations (similarly to Hartree-Fock method). Such Kohn-Sham orbitals can be linearly expanded on a set of basis functions, whose linear coefficients are optimized to obtain the charge density corresponding to the ground state.

The KS equations are defined as:

$$F_{KS}(i)\,\varphi_{u,KS}(i) = \varepsilon_{u,KS}\,\varphi_{u,KS}(i) \qquad (2\text{-}26)$$

where the F_{KS} operator is defined as:

$$F_{KS}(i) = -\frac{1}{2}\nabla_i^2 - \sum_A \frac{Z_A}{|r_A - r_i|} + \int \frac{\rho(r_i)}{|r_i - r_j|} d\tau_i + V_{xc}(i) \qquad (2\text{-}27)$$

The exchange-correlation operator V_{xc} is the functional derivative of the exchange-correlation energy $E_{xc}[\boldsymbol{\rho}]$, as shows in the following equation:

$$V_{xc}(i) = \frac{\partial E_{xc}[\boldsymbol{\rho}]}{\partial \rho} \qquad (2\text{-}28)$$

So, before solving the KS mono-electronic equations, you need to specify the expression for the exchange-correlation functional $E_{xc}[\boldsymbol{\rho}]$, calculate the V_{xc} functional derivative and insert it into the F_{KS} operator. Once the form of $E_{xc}[\boldsymbol{\rho}]$ has been set, the KS-SCF method is variational. The forms proposed for $E_{xc}[\boldsymbol{\rho}]$ are numerous and represent the attempt to approximate the true expression of $E_{xc}[\boldsymbol{\rho}]$.

2.3.3. Exchange-correlation functionals

The XC functional could take different shapes, even extremely complex. However, it can be reasonably expected as a quantity that depends in some way on the integral of the density over all the space.

2.3.3.1. Local density approximation (LDA)

In the local density approximation (LDA), the exchange-correlation functional $E_{xc}[\rho]$ depends only on the local value of the electronic charge density $\rho(\boldsymbol{r})|_{\boldsymbol{r}=\boldsymbol{r}'}$:

$$E_{xc}^{LDA} = E_{xc}[\rho(\boldsymbol{r})|_{\boldsymbol{r}=\boldsymbol{r}'}] \qquad (2\text{-}29)$$

The LDA already represents a strong limitation of the possible shape of the functional. Indeed, the integral on the variable $\boldsymbol{r}'$ is limited to the value that the density assumes only in $\boldsymbol{r}'$ and we do not give any importance to the trend of $\rho(\boldsymbol{r})$ around $\boldsymbol{r}'$. In other words, the values that the density assumes in the different points of space all enter with the same “weight” in the E_{xc}^{LDA} calculation.

In the homogeneous electron gas model $\rho(\boldsymbol{r})$ is constant and therefore the LDA is not an approximation. For example, in the case of metals, LDA provides acceptable results, and therefore considering the electron density $\rho(\boldsymbol{r})$ to be uniform is a reasonable approximation. Instead, when LDA is applied to molecules, the results are often disappointing since $\rho(\boldsymbol{r})$ is not uniform in space.

2.3.3.2. Gradient generalized approximation (GGA)

The electron density of a molecule has a highly irregular pattern near the nuclei, while it tends asymptotically to zero for $\boldsymbol{r} \to \infty$. This led to functionals that do not depend only on the local value of the density $\rho(\boldsymbol{r})|_{\boldsymbol{r}=\boldsymbol{r}'}$, but also on the local value of the density gradient $\nabla\rho(\boldsymbol{r})|_{\boldsymbol{r}=\boldsymbol{r}'}$:

$$E_{xc}^{GGA} = E_{xc}[\rho(\boldsymbol{r})|_{\boldsymbol{r}=\boldsymbol{r}'}, \nabla\rho(\boldsymbol{r})|_{\boldsymbol{r}=\boldsymbol{r}'}] \qquad (2\text{-}30)$$

The local values of density derivatives allow to have an approximation of the trend of $\rho(\boldsymbol{r})$ nearby $\boldsymbol{r}'$.

The GGA represents therefore a step forward compared to the LDA because it takes into account the "form" of $\rho(\boldsymbol{r})$ near $\boldsymbol{r}'$ and not only its value in the point $\boldsymbol{r}'$. The “weight” of $\rho(\boldsymbol{r})$ at each point depends on the the gradient $\nabla\rho(\boldsymbol{r})$ calculated in that point.

Among the many GGA functionals available, the Perdew–Burke-Ernzerhof (PBE) functional[122] is one of the best known and used for the study of solids. Thus, most of the calculations of this work have been carried out using this functional.

2.3.4. The DFT limitations

Although density functional theory has been successfully employed in several computational studies thanks to the good compromise between its computational cost and accuracy, it still has some limitations, as discussed below.

One shortcoming of the LDA/GGA functionals is their inability of predicting correct bandgaps in semiconductors and insulators, which are systematically underestimated. Since the inaccuracy is related to how the exchange part is described, one possible approach to overcome such a limitation is by mixing some amount of the HF exchange into the LDA/GGA exchange functional, thus constructing a hybrid functional. The success of hybrid functionals in correcting the band gap values is often attributed to the fact that the HF exchange is exact. Indeed, the introduction of a certain amount of the HF exchange induces to over-localization of the electronic states, which can compensate for the tendency of standard DFT to delocalize electronic states. This implies that hybrid functionals lead to a systematic cancellation of errors and therefore to correct band-gap energies.

Another big limitation of using DFT is the description of van der Waals forces. Such interactions are caused by dynamical correlations between fluctuating charge distributions and are therefore related to how the correlation part is defined. Since the correlation functionals are local/semi-local within the LDA/GGA formalism, standard DFT methods are not able to accurately describe these long-range interactions.

Nevertheless, their crucial importance has led to the development of different strategies to remedy this shortcoming. On the one hand, the energy calculated within the LDA/GGA formalism can be corrected through a simple pair-wise force field, which is optimized for several DFT functionals. Such an approach has been introduced in 2006 by S. Grimme[123] and it is called DFT-D (in which D stands for dispersion). Specifically, if we consider the D2 version,[124] the Kohn-Sham energy (E_{KS-DFT}) corrected for the dispersion contribution (E_{disp}) is defined as follows:

$$E_{DFT-D2} = E_{KS-DFT} + E_{disp} \qquad (2\text{-}31)$$

where the term E_{disp}, in the formalism developed by Grimme, is calculated as follows:

$$E_{disp} = -s_6 \sum_{i=1}^{N-1} \sum_{j=i+1}^{N} \left(\frac{c_6^{ij}}{R_{ij}^6} f_{dmp}\left(R_{ij}\right)\right) \qquad (2\text{-}32)$$

where s_6 is a scale factor depending only on the type of functional used, N is the number of atoms in the system, c_6^{ij} and R_{ij}^6 are the dispersion coefficient and the distance between a pair of ij atoms, respectively, and $f_{dmp}\left(R_{ij}\right)$ is a dumping function.

Although DFT-D2 is one of the most popular methods for the modeling of molecules and solids, it presents many empirical terms that have been optimized on specific sets of molecules.

An alternative to DFT-D methods is the use of functionals (vdW-DF[125,126]) appropriately designed to describe the van der Waals interactions. These functionals divide the exchange-correlation term into a "local" part and a non-local correlation:

$$E_{xc} = E_{xc}^0 + E_c^{nl} \qquad (2\text{-}33)$$

where E_{xc}^0 is the local XC functional (LDA/GGA) and E_c^{nl} is the non-local correlation part which takes into account long-range interactions.

Unlike Grimme’s approach which only corrects the energy of the system (and consequently also the forces acting on the atoms), it is now clear that only one energy is directly calculated in this case.

Most of the calculations of this thesis were carried out by employing the vdW-DF2$^{\text{C09x}}$ functional.[127] Such a functional, as demonstrated by several works in the literature, provides the best description for systems consisting of a graphene layer adsorbed on a metal surface.[128]

2.4. Periodic Boundary Conditions

A crystal is a solid material whose constituents are arranged in a highly ordered structure, forming a crystal lattice. Such a system can be described through the Born-von Karman boundary conditions, which impose a periodic wavefunction on a certain Bravais lattice (whose lattice vectors are $\boldsymbol{a}_1$, $\boldsymbol{a}_2$, and $\boldsymbol{a}_3$).

2.4.1. Bloch theorem and Brillouin zone sampling

When we are dealing with solid systems, the potential $V(\boldsymbol{r})$ is periodic:

$$V(\boldsymbol{r}) = V(\boldsymbol{r} + \boldsymbol{R}) \qquad \text{(2-34)}$$

where $\boldsymbol{R} = n_1\boldsymbol{a}_1 + n_2\boldsymbol{a}_2 + n_3\boldsymbol{a}_3$, i.e. same periodicity of the direct lattice.

Under this condition, the mono-electron wave functions, which are the basis of the Kohn-Sham formalism (2.3.2), must respect the Bloch theorem. Such a theorem states that the solutions (known as Bloch functions) of a single electron Schrödinger equation with a periodic potential take the form of a plane wave modulated by a periodic function:

$$\psi_k(\mathbf{r}) = \mathrm{u}_k(\mathbf{r})\, e^{i\boldsymbol{k}\cdot\mathbf{r}} \qquad \text{(2-35)}$$

where $\mathrm{u}_k(\mathbf{r})$ is the periodic function with the same periocity as the crystal (i.e. $\mathrm{u}_k(\mathbf{r}) = \mathrm{u}_k(\mathbf{r} + \mathbf{R})$) and the wave vector $\boldsymbol{k}$ is the crystal momentum vector.

As a result, equation (2-35) may also be expressed as follows:

$$\psi_k(\mathbf{r} + \mathbf{R}) = e^{i\boldsymbol{k}\cdot\mathbf{R}}\psi_k(\mathbf{r}) \qquad \text{(2-36)}$$

The periocity carries out a fundamental role to describe the properties of a crystal. Indeed, in a real finite solid, the surface effects (which are a violation of translation symmetry) involve only a small fraction of atoms. Therefore, from a computational point of view, the solid is thought as an infinite crystal obtained from a finite crystal consisting of N cells repeated periodically. For example, considering a 1D chain of atoms and applying the Born-von Karman boundary conditions to the Bloch function defined in eq. (2-36), we get:

$$\psi_k(\mathbf{r} + N_i\boldsymbol{a}_i) = e^{iN_i\boldsymbol{k}\cdot\boldsymbol{a}_i}\psi_k(\mathbf{r}) = \psi_k(\mathbf{r}) \qquad \text{(2-37)}$$

from which it follows that:

$$e^{iN_i\boldsymbol{k}\cdot\boldsymbol{a}_i} = 1 \qquad \text{(2-38)}$$

which results in:

$$N_i \boldsymbol{k}_i \boldsymbol{a}_i = 2\pi r_i \qquad \text{(2-39)}$$

with r_i is an integer number. The allowed wave vectors $\boldsymbol{k}$ are then:

$$\boldsymbol{k} = \frac{r_1}{N_1}\frac{2\pi}{\boldsymbol{a}_1} + \frac{r_2}{N_2}\frac{2\pi}{\boldsymbol{a}_2} + \frac{r_3}{N_3}\frac{2\pi}{\boldsymbol{a}_3} \qquad \text{(2-40)}$$

where the basis vectors:

$$\boldsymbol{b}_i = \frac{2\pi}{\boldsymbol{a}_i} \qquad \text{(2-41)}$$

are the reciprocal lattice vectors.

If we use now the Bloch function, as defined in eq. (2-35), into the single-particle Schrödinger equation and remove the exponential factor from both terms, we obtain the following equation:

$$\left[\frac{1}{2}(-i\nabla + \boldsymbol{k})^2 + V(\boldsymbol{r})\right] u^{\boldsymbol{k}}(\boldsymbol{r}) = \varepsilon^{\boldsymbol{k}} u^{\boldsymbol{k}}(\boldsymbol{r}) \qquad \text{(2-41)}$$

where V (the periodic potential) and $u^{\boldsymbol{k}}$ have the same period. This allows us to consider the equation only in the volume of the unit cell. The eigenvalues $\varepsilon^{\boldsymbol{k}}$ return a continuous function in $\boldsymbol{k}$ (since the Hamiltonian contains $\boldsymbol{k}$ as a continuous parameter) and discrete in n, where n labels the elements of the infinite set of eigenvalues. In this sense, the Schrödinger equations that determine the monoelectronic functions must be solved at different points k in the reciprocal unit cell.

The use of the Wigner-Seitz cell in reciprocal space defines the first Brillouin zone (BZ). The characterization of eigenvalues and eigenvectors within BZ allows one to define completely the electronic structure of the studied system. From a computational point of view, grids with different k-points, along the three lattice vectors of the reciprocal cell, are used to sample the reciprocal space and solve equations in the form of (2-41).

2.5. Basis Sets

2.5.1. Plane waves basis set

The periodic function $\mathrm{u}_k(\mathbf{r})$, already introduced in section 2.4.1, can be expanded on a set of basis functions consisting of plane waves. This choice is particularly suitable when dealing with metal systems, whose correct description requires the use of non-localized functions. A plane wave can be written as follows:

$$\chi_{\boldsymbol{k}}(\boldsymbol{r}) = e^{i\boldsymbol{kr}} \qquad (2\text{-}42)$$

where $\boldsymbol{r}$ is the position vector and $\boldsymbol{k}$ is the wave vector. This last term can be thought as a frequency factor where high values of $\boldsymbol{k}$ indicate rapid wave oscillations.

The use of plane waves has many advantages over localized basis sets. For instance, the number of basis functions depends only on the cell volume and the plane wave energy cut-off (in practice a maximum value of $\boldsymbol{k}$ must be chosen), regardless of the number and nature of the atoms in the system. In addition, these basis functions do not have any optimized parameter, which is common to have with localized Gaussian basis functions.

Finally, the use of plane waves is particularly suitable for the study of chemical reactivity, as it prevents the well-known basis set superposition error (BSSE): an error which may occur when the number of localized basis functions is not sufficient and leads to an overestimation of the binding energies.

2.5.2. Pseudopotentials

The description of localized states on atomic nuclei by using a plane wave basis set requires functions with a small wavelenght, i.e. plane waves with high **k** values. Due to this, a high kinetic energy energy cut-off is needed, making their computational cost very prohibitive.

However, it is often possible to replace a difficult problem with a simpler one, For example, an effective potential (even called pseudopotential) can replace the atomic all-electron potential (full-potential), such that core states are eliminated and the valence electrons are described by pseudo-wavefunctions with significantly fewer nodes (see Figure 2-1), making plane-wave basis sets more practical to use. In this approach only the “chemically active” valence electrons are dealt with explicitly, while the core electrons are “frozen”, being considered together with the nuclei as rigid non-polarizable ion cores.

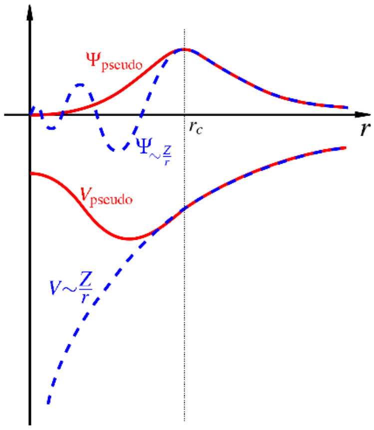

Figure 2-1: Comparison of a wavefunction in the Coulomb potential of the nucleus (blue) to the one in the pseudopotential (red). The real and the pseudo wavefunction and potentials match above a certain cutoff radius r_C.

All the caculations of this thesis have been carried out using ultrasoft pseudopotentials (USPP),[129] which are much softer in the core region than ordinary norm-conserving pseudopotentials (NCPP).[130] Futher details will be provided in Chapter 3.

2.6. Electronic properties

In this paragraph, we introduce some important properties that can be calculated using the methods previously discussed. Such properties are linked to experimental quantities and can therefore be used for direct comparison with experiments, as shown in the following chapters.

2.6.1. Density of states (DOS) and Projected Density of States (PDOS)

The density of states (DOS) describes the number of electronic states that are available in a system at each energy. In other words, it is a useful tool that provides a counting of the states at the energy E (for simplicity, the spin polarization is not explicitly considered in the following expression):

$$DOS(E) \propto \int_{BZ} d\boldsymbol{k}\,\delta(\varepsilon(\boldsymbol{k}) - E) \qquad \text{(2-43)}$$

where $\varepsilon(\boldsymbol{k})$ is a generic eigenvalue of KS equations.

In addition, to better analyze the character of bonds between different atoms, it is useful to introduce the projected density of states (PDOS), which is defined as follows:

$$PDOS(\alpha, E) \propto \int_{BZ} d\boldsymbol{k} |\langle \phi_{\alpha}^{at} | \psi_{\boldsymbol{k}} \rangle|^2 \delta(\varepsilon(\boldsymbol{k}) - E) \qquad \text{(2-44)}$$

where ϕ_{α}^{at} is the atomic orbital with quantum number α centered on the atom of interest.

2.6.2. Scanning Tunneling Microscopy (STM)

As discussed in the Introduction, one of the most important experimental techniques for the surface analysis that one can simulate is the scanning tunneling spectroscopy (STM). To compute that, it is necessary to introduce the integrated local density of states (ILDOS), which is defined as follows:

$$ILDOS(\boldsymbol{r}) = \int_{\varepsilon_F}^{\varepsilon_F + V_{bias}} dE \; LDOS(\boldsymbol{r}, E) \qquad \text{(2-45)}$$

with the local density of states (LDOS) defined in the following way:

$$LDOS(\boldsymbol{r}, E) = \int_{BZ} d\boldsymbol{k} |\psi_i(\boldsymbol{k})|^2 \delta(\varepsilon(\boldsymbol{k}) - E) \qquad \text{(2-46)}$$

where ε_F is the Fermi energy of the system and V_{bias} is the electrostatic potential energy difference between the tip and the sample under investigation.

Although several formalisms have been developed for the study of the tunneling process, which is a many-body problem, the Tersoff-Hamman approximation[131] is the one that has been most successfully used for its simplicity and effectiveness (although in some cases there are limits). Within this formalism, the tip is modeled as a spherical potential in which only the s-wave solution is considered. Under this assumption, it is possible to demonstrate that the tunneling current I, between the tip and the sample, is proportional to the ILDOS:

$$I(\boldsymbol{r}) \propto ILDOS(\boldsymbol{r}) \qquad \text{(2-47)}$$

From an experimental point-of-view, STM measurements can be performed in the modes of constant current or of constant height.

The constant height mode is easiest to simulate: it is sufficient to extract the ILDOS values at a fixed height z in order to build a 2D constant height STM image.

Instead, a constant current map requires to choose a certain value I for the current, defining an ILDOS isosurface in the 3D space, and then search, for each point of the xy plane of the cell, the corresponding value of the height z that meets the chosen isosurface.

Simulated STM images (within Tersoff-Hamman approximation) are shown in Chapters 3 (h-BN/Cu), 6 (N-Gr/Ni), and 7 (Gr/CO/Ni and N-Gr/CO/Ni).

2.6.3. Scanning Tunneling Spectroscopy (STS)

Another experimental technique based on the quantum tunneling effect is the scanning tunneling spectroscopy (STS), as already discussed in Chapter 1.3.1.

STS provides informations about the density of surface electrons in a sample as a function of their energy, by measuring the differential conductance (dI/dV), which is proportional to the LDOS:

$$\frac{dI(\boldsymbol{r},E)}{dV} \propto LDOS(\boldsymbol{r},E) \qquad (2\text{-}48)$$

As in STM experiments, it is possible to obtain constant height and constant current STS maps. The constant height mode requires to extract all the LDOS values at a fixed height z, resulting in a 2D constant height STS map.

Simulated constant height STS maps are shown in Chapter 6 (N-Gr/Ni).

2.7. Computational Thermochemistry

This paragraph reviews the main methods and approximations for the calculation of free energies, which are fundamental quantities in catalysis and electrocatalysis (as discussed in the next paragraph).

Two cases are currently presented by this section: the ideal-gas limit (in which translational and rotational degrees of freedom are taken into account) and the harmonic limit (generally used for adsorbates, in which all degrees of freedom are treated harmonically).

2.7.1. Ideal gas: molecules

In the ideal gas approximation, all the thermodynamic quantities are calculated by assuming that all spatial degrees of freedom are independent and separable into translational, rotational, and vibrational degrees of freedom.

The conversion of electronic energies, as obtained by DFT calculations, to thermodynamic properties in the ideal-gas framework is well established.[132]

The enthalpy, at the temperature T of interest, is calculated as follows (for an ideal gas, the enthalpy is not a function of pressure):

$$H(T) = E_{elec} + E_{ZPE} + \int_0^T C_p dT \qquad (2\text{-}49)$$

where E_{elec} is the electronic energy, E_{ZPE} is the zero-point energy, and C_p is the constant-pressure heat capacity.

The heat capacity is separable into translational ($C_{v,trans}$), rotational ($C_{v,rot}$), vibrational ($C_{v,vib}$), and electronic parts ($C_{v,elec}$), plus a term of k_B to switch from constant-volume to constant-pressure):

$$C_p = k_B + C_{v,trans} + C_{v,rot} + C_{v,vib} + C_{v,elec} \qquad (2\text{-}50)$$

The terms in equation (2-) are defined in the following way:

$$C_{v,trans} = \frac{3}{2} k_B \qquad (2\text{-}51)$$

$$C_{v,rot} = \begin{cases} 0\,, & monoatomic\ species \\ k_B\,, & linear\ molecule \\ \frac{3}{2} k_B\,, & nonlinear\ molecule \end{cases} \qquad (2\text{-}52)$$

$$C_{v,elec} = 0 \qquad (2\text{-}53)$$

The vibrational heat capacity contains 3N−6 degrees of freedom (DOF) for non-linear molecules (or 3N−5 degrees of freedom for linear molecules). The integrated form of the vibrational heat capacity is:

$$\int_0^T C_v dT = \sum_i^{vib\ DOF} \frac{\epsilon_i}{e^{\epsilon_i / k_B T} - 1} \qquad (2\text{-}54)$$

where ϵ_i are the energies associated with the vibrational frequencies ($\epsilon_i = h\omega_i$). Vibrational frequencies are computed by determining the second derivatives of the energy with respect to the Cartesian nuclear coordinates and then transforming to mass-weighted coordinates.

The ideal gas entropy can be calculated as a function of temperature and pressure in the following manner:

$$S(T,P) = S(T,P^0) - k_B \ln\left(\frac{P}{P^0}\right) = S_{trans} + S_{rot} + S_{vib} + S_{elec} - k_B \ln\left(\frac{P}{P^0}\right) \qquad (2\text{-}55)$$

where the translational, rotational, electronic, and vibrational components are calculated as below:

$$S_{trans} = k_B \left\{ln\left[\left(\frac{2\pi M k_B T}{h^2}\right)^{\frac{3}{2}} \frac{k_B T}{P^0}\right] + \frac{5}{2}\right\} \qquad (2\text{-}56)$$

$$S_{rot} = \begin{cases} 0 & ,if\ monoatomic \\ k_B \left[\ln\left(\frac{8\pi^2 I k_B T}{\sigma h^2}\right) + 1\right] & ,if\ linear \\ k_B \left\{\ln\left[\frac{\sqrt{\pi I_A I_B I_C}}{\sigma}\left(\frac{8\pi^2 k_B T}{h^2}\right)^{\frac{3}{2}}\right] + \frac{3}{2}\right\} & ,if\ nolinear \end{cases} \qquad (2\text{-}57)$$

$$S_{vib} = k_B \sum_i^{vib\ DOF}\left[\frac{\epsilon_i}{k_B T\ (e^{\epsilon_i/k_B T} - 1)} - \ln\left(1 - e^{-\frac{\epsilon_i}{k_B T}}\right)\right] \qquad (2\text{-}58)$$

$$S_{elec} = k_B \ln\left[2 \times (total\ spin) + 1\right] \qquad (2\text{-}59)$$

where I_A, I_B, and I_C are the three principal moments of inertia for a non-linear molecule, I is the degenerate moment of inertia for a linear molecule, and σ is the symmetry number of a molecule.

Once these thermodynamic quantities are defined, the ideal-gas Gibbs free energy is then just calculated from the combination of the enthalpy and entropy:

$$G(T,P) = H(T) - TS(T,P) \qquad (2\text{-}60)$$

2.7.2. Harmonic limit: adsorbates on surfaces

Moving from molecules (which are finite systems) to periodic systems, things start to get more complicated. Indeed, the conversion of electronic energies into thermodynamic properties is less established for adsorbates on surfaces. The simplest approach to deal with thermochemistry is by treating all 3N degrees of freedom of the adsorbate harmonically since the adsorbate often has non-real translational or rotational degrees of freedom. Thus, the internal energy and entropy of the adsorbate are calculated as follows:

$$U(T) = E_{elec} + E_{ZPE} + \sum_i^{harm\,DOF} \frac{\epsilon_i}{e^{\epsilon_i/k_B T} - 1} \qquad \text{(2-61)}$$

$$S = k_B \sum_i^{harm\,DOF} \left[\frac{\epsilon_i}{k_B T\,(e^{\epsilon_i/k_B T} - 1)} - \ln\left(1 - e^{-\frac{\epsilon_i}{k_B T}}\right) \right] \qquad \text{(2-62)}$$

and the Helmholtz free energy is calculated as:

$$F(T) = U(T) - TS(T) \qquad \text{(2-63)}$$

Within the harmonic limit approximation, the number of harmonic energies (ϵ_i) is 3N, where N is the number of atoms in the adsorbate. If one assumes that the pV term in $H = U + pV$ is negligible, then the Helmholtz free energy can be used to approximate the Gibbs free energy, as $G = F + pV$.

2.8. Computational electrochemistry

In this paragraph, we review the approaches to computational electrochemistry and present the method used in Chapters 4 (OER) and 5 (HER).

One of the most significant steps forward in this field has been made through the approach proposed by Nørskov et al.,[133] which relates the thermochemistry of the electrochemical reactions to the stability of the reaction intermediates as calculated by means of DFT. This method was originally proposed for the ORR over Pt(111), but it is formulated in a general approach, thus being in principle transferable to other electrochemical reactions as well as other catalysts. The model predicts a volcano-shaped relationship between the activity at the electrode and the stability of the reaction intermediates. In perfect agreement with experiments, it is computed that Pt and Pd metals are the best catalyst for the ORR process, but calculations suggest that a careful modification and targeted tuning of the substrate can be achieved to improve the fuel cells performance.

The computational background for the calculation of the Gibbs free energy differences (ΔG):

$$\Delta G = \Delta E_{w,water} + \Delta E_{ZPE} - T\Delta S + \Delta G_U + \Delta G(pH) + \Delta G_{field} \qquad (2\text{-}64)$$

to be calculated within a slab approach, along the electrochemical reaction path, is built up through simple yet important steps and assumptions:

1. The reference potential electrode is the standard hydrogen electrode (SHE), for which at pH = 0 (in the electrolyte solution) and at an electrode potential U = 0 V (vs. SHE) the anodic reaction $H^+ + e^- \rightarrow \frac{1}{2} H_2$ is in equilibrium at 1 bar H_2 in the gas-phase at 298 K, thus $G(H^+ + e^-) = G(\frac{1}{2} H_2)$, which becomes computationally affordable.

2. The solvent environment of the electrochemical cells can be modeled by one or more layers of water molecules, obtaining the solvent corrected electronic energy $\Delta E_{w,water}$. Most of the times this term is estimated as a constant correction added to the free energies.[134]

3. The bias effect (ΔG_U) on the energy of all states involving an electron in the electrode is accounted for by shifting the energy of the specific state by –eU, where U is the electrode potential.

4. The possible effect of the electrical field (ΔG_{field}) originated by the electrochemical double layer outside the surface on the adsorption energies is considered very small, thus negligible.[135]

5. The free energy of H^+ ions is corrected at pH ≠ 0 by $\Delta G(pH) = \pm k_B T ln([H^+]) = \pm k_B T ln(10) \times pH$; the sign will depend on whether H^+ is a reactant or a product (reduction or oxidation, respectively).

6. The free energy of the intermediates, at U = 0 V and pH =0 V, is obtained by correcting the electronic energy by the zero point energy contribution and entropy change: $\Delta E_{ZPE} - T\Delta S$. The corrections are not directly computed, but extracted from tabulated values for gas-phase molecules or previously reported DFT calculations.[136] Note that the free energy of liquid water (which is important when studying ORR and OER) is derived from gas-phase calculations by modifying the entropic term.[137,138]

Using this procedure, it is possible to obtain the electrode potential dependent free energy diagrams for a specific process at the electrode and consequently an estimate of the overpotential necessary to drive the reaction. To have no overpotential (ideal situation), all reaction steps need to be downhill by the equilibrium potential (U_0) of the corresponding reaction.

The approach proposed by Nørskov et al. allows one to identify the proper thermodynamic descriptors (like the adsorption energies of –O and –OH, in the case of ORR), which can explain the electrocatalytic performances of a specific substrate or give guidelines to identify the ideal catalysts. Linear scaling relations were discovered between the adsorption energies of different reaction intermediates on various transition-metal and oxide surfaces. For instance, there is a constant energetic separation between *OH and *OOH adsorbates, which is a source of an intrinsic overpotential for ORR. For such reasons, an ideal energy landscape cannot be achieved by common electrocatalysts. Indeed, this approach has been extensively used in computational electrochemical studies for elemental metal substrates[139] and metal alloys,[140] as well as to propose new and more efficient electrocatalysts with lower overpotentials and/or better performances.[141]

A technical, yet very important aspect to consider when building a theoretical knowledge of an electrochemical process concerns the estimation of the activation barriers along the oxidation or reduction steps, which has not been explicitly considered in the methodology by Nørskov et al. Indeed, beside the value of the free energy difference between two electrochemical steps (ΔG), the reaction barrier can significantly influence the reaction rate, thus the performance of the electrocatalyst. Computing the energy barriers ($\Delta E^{\ddagger}$ or $\Delta G^{\ddagger}$) through a periodic approach, in particular when involving heavy atoms (like the metal or metal oxide catalysts) is not, however, an easy task. As a consequence, the kinetic aspects of the electrochemical processes are often neglected or approximated with different transition states methodologies (e.g., nudged elastic band, NEB, method),[142] but a fully consistent frequency analysis is not performed. Moreover, activation barriers can discriminate between different reaction paths (for example associative vs. direct O_2 recombination for the OER, see paragraph 4.3) and rate determining steps can vary, similarly to what is observed for the free energy values, when including solvation effects.[143] The inclusion of the solvent in the quantum chemical setup is often crucial when describing free-energy profiles of reaction pathways, catalytic reactivity, spectroscopic properties, electrochemical steps in fuel cells or generally when describing chemical and physical processes taking place in solution. This can be done explicitly, by adding an adequate amount of solvent molecules, or implicitly, through continuum solvation models, such as the polarizable continuum model (PCM[144]), or with a suitable combination of the two, when a first solvation sphere is made of explicit molecules, often accounting for specific interactions (such as hydrogen bonds), and an outer solvation sphere is made of a dielectric medium.

It is clear that the computational description of an electrochemical process is a generally applicable and powerful tool for unraveling the reaction mechanisms and helping the design of new catalysts. This should nowadays become a preliminary step for checking the catalytic activity and stability before the experimental synthesis of new materials is performed.

3. h-BN Defective Layers as Giant N-Donor Macrocycles for Cu Adatom Trapping from the Underlying Metal Substrate

In this chapter, ab-initio simulations based on dispersion-corrected density functional theory calculations were performed to deeply investigate the interface formed between a pristine or defective h-BN monolayer and a Cu(111) surface. In the first part we focused on the structural and electronic properties of free-standing h-BN, as a reference for the corresponding Cu(111)-supported systems, by analyzing especially the effect of simple defects such as mono- and pluri-atomic vacancies. Subsequently, we investigated the role of the underlying Cu(111) substrate, discovering how unexpected effects can take place in the confined zone between h-BN and the metal. Interestingly, we show that when a defective h-BN layer is grown on a Cu (111) surface, metal adatoms spontaneously pop up from the bulk to fill the holes in the structure. Such Cu-trapping structures may be interesting for catalytic purposes.

The results reported in this chapter have been published in: Perilli, D., Selli, D., Liu, H., Bianchetti, E., Di Valentin, C., J. Phys. Chem. C 2018, 122(41), 23610-23622.

3.1. Introduction

The h-BN/metal interface is an interesting platform for many applications including catalysis, electrocatalysis and corrosion protection.[4,109] Both physical and chemical properties of bidimensional layers of h-BN were shown to be affected by the presence of an underlying substrate and of defects,[145,146] which may alter its insulating properties and chemical inertness. Cu is a very attractive substrate because of the possibility of using Cu foils and, thus, of moving towards large scale preparations for commercial use.[147] It is considered to be "weakly" interacting if compared to other substrates, such as Ni and Rh surfaces, with an equilibrium distance between 3.24-3.38 Å.[53,82] The growth of h-BN through chemical vapour deposition (CVD) on Cu (111) surface results in a non-perfect h-BN layer with several defects and grain boundaries.[148] Vacancies can also be created on purpose through selective sputtering by electron beam[54,55] or electron knock-on damage.[56] Holes of different sizes have been observed through transmission electron microscopy (TEM).[55,56,149] The shape is typically triangular, and they mostly expose N-terminated edges, although this was proved to depend on the preparation conditions by Cretu et al.,[150] who investigated varying conditions of temperature and of imaging, observing both N- and B-terminated defects.

Several theoretical studies have analyzed the possible models of monoatomic and multiatomic vacancies in free standing bidimensional h-BN.[74,151] In those works, density functional theory, in the gradient corrected approximation (GGA), was applied to determine electronic, magnetic, and chemical properties towards the reaction with small molecules (such as O_2, CO, etc..) of defective h-BN. Although, most of the theoretical investigations focus on monoatomic vacancies of N or B in free standing h-BN, some works are concerned with multiatomic vacancies, such as tetravacancies but also larger ones.[152,153] Those defects require very big supercell models to be correctly described and energetics could be largely affected by the availability of extra electron charge on the h-BN layer.

Electron rich h-BN sheets can be obtained by interfacing them with donor metals. Cu(111) surface is again a good candidate, since it was shown theoretically that some n-type doping derives from interfacing 2D h-BN with a Cu surface.[85,154] The lattice mismatch between these two materials is relatively small (1.8 %).[52] With a (24 × 24) supercell model Koitz et al. succeeded in modeling one experimentally observed moiré pattern.[78] In this same study they proved that the electronic properties of such system do not differ from the much less computationally expensive h-BN/Cu(111) commensurate interface. The most favorable registry was proven to present B atoms on the fcc position and N atoms on the top position with respect to the Cu atoms on the topmost surface metal layer, by both experiments and theory. Using this model, several groups have investigated electronic properties and molecular adsorption. Only in one work, monoatomic vacancies and Stone-Wales defects were introduced in the h-BN layer on top of the Cu(111) surface.

In the present work, we go beyond state-of-the-art calculations, first by applying hybrid functional methods to model defects in h-BN and, secondly, by investigating defective h-BN supported on a Cu(111) surface with larger supercell sizes that provide realistic vacancy concentration values. On top of that, we provide the first computational evidence of an interesting interface effect: we computed a thermodynamic driving force for metal atoms to pop up from the metal bulk and stabilize on the surface at the interface defects between bidimensional h-BN and the Cu(111) surface. In particular, the presence of holes in the h-BN lattice, in the form of monoatomic or pluriatomic vacancies, stimulates the formation of surface adatoms that eventually aggregate to completely fill the fault. This observation shows that the h-BN/Cu interface, which is generally recognized as a weakly interacting interface, could become chemically reactive in the presence of atomic vacancies. The metal adatoms, which are found to spontaneously pop up and emerge on the surface, could be active catalytic sites for specific chemical processes. This has been suggested by a recent study where surface nickel adatoms were observed to play a key role in the graphene growth on a Ni substrate. Our unexpected observation can be rationalized in terms of a high affinity of Cu atoms to N-donor ligands. Defective h-BN exposing N-terminated edges is a large multi N-donor macrocyclic ligand that can encapsulate metal atoms as a consequence of a huge stabilization effect deriving from the Cu-N bond formation. These conclusions could be generalized and possibly applied to other metal surfaces, or they could stimulate the idea of trapping different transition metal atoms (more precious but more active) from those of the underlying surface for catalytic purposes (as discussed in Chapter 5). Similarly, graphene-confined metal atoms were recently found to be efficient catalysts for methane conversion[155] and for benzene oxidation.[156] The metal atoms are stabilized by interposing N atoms into the C matrix

(Metal-N-C). These systems mimic metal-porphyrins, which are also excellent single-atom catalysts for crucial processes.

3.2. Computational Details

DFT calculations were mainly performed using the plane-wave-based Quantum ESPRESSO package (QE).[157] The ultrasoft pseudopotentials were adopted to describe the electron-ion interactions with Cu (3d, 4s), B (2s, 2p), N (2s, 2p) treated as valence electrons.[129] Energy cutoffs of 30 Ryd and 240 Ryd (for kinetic energy and charge density expansion, respectively) were adopted for all calculations. The convergence criterion of 0.026 eV/Å for the forces was used during geometry optimization and the convergence criterion for the total energy was set at 10^{-6} Ryd. For free-standing h-BN monolayer, calculations were also performed by using the CRYSTAL14 package (CRY14),[158] based on localized atomic basis set for comparison with the results from QE. The all-electron basis sets are 6-24++(d1) for B and 6-24++(d1) for N. The convergence criterion of 0.023 eV/Å for the forces was used during geometry optimization and the convergence criterion for the total energy was set at 10^{-6} Hartree.

For the pristine h-BN monolayer, a primitive cell was used with a large number of k-points, a mesh of 72 × 72 × 1 for geometry relaxation and of 144 × 144 × 1 for density of states (DOS) evaluation. Calculations were performed using both QE and CRY14 code. Perdew−Burke−Ernzerhof (PBE),[122] van der Waals (vdW-DF2^{C09x})[128] and hybrid (HSE[159] and B3LYP[160,161]) functionals were considered.

To model the boron and nitrogen monovacancy in the free-standing monolayer h-BN, a (8 × 8) supercell was used with the vdW-DF2^{C09x}/QE, PBE/QE, PBE/CRY14 and B3LYP/CRY14 methods. K-points meshes of 3 × 3 × 1 and 12 × 12 × 1 were used for the geometry relaxation and DOS. For the boron and nitrogen pluriatomic vacancy, a (10 × 10) supercell was used to avoid the interactions between adjacent periodic defects and the calculations were performed with the vdW-DF2^{C09x} functional as implemented in the QE code. K-points meshes of 2 × 2 × 1 and 11 × 11 × 1 were used for the geometry relaxation and DOS, respectively. Spin polarization was always included.

The Cu(111) surface was modeled by a four-layer slab model with the two bottom layers fixed to the bulk positions during the geometry relaxation to mimic a semi-infinite solid.

To avoid interactions between adjacent periodic images, a vacuum space of 20 Å was included in the slab model. For boron and nitrogen monovacancy in Cu (111) supported h-BN, (6 × 6) supercells of h-BN and Cu (111) were used with a lattice mismatch of 0.40 % (the h-BN lattice parameter was used according to experimental results[52]). K-points meshes of 3 × 3 × 1 and 18 × 18 × 1 were used for the geometry relaxation and DOS. For boron and nitrogen pluriatomic vacancy in Cu(111) supported h-BN, (10 × 10) supercells of h-BN and Cu (111) were used. K-points meshes of 2 × 2 × 1 and 11 × 11 × 1 were used for the geometry relaxation and DOS. For Cu (111) surface and all the Cu (111) supported h-BN systems, calculations were done only with the QE code. To properly take into account weak interactions, the van der Waals density functional vdW-DF2^{C09x}, which has been reported to have good overall performances for adsorption distances of graphene on metal surfaces,[60] was used.

The STM images for the Cu(111)-supported defective h-BN systems were simulated by using the Tersoff-Hamann approximation[87] with a constant height of 3 Å above the top atom.

3.3. Electronic properties of pristine h-BN

The description of the electronic band gap of insulators is still a challenge for standard density functional theory, which systematically underestimates it. The introduction of some exact exchange in the exchange-correlation functional can partially solve the problem and hybrid density functional methods produce more accurate band gap values when compared with experimental data. The band structure and density of states of pristine h-BN are shown in **Figure 3-1**, as obtained by PBE and hybrid functional B3LYP plane wave calculations (vdW-DF2^{C09x} and HSE06 provide similar results to PBE and B3LYP, respectively).

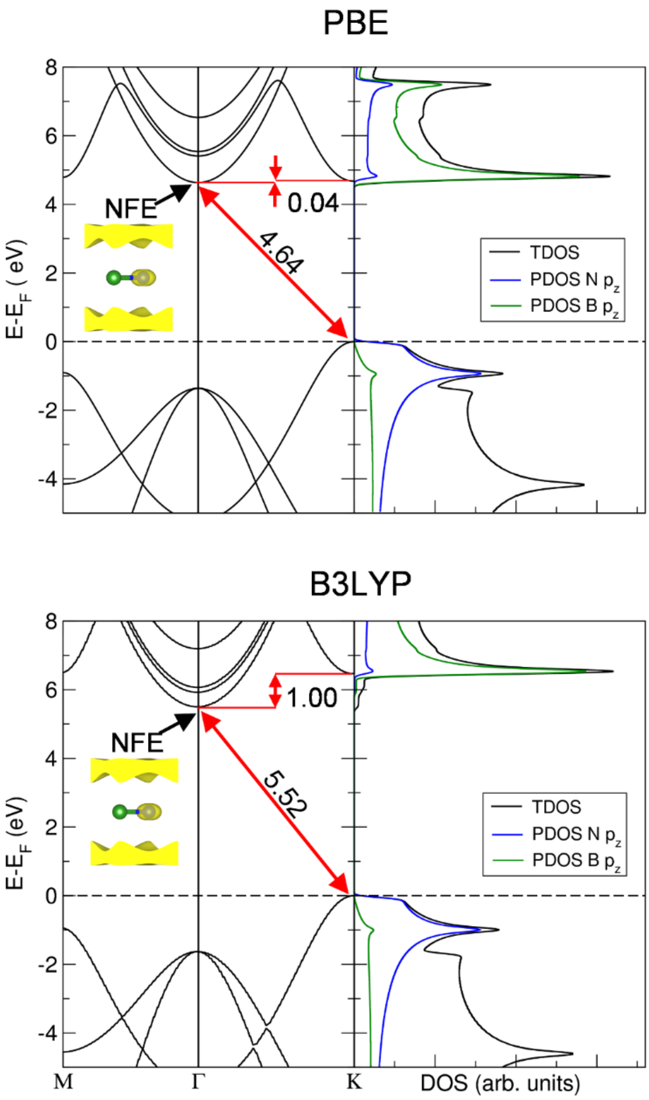

Figure 3-1: Band structures and total (TDOS) and projected (PDOS) density of states of monolayer h-BN obtained by PBE/QE and B3LYP/QE. The indirect band gaps are indicated by red arrows (with the corresponding value in eV) and the charge density plot of the bottom of the conduction band at Γ point ("nearly free electron" or NFE state) is shown in the inset. Legend of colors for TDOS and PDOS is given in each panel. Fermi levels are scaled to zero and indicated by dashed lines.

An indirect band gap is observed in all cases, with the top of the valence band in the K point and the bottom of the conduction band in the Γ point. For PBE, the direct and indirect band gaps are almost degenerate. The B3LYP band gap value is in better agreement with experiments, as expected.[65,162] The top edge of the valence band is mostly composed of the N p_z states, whereas the lowest unoccupied state of the conduction band at Γ is what is called the "nearly free electron" (NFE) state (see insets in **Figure 3-1**).

This peculiar state is characterized by a peak of electron density at about 2 Å above and below the atomic plane and it was already observed in previous works but only when using a plane wave basis set.[73] The highly delocalized nature of this state cannot be caught by a localized basis set CRY14 calculation. However, by adding gaussian functions in the empty zone above and below the atomic plane we succeed in getting the correct band structure.

3.4. Electronic properties of defective h-BN

3.4.1. Monoatomic B vacancy: h-B^{V}N

The monoatomic B vacancy is formed upon removal of one B atom (**Figure 3-2**, top row). In order to keep the concentration of defects in the lattice low (0.8%), a large supercell must be used (8 × 8). Hybrid functional calculations for such large models are computationally very demanding for plane wave codes. On the contrary, it is still affordable for localized basis set ones, such as CRY14. Therefore, in this section we will compare PBE/QE, vdW-DF2^{C09x}/QE and PBE/CRY14 calculations with B3LYP/CRY14 one.

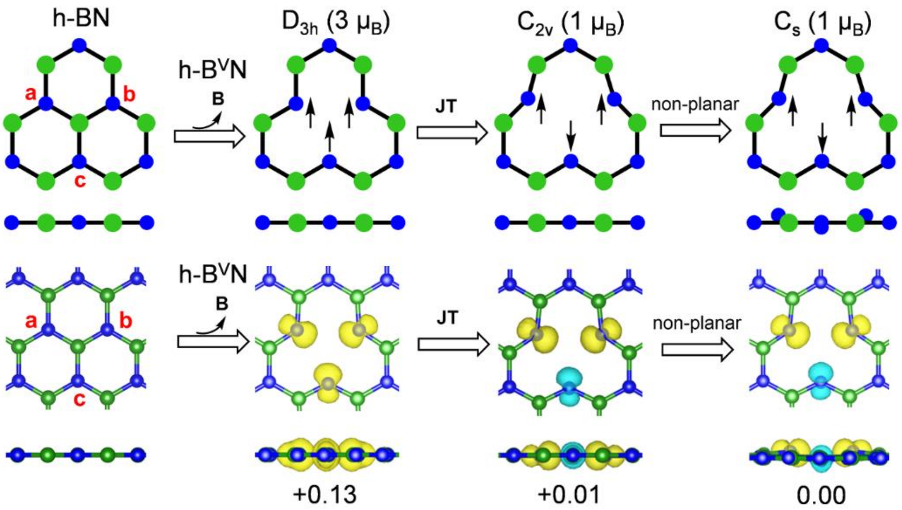

Figure 3-2: In the first row, schematic top and side view representations of the B monovacancy defect models in a 2D h-BN model (h-B^{V}N). The local point group symmetry and the resulting total magnetization in μB (black arrows indicate the unpaired electron localization) are shown together with the type of distortion involved: JT (Jahn−Teller) and non-planar. Undercoordinated N atoms are labeled as a, b, and c. In the bottom row, the corresponding spin density plots by PBE/CRY14 are shown (isosurface level is 0.02 e^{-}/bohr^{3}). Yellow and cyan colors indicate

positive and negative density, respectively. Green and blue balls represent B and N atoms, respectively.

If the D_{3h} symmetry is kept, the preferred magnetization is 3 μ_B, with an unpaired electron on each undercoordinated N atom, i.e. a ferromagnetic quartet. If the symmetry constraint is removed, the system undergoes Jahn-Teller distortion and spin reorganization, leading to more distant undercoordinated N atoms in C_{2v} symmetry and to a reduced magnetization of 1 μ_B, i.e. a ferrimagnetic doublet. Further atomic out-of-plane distortion reduces the point symmetry to C_S but the magnetization of 1 μ_B is maintained. The spin density plots of the models in different point symmetry are shown in **Figure 3-2** (bottom row).

The C_S model is the most stable, although the C_{2V} one is only 0.01 eV higher in energy. The D_{3h} model is rather higher, +0.13 eV with PBE and +0.89 eV with B3LYP. In none of these structures we observe formation of N-N bonds. We also computed the formation energy of the monoatomic B vacancy according to the following equation (for the neutral state):

$$E_F(h-B^VN) = E_{h-B^VN} + E_B - E_{h-BN} \qquad (3\text{-}1)$$

where E_{h-BN} is the energy of the pristine h-BN monolayer, E_{h-B^VN} is the energy of the B defective model and E_B is the energy of a single B atom, as obtained from the following equations (N-rich condition):

$$E_{BN} = E_B + E_N \qquad (3\text{-}2)$$

$$E_N = \frac{1}{2}E_{N_2} \rightarrow \; E_B = E_{BN} - \frac{1}{2}E_{N_2} \qquad (3\text{-}3)$$

where E_{BN} is the total energy of a BN pair in pure h-BN. The formation energy is +7.3 eV with PBE/QE. We trust these as the most reliable estimations given the converged plane wave basis set.

The electronic structures of the defective models are shown in **Figure 3-3a** and **b**. In the lowest energy C_s configuration, three single-particle KS states appear in the gap, with both PBE/CRY14 and B3LYP/CRY14, although the position in the gap is quite different with the two functionals.

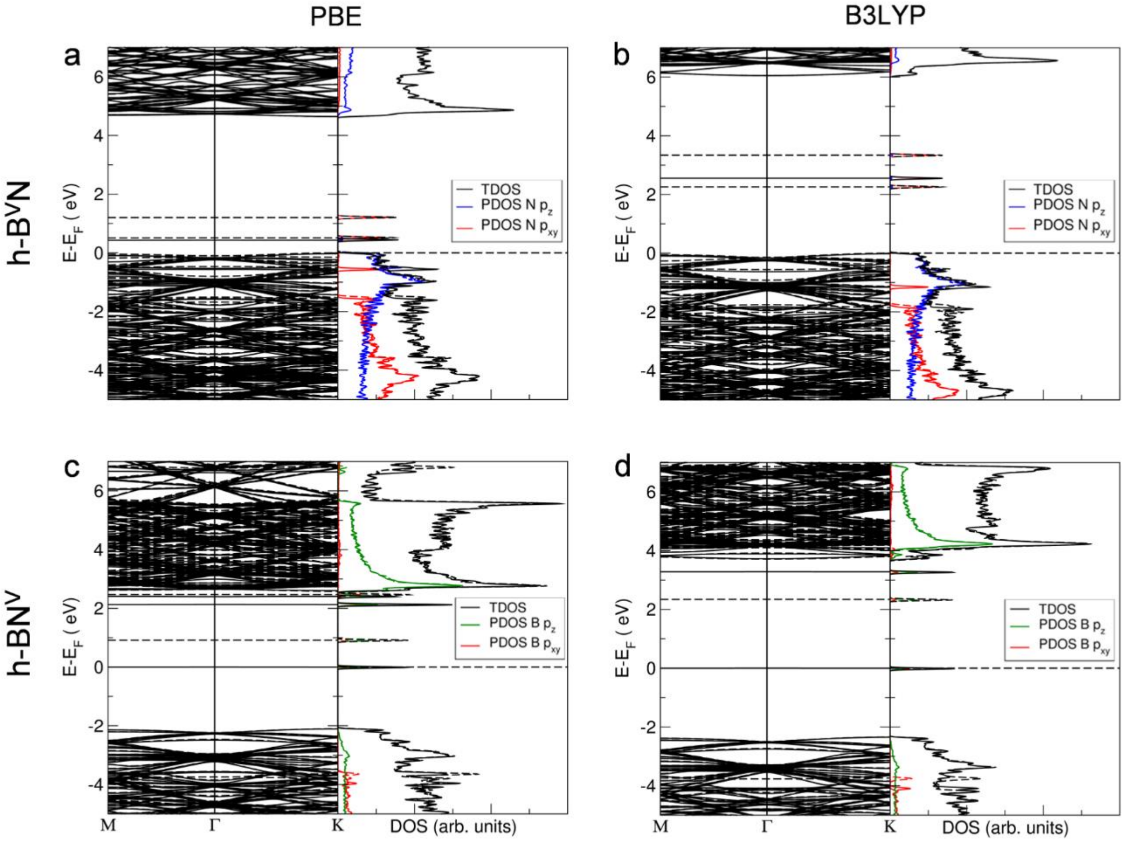

Figure 3-3: Band structures, total (TDOS) and projected (PDOS) density of states of the most stable configuration (C_s) for the B (a and b) and N (c and d) monovacancies obtained by PBE/CRY14 (on the left) and B3LYP/CRY14 (on the right). Full and dashed lines represent spin up and spin down states. Legend of colors for TDOS and PDOS is given in each panel. The Fermi level is scaled to zero.

3.4.2. Monoatomic N vacancy: h-BN^V

For the monoatomic N vacancy, we use the same supercell model as in the previous section. When one N atom is removed, different solutions can be obtained (**Figure 3-4**, top row).

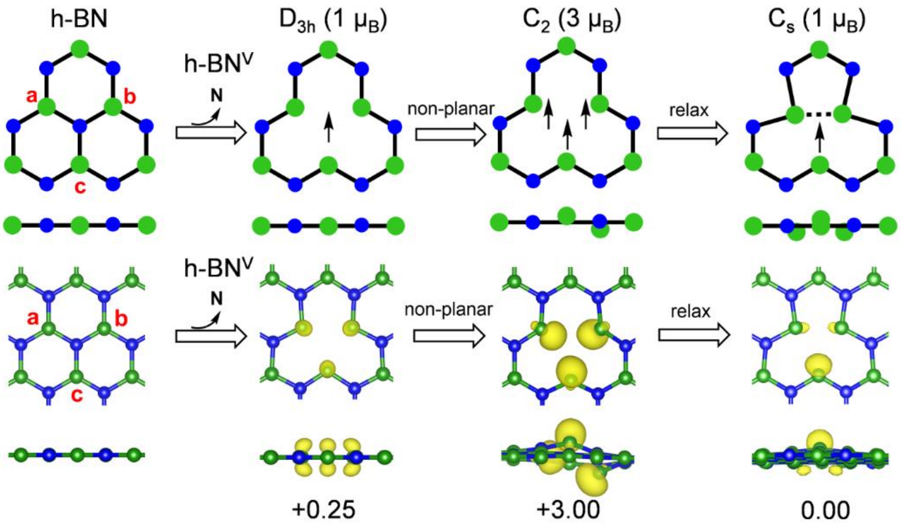

Figure 3-4: In the first row, schematic top and side view representation of the N monovacancy defect models created in a 2D h-BN model (h-B^{V}N). The local point group symmetry is shown together with the type of distortion and the resulting total magnetization in μ_B (black arrows indicate the unpaired electron localization). Undercoordinated B atoms are labeled as a, b, and c. In the bottom row, the corresponding spin density plots by PBE/CRY14 are shown (isosurface level is 0.02 e$^-$/bohr^3). Green and blue balls represent B and N atoms, respectively.

The one with the highest magnetization (3 μ_B), which is the ferromagnetic quartet, in a non-planar C_2 point symmetry is always much higher in energy (> 3 eV) and, therefore, it will not be further considered. In the D_{3h} and C_s point symmetries, the solutions present only a magnetization of 1 μ_B. The spin density plots (**Figure 3-4**, bottom row) show clearly that the unpaired electron in the D_{3h} configuration is equally shared among the p_z orbitals of the three undercoordinated B atoms. In the C_s symmetry, through an out-of-plane distortion, the unpaired electron is more localized on a sp^3 state of one B atom (atom c in **Figure 3-4**).

The formation energy of the monoatomic N vacancy is calculated according to the following equation:

$$E_F(h - BN^V) = E_{h-BN^V} + E_N - E_{h-BN} \qquad (3\text{-}4)$$

The value obtained with PBE/QE is +7.5 eV.

The electronic structure investigation (Figure **3-3c** and **d**) indicates the presence of occupied and unoccupied defect states in the gap.

3.4.3. Pluriatomic vacancies: h-BN(B_1N_3)^V and h-BN(N_1B_3)^V

We have investigated two types of pluriatomic vacancies, using a large (10 × 10) supercell model, to keep the defect concentration reasonably low (0.5 %): 1) (B_1N_3)^V, where we remove one B atom and three surrounding N atoms, creating a triangular hole in the lattice exposing B atoms at the edges (**Figure 3-5a**) and 2) (N_1B_3)^V, where we remove one N atom and three surrounding B atoms, creating a triangular hole in the lattice exposing N atoms at the edges (**Figure 3-5b** and **c**). Upon removal, we allow for full atomic and spin relaxation.

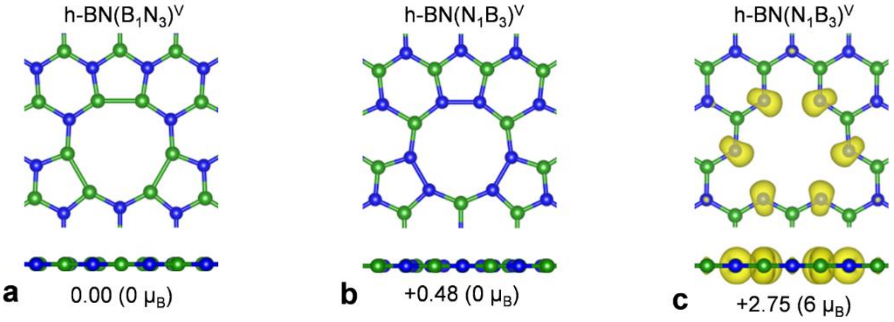

Figure 3-5: Top and side views of pluriatomic vacancy models: h-BN(B_1N_3)^V (a) and closed (b) or open (c) shell solutions for h-BN(N_1B_3)^V, as obtained by vdW-DF2^{C09x}/QE. The resulting total magnetization (in μ_B) and relative energy (in unit of eV) with respect to h-BN(B_1N_3)^V are reported below each configuration. For (c) the spin density plot is also shown (isosurface level is 0.02 e$^-$/bohr^3). Green and blue balls represent B and N atoms, respectively.

The formation energy is estimated as follows:

$$E_F(h-BN(B_1N_3)^V) = E_{h-BN(B_1N_3)^V} + E_B + 3E_N - E_{h-BN} \qquad (3\text{-}5)$$

or

$$E_F(h-BN(N_1B_3)^V) = E_{h-BN(N_1B_3)^V} + 3E_B + E_N - E_{h-BN} \qquad (3\text{-}6)$$

where $E_{h-BN(B_1N_3)^V}$ and $E_{h-BN(N_1B_3)^V}$ are the energies of the defective models. The lowest formation energy is computed for h-BN(B_1N_3)^V (+12.09 eV). The closed-shell structure for h-BN(N_1B_3)^V is +0.48 eV higher, whereas the open-shell one (with 6 μ_B of magnetization) is much higher in energy (by +2.75 eV).

In the case of h-BN(B_1N_3)^V, we observe the formation of three B-B bonds, whereas in the case of h-BN(N_1B_3)^V, we observe the formation of three N-N bonds.

3.5. Pristine h-BN supported on Cu(111) surface

Experimentally, h-BN is typically grown on metal surfaces by chemical vapour deposition. On Cu (111) surface, moiré superstructures are formed, as a consequence of the lattice mismatch between the two materials. Several moiré domains have been observed, with a periodicity in the range between 4 and 14 nm. The most common is the one with 0° rotational angle between the two lattice vectors, which means that the h-BN is aligned with the Cu (111) lattice. The computational simulation of this moiré superstructure has been investigated at the DFT level in a previous work and proved to provide similar results to the commensurate model.[78] Therefore, in the following we present the study of a layer of h-BN (6 × 6) aligned to a four-layer surface of Cu (111), as detailed in the section of Computational Details. We can identify several stacking configurations for the h-BN layer on top of the Cu surface. The most stable one is that with B/N atoms in fcc/top position with respect to the Cu atoms at an average height of 3.06 Å (**Figure 3-6a**), in agreement with previous works.[80,85]

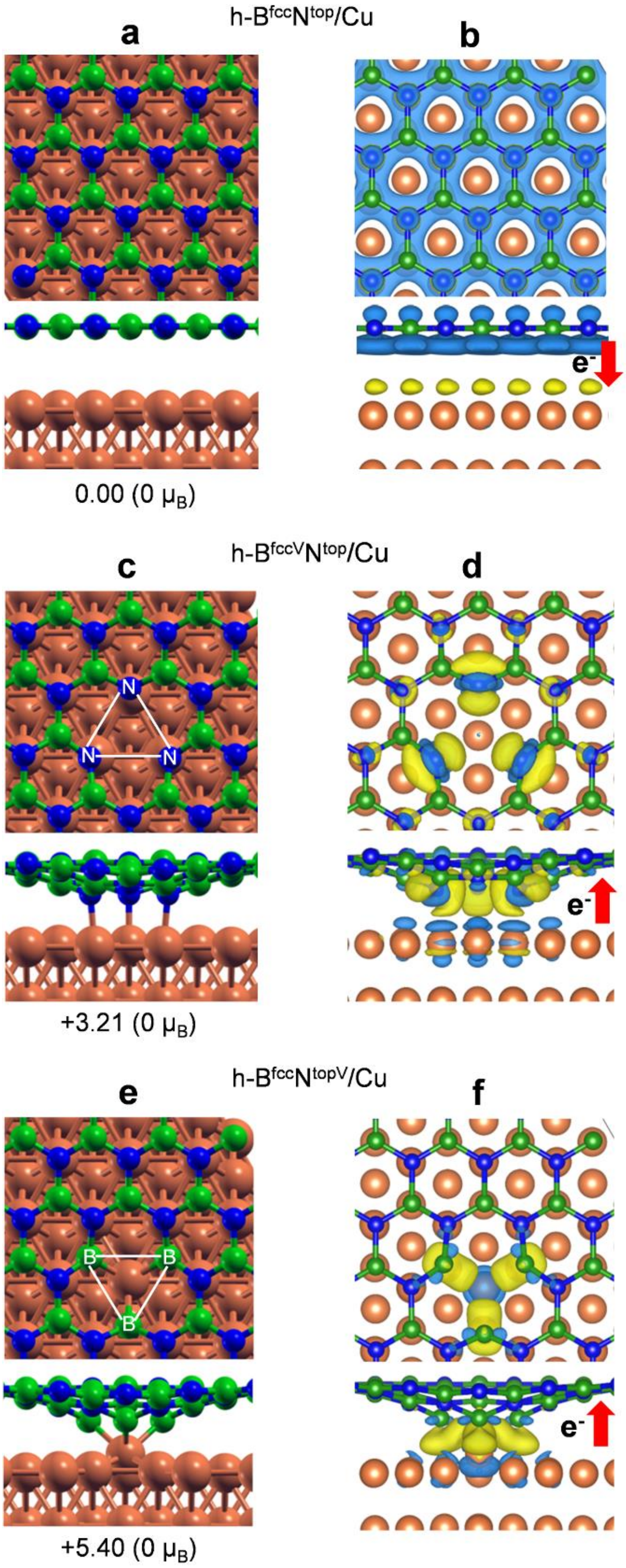

Figure 3-6: Top and side views for pristine and defective h-BN supported on Cu (111) surface: h-$B^{fcc}N^{top}$/Cu (a), h-$B^{fccV}N^{top}$/Cu (c) and h-$B^{fcc}N^{topV}$/Cu (e) with the corresponding charge density difference plots (b, d and f, respectively) obtained by vdW-DF2^{C09x}/QE. The resulting total

magnetization (in μ_B) and the relative energy (in unit of eV) with respect to h-$B^{fcc}N^{top}$/Cu are reported below each configuration. In (b), (d) and (f), electron accumulation is represented by yellow and electron depletion is represented by blue (isosurface level is 0.0006 $e^-/bohr^3$ for b, 0.005 $e^-/bohr^3$ for d and f). Red arrows show the direction of electron charge transfer. Green, blue, and orange balls represent B, N and Cu atoms, respectively.

The interaction between the h-BN monolayer and the Cu surface is rather weak. It is basically of Van der Waals nature with some charge transfer from h-BN to the metal (shown in **Figure 3-6b**). A little hybridization between the N p_z states and the Cu d states with a z component is also observed i) in the projected band structures in **Figure 3-7** (top row), when comparing them with the corresponding projections for the pristine Cu (111) slab (bottom row), and ii) in the projected density of states, where the N p_z states clearly split into three main peaks (**Figure 3-8a**). We may note that this N p_z splitting is less pronounced and soon disappears when the h-BN layer is turned away from the metal surface, as shown in **Figure 3-8b**, where the distance between the two surfaces is varied from 3.06 (equilibrium value) to 3.50 up to 12.0 Å.

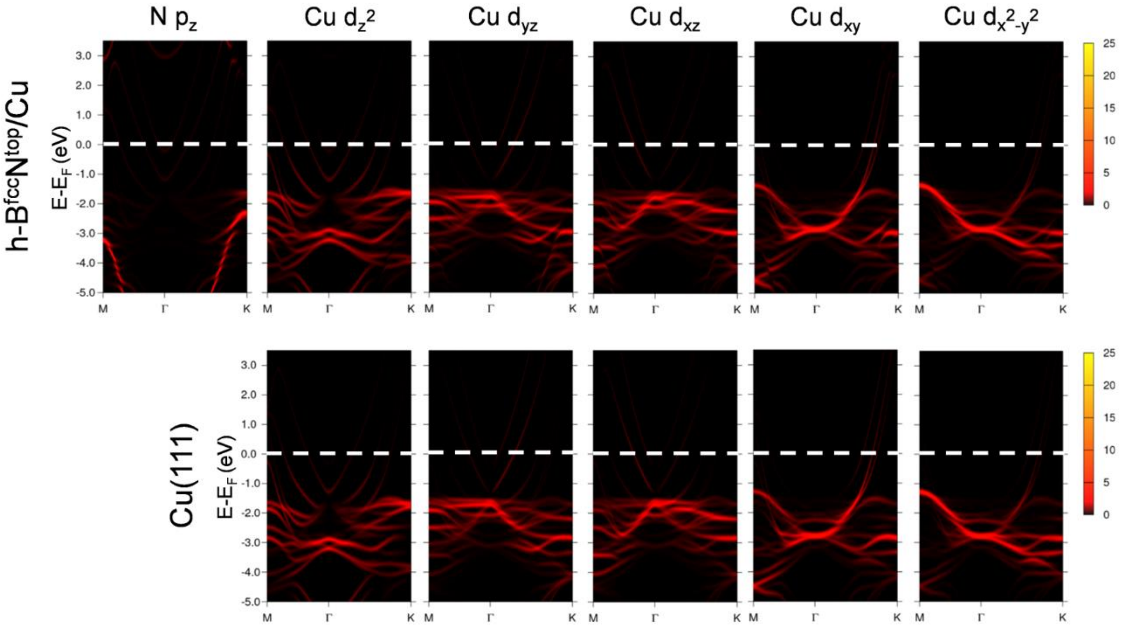

Figure 3-7: Projected band structures on N p_z and Cu d states for h-$B^{fcc}N^{top}$/Cu (top row) and on Cu d states for Cu clean (111) surface (bottom row), as obtained by vdW-DF2^{C09x}/QE. The color scale refers to the value of the projected DOS. The zero energy is set at the Fermi level (dashed line).

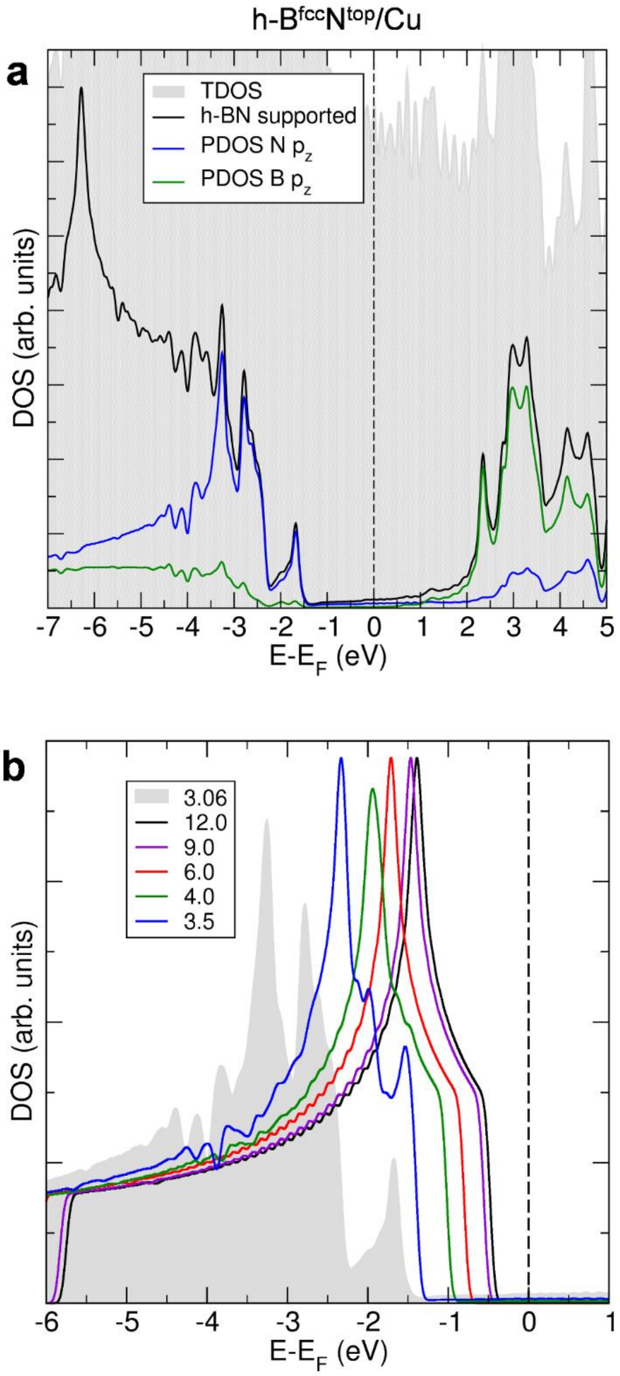

Figure 3-8: (a) Total (TDOS) and projected (PDOS) density of states by vdW-DF2^{C09x}/QE calculations for h-B^{fcc}N^{top}/Cu. (b) PDOS on N p_z for h-B^{fcc}N^{top}/Cu with different interlayer distances (in Å), calculated as a difference between the average z coordinate values of BN atoms and the average z coordinate values of Cu atoms in the surface layer. Legend of colors is given in each panel. The Fermi level is scaled to zero and indicated a dashed line.

3.6. Defective h-BN supported on Cu(111) surface

3.6.1. Monoatomic B vacancy: h-B^{V}N/Cu

We considered the formation of a monoatomic B vacancy in various inequivalent positions with respect to Cu, i.e. fcc, hcp or on top, in a (6 × 6) supercell model (defect concentration of 1.4%), and we found out that the most stable interface is created when removing one B atom in fcc position and with the N atoms on top of the Cu ones (h-B^{fccV}N**top**/Cu, Figure **3-6c**), i.e. removing one B atom from the lowest energy stoichiometric interface (h-$B^{fcc}N^{top}$/Cu), which was discussed in Section 3.5. No residual magnetization is found for all the relaxed supported models. In h-$B^{fccV}N^{top}$/Cu, the N dangling bonds are saturated by the underlying Cu atoms, forming three N-Cu bonds (bond length of 1.92 Å). The h-BN monolayer is only slightly distorted around the vacancy, otherwise it is essentially identical to the stoichiometric supported h-BN. From comparing the results for the (4 × 4), (6 × 6), (7 × 7) and (8 × 8) models, we can safely conclude that the relaxation effect is already recovered within the (6 × 6) one.

In **Figure 3-6d**, we report the charge density difference plot, which proves that the presence of the B monoatomic vacancy causes an inversion of the charge flow direction. Here, there is a clear electron charge depletion in the metal surface and an accumulation on the undercoordinated N atoms, opposite to what observed for the stoichiometric supported h-BN in **Figure 3-6b**. In **Figure 3-9a** we present the projected density of states. We observe a splitting of the pz peak as in the case of stoichiometric supported h-BN in Section 3.5 but also the additional presence of a peak due to the N sp^2 states, which are now filled and move down just below the Fermi level, as a consequence of the charge transfer from the metal surface (compare **Figure 3-9a** with **Figure 3-3a**).

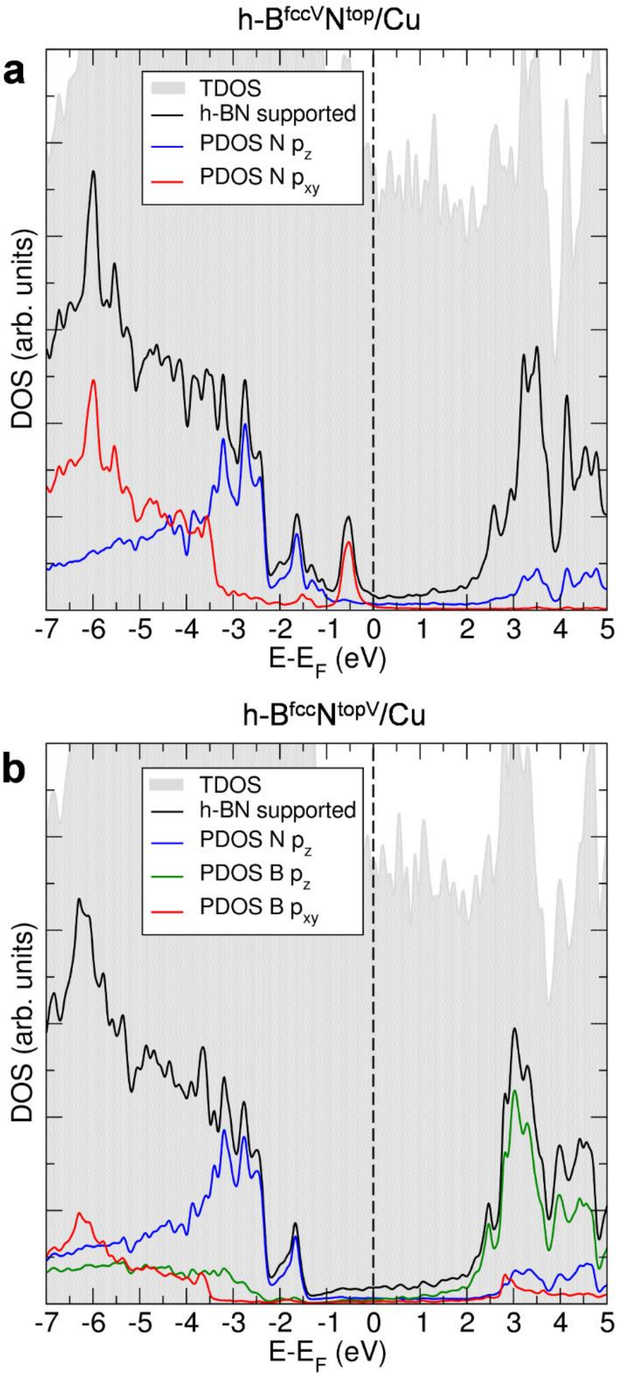

Figure 3-9: Total (TDOS) and projected (PDOS) density of states for h-B^{fccV}N^{top}/Cu (a) and h-B^{fcc}N^{topV}/Cu (b), as obtained by vdW-DF2^{C09x}/QE. Legend of colors is given in each panel. The Fermi level is scaled to zero and indicated by a dashed line.

In the following, we propose a scheme of energy decomposition, shown in **Figure 3-10**, that allows one to determine the energy contribution of deformation (positive, ΔE_{def}) and of binding (negative, ΔE_{bind}) to the adsorption energy ($\Delta E_{ads} = E_{h-B^VN/Cu} - (E_{Cu} + E_{h-B^VN})$) of defective h-BN on the Cu(111) surface (h-B^{V}N/Cu).

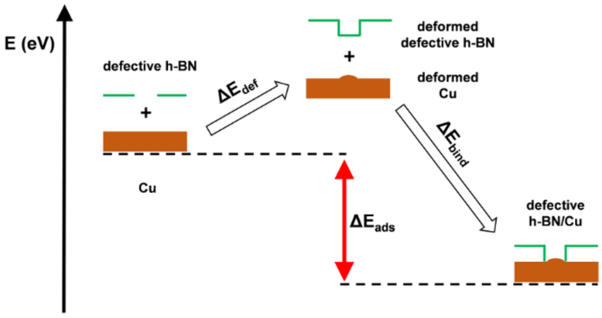

Figure 3-10: Schematic representation of the energy decomposition analysis for the energy contribution of deformation (positive, ΔE_{def}) and of binding (negative, ΔE_{bind}) to the adsorption energy (negative, ΔE_{ads}) of defective h-BN on the Cu(111) surface.

The deformation energy sums up to +1.17 eV but it is mainly due to the deformation in the h-B^{V}N layer (+1.02 eV), and mainly involves an elongation of the undercoordinated N---N distances. The binding between the distorted portions is of -10.59 eV. Therefore, the resulting adsorption energy (ΔE_{ads} in **Figure 3-10**) is -9.42 eV.

Finally, we have determined the formation energy of the monoatomic B vacancy, as it was done for the free-standing case in Section 3.4.1, according to the equation:

$$E_F(h - B^VN/Cu) = E_{h-B^VN/Cu} + E_B - E_{h-BN/Cu} \qquad (3\text{-}7)$$

$$E_N = \frac{1}{2}E_{N_2} \rightarrow E_B = E_{BN} - \frac{1}{2}E_{N_2} \qquad (3\text{-}8)$$

We note that the formation energy of this defect largely drops when it is formed on a Cu (111) surface from +7.5 eV (free standing with vdW-DF2^{C09}) to +3.2 eV.

3.6.2. Monoatomic N vacancy: h-BN^V/Cu

In analogy to the case of the monoatomic B vacancy, we have modeled the monoatomic N vacancy (h-BN^V/Cu) by considering various possible positions on the Cu (111) surface. Again, we find that the most stable defective configuration derives from the lowest energy stoichiometric aligned h-B^{fcc}N^{top}/Cu structure, thus, missing one N atom on top of a Cu atom (see **Figure 3-6e**). The three resulting undercoordinated B atoms in h-B^{fcc}N^{topV}/Cu bind with one surface Cu atom, which is pulled out of the surface level to reduce the strain on the h-BN sheet. In analogy to the h-B^VN/Cu model, we observe a distortion at the vacancy site, but the h-BN relaxed structure is restored moving away from the vacancy, making the (6×6) model sufficiently large, if compared with the (7×7) and the (8×8) ones. The other two configurations considered are much higher in energy (by +2.1 eV) and are found to be planar, only weakly interacting with the metal surface at about 3.3 Å from the top layer. In those cases, we observe a one electron transfer from the surface to the metal, with no net resulting magnetization. On the contrary, for the h-$B^{fcc}N^{topV}$/Cu structure, we observe an electron charge accumulation at the interfacing B—Cu bonds and an electron charge depletion in the metal top layer (see **Figure 3-6f**). The projected density of states is shown in **Figure 3-9b**.

When we analyze in further detail the adsorption energy ($\Delta E_{ads} = E_{h-BN^V/Cu} - (E_{Cu} + E_{h-BN^V})$ of the defective layer to the metal surface for the lowest energy h-$B^{fcc}N^{topV}$/Cu structure, according to the scheme in **Figure 3-10**, we observe a much larger positive $\mathit{\Delta} E_{def}$ (+3.49 eV) than the monoatomic B vacancy (+1.17 eV). This large distortion is clearly mostly associated to the elongation of the B—B distances in the defective h-BN supported layer (contribution of +2.95 eV) with respect to the free-standing one: these stretch from 2.2-2.4 to 2.8 Å. There is also some contribution (+0.54 eV) from the Cu atom upshift from the surface level. The $\mathit{\Delta} E_{bind}$ is of similar size (-10.84 eV vs -10.59 eV), leading to a much smaller ΔE_{ads} (-7.35 eV) in the case of the monoatomic N vacancy with respect to the B one.

Finally, we have determined the formation energy of the monoatomic N vacancy, as it was done for the free-standing case in Section 3.4.2, according to the equation:

$$E_F(h - BN^V/Cu) = E_{h-BN^V/Cu} + E_N - E_{h-BN/Cu} \qquad (3\text{-}9)$$

We note that the formation energy of this defect largely drops when it is formed on a Cu (111) surface from +7.6 eV (free standing with vdW-DF2^{C09}) to +5.4 eV, but it is still much more costly than for the supported monoatomic B vacancy (+3.2 eV). These results clearly indicate that N-Cu bonds are stronger than B-Cu bonds.

3.6.3. Cu@h-B^VN/Cu and Cu@h-BN^V/Cu

Since in the previous Sections 3.6.1 and 3.6.2 we have observed that the undercoordinated atoms formed upon removal of one B or N atom in h-BN have a high chemical affinity with the underlying Cu atoms from the surface, we decided to investigate whether there is a realistic possibility that one Cu atom pops up from the surface, becoming a surface adatom, having a higher geometrical and chemical flexibility to interact with the defective h-BN layer. The Cu adatom could also be already present on the surface in the experimental conditions and simply diffuse during the h-BN growth to be, then, eventually encapsulated into the covalent h-BN lattice.

We first considered the monoatomic B vacancy as the “trapping site” for a Cu adatom in the h-BN net. We considered various positions for the Cu adatom: on top, fcc and hcp. During atomic relaxation, however, from the on top position the Cu atom moves to the fcc one. In one case the calculation ended up into a symmetric structure with a C_3 rotational axis (**Figure 3-11b**), whereas in another into an asymmetric one, which is the most stable ($Cu^{asym\text{-}fcc}$@h-B^VN/Cu), as shown in **Figure 3-11a**. The hpc position for the Cu adatom is found to be less favourable than the fcc.

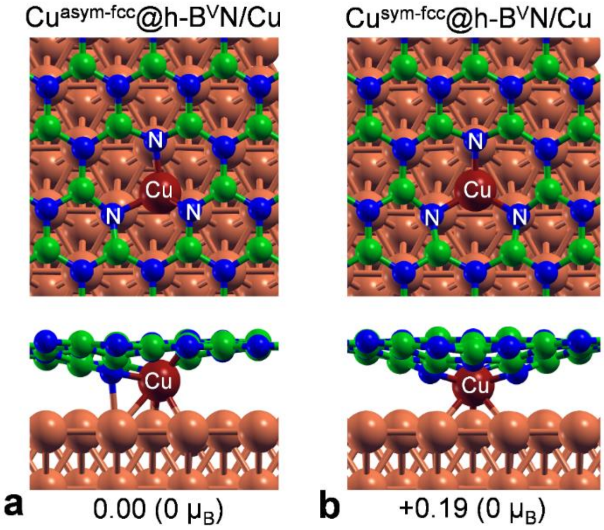

Figure 3-11: Top and side views of $Cu^{asym\text{-}fcc}$@h-B^VN/Cu (a) and of $Cu^{sym\text{-}fcc}$@h-B^VN/Cu (b), as obtained by vdW-DF2^{C09x}/QE. The resulting total magnetization (in μ_B) and relative energy (in unit of eV) with respect to $Cu^{asym\text{-}fcc}$@h-B^VN/Cu are reported below each configuration. Green, blue and orange balls represent B, N and Cu atoms, respectively.

Next we investigate whether there is an energy cost or gain to go from a defective supported h-B^VN/Cu layer and bring a bulk Cu atom to the surface (see **Figure 3-12**) to form the $Cu^{asym\text{-}fcc}$@h-B^VN/Cu structure, according to the equation:

$$\Delta E_{Cu-trap} = E_{Cu@h-B^V N/Cu} - (E_{Cu-bulk} + E_{h-B^V N/Cu}) \qquad (3\text{-}10)$$

where $E_{Cu-bulk}$ is the energy of a single Cu atom in its bulk structure.

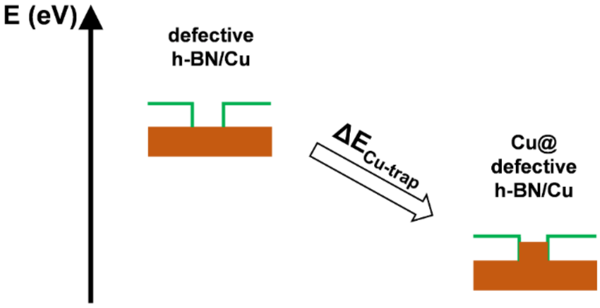

Figure 3-12: Schematic representation of energy change associated to Cu adatom/adatoms trapping by defective h-BN on Cu(111) from the bulk.

It is extremely interesting and surprising to note that this energy change is negative by -0.13 eV. Considering that the energy cost to make a surface Cu adatom is computed to be +0.86 eV, there is a considerable energy gain to stabilize this Cu adatom at the monoatomic B vacancy site at the h-BN/Cu interface.

The same is not true for the monoatomic N vacancy site, exposing B atoms on the edges. In this case, the trapping energy ($\Delta E_{Cu-trap} = E_{Cu@h-BN^V/Cu} - (E_{Cu-bulk} + E_{h-BN^V/Cu})$) is positive by at least +1.6 eV. Interestingly, we also performed the same type of calculations for a C monovacancy in a graphene layer on a Cu (111) surface and observed that there is an energy cost to drag a Cu atom from the bulk of +0.67 eV, in line with a previous work. This result and the one for the monoatomic N vacancy in h-BN prove that the monoatomic B vacancy in h-BN is a special trapping site for transition metals because it exposes N atoms that have a particularly strong affinity to Cu and transition metal atoms in general.

3.6.4. Pluriatomic vacancies: h-BN(B_1N_3)^V/Cu and h-BN(N_1B_3)^V/Cu

We now consider the effect of supporting a defective h-BN sheet with pluriatomic vacancies (discussed in Section 3.4.3) on a Cu(111) surface. To avoid defect/defect interactions, we use a (10 × 10) h-BN model with a defect concentration of 0.5 %.

For the case of h-BN(B_1N_3)^V/Cu, we observe the formation of pairs of interface B-Cu bonds (2.23 Å) on three surface Cu atoms, whereas, for the case of h-BN(N_1B_3)^V/Cu, we observe the formation of six N-Cu bonds (1.90 Å) on six Cu atoms, as shown in **Figure 3-13a** and **b**.

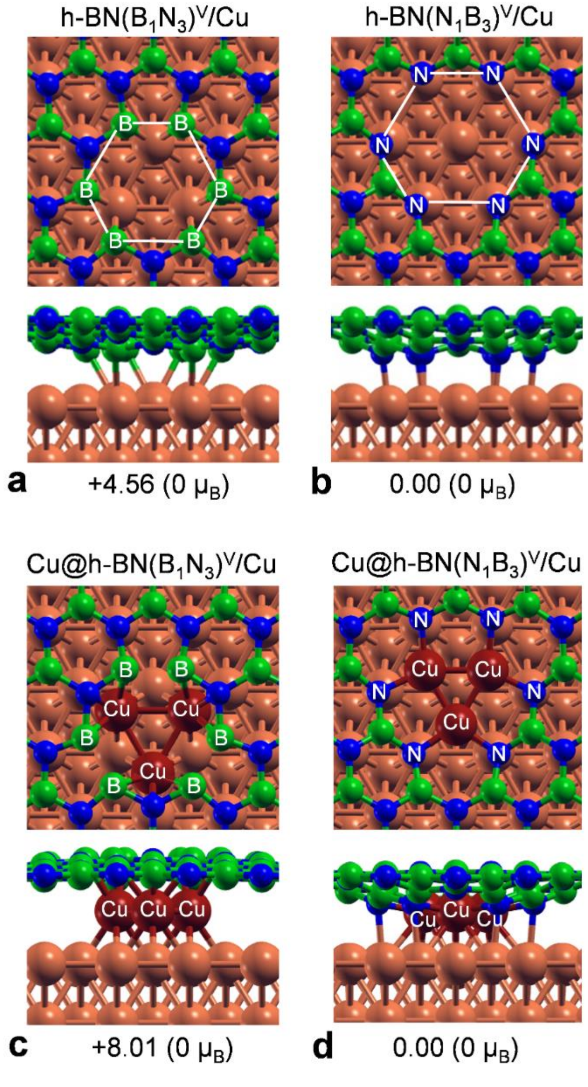

Figure 3-13: Top and side views of h-BN(B_1N_3)^V/Cu (a), h-BN(N_1B_3)^V/Cu (b), Cu@h-BN(B_1N_3)^V/Cu (c) and Cu@h-BN(N_1B_3)^V/Cu (d), as obtained by vdW-DF2^{C09x}/QE. The resulting null total magnetization and the relative energies (in unit of eV) with respect to h-BN(N_1B_3)^V/Cu for (a), (b) and with respect to Cu@h-BN(N_1B_3)^V/Cu for (c), (d) are reported below each configuration. Green, blue and orange balls represent B, N and Cu atoms, respectively.

The stability of these two different structures can be compared only in terms of formation energies, according to the following equations:

$$E_F(h-BN(B_1N_3)^V/Cu) = E_{h-BN(B_1N_3)^V/Cu} + 3E_N + E_B - E_{h-BN/Cu} \qquad (3\text{-}11)$$

and

$$E_F(h - BN(N_1B_3)^V/Cu) = E_{h-BN(N_1B_3)^V/Cu} + E_N + 3E_B - E_{h-BN/Cu} \quad (3\text{-}12)$$

The difference in the cost of formation is of +4.56 eV in favor of h-BN(N_1B_3)^V/Cu, indicating that the formation of N-Cu bonds is preferred over the formation of B-Cu ones, in agreement with what observed in the case of B and N monovacancies on Cu surface, discussed above in Sections 3.6.1 and 3.6.2. The N-Cu bonds result from a strong hybridization between the Cu d states and the N p_{xy} and p_z states, as one can clearly observe from the PDOS in **Figure 3-14a**.

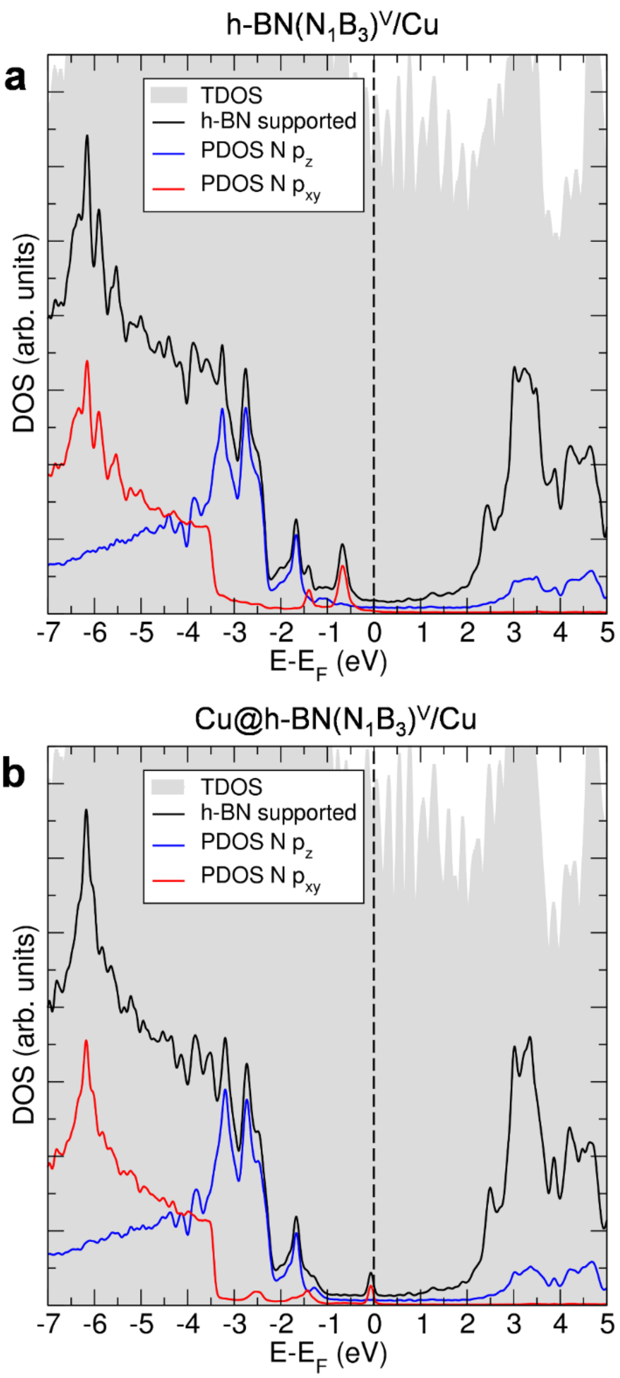

Figure 3-14: Total (TDOS) and projected (PDOS) density of states for h-BN(N_1B_3)^V/Cu (a) and Cu@h-BN(N_1B_3)^V/Cu (b), as obtained by vdW-DF2^{C09x}/QE. Legend of colors is given in each panel. The Fermi level is scaled to zero and is indicated by a dashed line.

The decomposition analysis (see the scheme in **Figure 3-10**) for h-BN(B_1N_3)^V/Cu and h-BN(N_1B_3)^V/Cu is detailed in **Table 3-1**. The adsorption energy of the latter ($\Delta E_{ads} = E_{h-BN(N_1B_3)^V/Cu} - (E_{Cu} + E_{h-BN(N_1B_3)^V})$) is much larger, -20.75 vs -15.71 eV, as a consequence of a larger binding energy (ΔE_{bind}) of -25.34 vs -17.67 eV and despite a larger deformation energy (ΔE_{def}) of +4.59 vs +1.96 eV.

Table 3-1: Energy contribution of deformation (positive, ΔE_{def}) and of binding (negative, ΔE_{bind}) to the adsorption energy (negative, ΔE_{ads}) of h-BN(B_1N_3)^V and h-BN(N_1B_3)^V on the Cu (111) surface, as shown in **Figure 3-10**.

	ΔE_{def} (eV)	**ΔE_{bind} (eV)**	**ΔE_{ads} (eV)**
h-BN(B_1N_3)^V/Cu	+1.96	-17.67	-15.71
h-BN(N_1B_3)^V/Cu	+4.59	-25.34	-20.75

3.6.5. Cu@ h-BN(B_1N_3)^V/Cu and Cu@ h-BN(N_1B_3)^V/Cu

Since the undercoordinated atoms in the pluriatomic vacancies are observed to form strong bonds with the surface Cu atoms, in analogy to what done for the monoatomic vacancies in Section 3.6.3, we have considered the possibility that some Cu atoms pop up to fill the vacancy in the h-BN layer and saturate the dangling bonds. We investigated both Cu adatoms in the h-BN(B_1N_3)^V/Cu and in the h-BN(N_1B_3)^V/Cu, although the formation of the latter was found to be preferred in the previous paragraph. We noticed that three Cu adatoms can pop up to completely fill the hole in the h-BN lattice, forming the two structures shown in **Figure 3-13c** and **d**: Cu@h-BN(B_1N_3)^V/Cu and Cu@h-BN(N_1B_3)^V/Cu.

If we compare the formation energies:

$$E_F(Cu@h-BN(B_1N_3)^V/Cu) = E_{Cu@h-BN(B_1N_3)^V/Cu} + 3E_N + E_B - E_{h-BN/Cu} - 3E_{Cu-bulk} \qquad (3\text{-}13)$$

$$E_F(Cu@h-BN(N_1B_3)^V/Cu) = E_{Cu@h-BN(N_1B_3)^V/Cu} + E_N + 3E_B - E_{h-BN/Cu} - 3E_{Cu-bulk} \qquad (3\text{-}14)$$

we conclude that Cu@h-BN(N_1B_3)^V/Cu is much more easily formed (-8.01 eV) with respect to Cu@h-BN(B_1N_3)^V/Cu. The undercoordinated N atoms in Cu@h-BN(N_1B_3)^V/Cu form bonds with both Cu adatoms and surface Cu atoms (1.86 Å), whereas the undercoordinated B atoms in Cu@h-BN(B_1N_3)^V/Cu form bonds only with the Cu adatoms (2.26 Å). The type of Cu and N states hybridization in Cu@h-BN(N_1B_3)^V/Cu is very similar to what observed for h-BN(N_1B_3)^V/Cu (compared PDOS for the two structure in **Figure 3-14a** and **b**), indicating a similar bond nature for the undercoordinated N atoms with Cu adatoms or surface Cu atoms.

More importantly, if we analyze the energy cost or gain to bring three bulk Cu atoms to the surface to form Cu@h-BN(N_1B_3)^V/Cu starting from h-BN(N_1B_3)^V/Cu, we make a remarkable observation (see the scheme in **Figure 3-12**). There is a net energy gain of -0.86 eV, as obtained from the equation:

$$\Delta E_{Cu-trap} = E_{Cu@h-BN(N_1B_3)^V/Cu} - (3E_{Cu-bulk} + E_{h-BN(N_1B_3)^V/Cu}) \qquad (3\text{-}15)$$

This is even larger than the value computed for the B monovacancy (-0.13 eV) in Section 3.4.3. Considering that the energy cost to make a Cu trimer species on the Cu (111) surface is + 2.03 eV, with Cu atoms in fcc position, there is a considerably large stabilization energy associated to the Cu trimer filling a pluriatomic vacancy (N_1B_3) in a supported h-BN sheet.

Again, this is not true for the corresponding (B_1N_3) vacancy where B atoms are exposed. In this case the $\Delta E_{Cu-trap}$ is +2.59 eV in favor of keeping the Cu atoms in the metal bulk.

3.7. Scanning tunneling microscopy (STM) simulations of defective and metal-doped h-BN/Cu(111) systems

The experimental literature for the identification and characterization of defects in Cu(111)-supported h-BN is quite poor to date. Great attention has been paid to the study of moiré superstructures, especially with STM studies, but nothing with atomic resolution. Although h-BN is an insulator material, it becomes metallic when it is placed on top of a metal substrate, making its characterization through a tunneling current possible. However, its imaging by STM is quite challenging and high bias voltages are usually required. According to our knowledge, only in one experimental work the atomically resolved h-BN structure on Cu(111) was shown.[163]

Since now we have no experimental evidence of our proposed models, we decided to simulate STM images, hoping what this will stimulate experimental groups to study point defects and hetero-atom doping in h-BN/Cu(111) systems.

3.7.1. Monoatomic and pluriatomic vacancies

We have initially considered empty vacancies, which we presented and analyzed in sections 3.6.1, 3.6.1, and 3.6.4.

In general, all images show a different contrast changing the bias polarity: at negative bias, N and B atoms are bright and dark, respectively, whereas, at positive bias, the contrast is reversed. This can be easily rationalized based on the projected density of states (PDOS) reported in **Figure 3-8a** (for pristine h-BN/Cu): below and above the Fermi level, the electronic states are mainly composed of N and B p_z states, respectively. It follows that at any bias considered, it is not possible to see the complete honeycomb lattice of h-BN, but only one of the two sublattices.

In **Figure 3-15**, at negative bias in the top row, all vacancies appear as a dark spot, whose size and shape depends on the defect considered: a triangular shape in the case of B (smaller dark spot) and N_1B_3 (larger dark spot) vacancies; a rhombohedral shape in the case of N (smaller) and B_1N_3 (larger) vacancies. At positive bias in the bottom row, although the dark spot remains, its size seems to be reduced, and even the shape is different, appearing like a dark round spot.

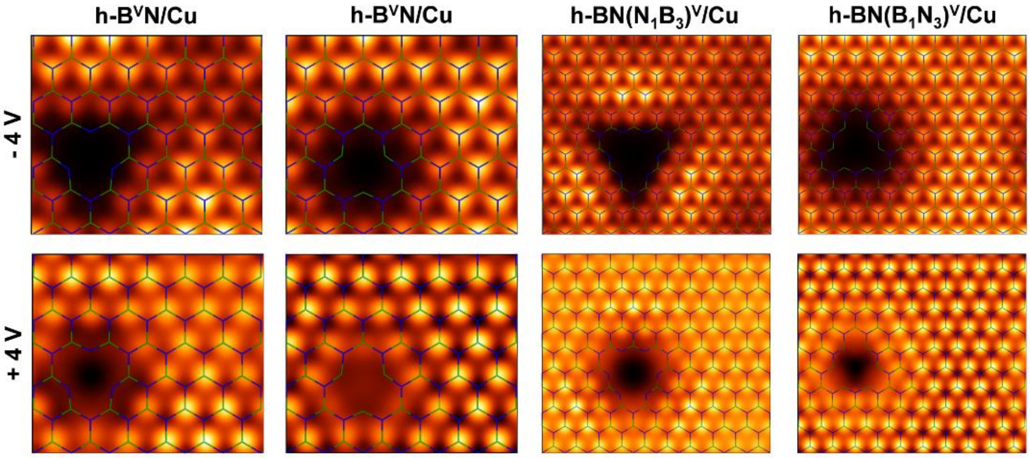

Figure 3-15: Constant height simulated STM images for various defective h-BN/Cu systems. Computational parameters: $V_{bias} = -4$ and +4 V; ILDOS iso-surface lying at 2 Å above h-BN. Color coding for the overlapped stick model: B atoms in green, N atoms in blue.

3.7.2. Metal-doped h-BN/Cu

Here, we analyzed filled vacancies by one or more Cu metal adatoms, as discussed in sections 3.6.3 and 3.6.5.

In **Figure 3-16**, the metal atom is not visible in whatever vacancy when it is trapped, because of its deep position with respect to the BN layer (see optimized geometries in **Figure 3-11a**, **3-13c**, and **3-13d**). In the case of Cu@h-B^{V}N/Cu (first column of **Figure 3-16**), at negative bias, one of the three neighboring N atoms appears bright, but moving to positive bias it becomes dark. Slightly different is the situation in the case of the N vacancy: at a negative bias, a triangular dark spot is clearly visible, which becomes bright at positive bias. However, this change seems to concern the B atoms at the vacancy site and not the trapped Cu atom.

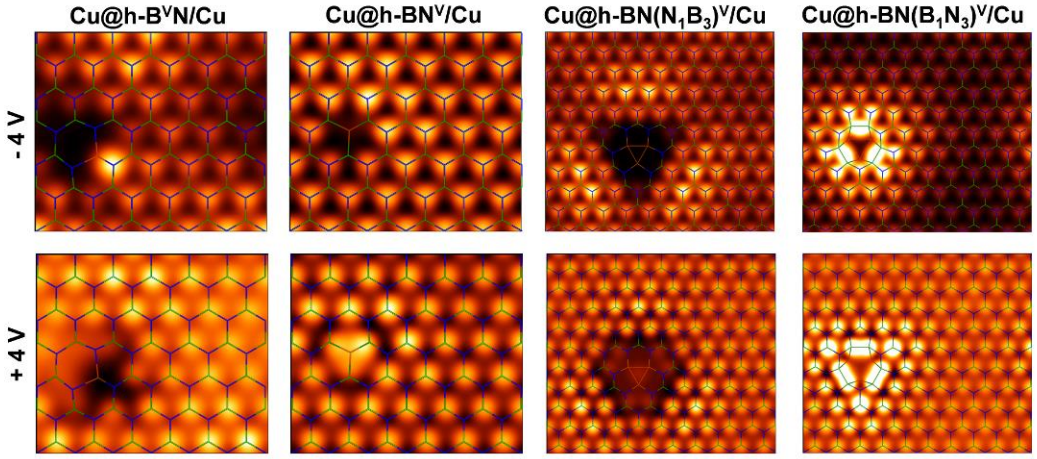

Figure 3-16: Constant height simulated STM images for various metal-doped h-BN/Cu systems. Computational parameters: $V_{bias} = -4$ and +4 V; ILDOS iso-surface lying at 2 Å above h-BN. Color coding for the overlapped stick model: B atoms in green, N atoms in blue, and Cu atoms in orange.

Turning to the case of large vacancies, we notice how Cu@h-BN(N$_1$B$_3$)^V/Cu appears similar to the corresponding empty system (see the third column in **Figure 3-15** for comparison), showing only some small difference at positive bias. Completely different is the case of Cu@h-BN(B_1N_3)^V/Cu, where B-B bonds appear bright both at negative and positive bias. Such an effect may be explained by analyzing the geometry of the system, as shown in **Figure 3-13c**: due to the presence of the interfacial Cu trimer, B atoms at the vacancy site are pushed up, and such wrinkling can make them brighter.

3.8. Conclusions

In this work, we present a comprehensive study of the interface that is formed upon growth of a defective h-BN monolayer on a Cu (111) surface. As discussed in the introduction, defects may derive from the preparation conditions or may be created on purpose.

In the sections 3.3 and 3.4, we first present a comparison of the electronic properties of pristine and defective free standing h-BN by using various type of functionals (standard, dispersion-corrected, hybrid) and large supercell sizes, which provide a realistic vacancy concentration. We investigated both monoatomic B and N vacancies and pluriatomic (B_1N_3) and (N_1B_3) vacancies, by allowing total relaxation of the atomic positions (through release of symmetry elements) and of the spin magnetization. The lowest symmetry solutions (C_s) are the lowest energy ones, both for the B and N monovacancy. (B_1N_3) multiatomic defect is less energetically expensive than (N_1B_3). The presence of the defects in the lattice leads to the disappearance of the NFE state at the bottom of the conduction band and to the appearance of defect states in the gap. The use of hybrid functionals (B3LYP or HSE) clearly improves the description of the gap and lifts the position of the defects levels in the gap but does not alter the qualitative picture obtained with standard GGA methods.

In section 3.5, we show the electronic interplay between a pristine h-BN layer with a Cu (111) surface using vdW corrected functionals to account for the weak dispersion forces. We observe a small electron charge transfer from the h-BN to the metal and some state hybridization emerging from the projected band structures in **Figure 3-7**. The p_z states of the N atoms, which lie on top of the Cu ones, are found to clearly split as a consequence of this hybridization in **Figure 3-8**.

As a next step, we study in detail the interface between defective h-BN and the Cu substrate. Here, the charge transfer is much larger and in the opposite direction, from the metal to the h-BN layer, independently of the type of vacancy. The B vacancy is energetically preferred with the undercoordinated N atoms forming strong bonds with the underlying Cu surface. If we allow one Cu atom to pop up from the bulk and fill the B vacancy, we observe an energy gain of -0.13 eV (**Figure 3-12**). The Cu-N bonds formed are evidently very strong and compensate for the cost to drag the Cu atom from the bulk. This exciting and unexpected result is even more evident when we consider a h-BN layer with a multiatomic vacancy. On a Cu substrate, the (N_1B_3) defect is more favorable than the (B_1N_3) one. Such defect is capable of lifting up to three Cu atoms from the metal surface, which fill completely the hole in the h-BN structure. Considering an overall energy cost of +2.03 eV to created three surface Cu adatoms, the observed net energy release of -0.86 eV is astonishing.

Therefore, based on what summarized above, we may conclude that defective h-BN layers, presenting N-terminated triangular holes in the lattice, behave as giant N-donor macrocyclic ligands, which can encapsulate Cu adatoms thanks to the huge stabilization effect deriving from the Cu-N bond formation. This result is extremely interesting and unexpected, given that the pristine non-defective h-BN/Cu (111) interface is generally recognized as a weakly interacting interface. Our observations could apply to other metal surfaces and could even stimulate the idea of trapping different metal atoms (more precious but more active) from those of the underlying surface for catalytic purposes.

4. Computational Electrochemistry of Water Oxidation on Metal-Doped and Metal-Supported Defective h-BN

In the last chapter, we showed that when a non-regular 2D h-BN layer is grown on a Cu(111) surface, metal adatoms may spontaneously emerge from the bulk to fill the atomic holes in the structure and become available for surface catalysis.
In this chapter, computational electrochemistry is used to investigate and compare the performance of Cu-doped and Cu-supported pristine and defective h-BN systems for the electrocatalytic water oxidation reaction. For the various model systems, the intermediate species of this multistep oxidation process are identified and the free-energy variations for each step of reaction are computed.

The results reported in this chapter have been published in: Perilli, D., Selli, D., Liu, H., Di Valentin, C., ChemSusChem 2019, 12, 1995-2007.

4.1. Introduction

Direct water splitting is a clean and renewable route towards the production of pure hydrogen. However, it is an uphill reaction requiring a lot of energy to be provided electrochemically. The overall electrochemical process is further hampered by large overpotentials, especially at the anode where the water oxidation reaction takes place to produce gaseous oxygen. Therefore, most of the scientific effort is devoted to the search for an efficient, inexpensive, stable O_2-evolving electrocatalyst for the water oxidation reaction, also known as the oxygen evolution reaction (OER):[164,165,166,167]

$$2\ H_2O_{(l)} \rightarrow O_{2(g)} + 4\ H^+ + 4\ e^- \quad E°=1.23\ \text{V vs. RHE} \qquad (4\text{-}1)$$

The optimal OER electrocatalyst should be: i) active for oxygen evolution at the thermodynamic potential with high current density, ii) made of earth-abundant elements, and iii) stable under strong oxidizing conditions, preferably in acidic media. Both homogeneous and heterogeneous catalysts have been investigated.[165,166,167] The latter are most based on metal oxide surfaces.[168,169,170] In particular, IrO_2 and RuO_2 were found to meet most of the required criteria and perform considerably better than elemental metals.[171,172] However, those metals are rare and costly. Non-precious metal oxides have also been extensively studied,[173,174,175] but they are stable only in alkaline conditions.[168]

An important emerging class of metal-free electrocatalysts for OER under alkaline conditions is that of doped graphenic systems. For example, N-doped graphene and Cu-supported graphene were found to perform better than Pt electrocatalysts for water oxidation at $T < 100$ °C.[176]

Other two-dimensional materials that could also be of potential interest for the OER, have previously been theoretically investigated for other types of redox reactions.[108,109] For example, metal-supported h-BN was theoretically studied by Koitz et al. as an electrocatalyst for the oxygen reduction reaction (ORR).[177] Cu(111) substrate was identified as the most promising in comparison to Ni (111) and Co (0001). Very recently, h-BN on analogous metal surfaces also emerged as an interesting electrocatalyst for CO_2 reduction.[154] Defective or doped h-BN sheets or nanoribbons have great potential for the ORR.[151] Moreover, computational studies have indicated that atoms of metals such as Au, Cu, and Mo on defective h-BN could be active electrocatalysts for CO oxidation[178,179] or nitrogen fixation.[180] From experimental studies, it is proposed that both precious and non-precious metal nanoparticles on highly defective h-BN nanosheets are excellent systems for the electrocatalysis of CO oxidation,[181] for the hydrogenation of nitroaromatics,[182] for the Suzuki-Miyaura reaction,[183] and for the Fischer-Tropsch synthesis.[184]

During the last decade, computational electrochemistry has been demonstrated to be a useful tool in the effort to understand the intermediate steps of electrochemical processes and the reaction mechanisms involved.[168,172,185] Moreover, through the identification of significant descriptors, it has become possible to provide a classification of promising and poor electrocatalysts, as well as to indicate the way towards their improvement.

In the present work we apply the computational electrochemistry approach to the case of Cu-doped and Cu-supported h-BN. This choice of systems is mainly for the following reasons. Firstly, Cu is a very attractive substrate because of the possibility of using Cu foils and, thus, of moving towards large-scale preparations for commercial use. Secondly, in a recent work[186] we reported that Cu adatoms from the substrate can emerge from the bulk material and become highly stabilized within the holes of defective h-BN sheets, as a consequence of Cu-N bond formation. Their surface exposure as single atoms or small clusters could induce some interesting and unexpected reactivity. Therefore, we present herein a detailed computational electrochemistry analysis to test the use of h-BN/Cu hybrid systems as electrocatalysts for water oxidation.

4.2. Computational Approach

4.2.1. Computational Details

All calculations were performed with the van der Waals (vdW-DF2^{C09x})[128] functional as implemented in the Quantum ESPRESSO (QE) package.[157] Vanderbilt ultrasoft pseudopotentials with an energy cutoff of 30 Ry and 240 Ry (for kinetic and charge density grids, respectively) were used.[129] A convergence criterion of 0.026 eV/Å for the forces was used during geometry optimization and the convergence criterion for the total energy was set at 10^{-6} Ry.

A periodic (6 × 6) supercell was used to model the pristine, B monovacancy, N monovacancy (only considered for the free-standing case), and Cu-doped models in the free-standing and Cu(111)-supported h-BN monolayer, with a 3 × 3 × 1 Monkhorst-Pack k-points mesh[187] used for the geometry relaxation. For the multiatomic vacancy in Cu(111)-supported h-BN, a (8 × 8) supercell of h-BN and of Cu(111) was used to avoid the interaction between adjacent periodic defects, with a 2 × 2 × 1 k-points mesh used for the geometry relaxation. To avoid the interactions between adjacent periodic images along the z axis, a vacuum space of 20 Å was employed.

The Cu(111) surface was modeled by a four-layer slab model with the two bottom layers fixed to the bulk positions during the geometry relaxation. Since the lattice mismatch between h-BN and Cu(111) is 2 % (2.50 Å for h-BN vs. 2.56 Å for Cu(111) hexagonal lattice), the lattice parameter of h-BN was used to describe properly the reactivity of the 2D sheet, which needs to be in its equilibrium geometry.

4.2.2. Thermodynamics from electronic structure calculations

The free energies of the intermediates were computed by correcting the electronic energies for the zero-point energy (ZPE) and the entropic terms. Corrections for the ZPE were included by calculating and diagonalizing the dynamical matrix at the Γ point. Additionally, for each molecular fragment bound to the surface, the rotational and vibrational entropy is estimated as follows [Eq. (2)]:

$$S_{\mathrm{rot}} = \mathrm{R}\left[\ln\left(\frac{8\pi^2\sqrt{8\hat{}\pi^3 I_x I_y I_y (k_{\mathrm{b}}T)^{\frac{3}{2}}}}{\sigma_{\mathrm{r}} h^3}\right) + \frac{3}{2}\right] \quad (4\text{-}2)$$

in which I_x, I_y, and I_z represent the inertia moment along the three principal axes, R is the ideal gas constant, k_b is the Boltzmann constant, T is the temperature, and σ_r represents the rotational symmetry numbers [Eq. (3)]:

$$S_{\mathrm{vib}} = R\sum_i^{\text{of modes}}\left(\frac{h\nu_i}{K_{\mathrm{b}}T(e^{\left(\frac{h\nu_i}{K_{\mathrm{b}}T}\right)}-1)} - \ln\left(1 - e^{\left(-\frac{h\nu_i}{K_{\mathrm{b}}T}\right)}\right)\right) \quad (4\text{-}3)$$

The translational entropy was assumed to be negligible for each species adsorbed on the surface. For a gas-phase H_2 molecule, standard tabulated entropy was used,[188] whereas the entropy of gas phase water was calculated at 0.035 bar because this is the equilibrium pressure in contact with liquid water at 298 K. The free energy of gas phase water at these conditions is equal to the free energy of liquid water.[189,190] The free-energy change of the total reaction 2 $H_2O_{(l)} \rightarrow O_{2(g)} + 2\ H_{2(g)}$ is fixed at the experimental value of +4.92 eV to avoid the calculation of the O_2 energy, which is difficult to calculate accurately at the DFT level. The contribution of bulk water was computed by using the self-consistent continuum solvation model (SCCS) implemented in the QE package.[191] All energies reported hereafter refer to full geometry optimization at the DFT/vdW-DF2$^{\mathrm{C09x}}$+SCCS level, always including the SCCS solvation contribution. Thus, the total Gibbs free energy is obtained as a sum of the following terms:

$$G(\mathrm{X}) = E_{\mathrm{SCCS}}(\mathrm{X}) + \mathrm{ZPE} - T(S_{\mathrm{vib}} + S_{\mathrm{rot}}) \quad (4\text{-}4)$$

where E_{SCCS} is the energy computed in the solvent, ZPE is the semi-sum of the normal vibrational modes, and S_{vib} and S_{rot} represent vibrational and rotational entropies.

In the case of the large models (8 × 8 supercells), owing to the large size of the system (380 atoms), the thermal contributions to the Gibbs free energy were calculated including only the h-BN layer and the two top metal layers and neglecting the contributions from the Cu atoms in the bottom layers.

4.3. Reaction mechanism

In this work, we consider several h-BN-based systems (pristine h-BN, defective h-BN, Cu-doped h-BN, and Cu-supported pristine and defective h-BN) and compare their electrocatalytic performances toward the water oxidation reaction by means of a computational electrochemistry analysis. We investigate two mechanisms of reaction: A) the associative path and B) the direct O_2 recombination paths, which consist of the following sets of reaction steps, as shown also in **Figure 4-1**:

A) Associative path

$$H_2O_{(l)} + * \rightarrow H_2O_{(phys)} \quad (A1)$$

$$H_2O_{(phys)} \rightarrow OH_{ads} + (H^+ + e^-) \quad (A2)$$

$$OH_{ads} \rightarrow O_{ads} + (H^+ + e^-) \quad (A3)$$

$$O_{ads} + H_2O_{(l)} \rightarrow OOH_{ads} + (H^+ + e^-) \quad (A4)$$

$$OOH_{ads} \rightarrow OO_{ads} + (H^+ + e^-) \quad (A5)$$

$$OO_{ads} \rightarrow O_{2(g)} \quad (A6)$$

B) Direct O_2 recombination paths

$$H_2O_{(l)} + * \rightarrow H_2O_{(phys)} \quad (B1)$$

$$H_2O_{(phys)} \rightarrow OH_{ads} + (H^+ + e^-)\ (B2)$$

$$OH_{ads} + H_2O_{(l)} \rightarrow OH_{ads} + OH_{ads} + (H^+ + e^-) \quad (B3a)$$

$$OH_{ads} \rightarrow O_{ads} + (H^+ + e^-) \quad (B3b)$$

$$OH_{ads} + OH_{ads} \rightarrow O_{ads} + OH_{ads} + (H^+ + e^-) \quad (B4a)$$

$$O_{ads} + H_2O_{(l)} \rightarrow O_{ads} + OH_{ads} + (H^+ + e^-) \quad (B4b)$$

$$O_{ads} + OH_{ads} \rightarrow O_{ads} + O_{ads} +(H^+ + e^-) \quad (B5a)$$

$$O_{ads} + OH_{ads} \rightarrow O_{ads} + O_{ads} + (H^+ + e^-) \quad (B5b)$$

$$O_{ads} + O_{ads} \rightarrow OO_{ads} \rightarrow O_{2(g)} \quad (B6a)$$

$$O_{ads} + O_{ads} \rightarrow OO_{ads} \rightarrow O_{2(g)}\ (B6b)$$

Since we have observed that the associative mechanism is always more favorable than the direct O_2 recombination path, in the following we will present and discuss the results for the former mechanism.

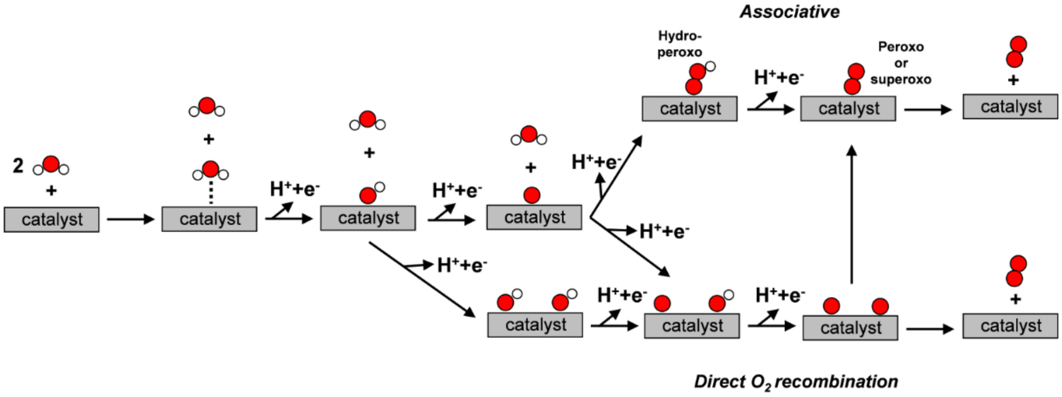

Figure 4-1: Reaction intermediates for the OER on a catalyst. Associative path involving the formation of a hydroperoxo intermediate (-OOH) is reported at the top, whereas direct O_2 recombination paths are shown at the bottom. Red and white balls represent oxygen and hydrogen, respectively.

4.4. Computational electrochemistry analysis

We simulated the electrochemical cell, together with the effect of an applied external potential, with the methodology originally proposed by Nørskov and co-workers,[133] as described in the following. The water oxidation reaction takes place at the anodic half-cell. The cathodic half-cell is the standard hydrogen electrode (SHE) or reference electrode. At pH = 0, when no external potential is applied, that is, U = 0 V (vs. SHE), the cathodic reaction:

$$\mathrm{H^+} + \mathrm{e^-} \leftrightarrow \frac{1}{2}\mathrm{H_{2(g)}} \quad (4\text{-}5)$$

is in equilibrium at 1 bar of $H_{2(g)}$ and 298 K. Thus, we can set: $G(\mathrm{H^+} + \mathrm{e^-}) = \frac{1}{2}G(\mathrm{H_2})$.

We first compute, by means of electronic structure calculations, the free-energy variation for each step of water oxidation at the catalyst surface and use those values to draw a free-energy diagram at U = 0 (**Figure 4-2**, black lines). Then, we apply an external potential (U > 0) with respect to the SHE, which has the effect of modifying the free energies of the intermediates along the path that involve an electron transfer. In practice, the free-energy values of such species are downshifted by $-eU$, where e is the elementary charge. In acidic conditions, U_0 (1.23 V) is the equilibrium potential or the minimum required potential allowed by thermodynamics (**Figure 4-2**, red lines). If some of the steps are found to be uphill even at equilibrium potential (as is the case in **Figure 4-2b**), a larger applied potential or U^{onset} is required to overcome the positive free-energy variations, determining an overpotential η that corresponds to the difference U^{onset}-U_0.

In summary, within this framework, it is possible to obtain electrode potential dependent free-energy diagrams for the OER at the anode and consequently an estimate of the overpotential (η) necessary to drive the reaction, which is one of the most important descriptors to evaluate the performance of electrocatalysts.

In **Figure 4-2**, we present two representative schemes for an ideal and a real electrocatalyst for OER. In the case of the ideal catalyst (**Figure 4-2a**), the free-energy separation between each step of oxidation is equal to +1.23 eV (black lines). The overall free-energy separation between reactants and products is $\Delta G = +1.23 \times 4 = +4.92$ eV. According to the relation between Gibbs free energy and the electromotive force $\Delta G = -n\mathrm{F}E^0 = +4.92\ \mathrm{eV}$, with $n = 4$, the minimum required external potential U_0 to be applied is +1.23 V to observe the oxygen evolution reaction, also defined as equilibrium potential. In practice, we subtract the equilibrium potential value to the free-energy variation at each oxidation step to obtain the free-energy profile at such potential (going from black to red lines in **Figure 4-2**). For the ideal catalyst, all the resulting red lines lie at the zero free-energy variation, that is, they are isoenergetic and may take place with no further need of external bias. In contrast, for a real catalyst (**Figure 4-2b**), at equilibrium potential there is still at least one uphill step (in the example, it is the third oxidation step). Therefore, one must apply a larger U or U^{onset}, to be subtracted from the original free-energy variations at each step of oxidation, in order to shift the resulting blue lines further down, allowing the path to become downhill (blue lines). We will name the oxidation step (involving an electron transfer) with the largest positive free-energy variation as the "potential-determining step" (PDS) and we will indicate the overpotential η as the difference: U^{onset}-U_0.

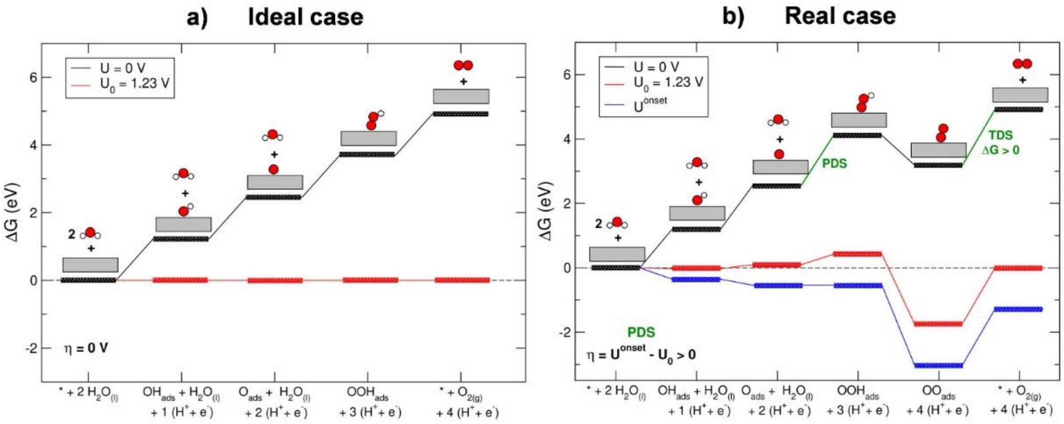

Figure 4-2: Free-energy diagram for an ideal (a) and real (b) catalyst along the OER steps. Black lines correspond to an electrode potential of $U = 0$ V, red lines correspond to the equilibrium potential U_0, and blue lines correspond to the onset potential U^{onset}. Each intermediate is shown together with a schematic representation of the structure. * in the *x* axis labels represents the catalyst. PDS and TDS are highlighted in green.

An important aspect to consider when studying an electrochemical process concerns the estimation of the activation barriers, which was not explicitly considered in the methodology reported by Nørskov and co-workers. For this reason, the theoretical overpotentials presented herein are a lower bound for the experimentally measured overpotentials, which could be higher due to non-zero kinetic barriers.

Another crucial aspect that is not considered in this approach is the presence of chemical steps that do not involve electron transfer and, therefore, are not affected by an external potential bias. In some cases, those steps are critical for the performance of an electrocatalyst, since they could be more demanding than any electron-transfer involving step. To further clarify this point, in **Figure 4-2b** we suppose for example that the O_2 release is more demanding than any of the previous oxidation steps. Then, one must distinguish between the PDS, as defined above (i.e., the oxidation step with the largest positive free-energy variation), and the "thermodynamic-determining step" (TDS), which is the step with the largest positive free-energy variation between any two intermediates along the reaction path. In some cases, the PDS coincides with the TDS, but in other cases they are two different steps, as it is the case in the representative example in **Figure 4-2b**.

4.5. Water oxidation reaction on pristine h-BN

Although pristine free-standing h-BN is not expected to be an excellent electrocatalyst, it is the reference system for this work and, therefore, it must be investigated.

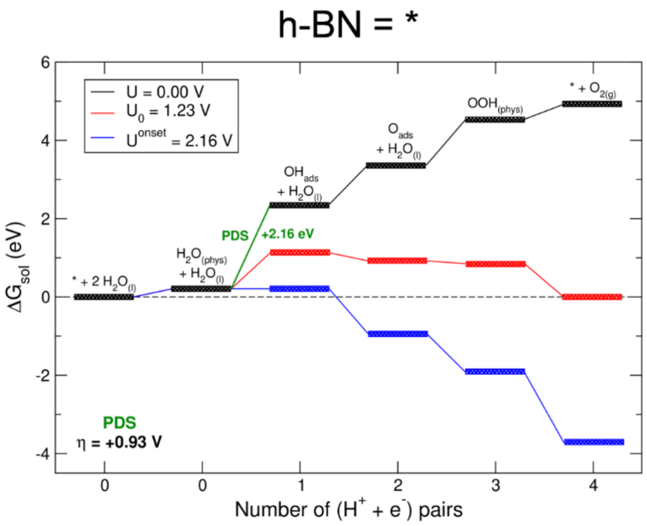

Figure 4-3: Free energy diagram (ΔG_{sol}) for the OER reaction along the associative path catalysed by the pure free-standing h-BN monolayer. Three different values of external potential are considered: zero, equilibrium and onset potentials (black, red, and blue lines, respectively). The value of the theoretical overpotential (η) is reported on the bottom left and the PDS is shown in green for the corresponding electronic step. In this case, PDS coincides with TDS.

In **Figure 4-3**, we show the free-energy diagram for the O_2 evolution reaction and we identify the first oxidation step (from a physisorbed water molecule to an adsorbed OH; see also **Figure 4-4**) as the PDS. The details of this procedure are discussed in Section 2.2. At the equilibrium potential U_0 = 1.23 V, this is still an uphill reaction step (red path). Only when the applied potential reached the onset value of 2.16 V does the overall multistep reaction process become downhill (blue path). Therefore, the resulting theoretical overpotential η is estimated to be +0.93 V.

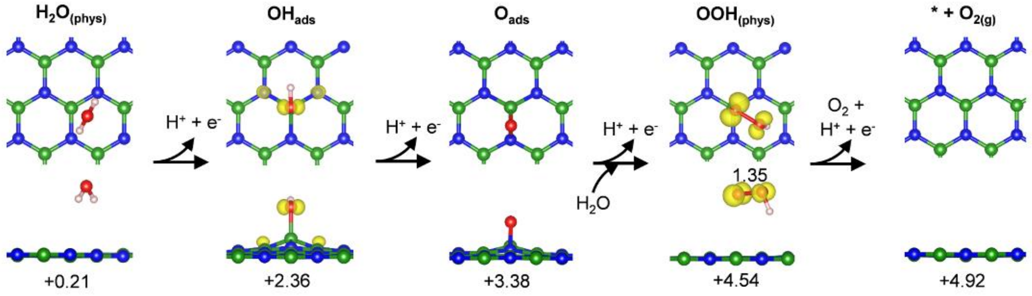

Figure 4-4: Ball-and-stick representations of the intermediates of the OER process along the associative path on pure free-standing h-BN monolayer (as reported in **Figure 4-3**), shown with the corresponding spin density plots (isosurface level is 0.02 $e^-/bohr^3$). Yellow and cyan colors indicate positive and negative densities, respectively. The ΔG_{sol} energies (in unit of eV) are reported below each structure. Color coding: B in green, O in red, N in blue and H in white. Distances are in Å.

In **Figure 4-4**, we present the ball-and-stick representation of all the intermediates along the reaction path in **Figure 4-3**, together with the electron spin density plot for those intermediates that present an unpaired electron.

4.6. Water oxidation reaction on defective h-BN

Defect engineering of two-dimensional materials is a promising approach to improve their electronic properties. When one atom from the lattice is absent, the monolayer includes some undercoordinated atoms, which can be very reactive. This condition might not necessarily improve the electrocatalytic properties of the system, because the intermediate oxygenated species, along the reaction path, could be bound too strongly to the substrate. The best electrocatalyst is the one characterized by a medium bonding strength to the intermediate species.

We have investigated both the boron (h-B^VN) and the nitrogen (h-BN^V) vacancy (**Figures 4-5** and **4-6**). The boron vacancy leaves three undercoordinated N atoms, whereas the nitrogen vacancy leaves three undercoordinated B atoms. The B atoms have a very large affinity towards oxygen (see below). For a detailed analysis of the structural, electronic, and magnetic properties of defective h-BN layers, one can refer to our previous work (Chapter 3).

Starting from the analysis of h-B^{V}N, we observe that the first oxidation step, leading to the formation of an adsorbed OH, is only slightly uphill, whereas the second, leading to the formation of an adsorbed O atom, is spontaneous, due to the high stability of this intermediate species where the O atom is bound to two N atoms, leaving one unpaired electron on the third N atom surrounding the vacancy. It is then very energetically demanding to go through the third oxidation step that involves another water molecule and leads to the formation of an OOH intermediate species, which is characterized by a much lower affinity towards the defective surface. Therefore, we identify this as the PDS step, causing a theoretical overpotential for the water oxidation reaction above 2 V. All the other steps of reaction, even those that do not involve any electron transfer and that are, thus, not affected by the applied external potential, present lower energy cost.

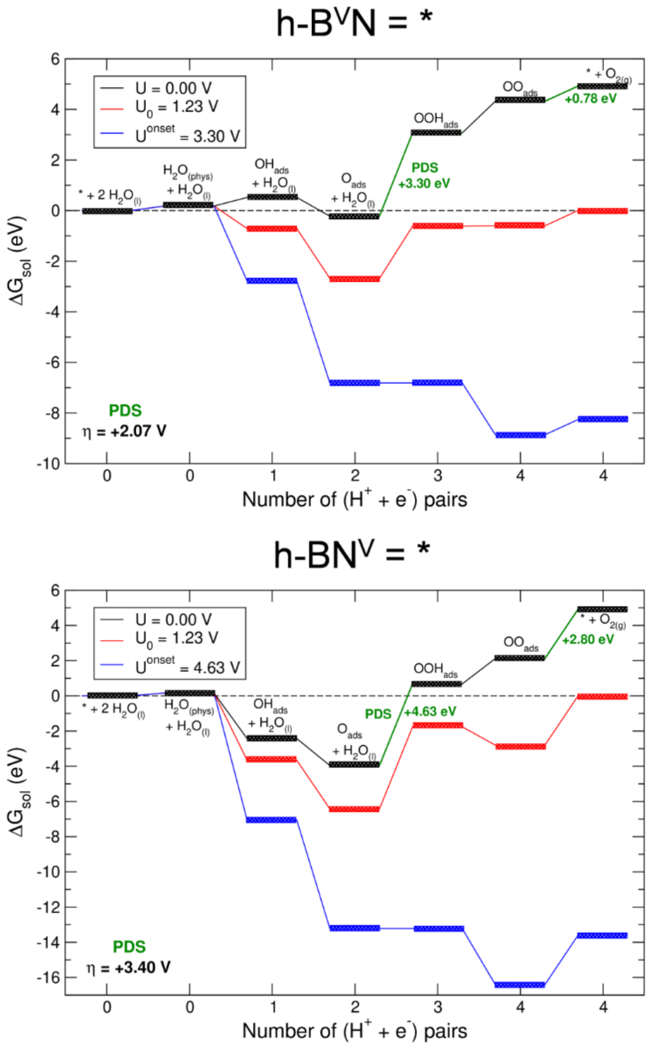

Figure 4-5: Free energy diagram (ΔG_{sol}) for the OER reaction along the associative path catalysed by defective free-standing h-BN monolayer (B monovacancy in the first row, N monovacancy in the second row). Three different values of external potential are considered: zero, equilibrium and onset potentials (black, red and blue lines, respectively). The value of the theoretical overpotential (η) is reported on the bottom left and the PDS is shown in green for the corresponding electronic step. In both cases, PDS coincides with TDS. The free energy cost for the O_2 gas release (last step) is also reported in green.

In the case of h-BN^V, all the oxygenated intermediates are excessively stable. For the first two steps of oxidation, we even observe a negative free-energy change. The potential-determining step is found to be the third one, which involves a second water molecule to form an adsorbed OOH species. The required onset potential to be applied is very high, leading to an enormous theoretical overpotential of 3.4 V. Even if the last reaction step of the O_2 gas evolution is rather endergonic, the energy cost is lower than that for the third oxidation step, which remains the determining one. Therefore, neither of the free-standing defective h-BN monolayer systems seems to be a potentially interesting and active substrate for the water oxidation electrocatalysis.

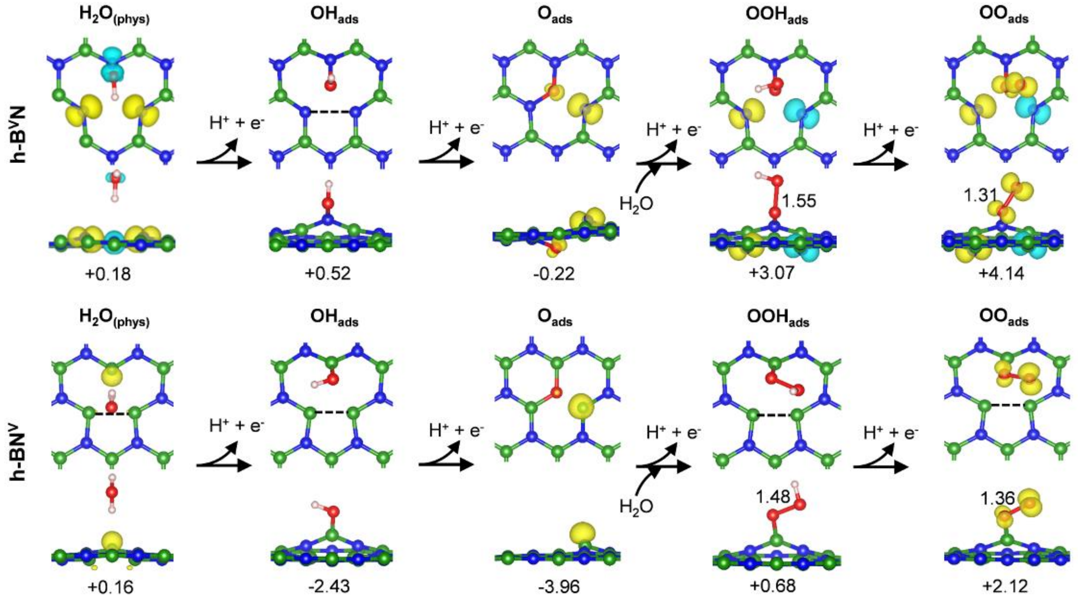

Figure 4-6: Ball-and-stick representations of the intermediates of the OER process along the associative path on defective free-standing h-BN monolayer (as reported in **Figure 4-5**), shown with the corresponding spin density plots (isosurface level is 0.02 $e^-/bohr^3$). Yellow and cyan colors indicate positive and negative densities, respectively. The ΔG_{sol} energies (in unit of eV) are reported below each structure. Color coding: B in green, O in red, N in blue and H in white. Black dashed lines indicate N–N or B–B bond formation. Distances are in Å.

Figure 4-6 shows all the intermediate species along the reaction paths for both h-B^VN and h-BN^V. The unpaired electrons localize at defect and reactive sites. For h-B^VN, when water physisorbs at the defect, the lowest spin configuration is an open-shell doublet, with three unpaired electrons on the three undercoordinated nitrogen sites (two of them have antiparallel spins in antiferromagnetic coupling). Upon first oxidation, one unpaired electron pairs up with the OH radical, whereas the other two unpaired electrons pair up together, forming an N-N bond. Upon further (second) oxidation, the unpaired electron formed localizes on an undercoordinated N atom. Successively, a second undercoordinated N atom gets an unpaired electron and finally, in the last step, the one further electron is removed at the expense of the peroxo species adsorbed on the surface, which transforms into a superoxo.

In the case of the h-BN^V, the initial system is a doublet, presenting only one unpaired electron on one undercoordinated B atom, with the other two B atoms involved in a B-B bond. Upon first oxidation, the unpaired electron is saturated by the newly formed OH radical. Successively, the next oxidation step forms an electron hole on one undercoordinated B atom with the O_{ads} species bridging the other two B atoms at the defect. Then, at the third oxidation step, we observe both the formation of an adsorbed OOH species and reestablishment of the B-B bond. Finally, the last oxidation step transforms the peroxo species into a superoxo.

4.7. Water oxidation reaction at Cu-doped h-BN

In this section, we consider the last free-standing h-BN system: a Cu-doped monolayer, where a Cu atom replaces a missing boron atom in the lattice. When a B atom is removed, three N atoms remain exposed and they are excellent donor species for metal atom coordination, as in metalloporphyrin systems. Trapped metal atoms were previously found to be good electrocatalysts for other reactions. Here, we test Cu-doped h-B^VN for the water oxidation reaction. The Cu atom is too large and does not perfectly fit in the hole left by the missing B atom. Therefore, it lies out of the plane, forming three Cu-N bonds, and it is favorably exposed to molecular adsorption for catalysis.

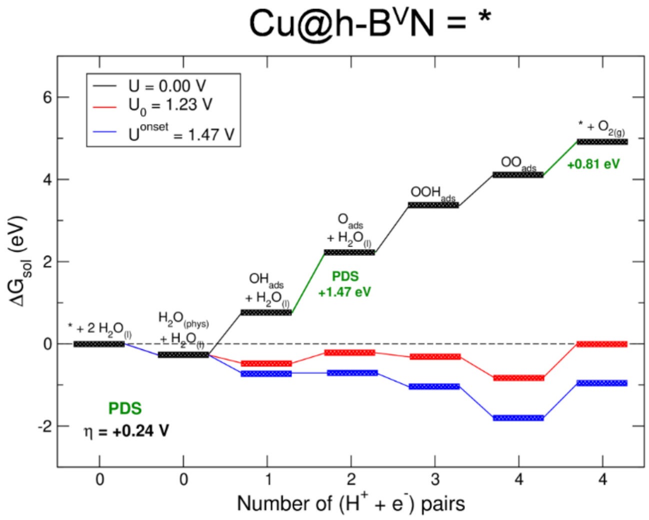

Figure 4-7: Free energy diagram (ΔG_{sol}) for the OER reaction along the associative path catalysed by free-standing Cu-doped h-BN monolayer. Three different values of external potential are considered: zero, equilibrium and onset potentials (black, red and blue lines, respectively). The value of the theoretical overpotential (η) is reported on the bottom left and the PDS is shown in green for the corresponding electronic step. In this case PDS coincides with TDS. The free energy cost for the O_2 gas release (last step) is also reported in green.

Figure 4-7 shows the free-energy diagram of the steps through the full water oxidation reaction. The energy cost for each step is rather close to the equilibrium value. The PDS is the second oxidation step, where the adsorbed OH (bound to the Cu atom; see OH_{ads} in **Figure 4-8**) is oxidized to an adsorbed O atom (bridging between the Cu atom and an N atom; see O_{ads} in **Figure 4-8**). The theoretical overpotential resulting from this PDS step is only 0.24 V. Consider that the last chemical step of O_2 molecular evolution from the chemisorbed OO_{ads} species, which does not involve any electron transfer and is, therefore, not affected by the applied external potential, is characterized by a free-energy cost of +0.81 eV.

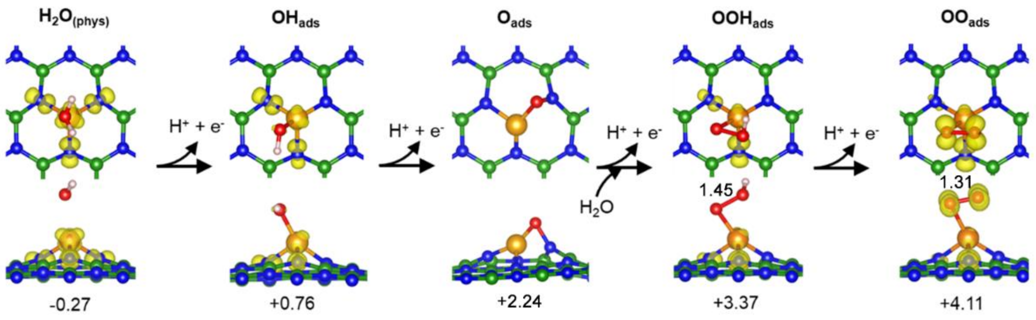

Figure 4-8: Ball-and-stick representations of the intermediates of the OER process along the associative path on free-standing Cu-doped h-BN monolayer (as reported in **Figure 4-7**), shown with the corresponding spin density plots (isosurface level is 0.02 $e^-/bohr^3$). Yellow and cyan colors indicate positive and negative densities, respectively. The ΔG_{sol} energies (in unit of eV) are reported below each structure. Color coding: B in green, O in red, N in blue, Cu in orange and H in white. Distances are in Å.

The intermediate structures shown in **Figure 4-8** have been fully relaxed both for the atomic positions and the total magnetization. The spin plots indicate some residual unpaired electrons in the system. The Cu-doped h-BN monolayer is characterized by two unpaired electrons. After the first oxidation step, the system has only one unpaired electron and through the second oxidation step a closed-shell configuration is reached. The third oxidation step again leaves an unpaired electron, delocalized on three atomic centers (N-Cu-N). Finally, the last electron is removed at the expense of the peroxo species bound to the Cu atom, which is transformed into a superoxo.

4.8. Water oxidation reaction at Cu-supported h-BN

4.8.1. Pristine h-BN and defective h-B^VN on Cu(111)

An underlying metal substrate to the h-BN layer can have relevant effects on the electronic properties and on the reactivity of the 2D material. As we mentioned in the introduction, Cu is a very attractive support since it can be produced in the form of extended foils and, therefore, suitable for scaled up applications. In our previous work (Chapter 3), we analyzed the electronic and chemical interplay between a pristine and defective h-BN layer on a Cu substrate. In this chapter, we investigate whether these interfaces can be of potential interest for the water oxidation reaction.

We start from pristine h-BN on a Cu (111) perfect surface. The free energy diagram is rather satisfactory (top of **Figure 4-9**). The PDS is the third oxidation step going from an adsorbed O atom to the formation of a hydroperoxo species through the addition of a water molecule. The theoretical overpotential associated to this step is as low as 0.30 V. However, the critical and thermodynamic determining step (TDS) along the reaction path is the final step, where O_2 gas is evolved from the surface. This step does not involve any electron transfer, thus it remains unchanged at any applied potential, as one can observe from the top diagram in **Figure 4-9**. The free energy cost associated to the O_2 detachment from the surface is of +1.68 eV.

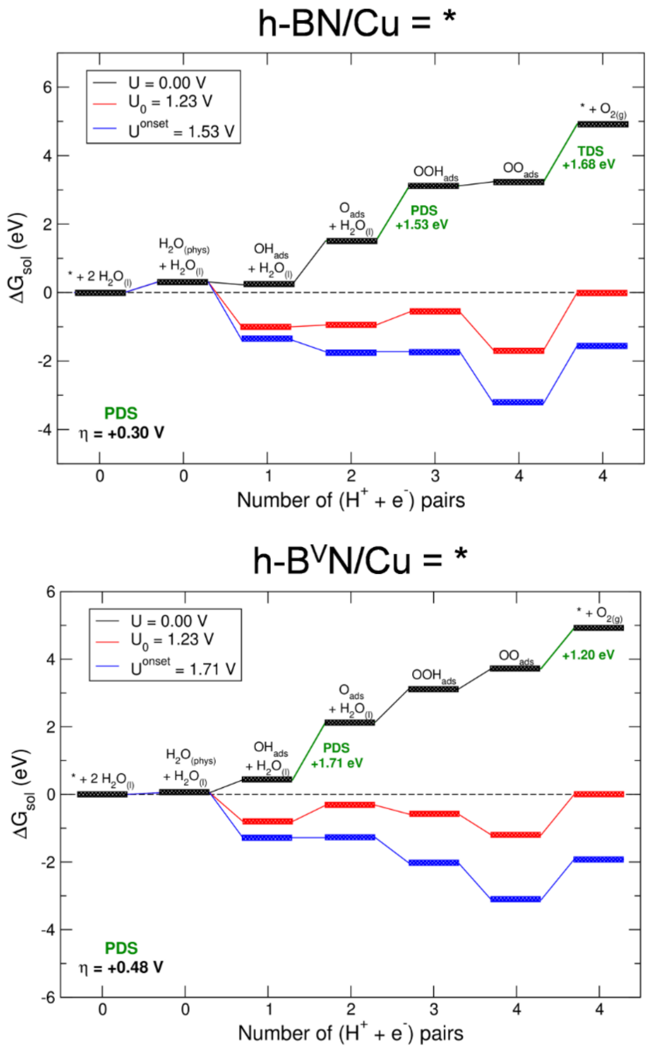

Figure 4-9: Free energy diagram (ΔG_{sol}) for the OER reaction along the associative path catalysed by pure and defective h-BN supported on Cu (pristine in the upper panel, B monovacancy in the lower panel). Three different values of external potential are considered: zero, equilibrium and onset potentials (black, red and blue lines, respectively). The value of the theoretical overpotential (η) is reported on the bottom left and the PDS is shown in green for the corresponding electronic step. For h-BN/Cu, the PDS does not coincide with the TDS, whereas for h-B^VN/Cu, the PDS coincides with the TDS. The free energy cost for the O_2 gas release (last step) is also reported in green and is identified as TDS when it is the case.

The intermediate structures along the reaction path are shown on the top row in **Figure 4-10**. The magnetization is zero in all cases as a consequence of the presence of the underlying metal substrate. The chemisorbed OO_{ads} species is too much stabilized by the surface. It is a peroxo species bridging two B atoms. The O-O distance is 1.51 Å, which is typical of a peroxo species. This is an interesting observation since it implies that the last oxidation step has removed an electron from the Cu substrate, differently from all what we have observed before for free standing h-BN models, where the last electron was removed from the peroxo species that was oxidized to a superoxo one.

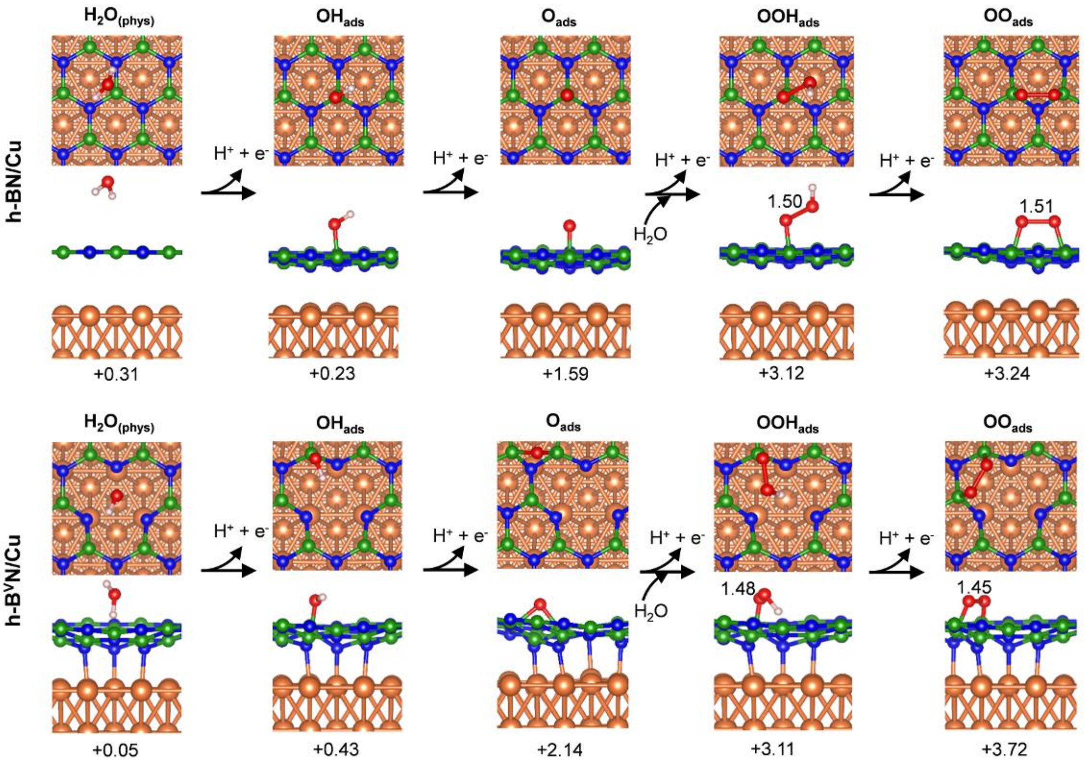

Figure 4-10: Ball-and-stick representations of the intermediates of the OER process along the associative path on pure and defective (B monovacancy) h-BN supported on Cu (as reported in **Figure 4-9**). The ΔG_{sol} energies (in unit of eV) are reported below each structure. Color coding: B in green, O in red, N in blue, Cu in orange and H in white. Distances are in Å.

Since, in section 4.6, we realized that oxygenated species are too strongly bound to the free standing h-BN monolayer with a missing nitrogen atom (h-BN^V), we decided only to investigate the B-defective h-BN monolayer (h-B^{V}N) supported on a Cu(111) substrate. What we observe is, however, a very similar reactivity to that of the not defective Cu-supported h-BN: compare intermediates and energies for h-BN/Cu and h-B^{V}N/Cu in **Figure 4-10**. Since the undercoordinated N atoms are involved in a strong bonding with the underlying Cu atoms, the oxygenated species prefer to bind to the nearby B atoms, in a similar fashion to the non-defective case. The PDS is the second oxidation step, with a theoretical overpotential of 0.48 V. The O_2 evolution step requires +1.20 eV, and although this free energy change is less than for the PDS step, it will not be affected by any external applied potential and will remain unvaried even at the onset potential that is required to zero the energy cost for the PDS.

4.8.2. Cu-doped h-B^VN on Cu(111)

In our previous work, we have shown that Cu adatoms from the metal substrate can be trapped in the defective h-BN lattice and be stabilized by formation of very stable Cu-N bonds. These isolated Cu atoms could be potentially active single-atom catalysts, as we observed in the free-standing case in section 4.7. Therefore, in the following we will consider two cases of trapped Cu atom: i) the Cu atom is exposed towards the vacuum and it does not have any contact with the underlying copper substrate where it comes from (Cu^{up}@h-B^VN/Cu); ii) the Cu atom is in the interfacing region where it is still in contact with the underlying surface but it is also bound to the undercoordinated N atoms in the defective h-BN layer (Cu^{down}@h-B^VN/Cu).

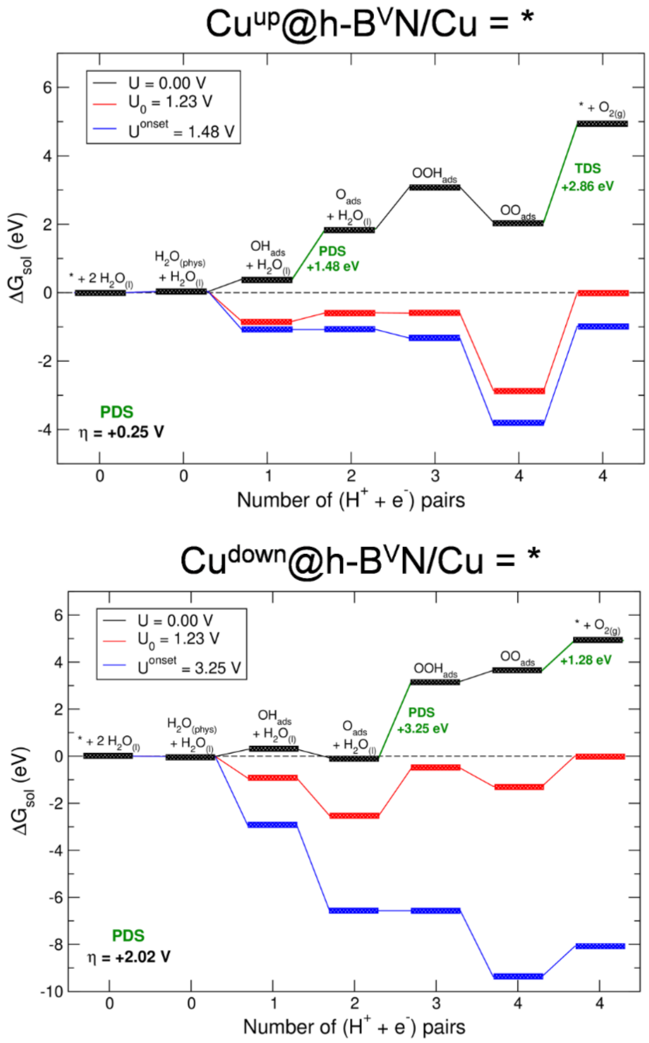

Figure 4-11: Free energy diagram (ΔG_{sol}) for the OER reaction along the associative path catalysed by Cu-doped h-B^VN supported on Cu (Cu up in the first row, Cu down in the second row). Three different values of external potential are considered: zero, equilibrium and onset potentials (black, red and blue lines, respectively). The value of the theoretical overpotential (η) is reported on the bottom left and the PDS is shown in green for the corresponding electronic step. For Cu^{up}@h-B^VN/Cu, PDS does not coincide with TDS, whereas for Cu^{down}@h-B^VN/Cu, PDS coincides with TDS. The free energy cost for the O_2 gas release (last step) is also reported in green and identify as TDS when it is the case.

We expected the first configuration, Cu^{up}@h-B^VN/Cu, to behave similarly to the Cu-doped free-standing model. On the contrary, we found out that the underlying substrate plays a crucial role. When comparing **Figure 4-7** and **4-8** with top of **Figure 4-11** and of **Figure 4-12**, one can identify several differences. The PDS is the same in the two cases, i.e. the second oxidation step from OH_{ads} to O_{ads}. The resulting theoretical overpotential is approximately the same as the free-standing case: 0.25 vs 0.24 V. However, we observe a very critical thermodynamic determining step (TDS) for the O_2 evolution from the peroxo (OO_{ads}) species formed on the surface (top of **Figure 4-12**), with a free energy variation of +2.86 eV. This is extremely tightly bound to the Cu adatom, in contrast to the free-standing case, where the release of O_2 would start from a superoxo species with only one of the O atoms bound to the N-encapsulated Cu atom. This large stability of the OO_{ads} intermediate is due to an electron transfer from the underlying Cu substrate. The surface Cu atoms involve the N atoms of the h-BN into some direct bonds, releasing the trapped Cu atom for a stronger interaction with the OO moiety than in the free-standing case, where an end-on superoxo is formed (see **Figure 4-8**).

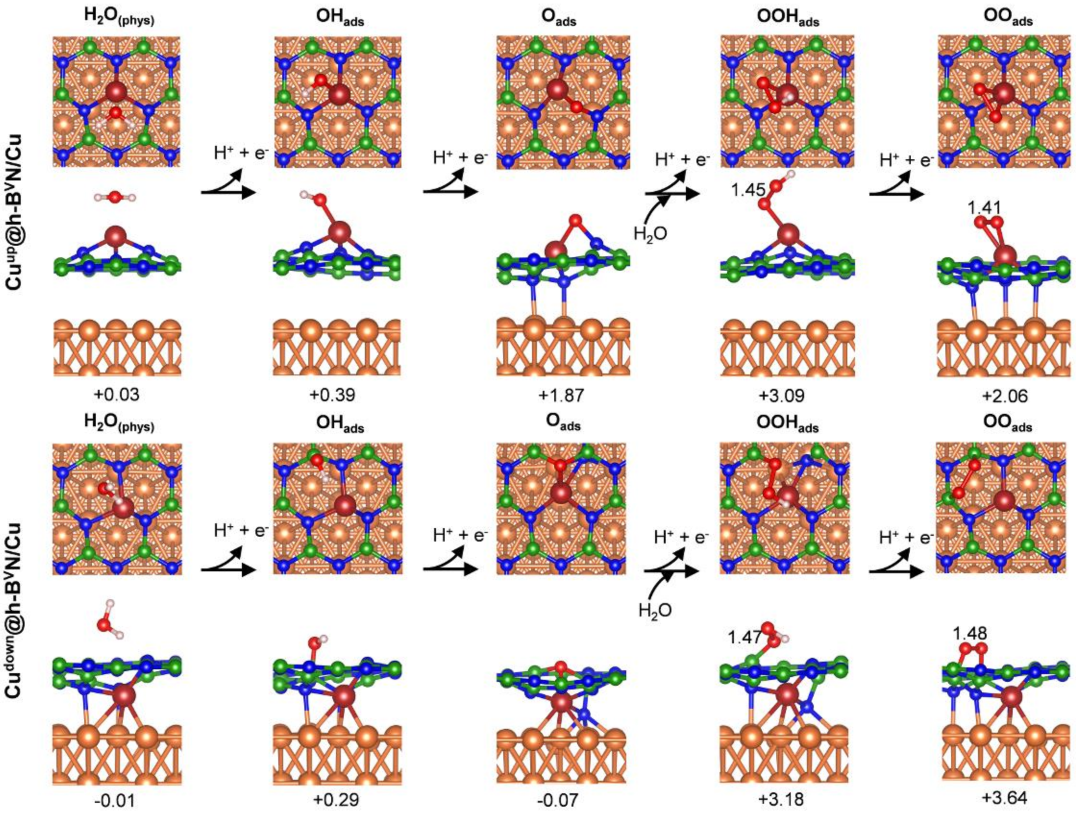

Figure 4-12: Ball-and-stick representations of the intermediates of the OER process along the associative path on Cu-doped h-B^{V}N supported on Cu (as reported in **Figure 4-11**). The ΔG_{sol} energies (in unit of eV) are reported below each structure. Color coding: B in green, O in red, N in blue, Cu in orange, Cu adatom in dark red and H in white. Distances are in Å.

For the second configuration, Cu^{down}@h-B^{V}N/Cu, we observe a completely different scenario. Here, the Cu adatom is still strongly bound to the copper surface, as one can clearly note in the bottom of **Figure 4-12**. For this reason, the oxygenated species prefer to bind to the B atom in the h-BN layer than to the Cu atom. The PDS results to be the third oxidation step because the starting O_{ads} intermediate is excessively stable. Something much unexpected happened during the geometry relaxation of this structure. The adsorbed O atom replaces one of the undercoordinated N atoms in the defective h-BN lattice, whereas the substituted N atoms moves in the interfacing region to bridge the Cu adatom with other surface Cu atoms. The resulting configuration is characterized by a very low energy, which is the cause for the very high free energy change to the next oxidized intermediate along the reaction path (OOH_{ads}), leading to a theoretical overpotential of more than 2 V.

4.8.3. Cu adatom clustering at larger h-BN defect sites on Cu(111)

We have shown in Chapter 3 that not only single adatoms can be favorably trapped at atomic vacancies in Cu-supported h-BN, but also clusters of few Cu adatoms. In the following, we will consider trimers (Cu_3) and tetramers (Cu_4) that are trapped at a pluriatomic vacancy $(N_1B_3)^V$ in the h-BN layer.

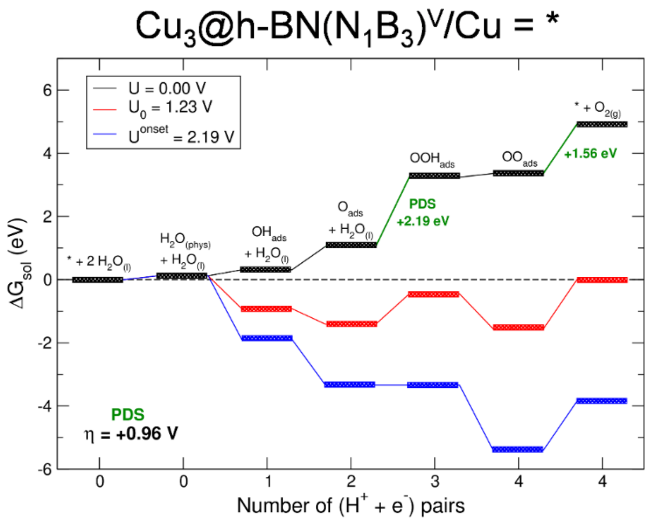

Figure 4-13: Free energy diagram (ΔGsol) for the OER reaction along the associative path catalysed by trimer (Cu_3) trapped at the pluriatomic vacancy $(N_1B_3)^V$ in the h-BN layer supported on Cu. Three different values of external potential are considered: zero, equilibrium and onset potentials (black, red and blue lines, respectively). The value of the theoretical overpotential (η) is reported on the bottom left and the PDS is shown in green for the corresponding electronic step.

In this case, the PDS coincides with the TDS. The free energy cost for the O2 gas release (last step) is also reported in green.

In the case of the trimer (Cu_3) (see **Figure 4-13** and **Figure 4-14**), the oxygenated species are rather too stable, especially as regards OH_{ads} and O_{ads}. Therefore, the PDS is the third oxidation step, leading to a theoretical overpotential of 0.99 V.

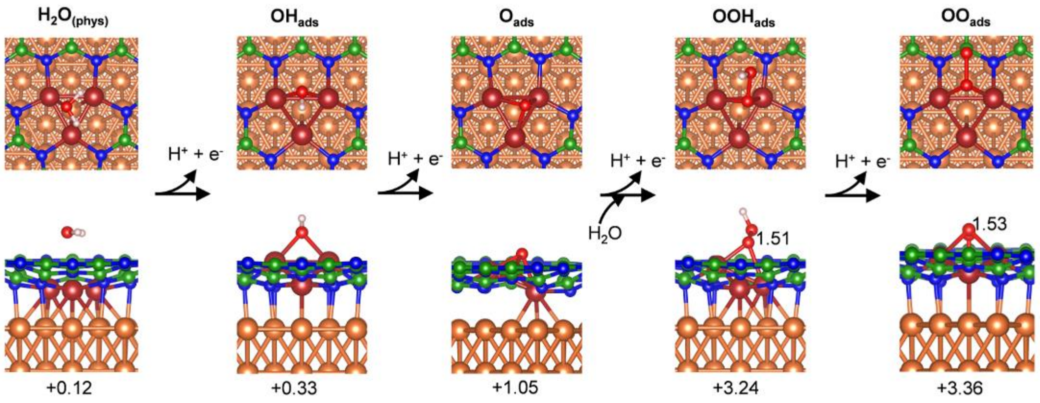

Figure 4-14: Ball-and-stick representations of the intermediates of the OER process along the associative path on Cu trimer (Cu_3) trapped at the pluriatomic vacancy $(N_1B_3)^V$ in the h-BN layer supported on Cu (as reported in **Figure 4-13**). The ΔG_{sol} energies (in unit of eV) are reported below each structure. Color coding: B in green, O in red, N in blue, Cu in orange, Cu adatom in dark red and H in white. Distances are in Å.

When we add a fourth Cu adatom to the cluster to form a tetramer (Cu_4) in the h-BN hole, we put it on top of the triangle of the other three Cu atoms (see **Figure 4-16**). A small pyramid is formed, which exposes the added Cu atom to the vacuum, making it more available for reactivity. This system is indeed very interesting as a potentially active electrocatalyst for the water oxidation reaction.

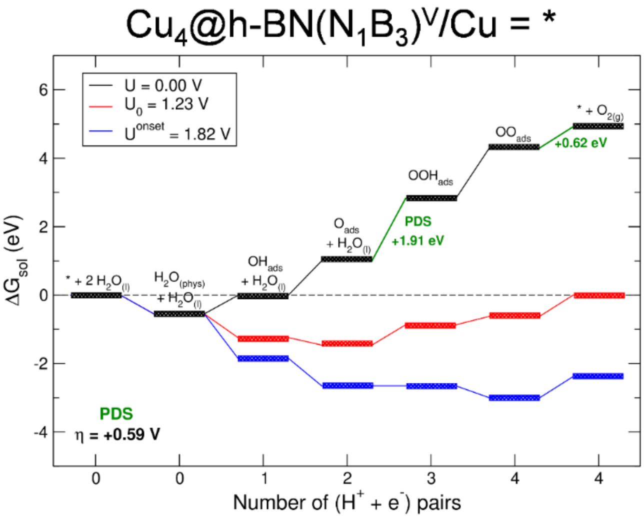

Figure 4-15: Free energy diagram (ΔG_{sol}) for the OER reaction along the associative path catalysed by tetramer (Cu_4) trapped at the pluriatomic vacancy $(N_1B_3)^V$ in the h-BN layer supported on Cu. Three different values of external potential are considered: zero, equilibrium and onset potentials (black, red, and blue lines, respectively). The value of the theoretical overpotential (η) is reported on the bottom left and the PDS is shown in green for the corresponding electronic step. In this case, PDS coincides with TDS. The free energy cost for the O_2 gas release (last step) is also reported in green.

The consecutive steps of reaction have a uniform increase in free energy (**Figure 4-15**), with a PDS that is just slightly higher than the other steps. The computed theoretical overpotential is reasonably low, i.e. 0.68 V. The last step of O_2 release costs only +0.45 eV, because the end-on superoxo species is not too strongly bound to the Cu on the pyramid vertex.

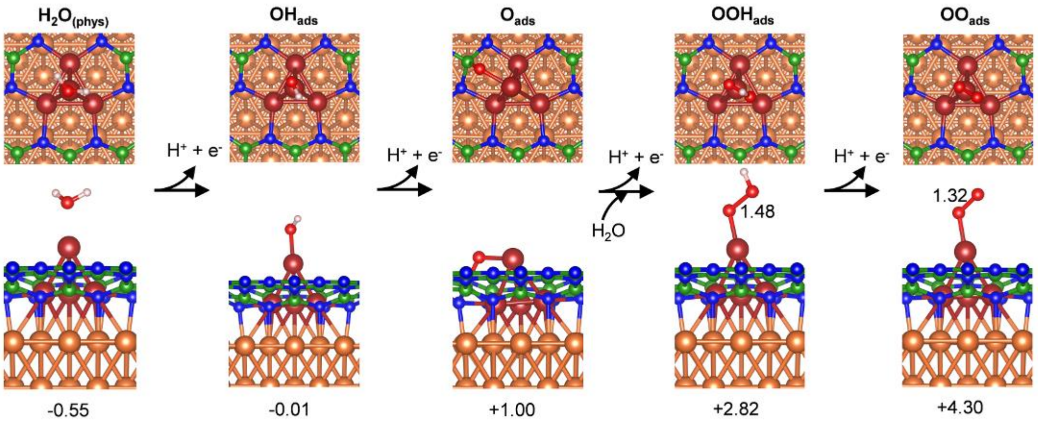

Figure 4-16: Ball-and-stick representations of the intermediates of the OER process along the associative path on Cu tetramer (Cu_4) trapped at the pluriatomic vacancy $(N_1B_3)^V$ in the h-BN

layer supported on Cu (as reported in **Figure 4-15**). The ΔG_{sol} energies (in unit of eV) are reported below each structure. Color coding: B in green, O in red, N in blue, Cu in orange, Cu adatom in dark red and H in white. Distances are in Å.

Therefore, the results for the Cu tetramer cluster trapped in a defective h-BN lattice on a Cu (111) substrate are encouraging, since they indicate a rather low potential determining step together with a low free energy cost for the O_2 final release. Both these favorable conditions were not observed for any of the h-BN based systems discussed above in this work.

In order to rationalize the favorable behavior of the trapped Cu tetramer with respect to the other systems considered, we have analyzed and compared their electronic structure in terms of total and projected density of states (DOS and PDOS), which are reported in **Figure 4-17**.

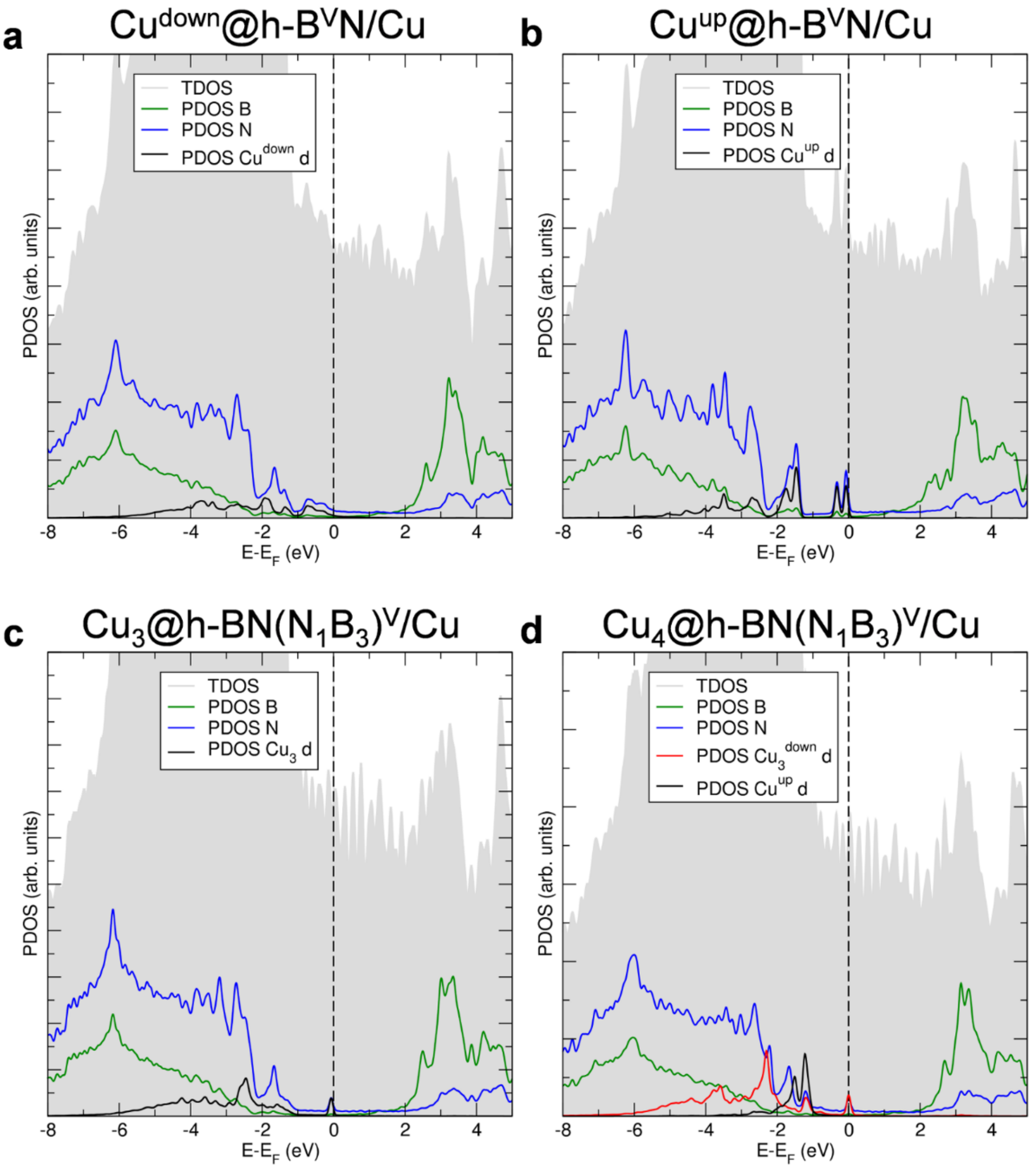

Figure 4-17: Total (TDOS) and projected (PDOS) density of states for Cu^{down}@h-B^VN/Cu (a), Cu^{up}@h-B^VN/Cu (b), Cu_3@h-BN$(N_1B_3)^V$/Cu (c) and Cu_4@h-BN$(N_1B_3)^V$/Cu (d) as obtained by vdW-DF2^{C09x}/QE. Legend of colors is given in each panel. The Fermi level is scaled to zero and is indicated by a dashed line.

The projections are on all the B, all the N and the Cu adatoms. In the case of the trapped Cu tetramer we further distinguish between the three Cu atoms interacting with the h-BN lattice and the Cu support and the forth Cu atom at the vertex of the pyramid, which is the one directly involved in the electrocatalysis of water to O_2. The contribution by the rest of Cu atoms in the underlying substrate can be derived by subtraction of the projection from the total density of states. There is a clear difference in the PDOS of the trapped

Cu_4 with respect to the trapped Cu_3 and the trapped Cu single atoms (in both up and down configurations): the d states associated to the Cu atom at the vertex of the Cu_4 pyramid do not lie in the proximity of the Fermi energy but at least -1 eV below, in contrast to all the other cases, where the trapped Cu atoms d states have a considerable portion near the Fermi energy. Therefore, only the Cu atom at the Cu_4 vertex is not electron rich, i.e. is not prompted to donate d electrons to any bound chemical species. We consider this the reason why such system is the best electrocatalyst for the water oxidation reaction. Being an oxidation reaction, it is required that the electron is removed from the water species and not from the Cu atoms. A confirmation of the poor electron donor properties of the trapped Cu_4 systems comes from the fact that the adsorbed OO species before O_2 release is a superoxo (with one extra electron), whereas in all the other cases of trapped Cu atoms (single up or down or Cu_3) it is a peroxo (with two extra electrons). The O_2 release from a stabilized side on $-(O-O)^{2-}-$ species is energetically more demanding than from an end-on $-(O-O)^{-}$, which is confirmed by our data, as discussed above.

4.9. Conclusions

In this work, we have performed a computational electrochemistry analysis based on van-der-Waals corrected density functional theory calculations to establish the performance of Cu-doped and Cu-supported defective h-BN as electrocatalyst for the water oxidation reaction. Both the associative and the direct O_2 recombination mechanisms (see **Figure 4-1**) have been investigated in this work. The associative path is found to be more energetically favourable with respect to the direct O_2 recombination one.

In section 4.5 we have first investigated the free energy diagram for water oxidation reaction for free-standing pristine h-BN, as reference to our work. We compute a very high overpotential of 0.93 V due to a highly expensive first step of oxidation forming an adsorbed OH species on a B atom of the monolayer.

In section 4.6 we have analyzed the case of free-standing defective h-BN, presenting either a B or a N monovacancy in the lattice. The residual undercoordinated atoms are very reactive towards the oxygenated species along the water oxidation; therefore, the intermediates of reaction are too stable, which causes very high overpotentials (2.07 and 3.40 V, respectively).

In section 4.7 we have investigated how free-standing Cu-doped h-BN performs in the electrocatalysis of the water oxidation reaction, considering that the water oxidation intermediates bind to the encapsulated Cu atom. Based on our previous study, we focus on Cu trapped into a B monovacancy (not into an N monovacancy), which is characterized by the formation of three Cu-N stable bonds. The Cu atom is found to lie out of plane with respect to the monolayer. This system is an interesting electrocatalyst with a low theoretical overpotential (0.24 V) but presents a large free energy cost for the final step of O_2 gas release (0.81 eV).

In section 4.8.1 we analyzed the effect of a Cu (111) underlying support on the activity of both pristine and defective h-BN. Supported pristine h-BN confirms the low theoretical overpotential of free-standing h-BN with a high free energy cost for the O_2 release. The presence of the support under defective h-BN (with a B monovacancy) is quite interesting: the undercoordinated N atoms in the monolayer become involved in a strong interaction with surface Cu atoms and are not available for water oxidation intermediates adsorption. Therefore, the water oxidation reaction is catalyzed by B atoms of the h-BN layer and the reaction profile is then similar to what observed for supported pristine h-BN.

In section 4.8.2 Cu-doped h-BN is supported on Cu (111) surface. The Cu dopant can be either pointing outward towards the vacuum or interacting with the underlying substrate. None of these is an excellent electrocatalyst for water oxidation reaction, because the former presents a low theoretical overpotential (0.25 V) but a large free energy cost for the final O_2 release step due to a strong interaction of the O_2 molecule with Cu, whereas the latter is characterized by a high overpotential of 2.02 V at the third oxidation step due to a too strong stabilization of the O_{ads} intermediate of reaction.

Finally, in section 4.8.3 we have considered the possibility of having some small Cu clusters filling larger lattice defects in the h-BN lattice. Trapped clusters of three Cu atoms still present large theoretical overpotentials (0.99 V) due to overstabilization of the O_{ads} intermediate of adsorption. On the contrary, trapped Cu tetramers, in the form of pyramids, expose one Cu atom toward the vacuum, which becomes available for catalysis. Such systems have a relatively low overpotential (0.68 V) and a low free energy cost (0.45 eV) for the final step of O_2 release. Therefore, they are extremely interesting systems for the electrocatalysis of the water oxidation reaction. We rationalized this favorable behavior through the analysis of the electronic structure, showing that the Cu atom at the vertex of the Cu_4 pyramid, which is the one involved in the water oxidation electrocatalysis, is electron poor and does not present d states at the Fermi level (in contrast to the other trapped Cu systems consider in this work). This characteristic makes it a better candidate for an oxidation reaction where O_2 molecules must be released from the surface: the lower the degree of electron donation to the reaction intermediates along the oxidation path and to the final adsorbed O_2 (superoxo vs peroxo species), the easier the O_2 evolution from the surface.

These results pave the way for a rational engineering of the interface between bidimensional materials and the underlying metal support for preparation of active electrocatalysts for O_2 evolution reaction (OER), discussed in this work, but also for other oxidation or reduction processes.

5. Can Single Metal Atoms Trapped in Defective h-BN/Cu (111) Improve Electrocatalysis of the H_2 Evolution Reaction?

In Chapter 3, we have shown that when a non-regular h-BN 2D layer is grown on a Cu (111) surface, metal adatoms spontaneously pop up from the bulk to fill the atomic holes in the structure and become available for surface reactivity. These defective 2D/metal interfaces are promising platforms for several chemical and electrochemical processes, as we have found in Chapter 4 for small Cu clusters trapped at large atomic voids (multiatomic vacancies) in a Cu-supported h-BN layer that present a reasonably low overpotential for the electrocatalysis of the oxygen evolution reaction (OER).

Stimulated by these findings, in this Chapter we present a thorough computational electrochemistry investigation, based on a wide set of dispersion-corrected density functional theory calculations, to assess the performance of various single metal atoms (Cu, Ni, Co, Fe) trapped at defective (mono and divacancies) h-BN/Cu(111) interfaces as electrocatalysts for the hydrogen evolution reaction. By calculating the hydrogen binding energy (ΔG_{*H}) at different coverage conditions, we observe how the interaction between the defective/metal-doped h-BN layer and the Cu(111) substrate plays a key role in tuning the reactivity, leading to a thermoneutral hydrogen adsorption step (i.e. $\Delta G_{*H} \approx 0$), which is the optimal condition.

The results of this study could be useful to rationalize other h-BN/M interfaces and to design improved electrocatalytic systems for the hydrogen evolution reaction.

The results reported in this chapter have been published in: Perilli, D., Di Valentin, C., Studt, F., J. Phys. Chem. C, 2020, 124 (43), 23690-23698.

5.1. Introduction

The use of molecular hydrogen (H_2) as an energy carrier is considered a viable alternative to fossil fuels for the energy supply.[192,193] However, H_2 does not exist naturally on Earth and must be produced in a cost-effective way. Nowadays most of the hydrogen is obtained industrially by steam reforming, which employs fossil fuels, emits carbon dioxide, and produces H_2 of low purity. An alternative clean and renewable route towards the production of pure molecular hydrogen is the direct water splitting,[194] which is an uphill reaction but can be conducted electrochemically, thus potentially stemming from renewable sources, such as wind and solar.[168,195]

Hydrogen evolution is a two-electron reduction process that can follow two possible mechanisms: a) the Volmer−Heyrovsky and b) the Volmer−Tafel paths, which consist of the following sets of reaction steps (in acidic media):

a) Volmer−Heyrovsky path

$$* + (H^+ + e^-) \rightarrow *H \qquad \text{(A1)}$$

$$*H + (H^+ + e^-) \rightarrow * + H_{2,(g)} \qquad \text{(A2)}$$

b) Volmer−Tafel path

$$* + (H^+ + e^-) \rightarrow *H \qquad \text{(B1)}$$

$$*H + *H \rightarrow * + H_{2,(g)} \qquad \text{(B2)}$$

where * is a catalytic site and *H is a surface−bound hydrogen.

Since both mechanisms share the first electrochemical step (Volmer), previous theoretical works have identified the free binding energy of a hydrogen atom (ΔG_{*H}) as a simple descriptor of the electrocatalytic performance.[196,197] In fact, according to the Sabatier principle, the interaction between the catalyst and the adsorbate should be "just right"; that is, neither too strong nor too weak. If the interaction is too weak, a high overpotential will be required to bind H and no reaction will take place at a reasonable potential. On the other hand, if the interaction is too strong, the adsorbed H atoms will poison the catalyst and no H_2 will be formed. Thus, the optimum condition is satisfied when the binding of H atoms is close to thermoneutrality, i.e. $\Delta G_{*H} \approx 0$. Taking this simple approximation, it is possible to correlate the electrocatalytic activity with the thermodynamic parameter ΔG_{*H}, which can be calculated rather easily with quantum chemical methods such as DFT. This analysis allowed a rationalization of the reactivity trends among different catalysts (as e.g. expressed through so-called volcano relationships), but also to identify and predict potential new systems. However, it is worth to highlight how thermoneutrality is a necessary but not sufficient condition for a catalyst to be active for HER.[198]

Currently, state-of-the-art electrocatalysts in acidic media are mainly based on platinum and its alloys, which are rare, and costly, and therefore not suitable for large-scale use. For all these reasons, intense scientific efforts are devoted to search for an efficient, inexpensive, stable H_2-evolving electrocatalyst for the HER.[199] An emerging class of electrocatalysts, that have the potential to meet the above-mentioned requirements, are two-dimensional (2D) materials.[200,201] For example, (10-10) Mo-edges in MoS_2 nanocrystals were found to be active sites for the electrochemical hydrogen evolution, both experimentally,[103,104] and theoretically.[102,202,203] Also, in combined experimental and theoretical work, a metal-free hybrid system, made by coupling of graphitic-carbon nitride with nitrogen-doped graphene ($g\text{-}C_3N_4@NG$), was found to be an active electrocatalyst for the hydrogen evolution reaction.[107]

Another important 2D material that could be of potential interest for electrocatalysis is metal-supported hexagonal boron nitride (h-BN). Although pristine h-BN is intrinsically insulating and inert, when it is chemically modified by dopants, defects, or underlying metal substrates, its reactivity and band gap can be tuned.[108,177,151,154,204] For example, combining experiments and DFT calculations, Au-supported h-BN nanosheets were successfully studied for the oxygen reduction reaction (ORR)[109] and HER,[205] and h-BN edges were proposed to be the active sites for both processes. Recently, Liu et al. experimentally compared the performance of h-BN nanosheets on Cu (h-BN/Cu) and Au (h-BN/Au) and found that the interaction with the underlying metal substrate plays a key role in tuning the electrochemical activity.[77]

An alternative strategy to activate h-BN, and more generally 2D materials, is by metal doping. These isolated metal atoms could be potentially active sites for several catalytic and electrocatalytic processes, as previously observed in several theoretical works.[206,207,208,209] Different methods were developed to dope ad hoc 2D materials, such as ion implantation or e-beam evaporation from metal rods.[51] However, also impurities and adatoms already present on the metal surface could be incorporated into the 2D layer during its growth by chemical vapor deposition (CVD), as previously proved for epitaxial graphene on the Ni(111) surface.[210,211]

In our previous works, we analyzed the electronic interaction between a pristine and defective h-BN monolayer on a Cu(111) substrate (Chapter 3) and we studied these interfaces as potential electrocatalysts for the oxygen evolution reaction (Chapter 4).

In this chapter, we investigate whether defective (N and B monoatomic vacancies, and BN diatomic vacancy) and metal-doped (Cu, Ni, Co, and Fe) Cu-supported h-BN systems may be of potential interest for HER. We first analyze the structural and electronic properties and stability of such interfaces. Then, by computing the H binding energy at different coverage conditions, we evaluate the performance of these h-BN/Cu hybrid systems as electrocatalysts for the hydrogen evolution reaction.

5.2. Computational details

Density Functional Theory (DFT) calculations were performed using the plane-wave-based Quantum ESPRESSO package (QE).[157] The ultrasoft pseudopotentials were adopted to describe the electron-ion interactions with Cu (3d, 4s), Ni (3d, 4s), Co (3d, 4s), Fe (3d, 4s), B (2s, 2p), N (2s, 2p) and H (1s) treated as valence electrons.[129] Energy cutoffs of 30 Ry and 240 Ry (for kinetic energy and charge density expansion, respectively) were used for all calculations. The convergence criterion of 0.026 eV/Å for forces was used during geometry optimization and the convergence criterion for the total energy was set to 10^{-6} Ry. To properly take into account weak interactions, the van der Waals density functional vdW-DF2^{C09x} was used.[128] Spin polarization was considered when required.

For the simulation of h-BN/Cu(111) interfaces, a (6 × 6) supercell with a total of 108 Cu atoms and 72 atoms in the BN layer was used resulting in a lattice mismatch of only 0.40 %. The Cu(111) surface was modeled by a three-layer slab model with the bottom two layers fixed during the geometry relaxation to mimic a semi-infinite solid. A Monkhorst-Pack k-points mesh[187] of 3 × 3 × 1 and 9 × 9 × 1 was used for the geometry relaxation and density of states (DOS) evaluation, respectively. To avoid interactions between adjacent periodic images, a vacuum space of about 25 Å was included in the slab model.

The free energies (G) of the intermediates (at T = 298.15 K) were computed by correcting the electronic energies (E) for the zero-point energy (ZPE), heat capacity ($\int C_p dT$) and the vibrational entropic term (S_{vib}), calculated as follows:

$$G = E + ZPE + \int C_p dT - TS_{vib} \qquad (5\text{-}1)$$

Vibrational modes were calculated by performing a normal-mode analysis and all 3N degree of freedom of the adsorbates within the harmonic oscillator approximation. Corrections for the ZPE were included by calculating and diagonalizing the dynamical matrix at the Γ point only. For a gas-phase H_2 molecule, the standard tabulated entropy was used.[188]

The electrochemical cell was simulated using the Computational Hydrogen Electrode (CHE) model originally proposed by Nørskov and co-workers.[133] The Climbing Image−Nudged Elastic Band (CI−NEB)[142] method was employed to simulate the *Tafel* step at the Cu−supported defective h-BN, generating the minimum energy path of the reaction step and an evaluation of the energy barrier. A Löwdin population analysis, as implemented in the QE package,[212] was used to calculate the partial atomic charges. Ball-and-stick models were rendered with Xcrysden software.[213]

5.3. Structural and electronic properties of metal doped defective h-BN/Cu(111) systems

We previously observed that B vacancies, presenting N-terminated triangular holes in the lattice, can encapsulate Cu adatoms owing to the large stabilization effect deriving from the Cu-N bond formation. Therefore, we first considered the monoatomic B vacancy as the “trapping site” for a range of light transition metal atoms (M): Cu, Ni, Co, and Fe. According to the most stable stacking configuration for the h-BN layer on top of the Cu surface, where N/B atoms are in top/fcc position with respect to the Cu substrate, we considered only the fcc position for the extra metal atom.

We will consider two slightly different situations for the trapped M atoms: (1) the M atom is in the interfacial region where it is still in contact with the underlying surface but is also bound to the undercoordinated N atoms in the defective h-BN layer (M^{down}@1Vac, **Figure 5-1a**); (2) the M atom is exposed towards the vacuum and does not have any contact with the underlying copper substrate (M^{up}@1Vac, **Figure 5-1b**).

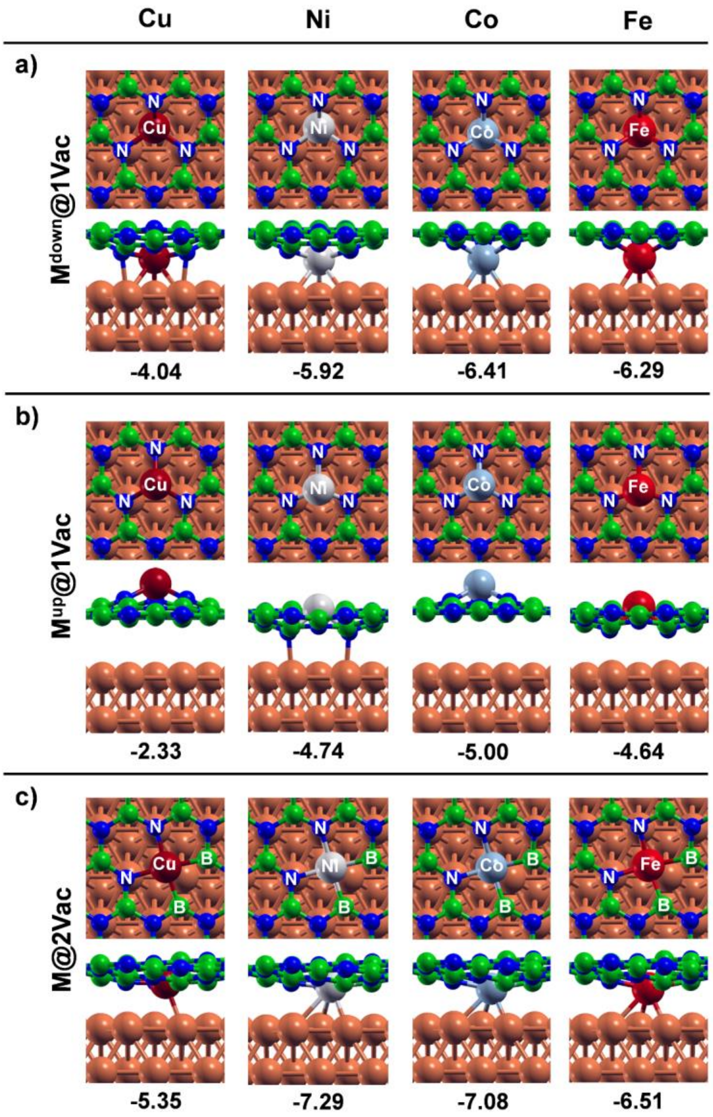

Figure 5-1: Top and side views for supported metal-doped h-BN in a single B vacancy (1Vac) with the embedded metal in (a) down and (b) up configuration, and into a (c) BN divacancy (2Vac). The corresponding formation energies are reported below each configuration. The formation energies are given relative to the corresponding metal atom in the gas–phase. Color coding: Cu surface atoms in orange, N atoms in blue, B atoms in green, and Cu, Ni, Co, and Fe trapped atoms in dark red, gray, cyan and red, respectively.

The M atoms tend to go either up or down because they are quite large and do not perfectly fit in the spatial hole left by the missing B atom. We could not localize a minimum energy structure with the M atom at the same height of the h-BN plane. Therefore, we decided to consider a larger vacancy (diatomic vacancy) where a BN atomic pair is missing, as shown in **Figure 5-1c** (M@2Vac). Even for this double vacancy model, all optimized structures show a significant distortion of the 2D layer, and the M atom is always closer to the Cu surface than the h-BN layer.

Next, we evaluated whether there is an energy cost or gain to go from a defective supported h-BN/Cu layer and trap a single M atom to form the M@1Vac/2Vac structure, according to the following equation:

$$E_F = E_{M@1Vac/2Vac} - E_{\frac{1Vac}{2Vac}} - E_{M-atom} \qquad (5\text{-}2)$$

where $E_{M@1Vac/2Vac}$, $E_{1Vac/2Vac}$, and E_{M-atom} are the total energies of the M-filled vacancy, empty vacancy, and the isolated metal atom, respectively. This energy change is always negative, although in the case of M^{up}@1Vac, the energy gain is considerably smaller. We rationalize this trend as a consequence of the fact that when the metal is in the up configuration, its interaction with the Cu substrate is completely suppressed. On the contrary, in the down configuration, the stabilization comes from the formation of bonds both with the undercoordinated N atoms from the defective h-BN layer and with the underlying Cu surface atoms.

In order to get further insight into the nature of the different trapped M atoms, we have analyzed and compared their electronic structure in terms of the total and projected density of states (DOS and PDOS; **Figure 5-2** and **5-3**) of the d states of the embedded M atoms.

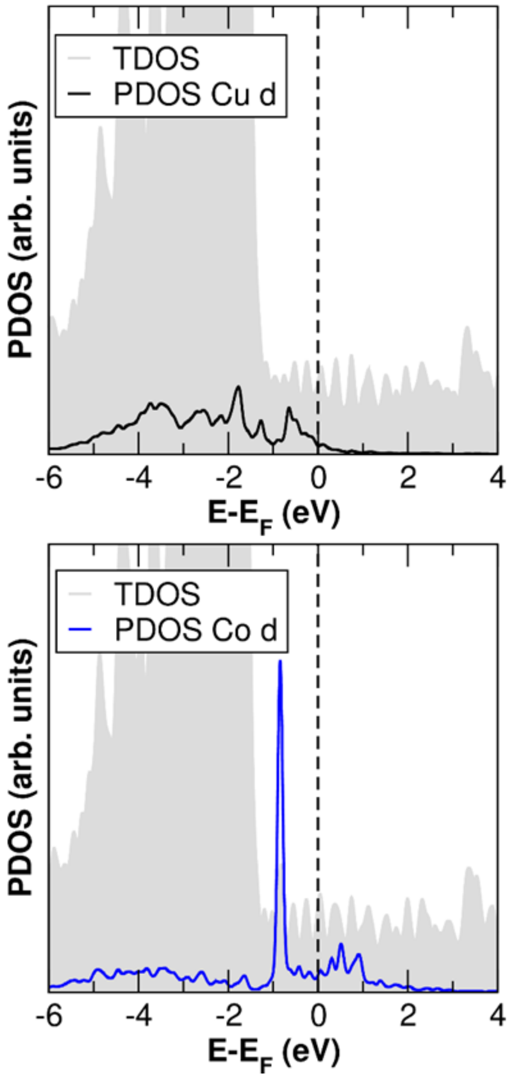

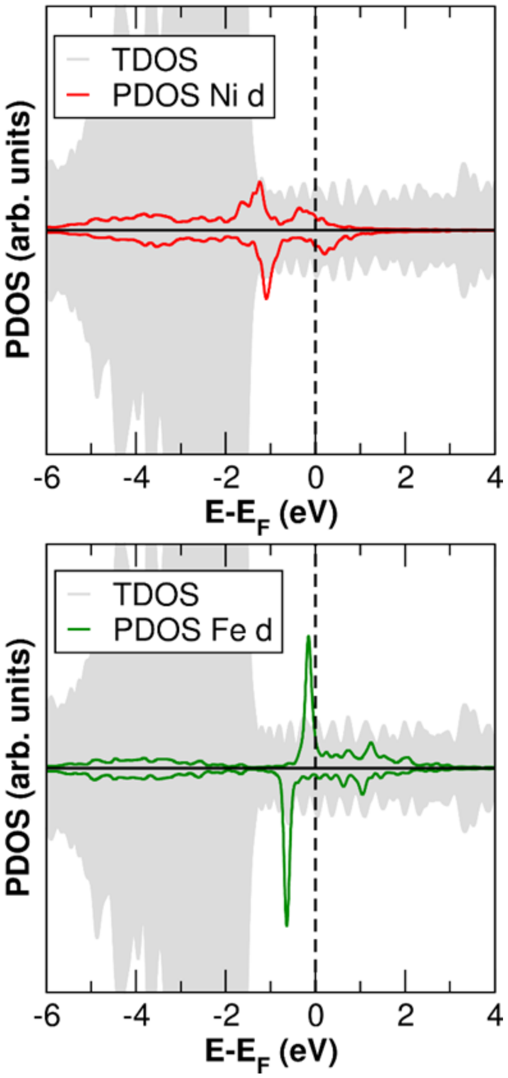

Figure 5-2: Total (TDOS) and projected (PDOS) density of states for (a) Cu^{down}@1Vac, (b) Ni^{down}@1Vac, (c) Co^{down}@1Vac, and (d) Fe^{down}@1Vac. The metal PDOS is multiplied by 10 in order to be displayed together with the TDOS. The Fermi level is scaled to zero and is indicated by a dashed line. For Ni and Fe, spin up and down are given.

In the case of the Cu^{down}@1Vac and Ni^{down}@1Vac systems, the d states associated with the single metal atom show a significant broadening due to the strong coupling with the Cu substrate and have a considerable fraction near the Fermi energy. On the contrary, in the case of the Co^{down}@1Vac and Fe^{down}@1Vac systems, the metal d states show a narrow peak in the proximity of the Fermi energy resembling a similar electronic structure as isolated or single metal atom catalyst.[38] Interestingly, only Ni- and Fe-doped systems show a residual magnetization after optimization, with a total magnetic moment per cell of 0.69 μ_B and -1.71 μ_B, respectively. By analyzing the atomic spin density values, such magnetic moment is found to be mainly localized on the trapped metal atoms.

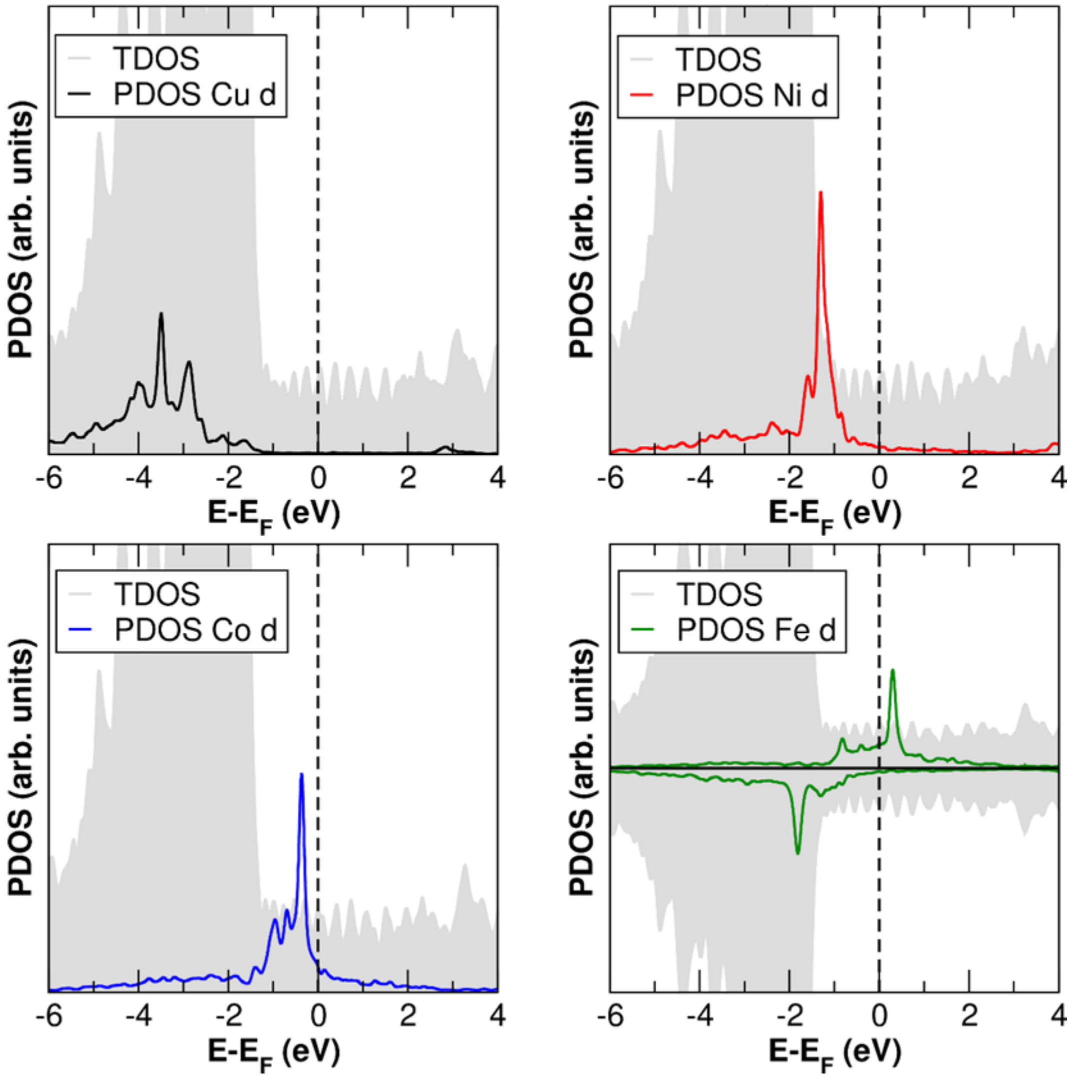

Figure 5-3: Total (TDOS) and projected (PDOS) density of states for (a) Cu@2Vac, (b) Ni@2Vac, (c) Co@2Vac, and (d) Fe@2Vac. The metal PDOS is multiplied by 10 in order to be displayed together with the TDOS. The Fermi level is scaled to zero and is indicated by a dashed line.

For the systems with a double vacancy, M@2Vac (**Figure 5-3**), we note that all projections exhibit less broadening compared to the mono vacancy cases, indicating smaller interactions with the Cu substrate: the Cu d-states are at a low energy (at least below -2 eV), the Ni and Co d-states show a full sharp peak close to the Fermi level (especially in the case of Co), whereas, in the case of Fe, we observe an empty narrow peak in the alpha channel (spin up electrons). Only in the latter case, we found a magnetic ground state, with a total magnetic moment per cell of -0.65 μ_B, which is mainly localized on the Fe atom.

We performed a Löwdin population analysis and found that the embedded metal atoms are positively charged due to an electron transfer to the Cu slab. Interestingly, we found that the amount of transferred charge is significantly lower for M@2Vac than for M@1Vac (as shown in **Figure 5-4a**).

As pointed out above, the electrochemical stability is another important condition to be satisfied by potential new electrocatalysts. For this reason, we investigated the stability of the trapped M atoms against the dissolution in water, according to a previously employed methodology.[84,139] **Figure 5-4b** shows the calculated dissolution potential of trapped metals ($U_{diss(M@V)}$) as a function of the formation energies (calculated as described above) of the metal-doped h-BN systems. Since the working potential to evolve $H_{2,(g)}$ is always negative (with respect to SHE), a positive dissolution potential will guarantee the stability of the trapped metal to its dissolution in water under electrochemical conditions. Therefore, systems in the upper left quadrant of **Figure 5-4b** ($U_{diss(M@V)} > 0$ V and formation energy < 0 eV) are promising in terms of stability.

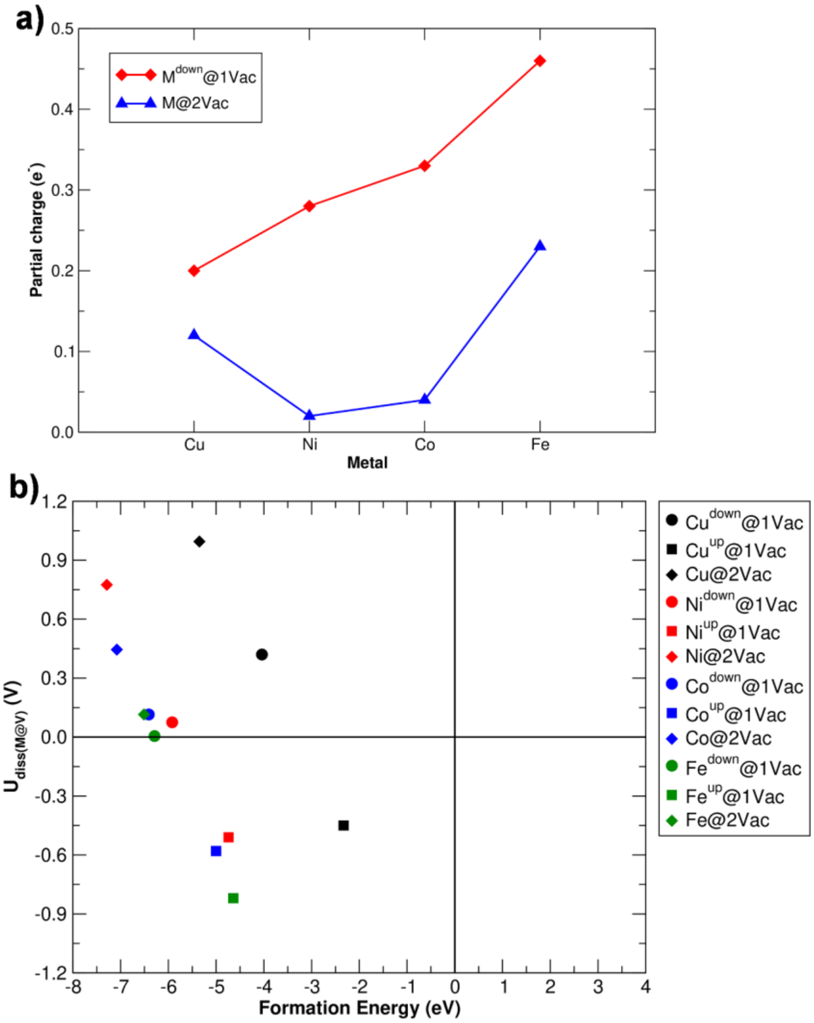

Figure 5-4: (a) Partial charges of trapped metals for M^{down}@1Vac and M@2Vac systems. (b) Dissolution potentials (with respect to SHE and pH = 0) of trapped metals ($U_{diss(M@Vac)}$) plotted versus formation energies for the different supported metal-doped h-BN systems.

It is interesting to note that all M^{up}@1Vac structures lie in the third quadrant and are therefore not stable, based on the criterion of electrochemical stability. Again, this is due to the absence of the interaction of the trapped metal atom with the underlying Cu substrate, which reduces the overall stability of the system.

In addition to the energy and electrochemical stability, we also considered the activation barrier for Cu and Ni atoms to pass through the B monovacancy, moving between the up (M^{up}@1Vac) and down (M^{down}@1Vac) structures. As shown in **Figure 5-5**, it is interesting to note that all M^{up} structures are not only significantly less stable than their

M^{down} counterparts, but the energy barriers from M^{up} to M^{down} are also very small (~0.1 eV). M^{up} structures are thus not catalytically relevant and will hence not be considered any further.

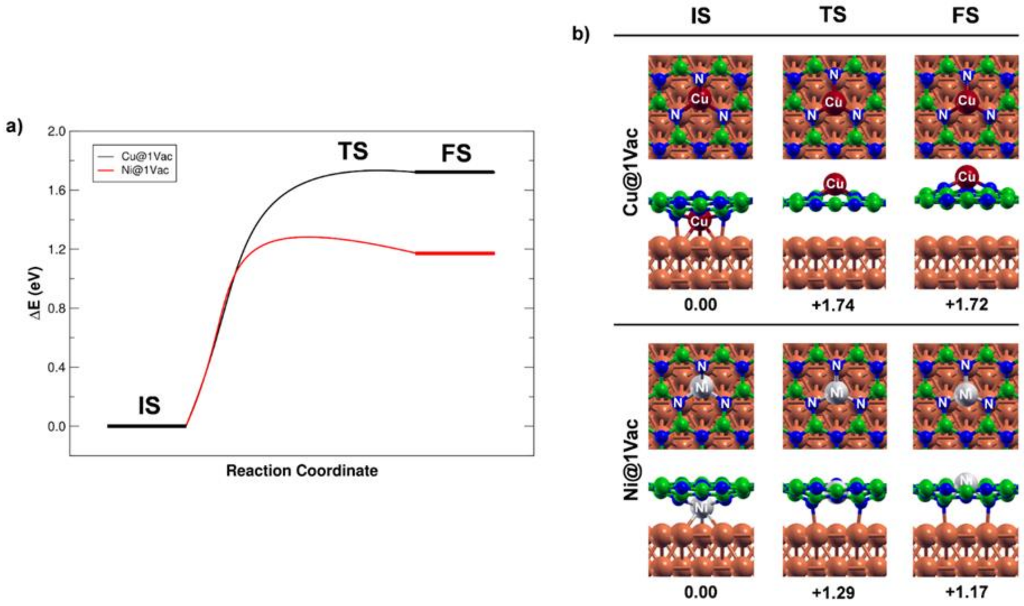

Figure 5-5: (a) Energy profile for the metal flipping through the vacancy site for Cu- and Ni-doped systems. (b) Corresponding ball-and-stick models for initial (IS), transition (TS), and final (FS) state for Cu- (upper panel) and Ni-doped (bottom panel). The corresponding electronic energies (ΔE), calculated with respect to the initial state, are reported below each structure. Color coding: Cu surface atoms in orange, N atoms in blue, B atoms in green, Ni atom in gray, and Cu adatom in dark red.

To conclude this section, we present the analysis, limited to the case of M^{down}@1Vac, of the interaction between M and the three coordinating N atoms. For this, the use of formation energy values, as defined above, is not suitable to compare the strength of the N-M bonds for the following reasons: (1) the formation energy takes the different deformation contributions into account due to both the atomic structural distortions and the change in adhesion strength between h-BN and Cu; (2) in the formation energy both the contributions of the metal atom interaction with the Cu substrate and with the BN-layer are present and cannot be easily separated. The first problem can be solved by employing a simple scheme of energy decomposition, as we used in Chapter 3. As shown in **Figure 5-6a**, this decomposition allows one to determine the energy contribution of deformation (positive, ΔE_{def}) and of binding (negative, ΔE_{bind}) to the adsorption energy ($\Delta E_{ads} = E_{M@1Vac} - E_{1Vac} - E_{M-atom}$) of

M^{down}@1Vac. Now, comparing the binding energies (ΔE_{bind}) obtained for the different metal-doped systems, we determined the following order, from the least to the most stable: Cu (-5.66 eV), Ni (-7.70 eV), Fe (-9.02 eV), and Co (-9.06 eV).

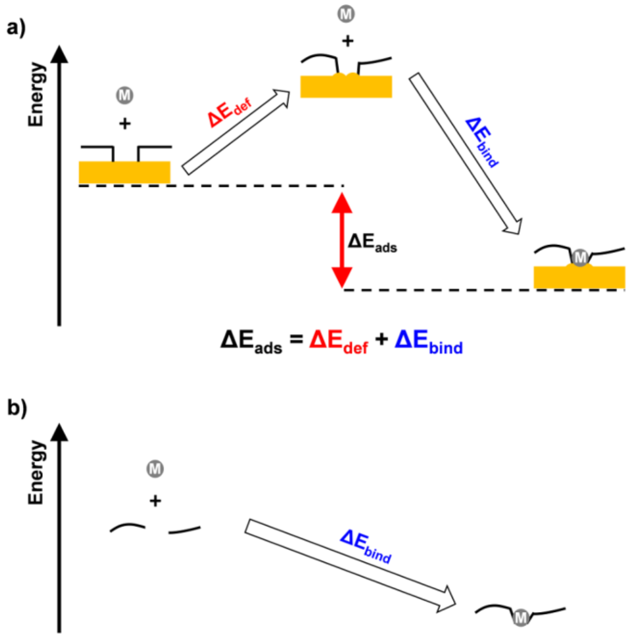

Figure 5-6: (a) Schematic representation of the energy decomposition analysis for the energy contribution of deformation (positive, ΔE_{def}) and of binding (negative, ΔE_{bind}) to the adsorption energy (negative, ΔE_{ads}) of the metal trapping in h-B^VN/Cu(111) interface. (b) Schematic representation of binding energy contribution deriving from the formation of N-M bonds.

As regards the second problem, to roughly estimate only the bonding contribution to the N atoms, we calculated the binding energy of a metal atom trapped in a free-standing h-B^VN layer, which is distorted as when lying over the Cu substrate, according to the scheme reported in **Figure 5-6b**. The M-N bond was estimated to increase as follows: -2.24 eV per Cu-N, -2.88 eV per Ni-N, -2.95 eV per Fe-N, and -3.14 eV per Co-N.

5.4. Assessment of the HER on defective and metal-doped h-BN/Cu(111) interfaces

Defect‒free h-BN/Cu(111) was suggested to be a good ORR catalyst based on theoretical calculations. While we do not necessarily expect that the same is true for HER, we will use h-BN/Cu(111) as our reference system.

We evaluate the stability of the H* intermediates of the HER in terms of Gibbs free energy as:

$$\Delta G_{*nH} = G_{*nH} - G_{*} - \frac{n}{2} G_{H_{2,(g)}} \qquad (5\text{-}2)$$

where G_{*nH}, G_{*}, and $G_{H_{2,(g)}}$are the Gibbs free energies for the catalyst with n hydrogen atoms adsorbed, the catalyst without any hydrogen atom, and an isolated H_2 molecule in the gas‒phase, respectively. From now on, we will refer to this quantity as the *hydrogen binding energy*.

Another way to evaluate the stability of the *H intermediates is through the *differential hydrogen binding energy*, which is the energy cost or gain to gradually increase the H* coverage, and is calculated as follows:

$$\Delta G_{*H}^{diff} = G_{*nH} - G_{*(n-1)H} - \frac{1}{2} G_{H_{2,(g)}} \qquad (5\text{-}3)$$

In the case of defect‒free h-BN/Cu, we found the electrochemical H adsorption to be unfavorable (ΔG_{*1H} = +1.27 eV), with the H bonded to a B atom. This result agrees well with what has been reported from experiments[77] and suggests that the rather weak interaction between the Cu substrate and the h-BN layer does not alter the activity of h-BN to a great extent (ΔG_{*1H} =+2.41 eV in the case of free-standing h-BN).

In the following subsections, we present the investigation of the HER mechanism for different defective and metal‒doped h-BN/Cu systems using the computational hydrogen electrode (CHE) model. For HER the most optimal electrocatalyst should have a *differential hydrogen binding energy* close to zero, i.e. $\Delta G_{*H}^{diff} \approx 0$ eV. As mentioned above, if the interaction is too weak ($\Delta G_{*H}^{diff} \gg 0$), a high overpotential will be required for the first proton/electron transfer process, whereas, if the interaction is too strong ($\Delta G_{*H}^{diff} \ll 0$), the adsorbed H bind too strongly, making the second proton/electron transfer step difficult. Thus, the thermoneutrality of this step is a necessary but not sufficient condition for a catalyst to be active for the HER.

5.4.1. Empty mono- and di-atomic vacancies

Point defects, such as vacancies, in h-BN are considered to improve its reactivity. When one atom is removed from the h-BN lattice, the monolayer contains some undercoordinated atoms, which become very reactive. Here we will investigate if this translates into a positive effect on the catalyst activity for HER.

We start considering the case of a boron monovacancy in free-standing h-BN (h-B^VN, **Figure 5-7** and **5-8a**), where the three nitrogen atoms at the vacancy site are truly undercoordinated (in contrast with the case on a Cu substrate where they can form bonds with the surface Cu atoms in **Figure 5-8b**) and prompt to form new bonds. Because of that, the binding energy for the first H atom added to the free-standing system is higher than in the corresponding Cu-supported h-B^VN. The increase in H coverage by further addition of H atoms leads to comparable energy gains for the various reaction steps (≈ 2 eV). In other words, without an underlying substrate, it is not possible to reach the thermoneutrality since there is nothing able to damp the huge energy gain due to the formation of N-H bonds.

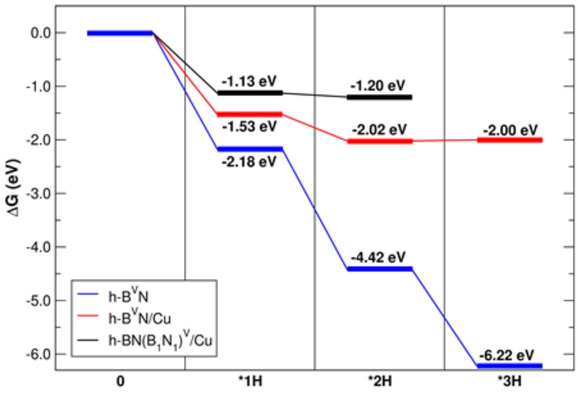

Figure 5-7: Free-energy diagram (ΔG) for the electrochemical hydrogen adsorption catalyzed by defective Cu-supported h-BN systems and coverage-dependence.

Next, we analyze and compare the boron (h-B^VN/Cu) monovacancy (red line in **Figure 5-7**), with the BN divacancy (h-$BN(B_1N_1)^V$/Cu, black line in **Figure 5-7**). The B vacancy induces three undercoordinated N atoms, whereas the BN divacancy gives rise to four undercoordinated N/B atoms (**Figure 5-8b** and **5-8c**, respectively). However, in all cases, the undercoordinated N atoms are passivated by Cu surface atoms, forming strong N-Cu covalent bonds, as we have detailed in Chapter 3.

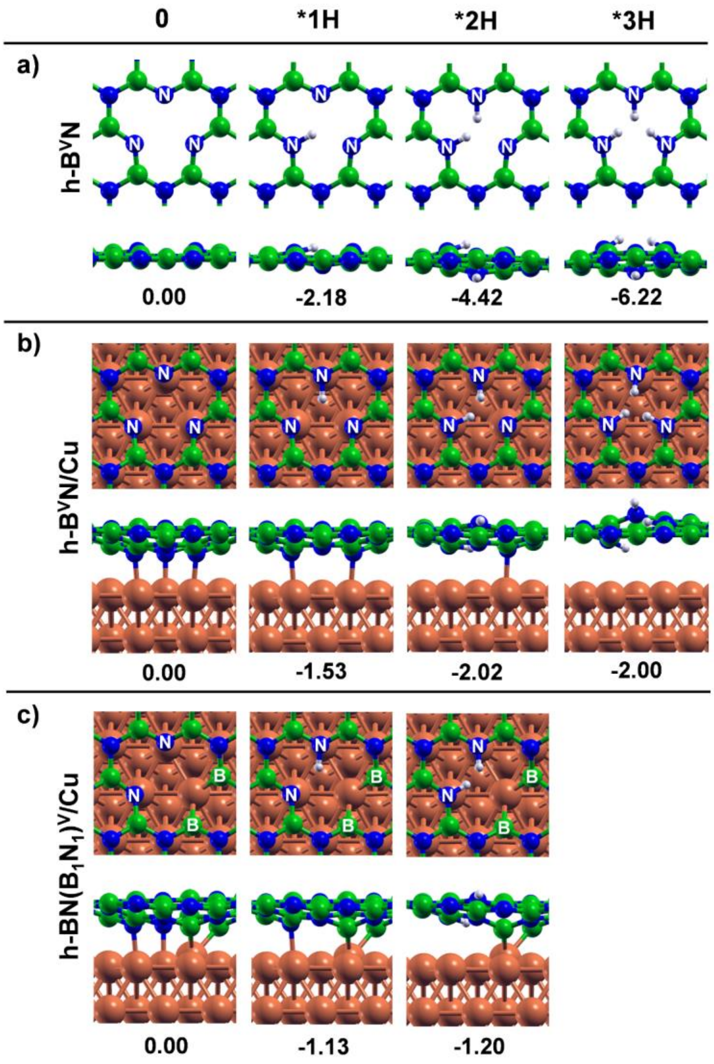

Figure 5-8: Top and side views of the intermediates of the hydrogen adsorption on (a) free standing and (b) Cu-supported B monovacancy, and (c) Cu-supported BN divacancy, as shown in **Figure 5-7**. The corresponding hydrogen adsorption energies (ΔG_{*nH}), are reported below each structure. Color coding: Cu surface atoms in orange, N atoms in blue, B atoms in green, and H in white.

In the case of h-BN^V/Cu, we calculate ΔG_{*1H} = +1.32 eV, with the H atom that does not bind to an undercoordinated B atom of the vacancy site but to an N atom next to the vacancy, resembling the pristine h-BN/Cu case.

For h-B^{V}N/Cu, we calculate a binding energy of -1.53 eV (ΔG_{*1H} = ΔG_{*H}^{diff}) for the first coupled proton/electron transfer step. The optimized geometry (second panel in **Figure 5-8b**) shows the formation of an N-H bond accompanied by a breaking of the previous interfacial N-Cu bond. The energy cost to break one bond is thus compensated by the large energy gain for the formation of the other. While the adsorption of the first hydrogen is rather strong, the calculated differential hydrogen adsorption energy (ΔG_{*H}^{diff}) decreases with an increase of adsorbed hydrogen and is only -0.49 eV and +0.02 eV for the second and third proton/electron transfer step. We rationalize this by the steric repulsion between H atoms (proximity effect), which is increasing with the increase in the number of H atoms. This is confirmed by the observation in **Figure 5-8b** that the N-H bonds are pointing out from the BN layer, either up or down, causing some distortion. It is interesting to note in **Figure 5-7** that the differential hydrogen adsorption energy for the third step is calculated to be thermoneutral (+0.02 eV). The calculations thus indicate that h-B^{V}N/Cu is a formidable HER catalyst, with the resting state (i.e. the state before thermoneutral reaction step) having 2 H* adsorbed.

For the double vacancy, h-BN(B_1N_1)^V/Cu (black line in **Figure 5-7**), our results are similar to the single B vacancy (red line): H binds to an undercoordinated N atom of the vacancy in a too stable intermediate (ΔG_{*1H} = -1.13 eV) for a catalytic process. Since we only have two “undercoordinated” N atoms, there are only two proton/electron transfer steps possible. The second is just slightly lower in energy by –0.07 eV, as shown in **Figure 5-7** (black line). On this basis, the activity by this defect site (BN divacancy) is predicted to lead to a good HER performance.

In order to get some insight into the kinetic aspect of the processes discussed in this section, we have also estimated activation barriers (by performing CI-NEB calculations) to suggest a possible reaction mechanism for the hydrogen evolution. Since *Heyrovsky* barriers are rather challenging to be computed for our systems, only *Tafel* barriers were investigated in the present work (**Figure 5-9**).

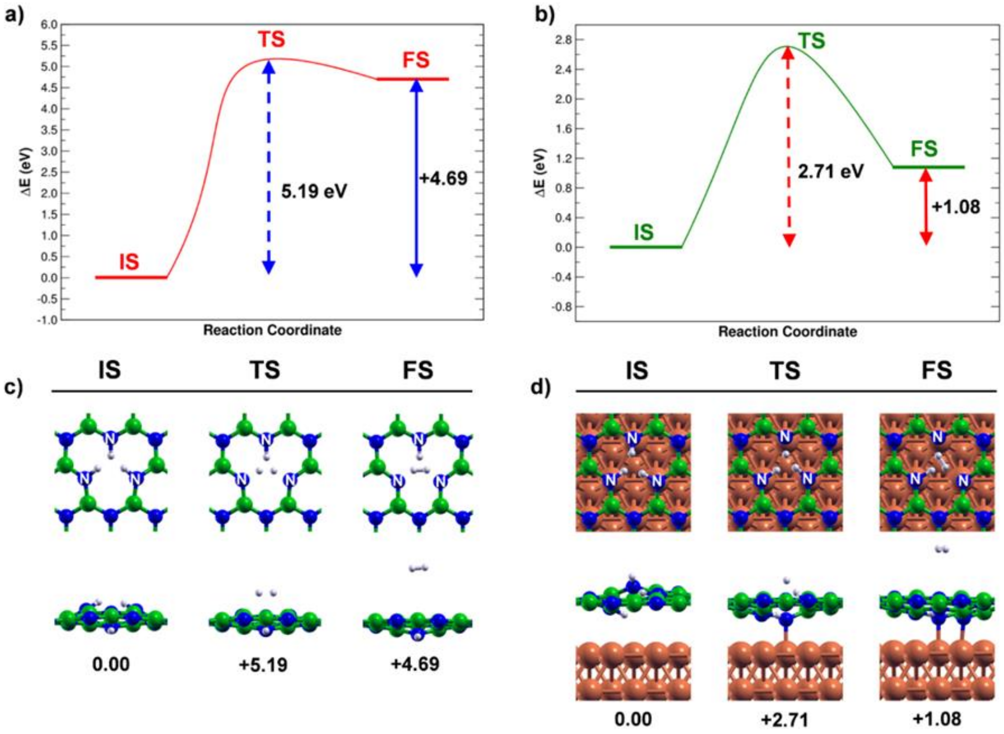

Figure 5-9. Energy profile for H_2 evolution through the *Tafel* mechanism for (a) free-standing and (b) Cu-supported h-B^{V}N. Corresponding ball-and-stick models for initial (IS), transition (TS), and final (FS) state for (c) h-B^{V}N and (d) h-B^{V}N/Cu. The corresponding electronic energies (ΔE), calculated with respect to the initial state, are reported below each structure. Color coding: Cu atoms in orange, N atoms in blue, B atoms in green, and H atoms in white.

In the case of h-B^{V}N/Cu, the activation barrier for the Tafel reaction was estimated to be as high as 2.71 eV (**Figure 5-9b**). On this basis, we would reasonably exclude a *Tafel* mechanism for the hydrogen evolution reaction, and suggest a *Heyrovsky* mechanism, in analogy to what previously observed for MoS_2-based catalysts.[202,203]

5.4.2. Trapped single metal atoms in mono- and di-atomic vacancies

Isolated metal atoms, trapped in a defective h-BN lattice, could be potential active sites for electrocatalysis, as observed in Chapter 4.

For the case of the metal atom trapped in a B monovacancy (M@1Vac in **Figure 5-10a**), we made several unsuccessful attempts to locate a structure with the H binding directly to the metal. This might be due to the low position of the metal atom with respect to the plane of the h-BN layer, which makes it rather inaccessible for reaction from the top side. The H atoms bind to the undercoordinated N atoms at the vacancy site, gradually decoupling the metal adatom from the BN layer. Due to this, at high H coverage, the metal atom moves to a next hcp site to allow full relax of the N-H bonds.

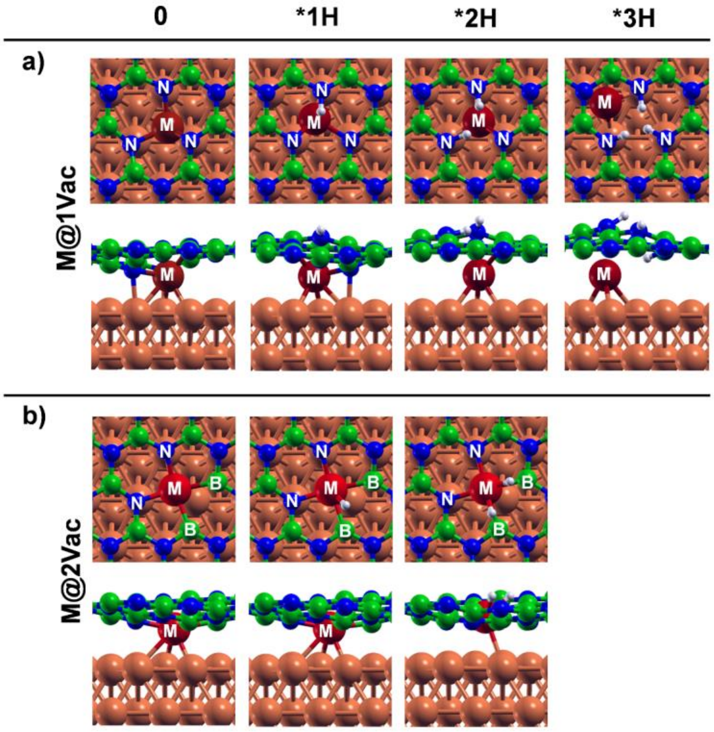

Figure 5-10: Top and side views of the intermediates of the hydrogen adsorption on supported M-doped h-BN systems: (a) M in a B monovacancy and (b) M in a BN divacancy, as shown in Figure 7a and b, respectively. Color coding: Cu atoms in orange, N atoms in blue, B atoms in green, H atoms in white, trapped M atom (M@1Vac) in dark red, and trapped M atom (M@2Vac) in red. Since all geometries are similar, for simplicity, we only show those with Cu and Fe in 1Vac and 2Vac, respectively.

Figure 5-11a shows the reaction energy profile (ΔG_{*nH}) at different H coverages (ranging from *1H to *3H) for systems with different metal dopants (i.e. Cu, Ni, Co, Fe). Considering the first H adsorption step, it is interesting to note that there is a clear energy trend among the different metals: in the case of Cu and Ni, H is strongly bound, whereas in the case of Fe and Co, the H interaction is rather weak and close to thermoneutral.

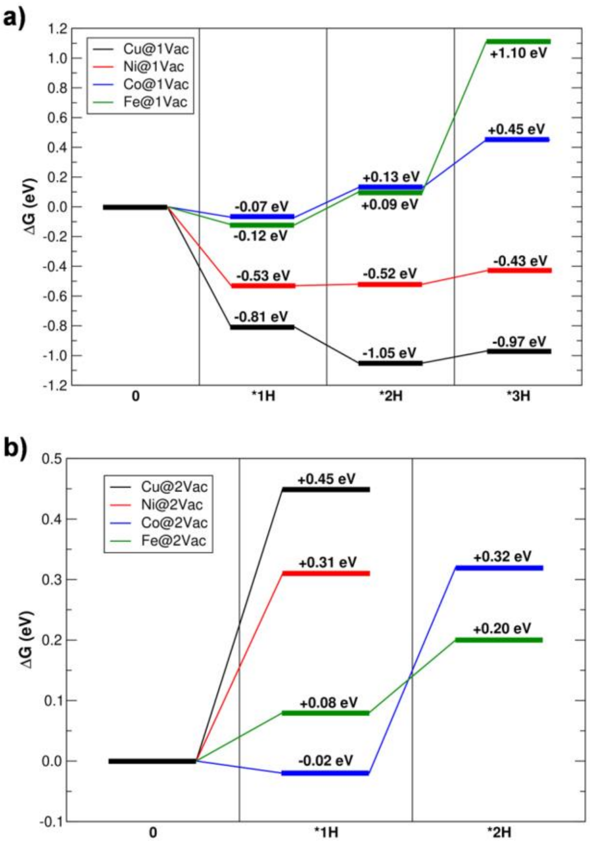

Figure 5-11: Free-energy diagram (ΔG) for the electrochemical hydrogen adsorption at different H coverage catalyzed by supported metal-doped h-BN systems: (a) filled B monovacancy and (b) filled BN divacancy.

In the case of Cu- and Ni-doped systems, the increase in the coverage leads to a decrease in the differential hydrogen adsorption energy (ΔG_{*H}^{diff}), thus moving closer to the ΔG_{*H} ≈ 0 condition at higher coverage, in a similar way as observed for the h-B^{V}N/Cu system in the previous section. It is interesting to note the correlation between the M-N bond strength and the reaction energy trend (ΔG_{*nH}) (see discussion in **Section 5.3**): when the M-N bond is weaker, the H adsorption energy is stronger (i.e. ΔG_{*nH} more negative). This can explain why in the case of Cu- and Ni-dopants, H is strongly bound, whereas in the case of Fe- and Co-dopants, the H interaction is significantly weaker.

In order to assess the feasibility of a *Tafel* mechanism for the hydrogen evolution on isolated metal atoms trapped in a B vacancy, we computed the corresponding activation barrier. This investigation was limited to the case of Ni@1Vac, which is the most promising according to the energy gain of -0.1 eV (*3H to *1H). Unfortunately, the *Tafel* barrier is computed to be +2.75 eV (electronic energy difference), similarly to what obtained for h-B^VN/Cu in the previous section. Therefore, again, we are prone to suggest a possible *Heyrovsky* mechanism, where the H_2 molecule evolves through a direct electrochemical step.

We now move to the case of single metal atoms trapped in a BN divacancy (M@2Vac in **Figure 5-10b**). In principle, three possible adsorption sites are available for adsorption: the “undercoordinated” N atom, the “undercoordinated” B atom, and the metal atom. We could locate an intermediate where an N-H bond is formed after breaking of one N-M bond (similarly to what observed for the M@1Vac above), but its stability, for all metals considered, is always lower (≈ +0.08/+0.28 eV) than other adsorption sites. We have indeed found a more favorable intermediate, almost identical among all metals, where H binds in a bridging configuration between the metal and the boron atom (see **Figure 5-10b**). To shed more light on the interaction between H and Fe@2Vac, in **Figure 5-12**, we calculated the charge density difference plot, which proves that the presence of the H atom causes a significant charge redistribution. Here, there is a clear electron charge depletion in the M-B bond and an accumulation between M and H, indicating the formation of an M-H bond. However, some charge accumulation is also located between H and B, indicating that some contribution to the H bond comes from the next B atom.

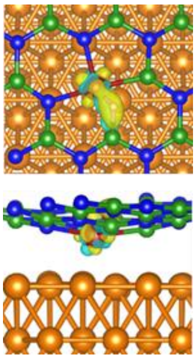

Figure 5-12: Charge density difference plot for Fe@2Vac. Electron accumulation and depletion are represented in yellow and cyan, respectively (isosurface level is 0.01 e^-/$bohr^3$). Green, blue, red, and orange balls represent B, N, Fe, and Cu atoms, respectively.

In **Figure 5-11b** we observe that the first electrochemical H adsorption is unfavorable for Cu- and Ni-doped systems, whereas the differential hydrogen adsorption free energy is close to zero for Co- and Fe-doped systems. We may explain these results considering the electronic structure details of the different metal-doped systems, as presented in Section 3.1: differently from the case of Cu and Ni trapped metals, which d states are deeper in energy and thus more stable, Co and Fe d states lie in the proximity of the Fermi energy, which, therefore, are expected to be more reactive for M-H bond formation. We have further analyzed the energy-coverage dependence in the case of the Fe- and Co-doped systems (green and blue lines in **Figure 5-11b**), as they are both characterized by the first *differential hydrogen binding energy* close to zero. In the latter case (Fe@2Vac), we found that a possibility to reach a high coverage at a reasonable energy cost exists. For this system, the activation barrier for the *Tafel* step was found to be +0.96 eV, significantly lower than for the Ni@1Vac case.

5.5. Conclusions

In this Chapter, we used dispersion-corrected density functional theory calculations to assess the potential of single metal atoms trapped in defective h-BN on a copper substrate as electrocatalysts for the hydrogen evolution reaction.

Several possible types of interface model systems can be designed when considering various light transition metal atoms, including Cu, Ni, Co, and Fe, as well as various types of h-BN defects (mono- and di-atomic vacancies), as we did in this study. For each model system, we have investigated the structural and electronic properties and we have evaluated the electrochemical stability and activity for HER.

The HER activity was assessed using arguments put forward by the computational hydrogen electrode model, that is the identification of a *differential hydrogen adsorption free energy* close to zero, i.e. $\Delta G_{*H}^{diff} \approx 0$ eV, that is the reference for an ideal electrocatalyst. Interestingly, h-BN/Cu(111) layers with mono- or di-vacancies were found to present differential free adsorption energies close to 0 eV. This is because only the first hydrogen binds very strongly on these systems, whereas the second (or third) hydrogen atoms are weakly adsorbed.

Next, we investigated how the presence of trapped single metal atoms (Cu, Ni, Co, and Fe) may affect the HER activity. Similarly as for defective h-BN/Cu(111), metal-doped h-BN/Cu(111) layers were found to present differential free adsorption energies close to 0 eV. Interestingly, the different metal-doped systems differ for the H coverage required to achieve such a condition. In the case of M@1Vac systems, we have observed a correlation between the N-M strength bond and the ΔG_{*H}^{diff}: when the N-M bond is weaker, the H adsorption is stronger (i.e. a more negative ΔG_{*H}^{diff}).

Therefore, our results suggest that both defective and single metal-doped h-BN/Cu(111) systems are potentially suitable catalysts for the HER.

Before concluding, we want to compare the systems proposed in this work with MoS_2-based systems, which are considered as the state-of-the-art two-dimensional catalysts for HER.[103] We note some similarities to our results: (1) the MoS_2 basal plane is inert whereas HER activity takes place at extended defects, such as Mo-edges; (2) typically, at low coverage the H atom is too strongly chemisorbed and only the step going from 0.25 to 0.5 ML coverage (corresponding to the differential adsorption free energy, ΔG_{*H}^{diff}) is thermoneutral.

To conclude, the results of the present study could be useful to guide the rational design of h-BN/M interfaces as H_2-evolving electrocatalysts through their defect-engineering and could also stimulate further theoretical as well as experimental investigations in this direction.

6. “Inside Out” Growth Method for High-Quality Nitrogen-Doped Graphene

In this chapter, we present a combined theoretical and experimental work carried out in collaboration with the laboratory of CNR-IOM in Trieste, performing the experimental part.

Our experimental colleagues propose a novel growth method which is scalable to produce high-quality nitrogen-doped graphene on nickel: following the standard chemical vapor deposition procedure, a previously nitrogen-doped nickel substrate is exposed to carbon-containing precursors so that nitrogen atoms, segregating to the surface, remain trapped in the growing graphene network. Morphological and chemical characterization by scanning tunneling microscopy and X-ray photoelectron spectroscopy demonstrates the homogeneity and high quality of the resulting nitrogen doped graphene layer.

The focus of this chapter will be mostly on a density functional theory investigation of possible structural models for a detailed description at the atomic scale of the various configurations of the nitrogen atoms observed in the graphene mesh. This growth method is suitable for the production of high-performance nano-devices with well-defined nitrogen centers, to be exploited as metal-free carbon-based catalysts in several applicative fields such as electrochemistry, energy storage or gas storage/sensing.

The results reported in this chapter have been published in: Fiori, S., Perilli, D., Panighel, M., Cepek, C., Ugolotti, A., Sala, A., Liu, H., Comelli, G., Di Valentin, C., Africh, C., Carbon 2021, 171, 704-710, where Fiori and Perilli equally contributed to the work.

6.1. Introduction

Graphene (Gr) has exceptional physical properties, such as high electrical and thermal conductivity, charge mobility, transparency, and flexibility, which are being successfully exploited in several research fields.[214,215,216] Nevertheless, pristine Gr suffers some severe limitations. Most notably, pristine Gr is a zero-band gap semiconductor, thus preventing its practical implementation in electronic devices.

Nowadays, doping of Gr is claimed to be a promising approach in order to tune its properties: for example, on the basis of ab initio calculations, it has been reported that the introduction of lithium atoms opens a band gap, turning Gr into a semiconductor material suitable for electronic applications; titanium-doped Gr is instead reported to enhance the gravimetric density for hydrogen storage applications,[217] while doping of Gr with boron and nitrogen (N) atoms results in a higher electrical conductivity[218] and enhances its electrocatalytic activity towards oxygen reduction reaction (ORR)[219] and its potential for energy storage.[220] In particular, nitrogen doped Gr (N-Gr) is predicted to have a strong potential as a 2D material for several applications, including, for example, gas sensing and gas storage.[221]

Unfortunately, the production of N-Gr is not trivial. Different synthesis methods have been proposed, following two main approaches: (i) a direct synthesis, in which N dopants are introduced during the Gr growth, and (ii) a post-synthesis approach, in which the Gr layer is doped after its growth. Among the direct synthesis methods, the most common is chemical vapor deposition (CVD),[222,223] in which a catalytic substrate is exposed to N- and C-containing precursors that dissociate on the surface, leading to the formation of high-quality N-Gr layer. However, the high pressure and temperature required for the growth process, the specific equipment and the dangerous precursors needed, make the production troublesome and pose serious safety issues. On the other hand, among the post-synthesis approaches, the most used method is the nitrogen plasma bombardment of a previously grown Gr layer, promoting the replacement of some C atoms with N atoms.[224] However, this procedure drastically reduces the quality of the Gr layer, due to the large defects induced by N bombardment.

An alternative approach, taking advantage of N segregation from the substrate in order to produce N-Gr, was proposed in the literature.[225] The authors engineered a system based on a SiO_2/Si substrate, on which a boron layer, where a trace amount of nitrogen species was spontaneously incorporated, was firstly deposited by e-beam evaporation; a nickel (Ni) film was then deposited above it. Upon vacuum annealing, boron-trapped nitrogen and nickel-trapped carbon impurities diffuse towards the nickel surface and form N-Gr, while boron atoms remain deeper in the layered substrate. The authors suggested therefore that boron film acts as a nitrogen source carrier, while maintaining the presence of boron atoms into the graphene below their detectable threshold.

Starting from that concept, our experimental colleagues developed an alternative, cleaner and highly reproducible growth method, based on a simpler and more controlled preparation procedure, which ensures the formation of high-quality layers and potentially is easily scalable, from small samples prepared under ultra-high vacuum (UHV) conditions to large foils produced in industrial lines. The resulting N-Gr layers were thoroughly characterized by Scanning Tunneling Microscopy (STM) and X-ray Photoelectron Spectroscopy (XPS). Further experimental details are given in the section 6.2 and in the Appendix.

From our computational side, we performed an extensive density functional theory (DFT) investigation, including simulated STM images and XPS spectra for a wide set of models for the N centers, to unveil their structural, morphological, and chemical properties, as it will be described below.

6.2. Experimental background

6.2.1. Growth method of N-Gr on Ni(111) substrate

The Ni(111) crystal was first exposed to a direct flux of porphyrins for few minutes at a temperature around 450 °C in UHV. The chosen temperature conditions and the catalytic nature of Ni promote the cracking of the molecules on the metal surface and, in synergy with the high N solubility in the Ni crystal (comparable to that one of C),[226] lead to the creation of a nitrogen reservoir in the metal bulk (see **Figure 5-1**). The standard CVD Gr growth process was then started: the Ni(111) substrate, kept at 580 °C, was exposed to ethylene (C_2H_4, partial pressure 5×10^{-7} mbar) for 1 h. This leads to the formation of a complete layer, as for pristine Gr.[227] Finally, the sample was kept at the growth temperature for 10 more minutes and cooled down to RT at a rate of 2 °C s^{-1}. In this way, some of the N atoms segregating to the surface were trapped into the growing carbon network, leading to the formation of N-Gr.

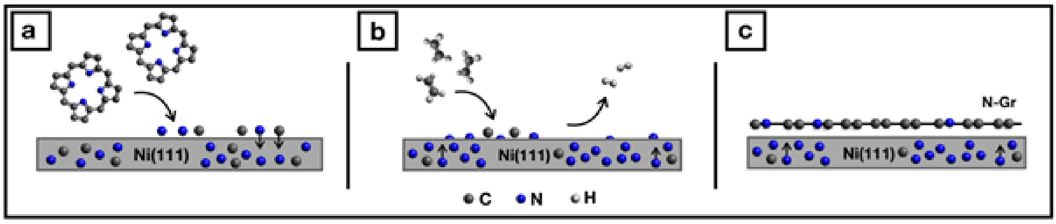

Figure 5-1: Schematic illustration representing: (a) Ni doping process with N atoms; (b) subsequent exposure to ethylene in UHV conditions; (c) formation of N-Gr.

6.2.2. Chemical characterization of as-grown N-Gr

We first investigated the chemical composition of the prepared sample by XPS, to verify the absence of contaminants and the presence of N in the 2D layer. Survey spectra ruled out the presence of any heterospecies except for the N introduced via exposure and cracking of porphyrin molecules. **Figure 5-2a** presents the typical XPS spectrum measured in the N1s region after several CVD cycles after nitrogen doping; the inset at the top left shows the spectrum acquired after just few cycles. The presence of several peak components indicates the co-existence of different chemical N configurations. Based on data fitting and on binding energies reported in literature, it is possible to distinguish different N-containing species, with concentrations changing with CVD cycling. At the beginning (see inset) N is present in the form of (i) nickel nitride (397.15 eV), stemming from N atoms in the very first layers of the Ni substrate in a Ni nitride-like coordination, (ii) pyridinic defects (398.6 eV), where N is placed at the edge of a C vacancy and bonds to two C atoms as part of a six-membered ring, and (iii) graphitic defects (400.6 eV), where N atom is substituting a C atom in the Gr network and bonds to three neighbor carbon atoms (see **Figure 5-2a**). The latter two components are a clear indication that N atoms are not exclusively stored in the Ni substrate, as evidenced by the lower energy component, but also trapped in the Gr mesh. After several CVD cycles, the nitride-like component is not visible anymore (see main spectrum in panel a), suggesting that the procedure has depleted the N content in the first Ni layers, while the fingerprint of N-doping of Gr is still evident. The XPS assignment above is confirmed by DFT simulations: the spectral separation calculated between the graphitic and pyridinic defects in Gr on Ni(111) is about 2.1 eV, in very good agreement with the experimental value of

2.0 eV. This value of the chemical shift is obtained for the most abundant graphitic and pyridinic defects observed by STM (see text below).

The typical LEED pattern of the epitaxial Gr phase on Ni(111) and the experimental STM images (in **Figure 5-2b**) show that a good quality Gr layer was obtained. The surface appears flat and regular, as normally observed for Gr grown epitaxially on the Ni (111) substrate. A grain boundary is visible, separating two regions that have the same top-fcc geometry.[59] This confirms that the Gr layer was formed on the surface starting from different seeds that, during the growth, have given rise to distinct Gr domains. This is totally analogous to the case of pristine Gr, thus indicating that the N doping method presented in this work does not affect significantly the standard epitaxial Gr growth process. The Gr surface appears sprinkled by a huge number of defects with diverse appearance. The large white spots, clearly visible in **Figure 5-2b** and in its inset (white circle), are also observed in the pristine case and have been previously assigned to Ni atoms trapped in the Gr network during the growth process. Indeed, it has been experimentally and theoretically demonstrated that Ni surface adatoms actively participate in the CVD Gr growth,[210] catalyzing the C-C bond formation, remaining at times trapped into the Gr network.[211] Besides the trapped Ni adatoms, new kinds of defects were observed in the high-resolution images. Since these defects were not present in the pristine Gr case, they can be tentatively linked to N atoms trapped in the Gr mesh. The inset reported in **Figure 5-2b** shows in detail two of the most abundant features of this kind, appearing as clover-like defects (blue circle) and dark triangles (red circles).

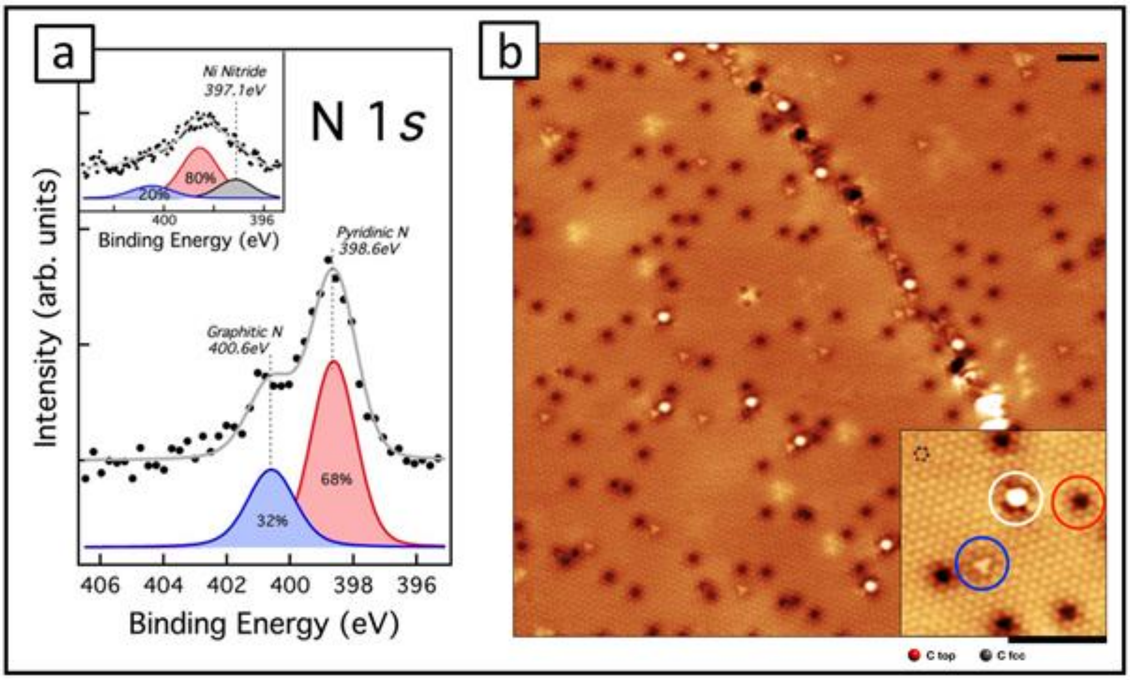

Figure 5-2: (a) XPS spectrum of the N 1*s* core level, after few (inset) and several (main spectrum) CVD cycles. Different N-containing species are highlighted. Photon energy hν = 1486.7 eV. (b) LT-STM image acquired at 77 K. Several defects are present on the surface. In the inset, the three most abundant types of defects are visualized: for explanation see main text. Scale bars 2 nm, I = 2.0 nA, V_{bias} = -0.2 V.

Atomically resolved images of all the observed N related defects are reported in the top row of **Figure 5-3**. For the defects in panels (**5-3a**) and (**5-3b**), the Gr network appears to be complete, with no vacancies in the mesh. This points to the presence of N atoms fully embedded in the Gr network, where they replace C atoms, in a graphitic configuration, in line with the XPS results discussed above. The clover-like defect (**Figure 5-3a**) is centered in a top site, with the first fcc neighboring C atoms appearing brighter than the other C atoms of the mesh, which suggests a localized increase in the density of states. On the other hand, for the defect centered in an fcc position (**Figure 5-3b**), a localized intensity decrease is present at the position of the first neighbours of the central atom, accompanied by the appearance of brighter clovers formed by C atoms in symmetric positions. Considering their registry, we assign these two defects to top (**5-3a**) and fcc (**5-3b**) graphitic N configurations, respectively.

6.3. Computational details

Density Functional Theory (DFT) calculations were performed using the plane-wave-based Quantum ESPRESSO package (QE).[157] Ultrasoft pseudopotentials were adopted to describe the electron-ion interaction with Ni (3d, 4s), C (2s, 2p), N (2s, 2p), treated as valence electrons.[129] Energy cutoffs of 30 Ry and 240 Ry (for kinetic energy and charge density expansion, respectively) were adopted for all calculations. The Perdew-Burke-Ernzerhof functional (PBE) was used for electron exchange-correlation.[122] In order to properly describe the Gr/Ni(111) interaction, semiempirical corrections accounting for the van der Waals interactions were included with the DFT-D2 formalism.[124] Spin polarization was always included.

For the simulation of Gr/Ni(111) interfaces, a 6 × 6 supercell with a total of 108 Ni atoms and 72 Atoms in the Gr layer was used, with a 2 × 2 × 1 Monkhorst-Pack k-points mesh and vacuum of about 15 Å in the direction perpendicular to the surface to avoid interaction between images. The Ni(111) surface was modeled by a three-layer slab with a bottom layer fixed to the bulk positions during the geometry relaxation to mimic a semi-infinite solid. STM simulations were performed using the Tersoff-Hamann approach,[131] according to which the tunneling current is proportional to the energy-integrated Local Density of States (ILDOS). Constant-current and voltage values for the STM simulations have been chosen to match the experimental values. Ball-and-stick models and STM images were rendered with VESTA[228] and Gwyddion software,[229] respectively. For further details, see our previous work on N-doped or defective graphene on other metal substrates. The XPS spectra of defective N-doped Gr have been calculated through the ΔSCF approach,[230] which includes a pseudopotential generated with a full core hole for each ionized inequivalent atom and allows the calculation of relative changes of binding energies, called core level shifts (CLS). To compare the CLSs of different defects, which are inserted into separated supercells, we have included into each system a single N_2 molecule, at a distance of 16 Å from the surface, minimizing their mutual interaction. Such an approach has already been successfully employed for the calculation of the XPS spectra of several N-containing molecules, for example as done in Ref. 231, although with a different exchange-correlation functional. However, we have validated this method with respect to a direct comparison using two free-standing models of graphitic and pyridinic single nitrogen defect on Gr, respectively: the same separation of ~ 4.1 eV between their CLSs has been calculated.

6.4. Results

The identification of such defects is confirmed by DFT calculations and simulated STM images of the proposed models, shown in the bottom panels, which nicely reproduce the appearance of these defects.

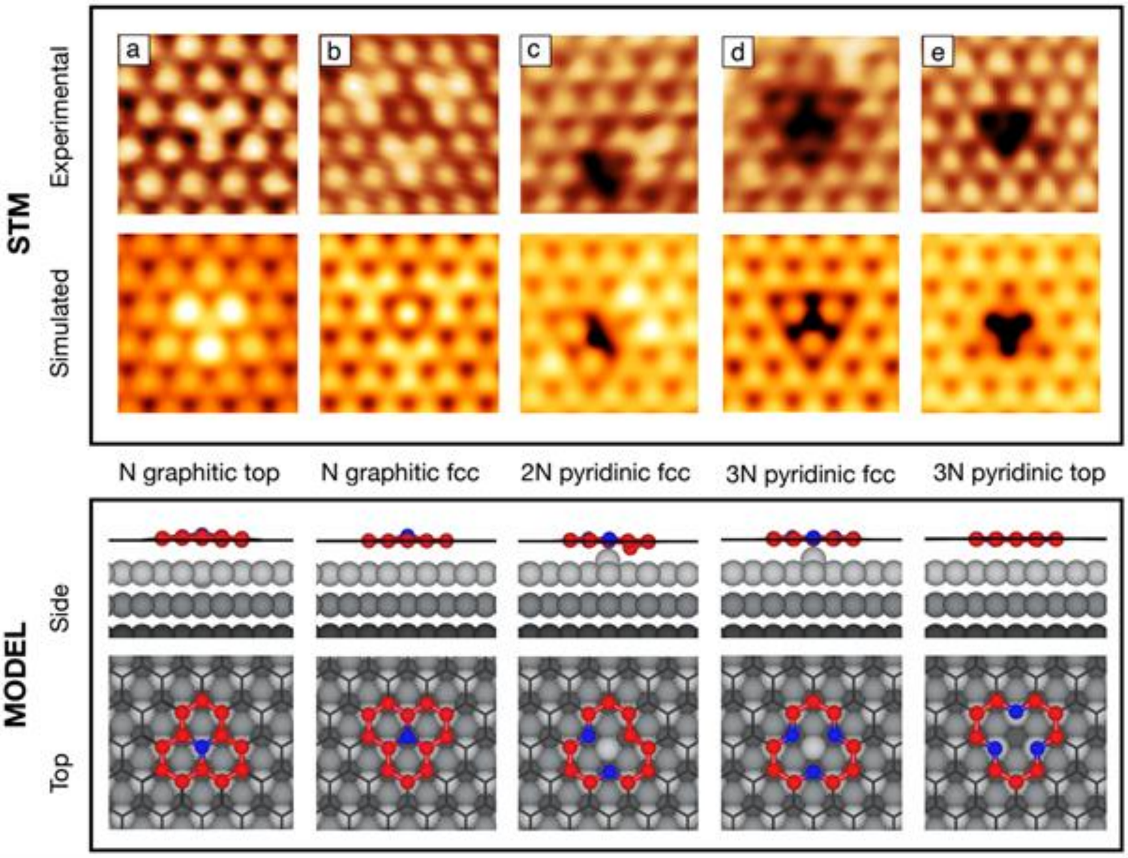

Figure 5-3: N defect configurations in Gr on Ni(111). Top panel: Experimental and simulated STM images for various defects. Image size: 1×1 nm^2. Structures are classified according to number of N atoms, configuration type and position. Experimental parameters: (3a) N graphitic top [I = 3 nA, V = -0.2 V], (3b) N graphitic fcc [I = 4 nA, V = -0.2 V], (3c) 2N pyridinic fcc [I = 0.6 nA, V = -0.2 V], (3d) 3N pyridinic fcc [I = 0.6 nA, V = -0.2 V] and (3e) 3N pyridinic top [I = 0.6 nA, V = -0.2 V]. Computational parameters: V_{bias}= - 0.2 V; ILDOS isosurface lying ≈ 2 Å above Gr and with ILDOS value of 5×10^{-5} $|e|/a_0^3$. Bottom panel: ball-and-stick model of DFT relaxed structures (side and top view). Color coding: Ni atoms in the first, second and third layer are rendered in dark grey, grey, and light grey, respectively; N atoms in blue; C atoms delimiting the defect site in red, Gr network in black.

At variance with **Figure 5-3a** and **5-3b**, **Figure 5-3c**, **5-3d** and **5-3e** show images characterized by a dark core, suggesting that the corresponding defects involve one or more atomic vacancies in the network. More specifically, the defect imaged in Figure 3c displays a mirror symmetry, whereas those in **Figure 5-3d** and **5-3e** show a threefold symmetric shape, centered in fcc and top positions, respectively. In **Figure 5-3d**, the down-pointing black triangle shows three protrusions in fcc position close to the corners, with a slightly less bright appearance than C atoms in the network; conversely, the triangular defect in **Figure 5-3e** displays a completely black core. Due to the likely presence of vacancies, it is reasonable to expect that these three defects involve nitrogen in pyridinic structures; however, to rule out other possibilities, we did not limit our models to such configurations. For the defects in **Figure 5-3c** and in **Figure 5-3e** we have considered a wide variety of possible models (involving different numbers of vacancies and N atoms and considering also possible Ni adatoms, as shown in **Figure 5-4**).

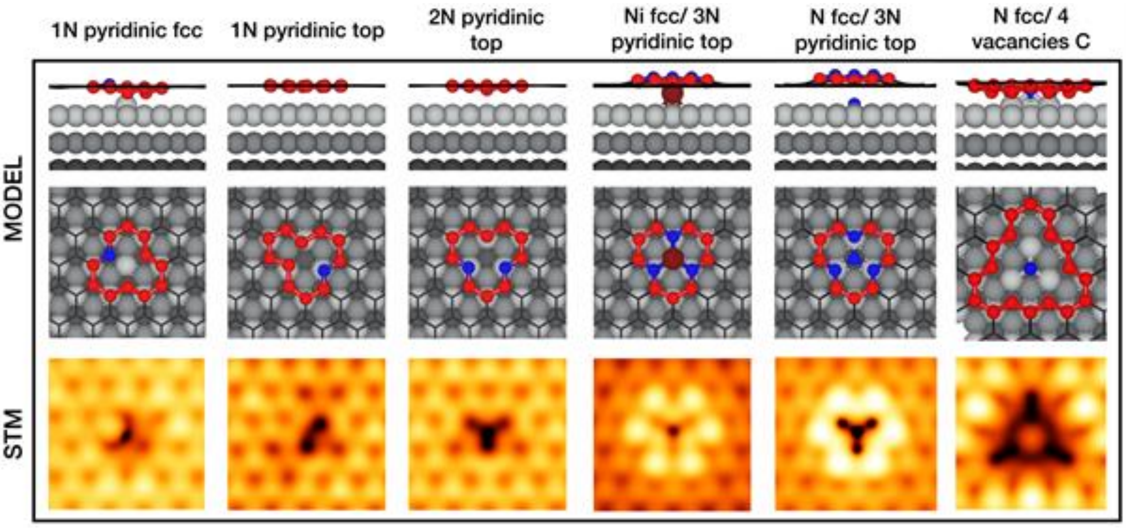

Figure 5-4: N dopant configurations in Gr on Ni(111): top and side views defects with the corresponding simulated STM images. The different structures are classified according to the number of N atoms, the configuration type, and the position. Computational parameters: $V_{bias} = -0.2$ V; ILDOS iso-surface lying ≈ 2 Å above graphene and with ILDOS value of 5×10^{-5} $|e|/a_0^3$. Color coding: Ni atoms in the first, second and third layer are rendered in dark grey, grey and light grey, respectively; Ni adatom in dark red; N atoms in blue; C atoms delimiting the vacancy site in red; Gr network in black.

The comparison between the experimental STM images and those obtained from the extensive DFT investigation lead to the following assignment (see bottom panels in **Figure 5-3**): the defect in **Figure 5-3c** is compatible with a 2N pyridinic fcc with mirror symmetry, whereas the ones in **Figure 5-3d** and in **Figure 5-3e** can be assigned to three-fold symmetric pyridinic configurations of three N species in fcc and top positions, respectively. These 3N pyridinic models consist of three N atoms, each bound to two C atoms, at the edge of a C vacancy.

The presence of pyridinic species in the N-Gr layer is fully consistent with the XPS measurements reported and discussed above. In particular, the 3N pyridinic top configuration is the one that best fits the experimentally observed XPS shift with respect to the graphitic top species (calc. 2.1 eV).

The following two facts are worth noting: 2N pyridinic fcc defects are very rare and their identification is not straightforward, while pyridinic configurations with 2N top, 1N top and 1N fcc, are never observed in our experimental STM images of the N-Gr layer. In order to understand why these structures are not present, we performed a set of DFT calculations aimed at evaluating the energy cost/gain of having N atoms at either pyridinic or graphitic positions in the lattice. We compared the total energy of three model configurations with the same number of N atoms (3N) but different relative positions (see **Figure 5-5**). The most stable model (3N pyridinic top) is taken as energy reference. Both the other tested structures (“2N pyridinic top+1N graphitic top” and “1N pyridinic top+2N graphitic top”) are characterized by higher total energies, +2.5 eV and +4.6 eV, respectively. This is a clear indication of the preference for the N atoms to be located at the edges of the C vacancy site rather than elsewhere, replacing a C atom within the Gr matrix, which explains the experimentally observed higher abundance of pyridinic defects with respect to graphitic ones. Such balance is likely related to the doping technique: adding N atoms during growth conditions favors the dynamic selection of defects with lower energy, with no constraint posed by the local abundance of N atoms required. Conversely, other doping techniques such as post-growth ion implantation favor defects with a different graphitic/pyridinic ratio, as a consequence of the ballistic formation process.[232,233]

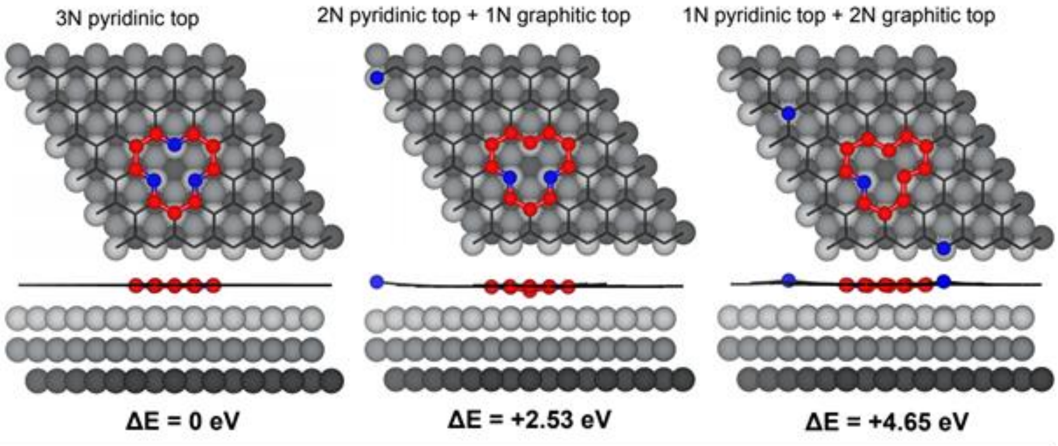

Figure 5-5: Top and side views of three different N-Gr models involving 3 Nitrogen atoms, classified according to the configuration type and position of the N atoms. The relative energy with respect to the most stable model (3N pyridinic top) is reported below each configuration. Color coding: Ni atoms in the first, second and third layer are rendered in dark grey, grey, and light grey, respectively; N atoms in blue; C atoms delimiting the defect site in red, Gr network in black.

We further characterize the electronic structure of the observed N defects by acquiring STM images at different bias voltages. This allows the empty and filled states near the Fermi level to be probed. The comparison between the experimental and the simulated STM images shows a good agreement for N graphitic top and fcc defects, as well as for the 3N pyridinic fcc defect (see **Figure 5-6**). Only in the case of the 3N pyridinic top defect, the simulated image did not adequately reproduce the experimental features for positive bias polarity. Indeed, for this case simulated STM images show a dark core at all the considered biases (negative and positive), while the experimental images display a dark core only at negative biases and bright protrusions at positive ones.

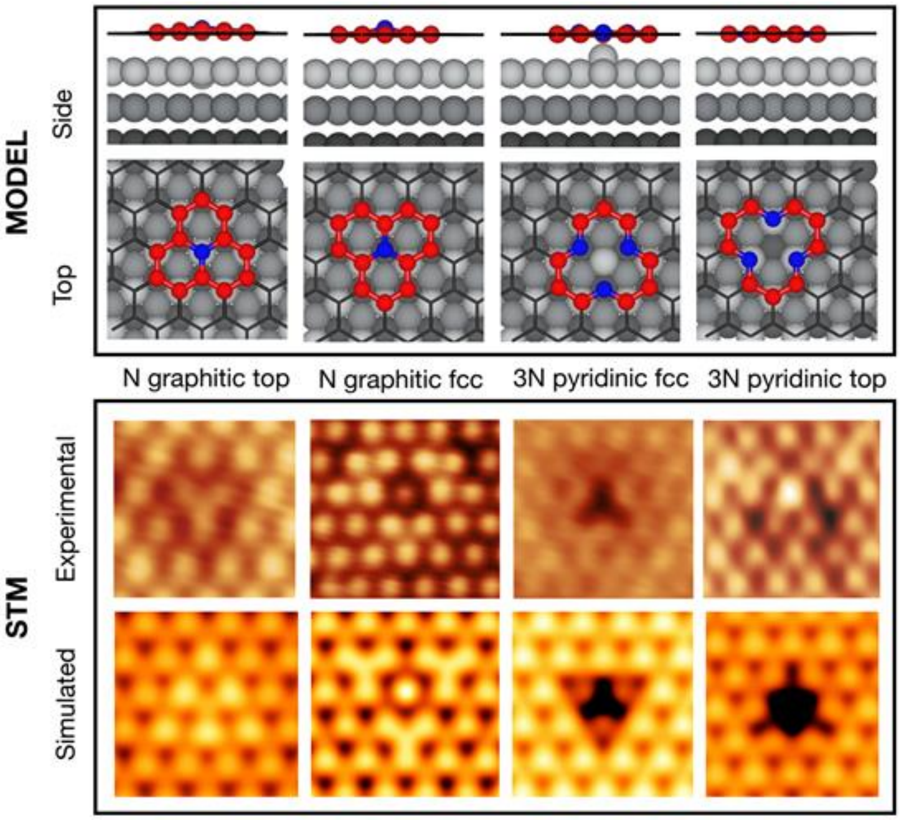

Figure 5-6: Experimental and simulated STM images of N defects at a different bias (+0.2 V).

To further corroborate our assignment based on the good agreement between experimental and calculated XPS shifts and STM images at negative bias, we have performed STS measurements at cryogenic temperature (77 K) to compare the spatial distribution of electron tunneling at specific energies with the localized density of states. Indeed, experimental dI/dV conductance maps of graphitic defects, acquired at several biases, nicely match the corresponding maps of LDOS, (see **Figure 5-7**), providing further support to our interpretation about the nature of the observed N defects.

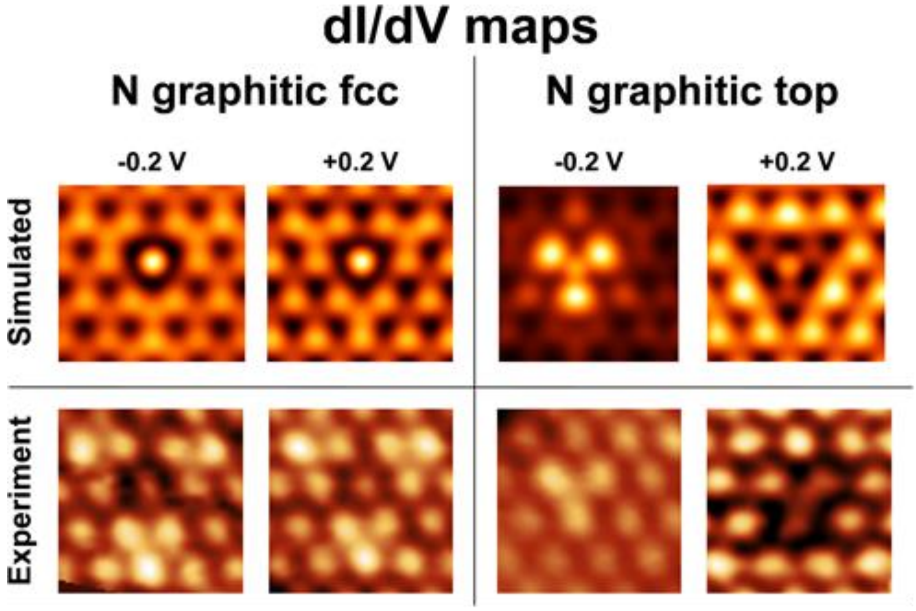

Figure 5-7: Simulated and experimental dI/dV conductance maps at constant height of the 1N graphitic fcc and 1N graphitic top defects, for two different biases, -0.2 and +0.2 V. Simulation parameters: LDOS iso-surface with a constant height of 2 Å above graphene. Experimental starting parameters: N graphitic fcc I_0 = 3.0 nA, V_0 = ±0.2 V, N graphitic top I_0 = 4.0 nA, V_0 = ±0.2 V. Lock-in parameters: Amplitude=16 mV, Frequency= 971.5 Hz.

6.5. Conclusions

In summary, we performed an extensive set of DFT simulations to support and corroborate the experimental evidence of our colleagues. They synthesized high-quality N-Gr on a Ni(111) substrate using an "inside out" growth method. These layers are obtained by dosing a commonly used hydrocarbon precursor (C_2H_4) on a hot Ni substrate, while N atoms segregate at the surface from a nitrogen reservoir previously created in the Ni bulk with a simple and reproducible doping process. The produced N-Gr layers were thoroughly characterized at the atomic level by STM and XPS in combination with DFT simulations. This approach yields very homogeneous and flat layers, with a variety of N defects in the graphene mesh that we have identified and fully characterized. The formation of these defects is highly reproducible in different preparations and can potentially play a relevant role in tailoring unexpected electronic, optical, and chemical properties of the graphene layer. Considering the increasing interest of the scientific community in the improved properties of doped Gr, this work can contribute to open a new way to produce high-quality N-Gr layers with well-defined functional defects, suitable for new nanotechnological applications.

APPENDIX

Experimental details

N-doped Gr layers were prepared in a UHV chamber with a base pressure of ~2 ×10^{-10} mbar. A Ni(111) single crystal was cleaned by several cycles of Ar^+ sputtering at 1.5 kV at room temperature (RT) and annealing at 700 °C, for a few minutes. Standard Gr growth was performed in UHV by low-pressure CVD, using ethylene (C_2H_4) as precursor. Low energy electron diffraction (LEED) and STM characterization was performed in UHV to assess the quality and homogeneity of the as-grown Gr sample. STM measurements were performed at room and cryogenic temperature (77 K) with an Omicron variable-temperature (VT) STM and an Omicron low-temperature (LT) STM. All topographic images were acquired in constant-current mode. All dI/dV conductance maps were acquired in constant-height mode using the lock-in technique. STM images were analyzed with the Gwyddion software package and moderate noise filtering has been applied. Crystallographic orientation of the images was obtained by analyzing the epitaxial structure formed by pristine Gr on the Ni(111) surface, as described in Ref 227. XPS measurements were performed ex-situ at the APE beamline and the ANCHOR-SUNDYN beamline at Elettra-Sincrotrone Trieste, with a base pressure in the range of 10^{-10} mbar. All the spectra were collected at RT in normal emission geometry using different experimental apparatuses, X-ray sources (hν = 1486.7 eV) and hemispherical electron energy analysers. All binding energies were calibrated by measuring the Fermi level. The N1s spectrum components have been evaluated by least square fitting with three Doniach-Sunjic peaks (with fixed positions at 400.6 eV, 398.6 eV, 397.1 eV) and a Shirley background.

7. Mechanism of CO Intercalation through the Graphene/Ni (111) Interface and Effect of Doping

The mechanism of molecular intercalation into the confined zone between a bidimensional graphene monolayer and the underlying substrate is still a big open question, although it is a crucial step in many relevant applications. In this chapter, through a combined theoretical and experimental approach, we have accomplished a major fundamental breakthrough in the comprehension and control of this critical process: we have identified the key sites where molecule intercalation is unlocked, we have proved and rationalized the facilitating role of nitrogen doping centers and we have explained the overall mechanism down to single molecule level.

The results reported in this chapter have been published in: Perilli, D., Fiori, S., Panighel, M., Liu, H., Cepek, C., Perissi, M., Comelli, G., Africh, C., Di Valentin, C., J. Phys. Chem. Lett. 2020, 11, 8887-8892.

7.1. Introduction

Molecule intercalation through the graphene (Gr) /metal (M) interface is a crucial process for several relevant applications, such as catalysis under cover,[17,234,235] large-scale preparation of single-layer graphene from chemical vapour deposition (CVD),[236] graphene-based electrochemistry[237] and gas trapping in highly pressurized graphene nanobubbles.[238]

Several experimental proofs exist of the fact that gases succeed in reaching the confined zone beneath Gr.[239,240,241,242,243] For example, scanning tunneling microscopy (STM) images reveal a change in the pattern when the gas intercalation decouples Gr from the substrate.[240] Furthermore, molecular chemical reactivity under graphene is probed by real-time low-energy electron microscopy (LEEM)/photoemission electron microscopy (PEEM), x-ray photoelectron spectroscopy (XPS) and high-resolution electron energy loss (HREELS) spectroscopy.[239,240,244]

However, gas or molecule intercalation still remains mostly an empirical observation: although crucial, the mechanism is not yet understood. It is even not yet established whether it is a general mechanism, or it is molecule-dependent. Researchers can prove it takes place, but they do not really know how.

What it is clearly known is that defect-free Gr is impermeable to any atomic or molecular species in gas or liquid phase.[245] Only the permeation of atomic and molecular hydrogen can be activated by the presence of some local curvature, due to a peculiar flipping mechanism, as recently reported.[246] Then, an important open question, which we want to address in the present paper, is: if Gr is impermeable, why do researchers observe gas intercalation at Gr/M interfaces?

One may expect that the mechanism of gas intercalation takes place in two main consecutive steps: 1) the gas permeation through the Gr layer; 2) the gas diffusion within the Gr/M interface. The first step is determined by the gas permeability of Gr layers, which has been a topic of intense discussion in the past.[247] The reason is that the ability to precisely control the quantity and location of molecular flux is of value in several graphene applications, such as molecular sieving membranes and sensor design, nanoscale 3D printing and catalysis.[248,249]

For large-sheet stacked graphene membranes, it has been established that gas permeation may take place by intercalation through structural defects, also known as inner-sheet pathway, whose kinetics largely depends on their size and concentration.[250] Discrete *Å*-sized pores, induced with a voltage pulse applied by a metallized atomic force microscope (AFM) tip on a single graphene sheet, have also been used to control gas transport and selectivity in molecular valves.[251]

It is reasonable to expect that structural defects may play a key role also for the intercalation of the gas molecules within Gr/M interfaces, as proposed in a recent experimental work. Moreover, a theoretical study suggested that the presence of dopants may influence graphene permeability.

In this Chapter, through a combined theoretical and experimental study, we propose a mechanism of CO intercalation through a Gr/Ni (111) interface, based on density functional theory calculations, which is consistent with the experimental observations of CO exposure on pristine graphene and N-doped graphene (N-Gr) grown on a Ni(111) surface by Low-Energy Electron Diffraction (LEED), XPS and STM.

7.2. Computational Details

Density Functional Theory (DFT) calculations were performed using the plane-wave-based Quantum ESPRESSO package (QE).[157] The ultrasoft pseudopotentials[129] were adopted to describe the electron-ion interaction with Ni (3d, 4s), C (2s, 2p), O (2s, 2p), N (2s, 2p), and H (1s), treated as valence electrons. Energy cutoffs of 30 Ry and 240 Ry (for kinetic energy and charge density expansion, respectively) were adopted for all calculations. The Perdew-Burke-Ernzerhof functional (PBE)[122] was used for electron exchange-correlation. To properly describe the Gr/Ni interaction, semiempirical corrections accounting for the van der Waals interactions were included with the DFT-D2 formalism.[124] Spin polarization was always included.

For the simulation of nickel(111)-supported epitaxial graphene interfaces (Gr/Ni) in the top-fcc registry, a $(2\sqrt{7} \times 2\sqrt{7})$ and (8×8) supercells were used for pristine and defective graphene, respectively.

The geometry relaxation of all considered systems was performed only at the Γ point, followed by a single self-consistent field (SCF) cycle calculation with a $2 \times 2 \times 1$ Monkhorst-Pack[187] k-points mesh to get more accurate total energies.

The Ni(111) surface was modeled by a three-layer slab with a bottom layer fixed to the bulk positions during the geometry relaxation to mimic a semi-infinite solid. To avoid interactions between adjacent periodic images, a vacuum space of about 15 Å in the direction perpendicular to the surface was used.

The Climbing Image–Nudged Elastic Band (CI–NEB)[142] method was employed to simulate the CO diffusion process at the Gr/Ni interface, generating the minimum energy path of the reaction step and an evaluation of the energy barrier.

STM simulations were performed using the Tersoff-Hamann approach,[131] according to which the tunneling current is proportional to the energy-integrated Local Density of States (ILDOS). Ball-and-stick models and STM images were rendered with XCrySDen and Gwyddion software, respectively.

The adsorption energy (ΔE_{ads}), as normalized on the number of CO molecules (n), was calculated as follows:

$$\Delta E_{ads} = (E_{nCO/system} - nE_{CO} - E_{system})/n \qquad (7\text{-}1)$$

where $E_{nCO/system}$ is the total energy of the system (Gr/Ni or 4VG-6H or 4VG-3CO or 4VG-6N) with n adsorbed CO molecules, E_{nCO} is the total energy of n isolated CO molecules in the gas phase, and E_{system} is the total energy of the optimized system without any adsorbed CO molecule.

In the following, we define the contributions for the energy decomposition analysis, as shown in **Figure 7-5** and reported in **Table 7-1**:

$$\Delta E_{decoupl} = [(E_{4VG\text{-}6N,dist} - E_{4VG\text{-}6N\text{-}fs,dist} - E_{Ni,dist}) - (E_{4VG\text{-}6N} - E_{4VG\text{-}6N\text{-}fs} - E_{Ni})]/n \qquad (7\text{-}2)$$

where $E_{4VG\text{-}6N,dist}$, $E_{4VG\text{-}6N\text{-}fs,dist}$, and $E_{Ni,dist}$ are the total energies of Ni-supported 4VG-6N, free-standing 4VG-6N, and Ni substrate, respectively, in the optimized geometry for nCO/4VG-6N, whereas $E_{4VG\text{-}6N}$, $E_{4VG\text{-}6N\text{-}fs}$, and E_{Ni} are the total energies of Ni-supported 4VG-6N, free-standing 4VG-6N, and Ni substrate, respectively, in the optimized geometry of 4VG-6N;

$$\Delta E_{dist} = [(E_{nCO,dist} - E_{nCO}) + (E_{4VG\text{-}6N\text{-}fs,dist} - E_{4VG\text{-}6N\text{-}fs}) + (E_{Ni,dist} - E_{Ni})]/n \qquad (7\text{-}3)$$

where $E_{nCO,dist}$ and E_{nCO} are the total energies of n CO molecules in the optimized geometry of nCO/4VG-6N and isolated in the gas-phase, respectively;

$$\Delta E_{bind} = (E_{nCO/4VG\text{-}6N} - E_{nCO,dist} - E_{4VG\text{-}6N,dist})/n \qquad (7\text{-}4)$$

where $E_{nCO/4VG\text{-}6N}$ is the total energy of nCO/4VG-6N in its optimized geometry; n is the number of adsorbed CO molecules.

7.3. Experimental evidence of CO intercalation

High-quality Gr and N-Gr layers on Ni(111) were grown by a standard low-pressure chemical vapour deposition (CVD) procedure. Carbon monoxide was then dosed at pressures in the mbar regime (more details in the Appendix). In the LEED patterns obtained for pristine Gr (**Fig. 7-1a** left), only after exposure to 500 mTorr of CO, new extra spots, besides the Ni and Gr markers, are visible forming a pattern in line with those reported in literature for CO on clean Ni(111) and compatible with the coexistence of c(4×2) and (√7×√7)R19° CO domains (nominal coverage of 0.5 and 0.57 ML, respectively). On the other hand, for N-Gr (**Fig. 7-1b** left), new spots are present already after exposure to 20 mTorr of CO, yielding one well-defined pattern corresponding to the (√7×√7)R19° CO superstructure on clean Ni (nominal coverage of 0.57 ML). On the basis of XPS and STM results, we can rule out that CO is adsorbed on a residual clean Ni region (not covered by Gr or N-Gr), implying that CO intercalation underneath N-Gr occurs at a pressure that is more than one order of magnitude lower than for pristine Gr.

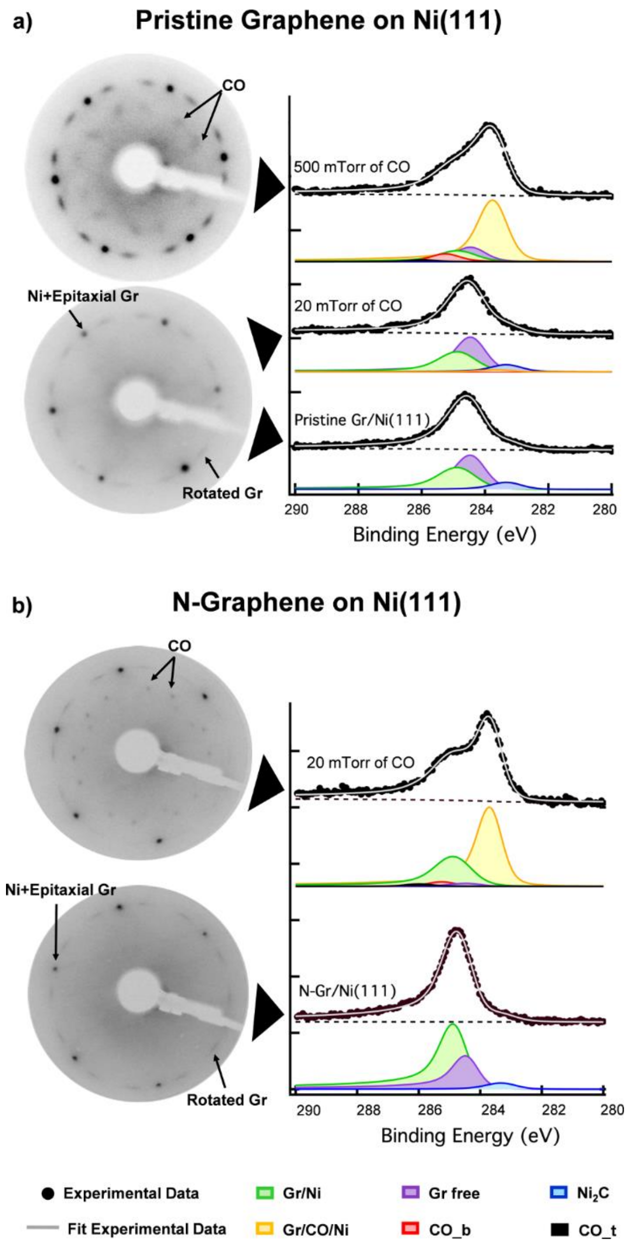

Figure 7-1: LEED patterns and XPS C 1s spectra of (a) pristine Gr and (b) N-Gr on Ni(111) substrates before and after the CO exposures in the millibar regime: for explanation, see main text.

XPS measurements carried out on Gr and N-Gr samples before and after CO exposure (**Fig. 7-1a** and **1b**, right) present features that confirm CO intercalation. In the C 1s spectrum, two new components raise after CO exposure, suggesting a detachment of the layer from the Ni substrate: the first at 283.6 eV is characteristic of C from a Gr layer decoupled from the metal substrate by intercalated CO;[252] the second at 285.3 eV has been attributed to C from CO on Ni(111) in bridge position.[253] The same features are observed in the N-Gr spectrum (**Fig. 7-1b** right) but at significantly lower CO pressure.

We further confirm CO intercalation by STM. In **Fig. 2a** the atomically resolved Gr layer imaged before CO exposure shows two triangular sublattices typical of the top-fcc arrangement. Due to the strong Gr/Ni interaction, the C atoms on fcc positions are imaged brighter than those on top, in agreement with DFT simulations (**Fig. 2d**). In **Fig. 2b**, after CO intercalation below Gr, the whole hexagon of the honeycomb lattice appears clearly, in agreement the simulated STM image in **Fig. 2e**. The presence of an intercalated buffer layer also affects the appearance of N defects in N-Gr, as evident in **Fig. 2c** for one of the most abundant species observed on the N-Gr/CO/Ni(111) surface. The bright protrusion at the center is surrounded by a √3x√3 pattern, not present before CO intercalation, which we ascribe to the typical quantum interference pattern due to scattering by one or more C vacancies in a Gr layer that is weakly interacting with the substrate. This defect is a 3N pyridinic species, as unambiguously confirmed by the simulated STM image in **Figure 7-2f**.

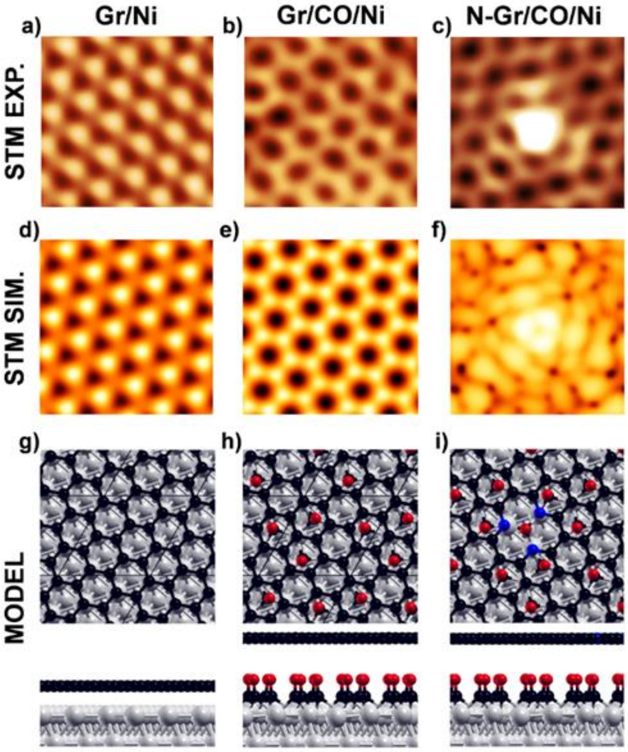

Figure 7-2: Pristine and N-doped Gr/Ni interfaces with and without intercalated CO molecules at 0.57 ML coverage. Experimental (panel a, b, and c) and DFT simulated (panel d, e, and f) STM images. Image size: 1.2 × 1.2 nm. Experimental parameters: (a) I = 0.1 nA, V_{bias} = -0.3 V; (b) I = 0.7 nA, V_{bias} = -0.2 V; (c) I =0.98, nA V_{bias} = -0.05 V. Computational parameters: (d and e) V_{bias} = -0.2 V, ILDOS isosurface lying at 2 Å above graphene; (f) V_{bias} = -0.05 V, ILDOS iso-surface lying ≈ 3 Å above graphene and with ILDOS value of 1×10^{-5} $|e|/a_0^3$. Panel g, h, and i: the ball-and-stick model of DFT relaxed structures (side and top view). Color coding: Ni atoms in grey; C atoms in black; O atoms in red; and N atoms in blue.

Thus, the morphological and chemical characterization of pristine Gr and N-Gr yields very similar results with all the applied techniques (both at the atomic scale with STM as well as by integrating methods like LEED and XPS), with the only crucial difference being the threshold pressure required to induce CO intercalation and Gr decoupling: 500 mTorr vs 20 mTorr, respectively.

7.4. Mechanism of CO intercalation

The next question to answer is: how did CO molecules get through the graphene layer and reach the Gr/Ni(111) interface? Since even H_2, the smallest molecule in nature, cannot penetrate directly through the center of the hexagon, graphene must result impermeable to CO molecules. Therefore, reasonably, there must be some vacancies in the graphene lattice. How big should these "holes" be to allow a CO molecule to pass? Then, why is it so much easier to reach the interface when Gr is doped with N?

The most common atomic defect in pristine Gr/Ni(111) is known to be a tri-atomic C vacancy where a Ni adatom becomes trapped (1Ni@3VG). However, this seems not to be the gate for intercalation: if we model a CO molecule on top of it, the C atom is found to fill one of the vacancies whereas O becomes very tightly bound to Ni. When we add a second CO molecule, we observe the formation of CO_2 with one C left in the defect (**Figure 7-3**).

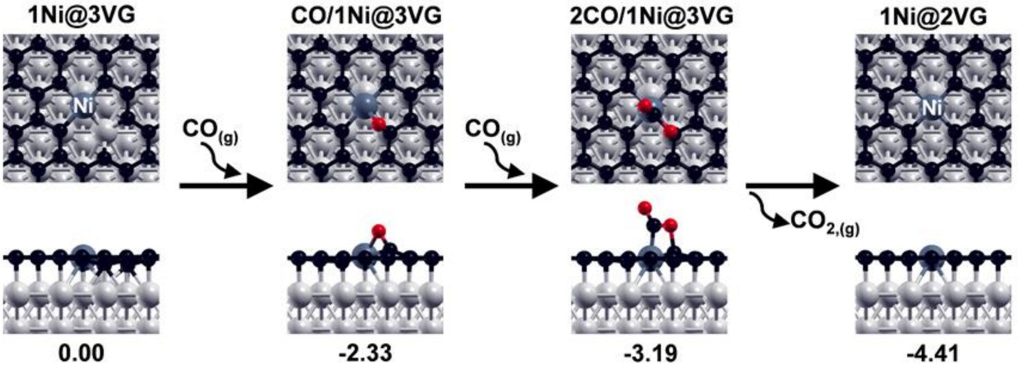

Figure 7-3: Top and side views of the intermediates along the CO reaction path on the most common defect in pristine Gr/Ni: a tri-atomic C vacancy where a Ni adatom becomes trapped (1Ni@3VG). The reaction energies (in eV) are reported below each structure. Color coding: Ni atoms in grey; Ni adatom in dark grey (indicated by a label); C atoms in black; and O atoms in red.

In the case of N-Gr/Ni(111), the most common atomic defect is a C monovacancy surrounded by three pyridinic N atoms, as discussed in Chapter 6. The adsorption of one CO in this C vacancy is however very unstable (+3 eV), because the defect is too small to accommodate it (**Figure 7-4**).

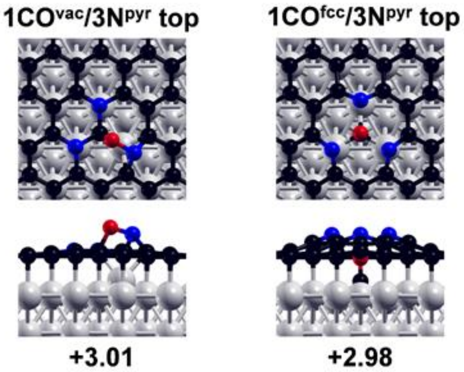

Figure 7-4: Top and side views of the two CO adsorption configurations on the most common defect of N-Gr/Ni: three pyridinic nitrogen atoms in top position ($3N^{pyr}$ top). The adsorption energies (in eV) are reported below each structure. Color coding: Ni atoms in grey; C atoms in black; O atoms in red; and N atoms in blue.

Therefore, one crucial aspect for the CO permeation through the graphene layer appears to be the critical size of the atomic holes allowing the molecules to pass through. Since the tri-atomic vacancy is found not to be suitable, we have investigated a tetra-atomic vacancy. The undercoordinated C atoms surrounding the vacancy are very reactive and either bind to the underlying Ni substrate, blocking the passage of the molecules into the confined zone between the Gr and the Ni(111) surface,[254] or they might react with residual hydrogen gas present in the chamber forming CH bond[32] or directly with the dosed CO molecules. These reactions yield the two models shown in **Figure 7-5** (**a** and **b**). Instead, for the case of defective N-Gr, we have found that N atoms tend to diffuse and segregate to the defect edges, where they become pyridinic. In other words, there is a downhill slope in energy, which favours the concentration of pyridinic N at the defect edges, stabilizing the defect towards reactivity with H_2 or CO. By simply comparing the structures of the three types of holes in **Fig. 7-5a**, **7-5b** and **7-5c** (4VG-6H, 4VG-3CO and 4VG-6N), there is an evident obstruction of the hole for the 4VG-3CO, whereas 4VG-6N appears to be the largest, with no steric hindrance. Moreover, the N atoms at the edges are much less strongly bound to the underlying Ni substrate than unsaturated C atoms.

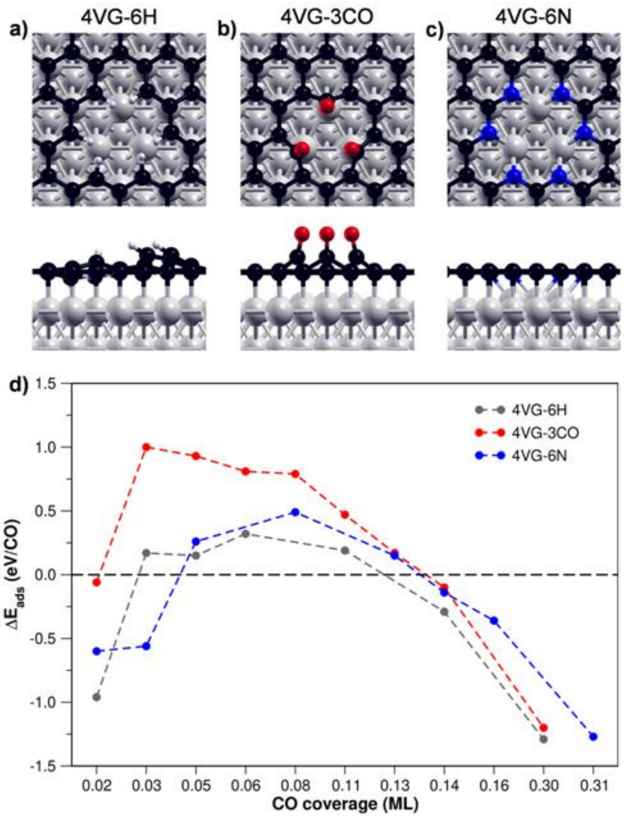

Figure 7-5: Top and side views for all the three models of vacancy considered: a) 4VG-6H, b) 4VG-3CO, and c) 4VG-6N. Color coding: Ni atoms in grey; C atoms in black; H atoms in white; O atoms in red; and N atoms in blue. d) Energy profile (normalized on the number of CO molecules) for the CO adsorption as a function of the CO coverage for all the model of vacancy: 4VG-6H, 4VG-3CO, and 4VG-6N in the grey, red, and blue line, respectively. The ball-and-stick representations of the structures at different CO coverage for 4VG-6N are shown in **Figure 7-7**.

We will focus the attention on the 4VG-3CO and on the 4VG-6N models, which, at variance with the 4VG-6H model, do not require dissociation of gas phase molecules for their formation. More specifically, we have investigated the energy profile for one CO molecule to vertically enter the atomic hole by moving the CO molecule along the z-direction and, at each different CO height, allowing all the atoms to fully relax (**Figure 7-6**). The two energy profiles for 4VG-3CO and for 4VG-6N are extremely different: for 4VG-3CO the energy goes up to almost 5 eV when the distance of CO from the Ni surface is 2.6 Å, whereas for 4VG-6N it only reaches a value of 0.19 eV, which represents a rough estimation of activation barrier. On this basis, we can draw an important conclusion: N-doping causes a chemical stabilization of multivacancies in Gr, which results in much less sterically hindered atomic holes in the 2D network facilitating molecule permeation. We expect this to have a tremendous effect on the threshold pressure for CO intercalation, as we will discuss in the following.

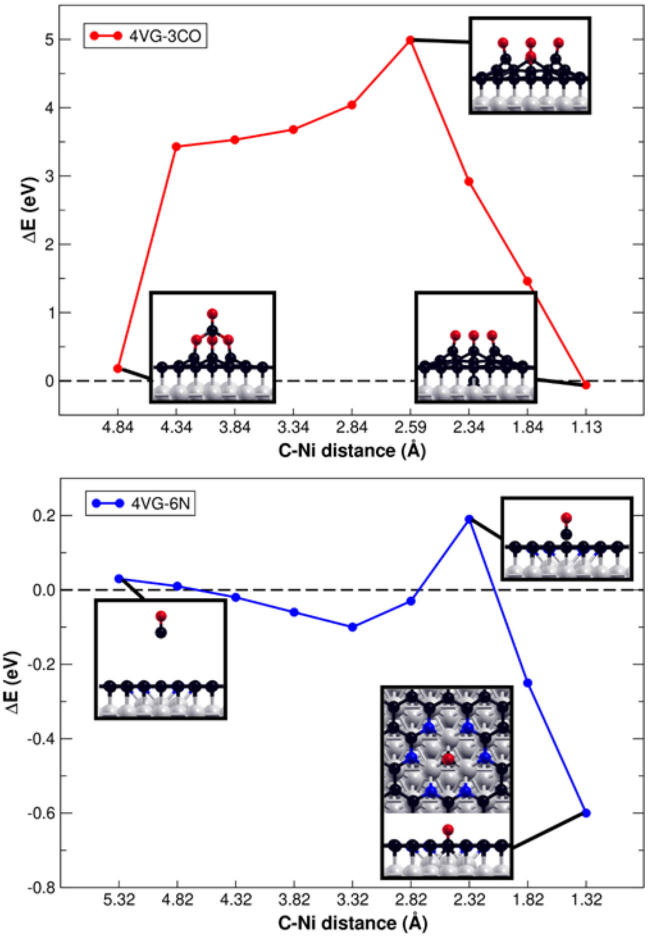

Figure 7-6: Energy profile for the adsorption step of the first CO molecule as a function of the C(O)-Ni distance on the 4VG-3CO (top panel) and 4VG-6N (bottom panel) models. Color coding: Ni atoms in grey; C atoms in black; H atoms in white; O atoms in red; and N atoms in blue.

For both 4VG-3CO and 4VG-6N, our calculations show that the first CO molecule is favourably bound to the Ni surface, by -0.06 eV and -0.60 eV, respectively. As a further step in our mechanistic study, we have added other CO molecules, one at a time, and analysed the variation in energy as normalized by the number of added CO molecules (see **Figure 7-5d**). We did this for all the three models of “hole”. The three curves are quite different in the first part of the graph, but tend to converge in the second part, starting from 0.11 ML. The 4VG-6N presents a very low energy profile that is similar to the one of 4VG-6H, where we do not expect any strong interaction of the CH groups with the underlying Ni substrate. This means that for 4VG-6N, it is not too energetically demanding not only for one CO molecule at a time to go through the hole (see **Figure 7-**

6), but also to intercalate in the confined zone between the Gr layer and the Ni surface (see **Figure 7-5d**). This is because the N atoms are not strongly interacting with the substrate and therefore there is a reasonable cost to lift one of them for the CO passage. All the structures at different CO coverages for 4VG-6N are shown in **Figure 7-7**.

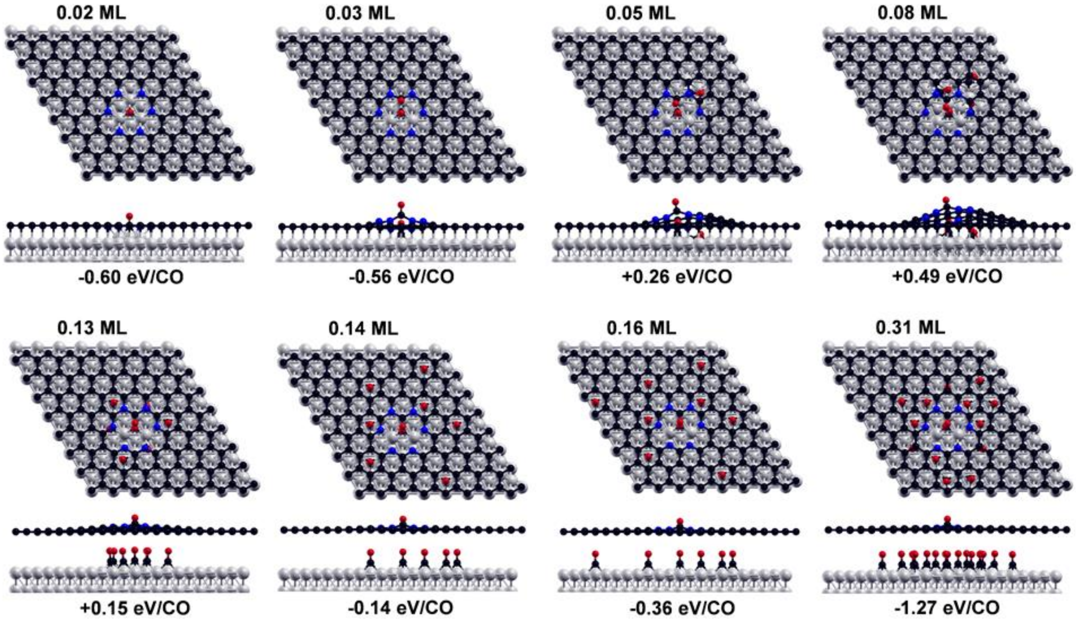

Figure 7-7: Top and side views of the intermediates of the CO intercalation process on 4VG-6N (as shown in **Figure 7-5d**). The adsorption energies (in eV), normalized by the number of CO molecules, are reported below each structure. Color coding: Ni atoms in grey; C atoms in black; O atoms in red; and N atoms in blue.

The highest energy value (0.5 eV) is registered at 0.08 ML coverage, then the curve starts to slope down. Very interestingly, at the turn between 0.13 and 0.14 ML we observe a twist in the energy, going to negative values. In other words, from 0.14 ML onwards, there is an energy gain for each CO that comes in. This twist is actually observed at 0.14 ML for all the models of multivacancy considered, therefore, we believe there must be something special related to it.

Some important insight comes from a similar analysis for a non-defective Gr layer on the Ni(111) substrate in **Figure 7-8**. Even in this case, where no defect is present in the Gr lattice, we observe that the cost to have CO molecules in the confined zone between the two materials reduces with the number of added molecules, turning into an energy gain for coverages ≥ 0.14 ML. Therefore, 0.14 ML corresponds to the critical point when the cost to detach the Gr layer from the Ni substrate is counterbalanced and even overcome by the gain of establishing a certain amount of Ni-CO bonds.

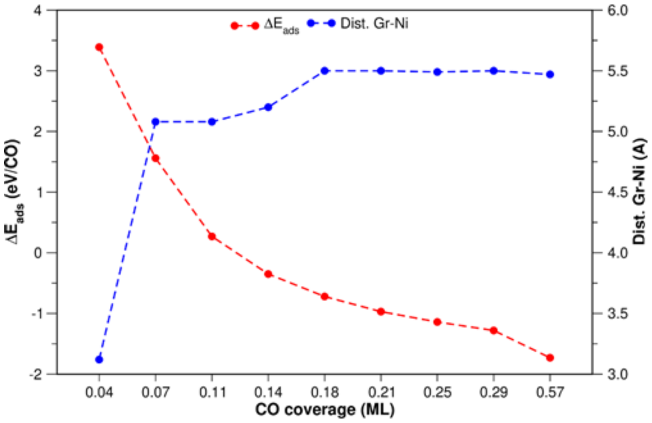

Figure 7-8: Energy profile (normalized by the number of CO molecules) and Gr-Ni vertical distance (in ångström, averaged on all the Ni atoms of the first layer and on all the C atoms of graphene) for the CO adsorption as a function of the CO coverage at the interface between defect-free Gr and Ni(111) surface (red and blue line, respectively).

We have performed an energy decomposition analysis for the 4VG-6N to establish the exact contributions from: 1) the cost to decouple Gr/Ni(111) (ΔE_{decoup}); 2) the cost to distort the Gr/Ni(111) to accommodate the CO molecules (ΔE_{dist}); 3) the binding energy for the Ni-CO bonds (ΔE_{bind}). The first two terms are energy costs, whereas the third one is an energy gain, as shown in **Figure 7-9** and detailed in **Table 7-1**. We carried out this analysis at the two critical coverages where there is an inversion in the energy balance: gain/cost at 0.03/0.05 ML and cost/gain at 0.13/0.14 ML (see **Figure 7-5d**). We observe that going from 0.03 to 0.05 ML there is a large increase in the energy cost of distortion (+1.02 eV/CO) but a small reduction in the cost for decoupling (-0.15 eV/CO), whereas the energy gain due to CO binding per molecule is about the same (difference of only -0.05 eV/CO). On the contrary, going from 0.13 to 0.14 ML we observe a small decrease both in the energy cost of distortion (-0.05 eV/CO) and of decoupling (-0.24 eV/CO) with a similar energy gain of binding per CO molecule (-0.02 eV/CO).

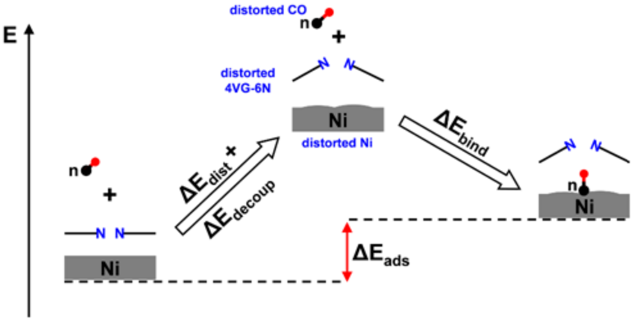

Figure 7-9: Schematic representation of the energy decomposition analysis for the energy contribution of distortion (positive, ΔE_{dist}), decoupling (positive, ΔE_{decoup}) and of binding (negative, ΔE_{bind}) to the adsorption energy (ΔE_{ads}) of CO at the interface between N-doped

graphene (4VG-6N) and Ni(111) surface. All the energy contributions are normalized on the number of CO molecules.

Table 7-1: Energy contributions of the energy decomposition analysis for CO adsorption on 4VG-6N of distortion (positive, ΔE_{dist}), decoupling (positive, ΔE_{decoup}) and of binding (negative, ΔE_{bind}) to the adsorption energy (ΔE) at different CO coverage. All terms are normalized on the number of CO molecules (eV/CO). The energy contributions are calculated using as a reference optimized 4VG-6N interface and isolated CO molecules in the gas-phase.

CO Coverage (ML)	ΔE_{ads} (eV/CO)	ΔE_{dist} (eV/CO)	ΔE_{decoup} (eV/CO)	ΔE_{bind} (eV/CO)
0.03	-0.56	+0.43	+0.59	-1.58
0.05	+0.26	+1.45	+0.44	-1.63
		+1.02	-0.15	-0.05
0.13	+0.15	+0.08	+2.66	-2.59
0.14	-0.14	+0.04	+2.42	-2.61
		-0.04	-0.24	-0.02

Another important aspect of the intercalation mechanism is related to the role played by the CO molecules distribution on the surface. We assumed that in the initial phase most of the CO molecules are close to the multiatomic hole through which they have reached the Ni surface; then, they gradually diffuse under the Gr layer and become more equally distributed on the surface. We have verified that this picture is compatible with the energy costs involved. First, we have compared the stabilization energy for 0.14 ML in two different CO distributions for 4VG-6N, as shown in **Figure 7-10**, i.e. (a) close to the hole edges and (b) more equally distributed beneath in the interface. From (a) to (b) there is an energy gain per CO molecule of -0.044 eV (×9 CO = -0.40 eV), which indicates a driving force for the CO molecules to better distribute, reducing the repulsive interaction among them.

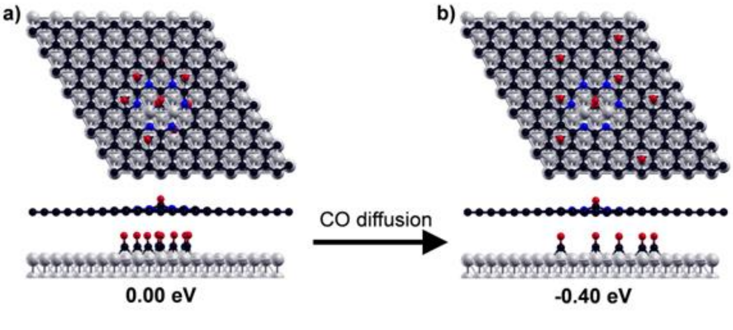

Figure 7-10: Top and side views of two different configurations at a CO coverage of 0.14 ML for 4VG-6N model. The two structures differ for the distribution of the intercalated CO molecules: a) close to the hole edges and b) most widespread. The relative energy (in unit of eV) with respect to the model (a) is reported below each configuration. Color coding: Ni atoms in grey; C atoms in black; O atoms in red; and N atoms in blue.

We estimated the activation barrier for the CO diffusion in the confined zone between Ni(111) and Gr through a nudged elastic band (NEB) calculation to be 0.19 eV (**Figure 7-11**), which is very close to what is computed for the corresponding process on the bare Ni(111) surface, experimentally observed already at 130 K, which is 0.15 eV.

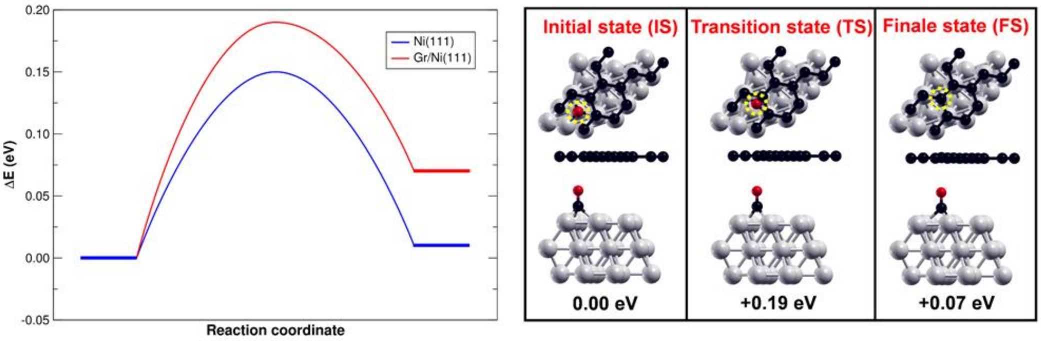

Figure 7-11: Energy profile (as calculated through a CI-NEB calculation) of the CO diffusion at a coverage of 0.14 ML for bare (red line) and Gr-covered (blue line) Ni (111) surface (left panel). Top and side views of the initial (hcp), transition (bridge), and final (fcc) configuration along the CO diffusion path of the Gr-covered system (right panel). The relative energy (in eV) with respect to the initial state is reported below each configuration. The position of the CO molecule is indicated by a dotted yellow circle in the top representation. Color coding: Ni atoms in grey; C atoms in black; and O atoms in red.

7.5. Do these large holes exist in graphene?

Finally, we prove by means of STM that defects with a size comparable to 4VG are rare in pristine Gr whereas they are often visualized on the N-Gr surface, both at the grain boundaries and in between the N-Gr domains. In **Figure 7-12a**, an example of a typical large defect present on N-Gr/Ni(111) is imaged at the atomic scale. It appears as a big dark triangular feature, which suggests a multi-atomic vacancy. This large defect is remarkably well reproduced by the simulated STM image of a tetratomic vacancy whose edges are decorated by 6 N atoms in top positions (**Figure 7-12b**) and, thus, it only differs from the 4VG-6N model proposed above for the registry to the substrate.

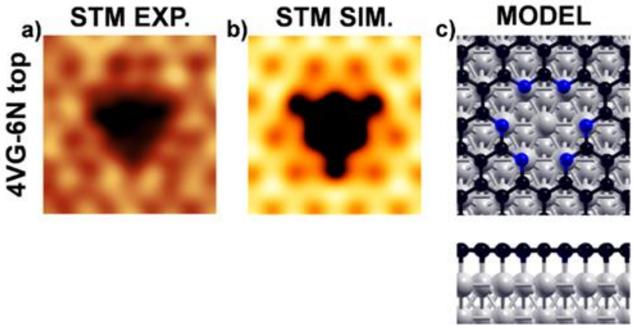

Figure 7-12: (a) Experimental and (b) simulated STM images of the 4VG-6N top configuration. (c) Ball-and-stick model in top and side view. Experimental parameters: (a) I = 1.4 nA, V_{bias} = -0.2 V; Computational parameters: V_{bias} = -0.2 V; ILDOS iso-surface lying ≈ 2 Å above graphene and with ILDOS value of 5×10^{-5} $|e|/a_0^3$. Color coding: Ni atoms in grey; C atoms in black; and N atoms in blue.

7.6. Conclusions

In conclusion, our work, based on the synergic contribution of DFT calculations, LEED, XPS and STM experiments, has unraveled and given proof of the mechanism of CO intercalation at the Gr/Ni interface, which is highly facilitated by the presence of N-dopants, stabilizing multi-atomic vacancy defects and turning them in narrow open doors to the confined zone between the two materials. Similar mechanisms are likely to apply to other cases of molecular intercalation at the Gr/M interface, where the process has been observed but not yet explained. A clear solution to this puzzle is a crucial step towards engineering the Gr/M interface in order to design and realize systems with tailored properties.

APPENDIX

a) Experimental details

Pristine Gr and N-Gr layers were prepared in a UHV chamber with a base pressure of ~2 ×10−10 mbar. The Ni(111) single crystals were cleaned by several cycles of Ar+ sputtering at 1.5 kV at room temperature (RT) and annealing at 700 °C, for a few minutes. For the N-Gr growth, a N-doped Ni(111) crystal was used (for the preparation details see Chapter 6). Standard Gr growth was performed in UHV by low-pressure CVD, using ethylene (C_2H_4) as precursor. Low energy electron diffraction (LEED) and STM characterization was performed in UHV in order to assess the quality and homogeneity of the as-grown Gr sample.

CO reactivity experiments have been carried out in-situ, in a home-made high-pressure cell inside a small chamber, connected to the experimental setup through a gate valve and kept in high vacuum (~10^{-9} mbar). STM measurements were performed in UHV at room temperature with an Omicron variable-temperature (VT) STM. All topographic images were acquired in constant-current mode. STM images were analyzed with the Gwyddion software package, after applying moderate noise filtering. Crystallographic orientation of the images was determined by analyzing the epitaxial structure formed by pristine Gr on the Ni(111) surface, as described in Ref. . XPS measurements were performed at a base pressure in the range of 10^{-9} mbar. All the spectra were collected at RT in normal emission geometry using a hemispherical electron energy analyser and a conventional Mg $K_{\alpha 1,2}$ (1253.6 eV) X-ray source, with an overall experimental energy resolution of ≈0.8 eV. All binding energies were calibrated by measuring the Fermi level. The spectra are normalized to the incident photon flux and analysed by performing a non-linear mean square fit of the data. We used a Shirley background and reproduced the C 1s photoemission peacks using asymmetric Doniach-Sunjic lineshapes.

b) Electronic structure analysis of G/CO/Ni systems

We present here a detailed analysis of the electronic properties of Gr/CO/Ni systems at different CO coverages. A similar analysis applied to N-Gr/CO/Ni will be the subject of a future work.

In **Figure 7-13a**, **b** and **c** we report the band structures projected on the Gr layer for three investigated Gr/CO/Ni(111) systems (corresponding to 0.14 ML, 0.50 ML and 0.57 ML CO coverages, respectively). All systems are similar from a geometrical point of view (see Figure 7-2h for comparison) and differ only on the number of intercalated CO molecules. The band structure has been evaluated along the Γ → M → K → Γ and Γ → X → S → Y → Γ high-symmetry paths for the $(\sqrt{7}\times\sqrt{7})R19^{o}$ and $2\times\sqrt{3})(2\times\sqrt{3})$ cell models, respectively. For all CO coverages, the decoupling from the metal substrate is complete. In addition, in all three cases we can observe a clear shift of the Dirac cone above the Fermi level, suggesting a net p-type doping effect that increases with the increasing number of intercalated CO molecules. We recall that Gr/Ni(111) is a n-type system. Therefore, the presence of intercalated CO molecules has a strong and opposite effect.

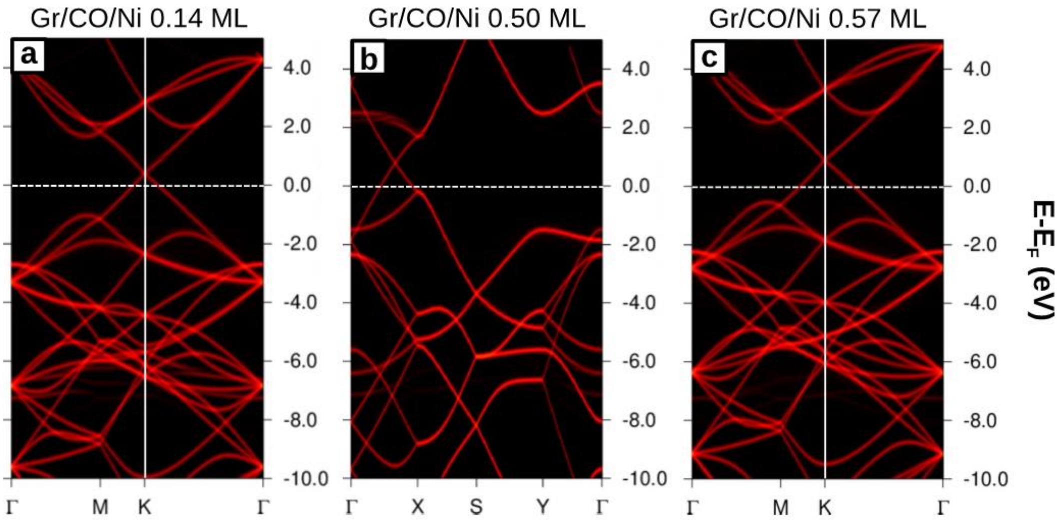

Figure 7-13: G-projected band structure along the high symmetry path for Gr/CO/Ni at different CO coverages: (a) 0.14 ML, (b) 0.50 ML, and (c) 0.57 ML. The Γ→M→K→Γ and Γ→X→S→Y→ Γ high symmetry paths were used for hexagonal (a and c) and orthorhombic cells (b), respectively. The colour scale refers to the value (states (eV)) of the projected DOS. All energies are referred to the corresponding Fermi energy of each system, as indicated by a dashed white line.

We further investigated this effect by analysing the density of states (DOS) projected on the C atoms of the Gr layer for the three different coverages discussed above: 0.14 ML (blue), 0.50 ML (green), 0.57 ML (red), in **Figure 7-14a**. The zero of the energy scales is set to the Fermi energy of the free-standing case. The plot clearly shows that the DOS of Gr, detached from the substrate by intercalated CO, recovers its free standing typical shape, but with a rigid shift towards higher energies, in perfect agreement with the projected band structures shown in **Figure 7-13**. The result is a sizeable p-doping effect, monotonically and linearly increasing with the CO coverage up to 0.86 eV at the saturation value (see **Figure 7-14b**).

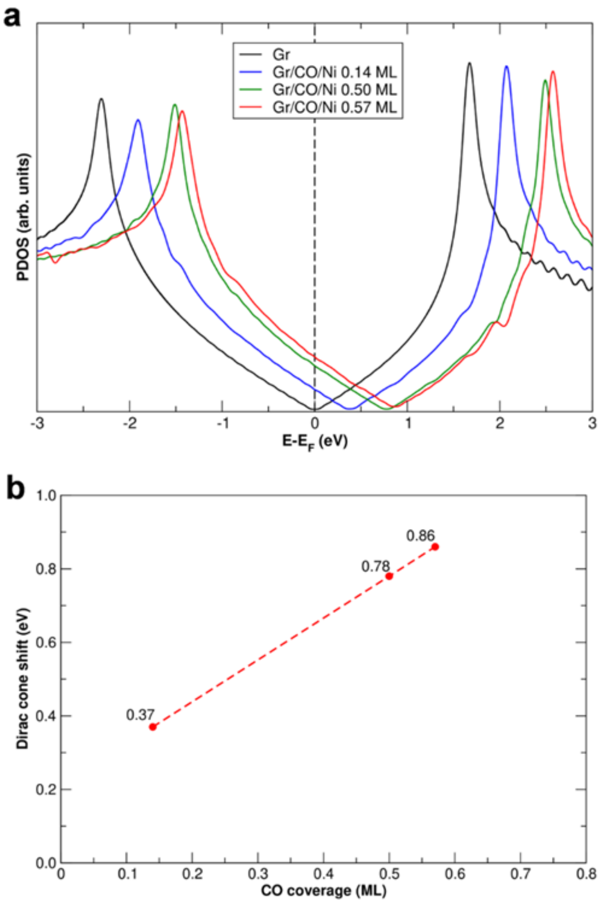

Figure 7-14: (a) Projected density of states (PDOS) onto the supported-graphene C p_z states for the optimized models of Gr/CO/Ni(111) at different CO coverages (0.14 ML, 0.50 ML, and 0.57 ML). The C p_z PDOS of free-standing graphene is shown for comparison. The PDOS value for each system is normalized to one C atom of graphene. All energies are referred to the corresponding Fermi energy of each system, as indicated by a dotted black line. (b) Linear relationship of the shift of the Dirac cone with respect to the Fermi energy for Gr/CO/Ni(111) (in eV) vs. the CO coverage.

From this electronic structure investigation, we conclude that an unexpected inversion in the doping of the Gr layer is observed before and after CO intercalation. The directly supported and, thus, strongly interacting Gr layer on a Ni(111) substrate (Gr/Ni(111)) is an n-type system, whereas even low amounts of intercalated CO molecules (0.14 ML) turn Gr/CO/Ni(111) into a p-type system. The more the intercalated CO molecules, the stronger the p-type doping effect. We expect that the electron density lost by Gr has been transferred to the underlying CO molecules, which are strong Lewis acids and, thus, excellent electron acceptors. This will be verified in the next section on the basis of differential electron density maps and of CO molecular descriptors, such as CO bond length and stretching frequency.

c) Electronic charge transfer analysis and molecular descriptors

In order to establish whether the electron density loss of the Gr layer observed upon CO intercalation is due to an electronic charge transfer to the underlying adsorbed CO molecules, we have investigated two molecular descriptors, which are the CO bond length and the CO stretching frequency, as reported in detail in **Tables 7-2, 7-3 and 7-4** for CO coverages of 0.14 ML, 0.50 ML and 0.57 ML, respectively. First of all, we observe that, at all three CO coverages, the presence of the Gr layer over the CO molecules adsorbed on the Ni(111) surface causes an elongation of the CO bond length (by 0.1 Å) and a corresponding decrease of the CO stretching frequency. These descriptors indicate that electron density is transferred to the CO π* states. This electron density comes probably not only from Gr but partly also from the Ni surface. We may notice that CO molecules on different adsorption sites (fcc or hcp) behave differently. When comparing the behaviour at different coverages, we notice that the CO stretching frequency shift is a more sensitive descriptor than the bond length, with a stronger variation observed for the higher coverages (0.50 and 0.57 ML) with respect to the case of low coverage (0.14 ML).

Table 7-2: CO stretching frequencies (in cm^{-1}) and bond distance (in Å) for CO/Ni and Gr/CO/Ni at 0.14 ML CO coverage. Each line is referred to a different stable CO adsorption position with respect to the metal substrate: fcc and hcp.

0.14 ML	CO/Ni		Gr/CO/Ni		**$\Delta\nu_{C\text{-}O}$ (cm^{-1})**
	dist. C-O (Å)	**$\nu_{C\text{-}O}$ (cm^{-1})**	**dist. C-O (Å)**	**$\nu_{C\text{-}O}$ (cm^{-1})**	
CO fcc	1.20	1744.3	1.21	1729.8	-14.5
CO hcp	1.20	1712.1	1.21	1686.1	-26.0

Table 7-3: CO stretching frequencies (in cm^{-1}) and bond distance (in Å) for CO/Ni and Gr/CO/Ni at 0.50 ML CO coverage. Each line is referred to a different CO adsorption position with respect to the metal substrate: fcc and hcp.

0.50 ML	CO/Ni		Gr/CO/Ni		**Δν$_{C-O}$ (cm^{-1})**
	dist. C-O (Å)	**ν$_{C-O}$ (cm^{-1})**	**dist. C-O (Å)**	**ν$_{C-O}$ (cm^{-1})**	
CO fcc	1.19	1801.3	1.20	1753.5	-47.8
CO hcp	1.20	1790.5	1.20	1751.0	-39.5

Table 7-4: CO stretching frequencies (in cm^{-1}) and bond distance (in Å) for CO/Ni and Gr/CO/Ni at 0.57 ML CO coverage in the configuration 3hcp+1fcc. Each line is referred to a different CO adsorption position with respect to the metal substrate: fcc and hcp.

0.57 ML	CO/Ni		Gr/CO/Ni		**Δν$_{C-O}$ (cm^{-1})**
	dist. C-O (Å)	**ν$_{C-O}$ (cm^{-1})**	**dist. C-O (Å)**	**ν$_{C-O}$ (cm^{-1})**	
CO fcc	1.19	1791.7	1.20	1752.5	-39.2
CO hcp	1.19	1792.2	1.20	1758.8	-33.4
CO hcp	1.19	1793.0	1.20	1754.8	-38.2
CO hcp	1.19	1793.4	1.20	1753.9	-39.5

8. Summary and Conclusions

Two-dimensional materials have attracted the attention of the scientific community due to their exceptional properties and promising applications. Nevertheless, over the last years, the frontline of research has moved towards the study of chemically modified 2D systems, such as defective, doped, and hybrid nanocomposites.

From a technological point of view, metal substrates are usually employed as heterogeneous catalysts for the CVD growth of 2D materials, which is one of the most promising growing methods in terms of scalability and cost. However, the role of such metal surfaces is often relegated to mere supports of growth, with a little attention to the properties that these hybrid interfaces (2D/M) offer.

In the present work of thesis, different types of 2D/metal interfaces have been characterized and investigated as potential electrocatalysts for crucial processes such as OER, HER, and as potential components of sensors.

In the first part of the work (Chapters 3, 4, and 5), the atomic structure of the interface between doped/defective h-BN and Cu(111) surface, together with its electronic properties and chemical reactivity, was systematically investigated by dispersion corrected density functional calculations. Cu is a very attractive substrate because of the possibility of using Cu foils and, thus, of moving towards large-scale preparations for commercial use.

In Chapter 3, we discovered that Cu adatoms from the substrate can emerge from the bulk material and become highly stabilized within the N-terminated holes of defective h-BN sheets, as a consequence of Cu-N bond formation. Their surface exposure as single atoms or small clusters could induce some interesting and unexpected reactivity, as investigated in the following chapters.

In Chapter 4, we apply the computational electrochemistry approach to the case of Cu-doped and Cu-supported h-BN systems as electrocatalysts for water oxidation (OER). In particular, trapped Cu tetramers, in the form of pyramids, expose one Cu atom toward the vacuum, which becomes available for catalysis. Such systems have a relatively low overpotential (0.68 V) and a low free energy cost (0.45 eV) for the final step of O_2

release. Therefore, they are extremely interesting systems for the electrocatalysis of the water oxidation reaction.

In Chapter 5, we explore the possibility of trapping single metal atoms of different chemical nature from that of the underlying metal surface for catalytic purposes. We designed several possible types of interface model systems considering various light transition metal atoms, including Cu, Ni, Co, and Fe, as well as various types of h-BN defects (mono- and di-atomic vacancies). For each model system, we have investigated the structural and electronic properties and we have evaluated the electrochemical stability and activity for HER. Our results suggest that both defective and single metal-doped h-BN/Cu(111) systems are potentially suitable catalysts for the HER.

In the second part of the work (Chapters 6 and 7), we investigated the graphene/nickel(111) interface and the nature and role of N dopants. Such a system is technologically important in the field of electrocatalysis and sensing. The work has been carried out in collaboration with the laboratory of CNR-IOM in Trieste, performing the synthesis and the characterization of the samples.

In Chapter 6, we performed an extensive set of DFT simulations to support and corroborate the experimental evidence on the nature of nitrogen atoms in graphene. Our experimental colleagues synthesized N-Gr layers by dosing a commonly used hydrocarbon precursor (C_2H_4) on a hot Ni substrate, while N atoms segregate at the surface from a nitrogen reservoir previously created in the Ni bulk with a simple and reproducible doping process. The produced N-Gr layers were thoroughly characterized at the atomic level by STM and XPS in combination with our DFT simulations in order to identify and fully characterize the N dopants. We observed how the majority of N atoms obtained through the method developed by CNR-IOM is in a pyridinic configuration and the second most common defect is graphitic N.

In Chapter 7, based on the synergic contribution of DFT calculations and experiments, we unraveled the mechanism of CO intercalation at the Gr/Ni interface, which is highly facilitated by the presence of N-dopants, stabilizing multi-atomic carbon vacancy defects and turning them in narrow open doors to the confined zone between the two materials. Similar mechanisms are likely to apply to other cases of molecular intercalation at the Gr/M interface, where the process has been observed but not yet explained. A clear solution to this puzzle is a crucial step towards engineering the Gr/M interface in order to design and realize systems with tailored properties.

To conclude, this work shows how the high surface area that two-dimensional materials offer can be used to trap objects like atoms or small metal clusters, activating the chemical reactivity of inert 2D materials.

9. References

---

[1] Khan, K., Tareen, A. K., Aslam, M., Wang, R., Zhang, Y., Mahmood, A., ... & Guo, Z. (2020). Recent developments in emerging two-dimensional materials and their applications. Journal of Materials Chemistry C.

[2] Novoselov, K. S., Fal, V. I., Colombo, L., Gellert, P. R., Schwab, M. G., & Kim, K. (2012). A roadmap for graphene. Nature, 490(7419), 192-200.

[3] Ferrari, A. C., Bonaccorso, F., Fal'Ko, V., Novoselov, K. S., Roche, S., Bøggild, P., ... & Garrido, J. A. (2015). Science and technology roadmap for graphene, related two-dimensional crystals, and hybrid systems. Nanoscale, 7(11), 4598-4810.

[4] Deng, D., Novoselov, K. S., Fu, Q., Zheng, N., Tian, Z., & Bao, X. (2016). Catalysis with two-dimensional materials and their heterostructures. Nature nanotechnology, 11(3), 218.

[5] Zhang, K., Feng, Y., Wang, F., Yang, Z., & Wang, J. (2017). Two dimensional hexagonal boron nitride (2D-hBN): synthesis, properties and applications. Journal of Materials Chemistry C, 5(46), 11992-12022.

[6] Choi, W., Choudhary, N., Han, G. H., Park, J., Akinwande, D., & Lee, Y. H. (2017). Recent development of two-dimensional transition metal dichalcogenides and their applications. Materials Today, 20(3), 116-130.

[7] Sun, Y., Wu, Q., & Shi, G. (2011). Graphene based new energy materials. *Energy & Environmental Science*, *4*(4), 1113-1132.

[8] Mounet, N., Gibertini, M., Schwaller, P., Campi, D., Merkys, A., Marrazzo, A., ... & Marzari, N. (2018). Two-dimensional materials from high-throughput computational exfoliation of experimentally known compounds. Nature nanotechnology, 13(3), 246-252.

[9] Slonczewski, J. C., & Weiss, P. R. (1958). Band structure of graphite. Physical review, 109(2), 272.

[10] Castellanos-Gomez, A., Vicarelli, L., Prada, E., Island, J. O., Narasimha-Acharya, K. L., Blanter, S. I., ... & Zandbergen, H. W. (2014). Isolation and characterization of few-layer black phosphorus. 2D Materials, 1(2), 025001.

[11] Mattheiss, L. F. (1973). Band structures of transition-metal-dichalcogenide layer compounds. Physical Review B, 8(8), 3719.

[12] Novoselov, K. S. (2011). Nobel lecture: Graphene: Materials in the flatland. Reviews of Modern Physics, 83(3), 837.

[13] Guo, Z., Zhang, H., Lu, S., Wang, Z., Tang, S., Shao, J., ... & Chu, P. K. (2015). From black phosphorus to phosphorene: basic solvent exfoliation, evolution of Raman scattering, and applications to ultrafast photonics. Advanced Functional Materials, 25(45), 6996-7002.

[14] Radisavljevic, B., Radenovic, A., Brivio, J., Giacometti, V., & Kis, A. (2011). Single-layer MoS 2 transistors. Nature nanotechnology, 6(3), 147.

[15] Wang, Q. H., Kalantar-Zadeh, K., Kis, A., Coleman, J. N., & Strano, M. S. (2012). Electronics and optoelectronics of two-dimensional transition metal dichalcogenides. Nature nanotechnology, 7(11), 699.

[16] Velický, M., & Toth, P. S. (2017). From two-dimensional materials to their heterostructures: An electrochemist's perspective. Applied Materials Today, 8, 68-103.

[17] Fu, Q., & Bao, X. (2017). Surface chemistry and catalysis confined under two-dimensional materials. Chemical Society Reviews, 46(7), 1842-1874.

---

[18] Cai, X., Luo, Y., Liu, B., & Cheng, H. M. (2018). Preparation of 2D material dispersions and their applications. Chemical Society Reviews, 47(16), 6224-6266.

[19] Tyagi, D., Wang, H., Huang, W., Hu, L., Tang, Y., Guo, Z., ... & Zhang, H. (2020). Recent Advances in Two-Dimensional Materials based Sensing Technology towards Health and Environmental Applications. Nanoscale.

[20] Novoselov, K. S., Geim, A. K., Morozov, S. V., Jiang, D., Zhang, Y., Dubonos, S. V., ... & Firsov, A. A. (2004). Electric field effect in atomically thin carbon films. Science, 306(5696), 666-669.

[21] Geim, A. K., & Novoselov, K. S. (2010). The rise of graphene. In Nanoscience and technology: a collection of reviews from nature journals (pp. 11-19).

[22] Rao, C. E. E., Sood, A. E., Subrahmanyam, K. E., & Govindaraj, A. (2009). Graphene: the new two-dimensional nanomaterial. Angewandte Chemie International Edition, 48(42), 7752-7777.

[23] Miró, P., Audiffred, M., & Heine, T. (2014). An atlas of two-dimensional materials. Chemical Society Reviews, 43(18), 6537-6554.

[24] Nan, H. Y., Ni, Z. H., Wang, J., Zafar, Z., Shi, Z. X., & Wang, Y. Y. (2013). The thermal stability of graphene in air investigated by Raman spectroscopy. Journal of Raman Spectroscopy, 44(7), 1018-1021.

[25] Bunch, J. S. et al. Impermeable atomic membranes from graphene sheets. Nano Lett. 8, 2458–2462 (2008).

[26] Nine, M. J., Cole, M. A., Tran, D. N., & Losic, D. (2015). Graphene: a multipurpose material for protective coatings. Journal of Materials Chemistry A, 3(24), 12580-12602.

[27] Varchon, F., Feng, R., Hass, J., Li, X., Nguyen, B. N., Naud, C., ... & Magaud, L. (2007). Electronic structure of epitaxial graphene layers on SiC: effect of the substrate. Physical review letters, 99(12), 126805.

[28] Li, X., Cai, W., An, J., Kim, S., Nah, J., Yang, D., ... & Banerjee, S. K. (2009). Large-area synthesis of high-quality and uniform graphene films on copper foils. science, 324(5932), 1312-1314.

[29] Chae, S. J., Güneş, F., Kim, K. K., Kim, E. S., Han, G. H., Kim, S. M., ... & Yang, C. W. (2009). Synthesis of large-area graphene layers on poly-nickel substrate by chemical vapor deposition: wrinkle formation. Advanced materials, 21(22), 2328-2333

[30] Banhart, F., Kotakoski, J., & Krasheninnikov, A. V. (2011). Structural defects in graphene. ACS nano, 5(1), 26-41.

[31] Liu, L., Qing, M., Wang, Y., & Chen, S. (2015). Defects in graphene: generation, healing, and their effects on the properties of graphene: a review. Journal of Materials Science & Technology, 31(6), 599-606.

[32] Patera, L. L., Bianchini, F., Troiano, G., Dri, C., Cepek, C., Peressi, M., ... & Comelli, G. (2015). Temperature-driven changes of the graphene edge structure on Ni (111): Substrate vs hydrogen passivation. Nano letters, 15(1), 56-62.

[33] Yazyev, O. V., & Louie, S. G. (2010). Topological defects in graphene: Dislocations and grain boundaries. Physical Review B, 81(19), 195420.

[34] Palacios, J. J., Fernández-Rossier, J., & Brey, L. (2008). Vacancy-induced magnetism in graphene and graphene ribbons. Physical Review B, 77(19), 195428.

[35] Subrahmanyam, K. S., Panchakarla, L. S., Govindaraj, A., & Rao, C. N. R. (2009). Simple method of preparing graphene flakes by an arc-discharge method. The Journal of Physical Chemistry C, 113(11), 4257-4259.

---

[36] Reddy, A. L. M., Srivastava, A., Gowda, S. R., Gullapalli, H., Dubey, M., & Ajayan, P. M. (2010). Synthesis of nitrogen-doped graphene films for lithium battery application. ACS nano, 4(11), 6337-6342.

[37] Wei, D., Liu, Y., Wang, Y., Zhang, H., Huang, L., & Yu, G. (2009). Synthesis of N-doped graphene by chemical vapor deposition and its electrical properties. Nano letters, 9(5), 1752-1758.

[38] Wang, Y., Mao, J., Meng, X., Yu, L., Deng, D., & Bao, X. (2018). Catalysis with two-dimensional materials confining single atoms: concept, design, and applications. Chemical reviews, 119(3), 1806-1854.

[39] Tang, L., Meng, X., Deng, D., & Bao, X. (2019). Confinement catalysis with 2D materials for energy conversion. Advanced Materials, 31(50), 1901996.

[40] Zhu, Y., Murali, S., Cai, W., Li, X., Suk, J. W., Potts, J. R., & Ruoff, R. S. (2010). Graphene and graphene oxide: synthesis, properties, and applications. Advanced materials, 22(35), 3906-3924.

[41] Giovannetti, G. A. K. P. A., Khomyakov, P. A., Brocks, G., Karpan, V. V., van den Brink, J., & Kelly, P. J. (2008). Doping graphene with metal contacts. Physical review letters, 101(2), 026803.

[42] Sokołowska, A., & Wronikowski, M. (1986). The phase diagram (P, T, E) of boron nitride. Journal of crystal growth, 76(2), 511-513.

[43] Pakdel, A., Bando, Y., & Golberg, D. (2014). Nano boron nitride flatland. Chemical Society Reviews, 43(3), 934-959.

[44] Elias, C., Valvin, P., Pelini, T., Summerfield, A., Mellor, C. J., Cheng, T. S., ... & Gil, B. (2019). Direct band-gap crossover in epitaxial monolayer boron nitride. Nature communications, 10(1), 1-7.

[45] Husain, E., Narayanan, T. N., Taha-Tijerina, J. J., Vinod, S., Vajtai, R., & Ajayan, P. M. (2013). Marine corrosion protective coatings of hexagonal boron nitride thin films on stainless steel. ACS applied materials & interfaces, 5(10), 4129-4135.

[46] Chen, T. A., Chuu, C. P., Tseng, C. C., Wen, C. K., Wong, H. S. P., Pan, S., ... & Fu, Q. (2020). Wafer-scale single-crystal hexagonal boron nitride monolayers on Cu (111). Nature, 579(7798), 219-223.

[47] Yu, J., Qin, L., Hao, Y., Kuang, S., Bai, X., Chong, Y. M., ... & Wang, E. (2010). Vertically aligned boron nitride nanosheets: chemical vapor synthesis, ultraviolet light emission, and superhydrophobicity. ACS nano, 4(1), 414-422.

[48] Jang, A. R., Hong, S., Hyun, C., Yoon, S. I., Kim, G., Jeong, H. Y., ... & Park, N. (2016). Wafer-scale and wrinkle-free epitaxial growth of single-orientated multilayer hexagonal boron nitride on sapphire. Nano letters, 16(5), 3360-3366.

[49] Kim, G., Jang, A. R., Jeong, H. Y., Lee, Z., Kang, D. J., & Shin, H. S. (2013). Growth of high-crystalline, single-layer hexagonal boron nitride on recyclable platinum foil. Nano letters, 13(4), 1834-1839.

[50] Bao, J., Jeppson, K., Edwards, M., Fu, Y., Ye, L., Lu, X., & Liu, J. (2016). Synthesis and applications of two-dimensional hexagonal boron nitride in electronics manufacturing. Electronic Materials Letters, 12(1), 1-16.

[51] Auwärter, W. (2019). Hexagonal boron nitride monolayers on metal supports: Versatile templates for atoms, molecules and nanostructures. Surface Science Reports, 74(1), 1-95.

[52] Joshi, S., Ecija, D., Koitz, R., Iannuzzi, M., Seitsonen, A. P., Hutter, J., ... & Barth, J. V. (2012). Boron nitride on Cu (111): an electronically corrugated monolayer. Nano letters, 12(11), 5821-5828.

---

[53] Schwarz, M., Riss, A., Garnica, M., Ducke, J., Deimel, P. S., Duncan, D. A., ... & Allegretti, F. (2017). Corrugation in the weakly interacting hexagonal-BN/Cu (111) system: structure determination by combining noncontact atomic force microscopy and X-ray standing waves. ACS nano, 11(9), 9151-9161.

[54] Meyer, J. C., Chuvilin, A., Algara-Siller, G., Biskupek, J., & Kaiser, U. (2009). Selective sputtering and atomic resolution imaging of atomically thin boron nitride membranes. Nano letters, 9(7), 2683-2689.

[55] Jin, C., Lin, F., Suenaga, K., & Iijima, S. (2009). Fabrication of a freestanding boron nitride single layer and its defect assignments. Physical review letters, 102(19), 195505.

[56] Kotakoski, J., Jin, C. H., Lehtinen, O., Suenaga, K., & Krasheninnikov, A. V. (2010). Electron knock-on damage in hexagonal boron nitride monolayers. Physical Review B, 82(11), 113404.

[57] Olsen, T., & Thygesen, K. S. (2013). Random phase approximation applied to solids, molecules, and graphene-metal interfaces: From van der Waals to covalent bonding. Physical Review B, 87(7), 075111.

[58] Vanin, M., Mortensen, J. J., Kelkkanen, A. K., Garcia-Lastra, J. M., Thygesen, K. S., & Jacobsen, K. W. (2010). Graphene on metals: A van der Waals density functional study. Physical Review B, 81(8), 081408.

[59] Bianchini, F., Patera, L. L., Peressi, M., Africh, C., & Comelli, G. (2014). Atomic scale identification of coexisting graphene structures on Ni (111). The journal of physical chemistry letters, 5(3), 467-473.

[60] I. Hamada, M. Otani Phys. Rev. B, 82 (2010), p. 153412

[61] Lee, H., Paeng, K., & Kim, I. S. (2018). A review of doping modulation in graphene. Synthetic Metals, 244, 36-47.

[62] Ferrighi, L., Trioni, M. I., & Di Valentin, C. (2015). Boron-doped, nitrogen-doped, and codoped graphene on Cu (111): A DFT+ vdW study. The Journal of Physical Chemistry C, 119(11), 6056-6064.

[63] Lv, R., Li, Q., Botello-Méndez, A. R., Hayashi, T., Wang, B., Berkdemir, A., ... & Kim, Y. A. (2012). Nitrogen-doped graphene: beyond single substitution and enhanced molecular sensing. Scientific reports, 2, 586.

[64] Lee, J. H., Kwon, S. H., Kwon, S., Cho, M., Kim, K. H., Han, T. H., & Lee, S. G. (2019). Tunable electronic properties of nitrogen and sulfur doped graphene: Density functional theory approach. Nanomaterials, 9(2), 268.

[65] Watanabe, K., Taniguchi, T., & Kanda, H. (2004). Direct-bandgap properties and evidence for ultraviolet lasing of hexagonal boron nitride single crystal. Nature materials, 3(6), 404-409.

[66] Kubota, Y., Watanabe, K., Tsuda, O., & Taniguchi, T. (2007). Deep ultraviolet light-emitting hexagonal boron nitride synthesized at atmospheric pressure. Science, 317(5840), 932-934.

[67] Watanabe, K., Taniguchi, T., Kuroda, T., & Kanda, H. (2006). Band-edge luminescence of deformed hexagonal boron nitride single crystals. Diamond and related materials, 15(11-12), 1891-1893.

[68] Silly, M. G., Jaffrennou, P., Barjon, J., Lauret, J. S., Ducastelle, F., Loiseau, A., ... & Rosencher, E. (2007). Luminescence properties of hexagonal boron nitride: cathodoluminescence and photoluminescence spectroscopy measurements. Physical review B, 75(8), 085205.

[69] Museur, L., & Kanaev, A. (2008). Near band-gap photoluminescence properties of hexagonal boron nitride. Journal of Applied Physics, 103(10), 103520.

[70] Museur, L., Feldbach, E., & Kanaev, A. (2008). Defect-related photoluminescence of hexagonal boron nitride. Physical review B, 78(15), 155204.

---

[71] Jaffrennou, P., Donatini, F., Barjon, J., Lauret, J. S., Maguer, A., Attal-Trétout, B., ... & Loiseau, A. (2007). Cathodoluminescence imaging and spectroscopy on a single multiwall boron nitride nanotube. Chemical physics letters, 442(4-6), 372-375.

[72] Jaffrennou, P., Barjon, J., Schmid, T., Museur, L., Kanaev, A., Lauret, J. S., ... & Attal-Tretout, B. (2008). Near-band-edge recombinations in multiwalled boron nitride nanotubes: Cathodoluminescence and photoluminescence spectroscopy measurements. Physical Review B, 77(23), 235422.

[73] Blase, X., Rubio, A., Louie, S. G., & Cohen, M. L. (1995). Quasiparticle band structure of bulk hexagonal boron nitride and related systems. Physical review B, 51(11), 6868.

[74] Huang, B., & Lee, H. (2012). Defect and impurity properties of hexagonal boron nitride: A first-principles calculation. Physical Review B, 86(24), 245406.

[75] Attaccalite, C., Bockstedte, M., Marini, A., Rubio, A., & Wirtz, L. (2011). Coupling of excitons and defect states in boron-nitride nanostructures. Physical Review B, 83(14), 144115.

[76] Laskowski, R., Blaha, P., & Schwarz, K. (2008). Bonding of hexagonal BN to transition metal surfaces: An ab initio density-functional theory study. Physical Review B, 78(4), 045409.

[77] Liu, D. Q., Tao, B., Ruan, H. C., Bentley, C. L., & Unwin, P. R. (2019). Metal support effects in electrocatalysis at hexagonal boron nitride. Chemical communications, 55(5), 628-631.

[78] Koitz, R., Seitsonen, A. P., Iannuzzi, M., & Hutter, J. (2013). Structural and electronic properties of a large-scale Moiré pattern of hexagonal boron nitride on Cu (111) studied with density functional theory. Nanoscale, 5(12), 5589-5595.

[79] Grimme, S. (2006). Semiempirical GGA-type density functional constructed with a long-range dispersion correction. Journal of computational chemistry, 27(15), 1787-1799.

[80] Diaz, J. G., Ding, Y., Koitz, R., Seitsonen, A. P., Iannuzzi, M., & Hutter, J. (2013). Hexagonal boron nitride on transition metal surfaces. Theoretical Chemistry Accounts, 132(4), 1350.

[81] Ziroff, J., Gold, P., Bendounan, A., Forster, F., & Reinert, F. (2009). Adsorption energy and geometry of physisorbed organic molecules on Au (1 1 1) probed by surface-state photoemission. Surface science, 603(2), 354-358.

[82] Brülke, C., Heepenstrick, T., Humberg, N., Krieger, I., Sokolowski, M., Weiß, S., ... & Soubatch, S. (2017). Long vertical distance bonding of the hexagonal boron nitride monolayer on the Cu (111) surface. The Journal of Physical Chemistry C, 121(43), 23964-23973.

[83] McDougall, N. L., Partridge, J. G., Nicholls, R. J., Russo, S. P., & McCulloch, D. G. (2017). Influence of point defects on the near edge structure of hexagonal boron nitride. Physical Review B, 96(14), 144106.

[84] Back, S., Kulkarni, A. R., & Siahrostami, S. (2018). Single Metal Atoms Anchored in Two-Dimensional Materials: Bifunctional Catalysts for Fuel Cell Applications. ChemCatChem, 10(14), 3034-3039.

[85] Gao, X., Wang, S., & Lin, S. (2016). Defective hexagonal boron nitride nanosheet on Ni (111) and Cu (111): stability, electronic structures, and potential applications. ACS applied materials & interfaces, 8(36), 24238-24247.

[86] Binnig, G., Rohrer, H., Gerber, C., & Weibel, E. (1982). Surface studies by scanning tunneling microscopy. Physical review letters, 49(1), 57.

[87] Tersoff, J., & Hamann, D. R. (1985). Theory of the scanning tunneling microscope. *Physical Review B*, *31*(2), 805.

[88] https://capricorn.bc.edu/wp/zeljkoviclab/research/scanning-tunneling-microscopy-stm/

---

[89] Deng, D., Pan, X., Yu, L., Cui, Y., Jiang, Y., Qi, J., ... & Sun, G. (2011). Toward N-doped graphene via solvothermal synthesis. *Chemistry of Materials*, *23*(5), 1188-1193.

[90] Zhao, L., He, R., Rim, K. T., Schiros, T., Kim, K. S., Zhou, H., ... & Nordlund, D. (2011). Visualizing individual nitrogen dopants in monolayer graphene. *Science*, *333*(6045), 999-1003.

[91] Wood, K. N., & Teeter, G. (2018). XPS on Li-battery-related compounds: analysis of inorganic SEI phases and a methodology for charge correction. *ACS Applied Energy Materials*, *1*(9), 4493-4504.

[92] Choudhury, D., Das, B., Sarma, D. D., & Rao, C. N. R. (2010). XPS evidence for molecular charge-transfer doping of graphene. *Chemical Physics Letters*, *497*(1-3), 66-69.

[93] Li, J., Li, X., Zhao, P., Lei, D. Y., Li, W., Bai, J., ... & Xu, X. (2015). Searching for magnetism in pyrrolic N-doped graphene synthesized via hydrothermal reaction. Carbon, 84, 460-468.

[94] Gottardi, S., Müller, K., Bignardi, L., Moreno-López, J. C., Pham, T. A., Ivashenko, O., ... & Stöhr, M. (2015). Comparing graphene growth on Cu (111) versus oxidized Cu (111). Nano letters, 15(2), 917-922.

[95] Verbitskiy, N. I., Fedorov, A. V., Profeta, G., Stroppa, A., Petaccia, L., Senkovskiy, B., ... & Yashina, L. V. (2015). Atomically precise semiconductor—graphene and hBN interfaces by Ge intercalation. Scientific reports, 5, 17700.

[96] Armaroli, N., & Balzani, V. (2007). The future of energy supply: challenges and opportunities. *Angewandte Chemie International Edition*, *46*(1-2), 52-66.

[97] Crabtree, G. W., Dresselhaus, M. S., & Buchanan, M. V. (2004). The hydrogen economy. *Physics today*, *57*(12), 39-44.

[98] Roger, I., Shipman, M. A., & Symes, M. D. (2017). Earth-abundant catalysts for electrochemical and photoelectrochemical water splitting. *Nature Reviews Chemistry*, *1*(1), 1-13.

[99] Alarawi, A., Ramalingam, V., & He, J. H. (2019). Recent advances in emerging single atom confined two-dimensional materials for water splitting applications. *Materials today energy*, *11*, 1-23.

[100] Wang, L., Sofer, Z., & Pumera, M. (2020). Will any crap we put into graphene increase its electrocatalytic effect?. *ACS nano*, *14*(1), 21-25.

[101] Zhang, H., & Lv, R. (2018). Defect engineering of two-dimensional materials for efficient electrocatalysis. *Journal of Materiomics*, *4*(2), 95-107.

[102] Hinnemann, B., Moses, P. G., Bonde, J., Jørgensen, K. P., Nielsen, J. H., Horch, S., ... & Nørskov, J. K. (2005). Biomimetic hydrogen evolution: MoS2 nanoparticles as catalyst for hydrogen evolution. *Journal of the American Chemical Society*, *127*(15), 5308-5309.

[103] Jaramillo, T. F., Jørgensen, K. P., Bonde, J., Nielsen, J. H., Horch, S., & Chorkendorff, I. (2007). Identification of active edge sites for electrochemical H2 evolution from MoS2 nanocatalysts. *science*, *317*(5834), 100-102.

[104] Kibsgaard, J., Chen, Z., Reinecke, B. N., & Jaramillo, T. F. (2012). Engineering the surface structure of MoS 2 to preferentially expose active edge sites for electrocatalysis. *Nature materials*, *11*(11), 963-969.

[105] Wu, J., Ma, L., Yadav, R. M., Yang, Y., Zhang, X., Vajtai, R., ... & Ajayan, P. M. (2015). Nitrogen-doped graphene with pyridinic dominance as a highly active and stable electrocatalyst for oxygen reduction. *ACS applied materials & interfaces*, *7*(27), 14763-14769.

[106] Jiao, Y., Zheng, Y., Jaroniec, M., & Qiao, S. Z. (2014). Origin of the electrocatalytic oxygen reduction activity of graphene-based catalysts: a roadmap to achieve the best performance. *Journal of the American Chemical Society*, *136*(11), 4394-4403.

---

[107] Zheng, Y., Jiao, Y., Zhu, Y., Li, L. H., Han, Y., Chen, Y., ... & Qiao, S. Z. (2014). Hydrogen evolution by a metal-free electrocatalyst. Nature communications, 5(1), 1-8.

[108] Lyalin, A., Nakayama, A., Uosaki, K., & Taketsugu, T. (2013). Functionalization of monolayer h-BN by a metal support for the oxygen reduction reaction. *The Journal of Physical Chemistry C*, *117*(41), 21359-21370.

[109] Uosaki, K., Elumalai, G., Noguchi, H., Masuda, T., Lyalin, A., Nakayama, A., & Taketsugu, T. (2014). Boron nitride nanosheet on gold as an electrocatalyst for oxygen reduction reaction: Theoretical suggestion and experimental proof. *Journal of the American Chemical Society*, *136*(18), 6542-6545.

[110] Liu, L., & Corma, A. (2018). Metal catalysts for heterogeneous catalysis: from single atoms to nanoclusters and nanoparticles. *Chemical reviews*, *118*(10), 4981-5079.

[111] Yang, X. F., Wang, A., Qiao, B., Li, J., Liu, J., & Zhang, T. (2013). Single-atom catalysts: a new frontier in heterogeneous catalysis. *Accounts of chemical research*, *46*(8), 1740-1748.

[112] Deng, D., Chen, X., Yu, L., Wu, X., Liu, Q., Liu, Y., ... & Si, R. (2015). A single iron site confined in a graphene matrix for the catalytic oxidation of benzene at room temperature. *Science advances*, *1*(11), e1500462.

[113] Cui, X., Li, H., Wang, Y., Hu, Y., Hua, L., Li, H., ... & Chen, X. (2018). Room-temperature methane conversion by graphene-confined single iron atoms. *Chem*, *4*(8), 1902-1910.

[114] Chen, Z., Vorobyeva, E., Mitchell, S., Fako, E., Ortuño, M. A., López, N., ... & Pérez-Ramírez, J. (2018). A heterogeneous single-atom palladium catalyst surpassing homogeneous systems for Suzuki coupling. *Nature nanotechnology*, *13*(8), 702-707.

[115] Byon, H. R., Suntivich, J., & Shao-Horn, Y. (2011). Graphene-based non-noble-metal catalysts for oxygen reduction reaction in acid. *Chemistry of Materials*, *23*(15), 3421-3428.

[116] Wu, H., Li, H., Zhao, X., Liu, Q., Wang, J., Xiao, J., ... & Guo, X. (2016). Highly doped and exposed Cu (I)–N active sites within graphene towards efficient oxygen reduction for zinc–air batteries. *Energy & Environmental Science*, *9*(12), 3736-3745.

[117] Han, Y., Wang, Y. G., Chen, W., Xu, R., Zheng, L., Zhang, J., ... & Chen, C. (2017). Hollow N-doped carbon spheres with isolated cobalt single atomic sites: superior electrocatalysts for oxygen reduction. *Journal of the American Chemical Society*, *139*(48), 17269-17272.

[118] Chen, W., Pei, J., He, C. T., Wan, J., Ren, H., Zhu, Y., ... & Lu, S. (2017). Rational Design of Single Molybdenum Atoms Anchored on N-Doped Carbon for Effective Hydrogen Evolution Reaction. *Angewandte Chemie International Edition*, *56*(50), 16086-16090.

[119] Fei, H., Dong, J., Feng, Y., Allen, C. S., Wan, C., Volosskiy, B., ... & An, P. (2018). General synthesis and definitive structural identification of MN 4 C 4 single-atom catalysts with tunable electrocatalytic activities. *Nature Catalysis*, *1*(1), 63-72.

[120] Hohenberg, P., & Kohn, W. (1964). Inhomogeneous electron gas. *Physical review*, *136*(3B), B864.

[121] Kohn, W., & Sham, L. J. (1965). Self-consistent equations including exchange and correlation effects. *Physical review*, *140*(4A), A1133.

---

[122] Perdew, J. P., Burke, K., & Ernzerhof, M. (1996). Generalized gradient approximation made simple. Physical review letters, 77(18), 3865.

[123] Grimme, S. (2006). Semiempirical GGA-type density functional constructed with a long-range dispersion correction. *Journal of computational chemistry*, *27*(15), 1787-1799

[124] Grimme, S., Antony, J., Ehrlich, S., & Krieg, H. (2010). A consistent and accurate ab initio parametrization of density functional dispersion correction (DFT-D) for the 94 elements H-Pu. *The Journal of chemical physics*, *132*(15), 154104.

[125] Dion, M., Rydberg, H., Schröder, E., Langreth, D. C., & Lundqvist, B. I. (2004). Van der Waals density functional for general geometries. *Physical review letters*, *92*(24), 246401.

[126] Lee, K., Murray, É. D., Kong, L., Lundqvist, B. I., & Langreth, D. C. (2010). Higher-accuracy van der Waals density functional. Physical Review B, 82(8), 081101.

[127] Hamada, I. (2014). van der Waals density functional made accurate. *Physical Review B*, *89*(12), 121103.

[128] Hamada, I., & Otani, M. (2010). Comparative van der Waals density-functional study of graphene on metal surfaces. Physical Review B, 82(15), 153412.

[129] Vanderbilt, D. (1990). Soft self-consistent pseudopotentials in a generalized eigenvalue formalism. Physical review B, 41(11), 7892.

[130] Hamann, D. R., Schlüter, M., & Chiang, C. (1979). Norm-conserving pseudopotentials. Physical Review Letters, 43(20), 1494.

[131] Tersoff, J., & Hamann, D. R. (1983). Theory and application for the scanning tunneling microscope. Physical review letters, 50(25), 1998.

[132] Cramer, C. J. (2013). Essentials of computational chemistry: theories and models. John Wiley & Sons.

[133] Nørskov, J. K., Rossmeisl, J., Logadottir, A., Lindqvist, L. R. K. J., Kitchin, J. R., Bligaard, T., & Jonsson, H. (2004). Origin of the overpotential for oxygen reduction at a fuel-cell cathode. The Journal of Physical Chemistry B, 108(46), 17886-17892.

[134] Greeley, J., Stephens, I. E. L., Bondarenko, A. S., Johansson, T. P., Hansen, H. A., Jaramillo, T. F., ... & Nørskov, J. K. (2009). Alloys of platinum and early transition metals as oxygen reduction electrocatalysts. Nature chemistry, 1(7), 552-556.

[135] Karlberg, G. S., Rossmeisl, J., & Nørskov, J. K. (2007). Estimations of electric field effects on the oxygen reduction reaction based on the density functional theory. Physical Chemistry Chemical Physics, 9(37), 5158-5161.

[136] Kandoi, S. G. A. A., Gokhale, A. A., Grabow, L. C., Dumesic, J. A., & Mavrikakis, M. (2004). Why Au and Cu are more selective than Pt for preferential oxidation of CO at low temperature. Catalysis Letters, 93(1-2), 93-100.

[137] Nørskov, J. K., Rossmeisl, J., Logadottir, A., Lindqvist, L. R. K. J., Kitchin, J. R., Bligaard, T., & Jonsson, H. (2004). Origin of the overpotential for oxygen reduction at a fuel-cell cathode. The Journal of Physical Chemistry B, 108(46), 17886-17892.

[138] Calle-Vallejo, F., & Koper, M. T. (2012). First-principles computational electrochemistry: Achievements and challenges. Electrochimica acta, 84, 3-11.

[139] Hansen, H. A., Rossmeisl, J., & Nørskov, J. K. (2008). Surface Pourbaix diagrams and oxygen reduction activity of Pt, Ag and Ni (111) surfaces studied by DFT. Physical Chemistry Chemical Physics, 10(25), 3722-3730.

---

[140] Holewinski, A., Idrobo, J. C., & Linic, S. (2014). High-performance Ag–Co alloy catalysts for electrochemical oxygen reduction. Nature chemistry, 6(9), 828-834.

[141] Stamenkovic, V., Mun, B. S., Mayrhofer, K. J., Ross, P. N., Markovic, N. M., Rossmeisl, J., ... & Nørskov, J. K. (2006). Changing the activity of electrocatalysts for oxygen reduction by tuning the surface electronic structure. Angewandte Chemie, 118(18), 2963-2967.

[142] Henkelman, G., Uberuaga, B. P., & Jónsson, H. (2000). A climbing image nudged elastic band method for finding saddle points and minimum energy paths. The Journal of chemical physics, 113(22), 9901-9904.

[143] Sha, Y., Yu, T. H., Liu, Y., Merinov, B. V., & Goddard III, W. A. (2010). Theoretical study of solvent effects on the platinum-catalyzed oxygen reduction reaction. The Journal of Physical Chemistry Letters, 1(5), 856-861.

[144] Tomasi, J., Mennucci, B., & Cammi, R. (2005). Quantum mechanical continuum solvation models. Chemical reviews, 105(8), 2999-3094.

[145] Al-Hamdani, Y. S., Alfè, D., Von Lilienfeld, O. A., & Michaelides, A. (2016). Tuning dissociation using isoelectronically doped graphene and hexagonal boron nitride: Water and other small molecules. The Journal of chemical physics, 144(15), 154706.

[146] Tran, T. T., Bray, K., Ford, M. J., Toth, M., & Aharonovich, I. (2016). Quantum emission from hexagonal boron nitride monolayers. Nature nanotechnology, 11(1), 37-41.

[147] Kim, K. K., Hsu, A., Jia, X., Kim, S. M., Shi, Y., Hofmann, M., ... & Kong, J. (2012). Synthesis of monolayer hexagonal boron nitride on Cu foil using chemical vapor deposition. Nano letters, 12(1), 161-166.

[148] Li, Q., Zou, X., Liu, M., Sun, J., Gao, Y., Qi, Y., ... & Liu, Z. (2015). Grain boundary structures and electronic properties of hexagonal boron nitride on Cu (111). Nano letters, 15(9), 5804-5810.

[149] Alem, N.; Erni, R.; Kisielowski, C.; Rossel, M. D.; Gannett, W.; Zettl, A. Atomically Thin Hexagonal Boron Nitride Probed by Ultrahigh-Resolution Transmission Electron Microscopy. Phys. Rev. B 2009, 80, No. 155425

[150] Cretu, O., Lin, Y. C., Koshino, M., Tizei, L. H., Liu, Z., & Suenaga, K. (2015). Structure and local chemical properties of boron-terminated tetravacancies in hexagonal boron nitride. Physical Review Letters, 114(7), 075502.

[151] Lyalin, A., Nakayama, A., Uosaki, K., & Taketsugu, T. (2013). Theoretical predictions for hexagonal BN based nanomaterials as electrocatalysts for the oxygen reduction reaction. Physical Chemistry Chemical Physics, 15(8), 2809-2820.

[152] Du, A., Chen, Y., Zhu, Z., Amal, R., Lu, G. Q., & Smith, S. C. (2009). Dots versus antidots: computational exploration of structure, magnetism, and half-metallicity in boron− nitride nanostructures. Journal of the American Chemical Society, 131(47), 17354-17359.

[153] Wang, Y., & Ding, Y. (2014). Tunable magnetic and electronic properties of BN nanosheets with triangular defects: a first-principles study. Journal of Physics: Condensed Matter, 26(43), 435302.

[154] Hu, G., Wu, Z., Dai, S., & Jiang, D. E. (2018). Interface engineering of earth-abundant transition metals using boron nitride for selective electroreduction of CO2. ACS applied materials & interfaces, 10(7), 6694-6700.

[155] Gao, X., Wang, S., & Lin, S. (2016). Defective hexagonal boron nitride nanosheet on Ni (111) and Cu (111): stability, electronic structures, and potential applications. ACS applied materials & interfaces, 8(36), 24238-24247.

---

[156] Deng, D., Chen, X., Yu, L., Wu, X., Liu, Q., Liu, Y., ... & Si, R. (2015). A single iron site confined in a graphene matrix for the catalytic oxidation of benzene at room temperature. Science advances, 1(11), e1500462.

[157] Giannozzi, P., Baroni, S., Bonini, N., Calandra, M., Car, R., Cavazzoni, C., ... & Dal Corso, A. (2009). QUANTUM ESPRESSO: a modular and open-source software project for quantum simulations of materials. Journal of physics: Condensed matter, 21(39), 395502.

[158] Dovesi, R., Orlando, R., Erba, A., Zicovich-Wilson, C. M., Civalleri, B., Casassa, S., ... & Noël, Y. (2014). CRYSTAL14: A program for the ab initio investigation of crystalline solids. International Journal of Quantum Chemistry, 114(19), 1287-1317.

[159] Krukau, A. V., Vydrov, O. A., Izmaylov, A. F., & Scuseria, G. E. (2006). Influence of the exchange screening parameter on the performance of screened hybrid functionals. The Journal of chemical physics, 125(22), 224106.

[160] Lee, C., Yang, W., & Parr, R. G. (1988). Development of the Colle-Salvetti correlation-energy formula into a functional of the electron density. Physical review B, 37(2), 785.

[161] Becke, A. D. J. (1993) Density-Functional Thermochemistry. III. The Role of Exact Exchange. Chemical Physics 98, 5648−5652.

[162] Cassabois, G., Valvin, P., & Gil, B. (2016). Hexagonal boron nitride is an indirect bandgap semiconductor. Nature Photonics, 10(4), 262-266.

[163] Chen, T. A., Chuu, C. P., Tseng, C. C., Wen, C. K., Wong, H. S. P., Pan, S., ... & Fu, Q. (2020). Wafer-scale single-crystal hexagonal boron nitride monolayers on Cu (111). Nature, 579(7798), 219-223.

[164] Giménez, S., & Bisquert, J. (2016). Photoelectrochemical solar fuel production (pp. 403-407). Switzerland: Springer.

[165] Tahir, M., Pan, L., Idrees, F., Zhang, X., Wang, L., Zou, J. J., & Wang, Z. L. (2017). Electrocatalytic oxygen evolution reaction for energy conversion and storage: a comprehensive review. Nano Energy, 37, 136-157.

[166] Suen, N. T., Hung, S. F., Quan, Q., Zhang, N., Xu, Y. J., & Chen, H. M. (2017). Electrocatalysis for the oxygen evolution reaction: recent development and future perspectives. *Chemical Society Reviews*, *46*(2), 337-365.

[167] Dau, H., Limberg, C., Reier, T., Risch, M., Roggan, S., & Strasser, P. (2010). The mechanism of water oxidation: from electrolysis via homogeneous to biological catalysis. ChemCatChem, 2(7), 724-761.

[168] Seh, Z. W., Kibsgaard, J., Dickens, C. F., Chorkendorff, I. B., Nørskov, J. K., & Jaramillo, T. F. (2017). Combining theory and experiment in electrocatalysis: Insights into materials design. Science, 355(6321).

[169] Stoerzinger, K. A., Qiao, L., Biegalski, M. D., & Shao-Horn, Y. (2014). Orientation-dependent oxygen evolution activities of rutile IrO2 and RuO2. The journal of physical chemistry letters, 5(10), 1636-1641.

[170] Seitz, L. C., Dickens, C. F., Nishio, K., Hikita, Y., Montoya, J., Doyle, A., ... & Jaramillo, T. F. (2016). A highly active and stable IrOx/SrIrO3 catalyst for the oxygen evolution reaction. Science, 353(6303), 1011-1014.

[171] McCrory, C. C., Jung, S., Ferrer, I. M., Chatman, S. M., Peters, J. C., & Jaramillo, T. F. (2015). Benchmarking hydrogen evolving reaction and oxygen evolving reaction electrocatalysts for solar water splitting devices. Journal of the American Chemical Society, 137(13), 4347-4357.

[172] J. Rossmeisl, Z.-W. Qu, H. Zhu, G.-J. Kroes, J. K. Nørskov, J. Electroanal. Chem. 2007, 607, 83–89.

---

[173] Valdés, Á., Qu, Z. W., Kroes, G. J., Rossmeisl, J., & Nørskov, J. K. (2008). Oxidation and photo-oxidation of water on TiO2 surface. The Journal of Physical Chemistry C, 112(26), 9872-9879.

[174] Li, Y. F., & Selloni, A. (2014). Mechanism and activity of water oxidation on selected surfaces of pure and Fe-doped NiO x. Acs Catalysis, 4(4), 1148-1153.

[175] Zhang, J., Zhao, Z., Xia, Z., & Dai, L. (2015). A metal-free bifunctional electrocatalyst for oxygen reduction and oxygen evolution reactions. Nature nanotechnology, 10(5), 444-452.

[176] Boukhvalov, D. W., Son, Y. W., & Ruoff, R. S. (2014). Water splitting over graphene-based catalysts: Ab initio calculations. ACS Catalysis, 4(6), 2016-2021.

[177] Koitz, R., Nørskov, J. K., & Studt, F. (2015). A systematic study of metal-supported boron nitride materials for the oxygen reduction reaction. Physical Chemistry Chemical Physics, 17(19), 12722-12727.

[178] Liu, X., Duan, T., Sui, Y., Meng, C., & Han, Y. (2014). Copper atoms embedded in hexagonal boron nitride as potential catalysts for CO oxidation: a first-principles investigation. RSC Advances, 4(73), 38750-38760.

[179] Mao, K., Li, L., Zhang, W., Pei, Y., Zeng, X. C., Wu, X., & Yang, J. (2014). A theoretical study of single-atom catalysis of CO oxidation using Au embedded 2D h-BN monolayer: a CO-promoted O 2 activation. Scientific reports, 4, 5441.

[180] Zhao, J., & Chen, Z. (2017). Single Mo atom supported on defective boron nitride monolayer as an efficient electrocatalyst for nitrogen fixation: a computational study. Journal of the American Chemical Society, 139(36), 12480-12487.

[181] Zhu, W., Wu, Z., Foo, G. S., Gao, X., Zhou, M., Liu, B., ... & Li, H. (2017). Taming interfacial electronic properties of platinum nanoparticles on vacancy-abundant boron nitride nanosheets for enhanced catalysis. Nature communications, 8(1), 1-7.

[182] Sun, W., Meng, Y., Fu, Q., Wang, F., Wang, G., Gao, W., ... & Lu, F. (2016). High-yield production of boron nitride nanosheets and its uses as a catalyst support for hydrogenation of nitroaromatics. ACS applied materials & interfaces, 8(15), 9881-9888.

[183] Fu, Q., Meng, Y., Fang, Z., Hu, Q., Xu, L., Gao, W., ... & Lu, F. (2017). Boron nitride nanosheet-anchored pd–fe core–shell nanoparticles as highly efficient catalysts for Suzuki–Miyaura coupling reactions. ACS applied materials & interfaces, 9(3), 2469-2476.

[184] Wu, J., Wang, L., Lv, B., & Chen, J. (2017). Facile fabrication of BCN nanosheet-encapsulated nano-iron as highly stable Fischer–Tropsch synthesis catalyst. ACS Applied Materials & Interfaces, 9(16), 14319-14327.

[185] Soriano-López, J., Schmitt, W., & García-Melchor, M. (2018). Computational modelling of water oxidation catalysts. Current Opinion in Electrochemistry, 7, 22-30.

[186] Perilli, D., Selli, D., Liu, H., Bianchetti, E., & Di Valentin, C. (2018). h-BN Defective Layers as Giant N-Donor Macrocycles for Cu Adatom Trapping from the Underlying Metal Substrate. The Journal of Physical Chemistry C, 122(41), 23610-23622.

[187] Monkhorst, H. J., & Pack, J. D. (1976). Special points for Brillouin-zone integrations. Physical review B, 13(12), 5188.

[188] http://www.webbook.nist.gov.

[189] Rossmeisl, J., Logadottir, A., & Nørskov, J. K. (2005). Electrolysis of water on (oxidized) metal surfaces. Chemical physics, 319(1-3), 178-184.

[190] Fisicaro, G., Genovese, L., Andreussi, O., Mandal, S., Nair, N. N., Marzari, N., & Goedecker, S. (2017). Soft-sphere continuum solvation in electronic-structure calculations. Journal of chemical theory and computation, 13(8), 3829-3845.

---

[191] Andreussi, O., Dabo, I., & Marzari, N. (2012). Revised self-consistent continuum solvation in electronic-structure calculations. The Journal of chemical physics, 136(6), 064102.

[192] Crabtree, G. W., Dresselhaus, M. S., & Buchanan, M. V. (2004). The hydrogen economy. Physics today, 57(12), 39-44.

[193] Barreto, L., Makihira, A., & Riahi, K. (2003). The hydrogen economy in the 21st century: a sustainable development scenario. International Journal of Hydrogen Energy, 28(3), 267-284.

[194] Grigoriev, S. A., Porembsky, V. I., & Fateev, V. N. (2006). Pure hydrogen production by PEM electrolysis for hydrogen energy. International Journal of Hydrogen Energy, 31(2), 171-175.

[195] Turner, J. A. (2004). Sustainable hydrogen production. Science, 305(5686), 972-974.

[196] Greeley, J., Jaramillo, T. F., Bonde, J., Chorkendorff, I. B., & Nørskov, J. K. (2006). Computational high-throughput screening of electrocatalytic materials for hydrogen evolution. Nature materials, 5(11), 909-913.

[197] Nørskov, J. K., Bligaard, T., Logadottir, A., Kitchin, J. R., Chen, J. G., Pandelov, S., & Stimming, U. (2005). Trends in the exchange current for hydrogen evolution. Journal of The Electrochemical Society, 152(3), J23-J26.

[198] Lindgren, P., Kastlunger, G., & Peterson, A. A. (2019). A Challenge to the G∼ 0 Interpretation of Hydrogen Evolution. ACS Catalysis, 10, 121-128.

[199] Vesborg, P. C., Seger, B., & Chorkendorff, I. B. (2015). Recent development in hydrogen evolution reaction catalysts and their practical implementation. The journal of physical chemistry letters, 6(6), 951-957.

[200] Wang, H., Tsai, C., Kong, D., Chan, K., Abild-Pedersen, F., Nørskov, J. K., & Cui, Y. (2015). Transition-metal doped edge sites in vertically aligned MoS2 catalysts for enhanced hydrogen evolution. Nano Research, 8(2), 566-575.

[201] Jin, H., Guo, C., Liu, X., Liu, J., Vasileff, A., Jiao, Y., ... & Qiao, S. Z. (2018). Emerging two-dimensional nanomaterials for electrocatalysis. Chemical reviews, 118(13), 6337-6408.

[202] Tsai, C., Chan, K., Nørskov, J. K., & Abild-Pedersen, F. (2015). Theoretical insights into the hydrogen evolution activity of layered transition metal dichalcogenides. Surface Science, 640, 133-140.

[203] Huang, Y., Nielsen, R. J., Goddard III, W. A., & Soriaga, M. P. (2015). The reaction mechanism with free energy barriers for electrochemical dihydrogen evolution on MoS2. Journal of the American Chemical Society, 137(20), 6692-6698.

[204] Back, S., & Siahrostami, S. (2019). Noble metal supported hexagonal boron nitride for the oxygen reduction reaction: a DFT study. Nanoscale Advances, 1(1), 132-139.

[205] Uosaki, K., Elumalai, G., Dinh, H. C., Lyalin, A., Taketsugu, T., & Noguchi, H. (2016). Highly efficient electrochemical hydrogen evolution reaction at insulating boron nitride nanosheet on inert gold substrate. Scientific reports, 6, 32217.

[206] Mao, K., Li, L., Zhang, W., Pei, Y., Zeng, X. C., Wu, X., & Yang, J. (2014). A theoretical study of single-atom catalysis of CO oxidation using Au embedded 2D h-BN monolayer: a CO-promoted O_2 activation. Scientific reports, 4, 5441.

[208] Cui, Q., Qin, G., Wang, W., Sun, L., Du, A., & Sun, Q. (2019). Mo-doped boron nitride monolayer as a promising single-atom electrocatalyst for CO2 conversion. Beilstein journal of nanotechnology, 10(1), 540-548.

[209] Tan, X., Tahini, H. A., Arandiyan, H., & Smith, S. C. (2019). Electrocatalytic Reduction of Carbon Dioxide to Methane on Single Transition Metal Atoms Supported on a Defective Boron Nitride Monolayer: First Principle Study. Advanced Theory and Simulations, 2(3), 1800094.

---

[210] Patera, L. L., Bianchini, F., Africh, C., Dri, C., Soldano, G., Mariscal, M. M., ... & Comelli, G. (2018). Real-time imaging of adatom-promoted graphene growth on nickel. Science, 359(6381), 1243-1246.

[211] Carnevali, V., Patera, L. L., Prandini, G., Jugovac, M., Modesti, S., Comelli, G., ... & Africh, C. (2019). Doping of epitaxial graphene by direct incorporation of nickel adatoms. Nanoscale, 11(21), 10358-10364.

[212] Löwdin, P. O. (1955). Quantum theory of many-particle systems. I. Physical interpretations by means of density matrices, natural spin-orbitals, and convergence problems in the method of configurational interaction. Physical Review, 97(6), 1474.

[213] Kokalj, A. (1999). XCrySDen—a new program for displaying crystalline structures and electron densities. Journal of Molecular Graphics and Modelling, 17(3-4), 176-179.

[214] Vicarelli, L., Vitiello, M. S., Coquillat, D., Lombardo, A., Ferrari, A. C., Knap, W., ... & Tredicucci, A. (2012). Graphene field-effect transistors as room-temperature terahertz detectors. Nature materials, 11(10), 865-871.

[215] Kostarelos, K., & Novoselov, K. S. (2014). Exploring the interface of graphene and biology. Science, 344(6181), 261-263.

[216] Mueller, T., Xia, F., & Avouris, P. (2010). Graphene photodetectors for high-speed optical communications. Nature photonics, 4(5), 297-301.

[217] Mashoff, T., Takamura, M., Tanabe, S., Hibino, H., Beltram, F., & Heun, S. (2013). Hydrogen storage with titanium-functionalized graphene. Applied Physics Letters, 103(1), 013903.

[218] Panchakarla, L. S., Subrahmanyam, K. S., Saha, S. K., Govindaraj, A., Krishnamurthy, H. R., Waghmare, U. V., & Rao, C. N. R. (2009). Synthesis, structure, and properties of boron-and nitrogen-doped graphene. Advanced Materials, 21(46), 4726-4730.

[219] Choi, C. H.; Park, S. H.; Woo, S. I. Binary and ternary doping of nitrogen, boron, and phosphorus into carbon for enhancing electrochemical oxygen reduction activity. ACS nano 2012, 6, 7084–7091.

[220] Wu, Z.-S.; Ren, W.; Xu, L.; Li, F.; Cheng, H.-M. Doped graphene sheets as anode materials with superhigh rate and large capacity for lithium ion batteries. ACS nano 2011, 5, 5463–5471.

[221] Celasco, E., Carraro, G., Lusuan, A., Smerieri, M., Pal, J., Rocca, M., ... & Vattuone, L. (2016). CO chemisorption at vacancies of supported graphene films: a candidate for a sensor?. Physical Chemistry Chemical Physics, 18(28), 18692-18696.

[222] Zhao, L., He, R., Rim, K. T., Schiros, T., Kim, K. S., Zhou, H., ... & Nordlund, D. (2011). Visualizing individual nitrogen dopants in monolayer graphene. Science, 333(6045), 999-1003.

[223] Usachov, D., Vilkov, O., Gruneis, A., Haberer, D., Fedorov, A., Adamchuk, V. K., ... & Laubschat, C. (2011). Nitrogen-doped graphene: efficient growth, structure, and electronic properties. Nano letters, 11(12), 5401-5407.

[224] Martín-Recio, A., Romero-Muñiz, C., Pou, P., Pérez, R., & Gómez-Rodríguez, J. M. (2016). Purely substitutional nitrogen on graphene/Pt (111) unveiled by STM and first principles calculations. Nanoscale, 8(40), 17686-17693.

[225] Zhang, C., Fu, L., Liu, N., Liu, M., Wang, Y., & Liu, Z. (2011). Synthesis of nitrogen-doped graphene using embedded carbon and nitrogen sources. Advanced materials, 23(8), 1020-1024.

[226] Hu, X., Björkman, T., Lipsanen, H., Sun, L., & Krasheninnikov, A. V. (2015). Solubility of boron, carbon, and nitrogen in transition metals: getting insight into trends from first-principles calculations. The Journal of Physical Chemistry Letters, 6(16), 3263-3268.

---

[227] Patera, L. L.; Africh, C.; Weatherup, R. S.; Blume, R.; Bhardwaj, S.; Castellarin-Cudia, C. et al., In situ observations of the atomistic mechanisms of Ni catalyzed low temperature graphene growth. ACS nano 2013, 7, 7901–7912.

[228] Momma, K., & Izumi, F. (2011). VESTA 3 for three-dimensional visualization of crystal, volumetric and morphology data. Journal of applied crystallography, 44(6), 1272-1276.

[229] Nečas, D., & Klapetek, P. (2012). Gwyddion: an open-source software for SPM data analysis. Open Physics, 10(1), 181-188.

[230] García-Gil, S., García, A., & Ordejón, P. (2012). Calculation of core level shifts within DFT using pseudopotentials and localized basis sets. The European Physical Journal B, 85(7), 239.

[231] Castrovilli, M. C., Bolognesi, P., Bodo, E., Mattioli, G., Cartoni, A., & Avaldi, L. (2018). An experimental and theoretical investigation of XPS and NEXAFS of 5-halouracils. Physical Chemistry Chemical Physics, 20(9), 6657-6667.

[232] Scardamaglia, M., Aleman, B., Amati, M., Ewels, C., Pochet, P., Reckinger, N., ... & Gregoratti, L. (2014). Nitrogen implantation of suspended graphene flakes: Annealing effects and selectivity of sp2 nitrogen species. Carbon, 73, 371-381.

[233] Sala, A., Zamborlini, G., Menteş, T. O., & Locatelli, A. (2015). Fabrication of 2D heterojunction in graphene via low energy N2+ irradiation. Small, 11(44), 5927-5931.

[234] Jin, L., Fu, Q., Dong, A., Ning, Y., Wang, Z., Bluhm, H., & Bao, X. (2014). Surface chemistry of CO on Ru (0001) under the confinement of graphene cover. The Journal of Physical Chemistry C, 118(23), 12391-12398.

[235] Li, H., Xiao, J., Fu, Q., & Bao, X. (2017). Confined catalysis under two-dimensional materials. Proceedings of the National Academy of Sciences, 114(23), 5930-5934.

[236] Ma, D., Zhang, Y., Liu, M., Ji, Q., Gao, T., Zhang, Y., & Liu, Z. (2013). Clean transfer of graphene on Pt foils mediated by a carbon monoxide intercalation process. Nano Research, 6(9), 671-678.

[237] Palacio, I., Otero-Irurueta, G., Alonso, C., Martínez, J. I., López-Elvira, E., Muñoz-Ochando, I., ... & Ellis, G. J. (2018). Chemistry below graphene: Decoupling epitaxial graphene from metals by potential-controlled electrochemical oxidation. Carbon, 129, 837-846.

[238] Zahra, K. M., Byrne, C., Alieva, A., Casiraghi, C., & Walton, A. S. (2020). Intercalation, decomposition, entrapment–a new route to graphene nanobubbles. Physical Chemistry Chemical Physics, 22(14), 7606-7615.

[239] Mu, R., Fu, Q., Jin, L., Yu, L., Fang, G., Tan, D., & Bao, X. (2012). Visualizing chemical reactions confined under graphene. Angewandte Chemie International Edition, 51(20), 4856-4859.

[240] Granas, E., Andersen, M., Arman, M. A., Gerber, T., Hammer, B., Schnadt, J., ... & Knudsen, J. (2013). CO intercalation of graphene on Ir (111) in the millibar regime. The Journal of Physical Chemistry C, 117(32), 16438-16447.

[241] Wei, M., Fu, Q., Yang, Y., Wei, W., Crumlin, E., Bluhm, H., & Bao, X. (2015). Modulation of surface chemistry of CO on Ni (111) by surface graphene and carbidic carbon. The Journal of Physical Chemistry C, 119(24), 13590-13597.

[242] Silva, C. C., Cai, J., Jolie, W., Dombrowski, D., Farwick zum Hagen, F. H., Martínez-Galera, A. J., ... & Busse, C. (2019). Lifting Epitaxial Graphene by Intercalation of Alkali Metals. The Journal of Physical Chemistry C, 123(22), 13712-13719.

[243] Petrović, M., Rakić, I. Š., Runte, S., Busse, C., Sadowski, J. T., Lazić, P., ... & Atodiresei, N. (2013). The mechanism of caesium intercalation of graphene. Nature communications, 4(1), 1-8.

---

[244] He, G., Wang, Q., Yu, H. K., Farías, D., Liu, Y., & Politano, A. (2019). Water-induced hydrogenation of graphene/metal interfaces at room temperature: Insights on water intercalation and identification of sites for water splitting. Nano Research, 12(12), 3101-3108.

[245] Bunch, J. S., Verbridge, S. S., Alden, J. S., Van Der Zande, A. M., Parpia, J. M., Craighead, H. G., & McEuen, P. L. (2008). Impermeable atomic membranes from graphene sheets. Nano letters, 8(8), 2458-2462.

[246] Sun, P. Z., Yang, Q., Kuang, W. J., Stebunov, Y. V., Xiong, W. Q., Yu, J., ... & Lozada-Hidalgo, M. (2020). Limits on gas impermeability of graphene. Nature, 579(7798), 229-232.

[247] Yoon, H. W., Cho, Y. H., & Park, H. B. (2016). Graphene-based membranes: status and prospects. Philosophical Transactions of the Royal Society A: Mathematical, Physical and Engineering Sciences, 374(2060), 20150024.

[248] Kim, H. W., Yoon, H. W., Yoon, S. M., Yoo, B. M., Ahn, B. K., Cho, Y. H., ... & Choi, J. Y. (2013). Selective gas transport through few-layered graphene and graphene oxide membranes. Science, 342(6154), 91-95.

[249] Pierleoni, D., Minelli, M., Ligi, S., Christian, M., Funke, S., Reineking, N., ... & Palermo, V. (2018). Selective gas permeation in graphene oxide–polymer self-assembled multilayers. ACS applied materials & interfaces, 10(13), 11242-11250.

[250] Ibrahim, A., & Lin, Y. S. (2018). Gas permeation and separation properties of large-sheet stacked graphene oxide membranes. Journal of Membrane Science, 550, 238-245.

[251] Wang, L., Drahushuk, L. W., Cantley, L., Koenig, S. P., Liu, X., Pellegrino, J., ... & Bunch, J. S. (2015). Molecular valves for controlling gas phase transport made from discrete ångström-sized pores in graphene. Nature nanotechnology, 10(9), 785-790.

[252] Wei, M., Fu, Q., Yang, Y., Wei, W., Crumlin, E., Bluhm, H., & Bao, X. (2015). Modulation of surface chemistry of CO on Ni (111) by surface graphene and carbidic carbon. The Journal of Physical Chemistry C, 119(24), 13590-13597.

[253] Held, G., Schuler, J., Sklarek, W., & Steinrück, H. P. (1998). Determination of adsorption sites of pure and coadsorbed CO on Ni (111) by high resolution X-ray photoelectron spectroscopy. Surface science, 398(1-2), 154-171.

[254] Dong, A., Fu, Q., Wu, H., Wei, M., & Bao, X. (2016). Factors controlling the CO intercalation of h-BN overlayers on Ru (0001). Physical Chemistry Chemical Physics, 18(35), 24278-24284.

List of publications

1. Fazio, G., Ferrighi, L., Perilli, D., & Di Valentin, C. (2016). Computational electrochemistry of doped graphene as electrocatalytic material in fuel cells. International Journal of Quantum Chemistry, 116(22), 1623-1640.
2. Ronchi, C., Datteo, M., Perilli, D., Ferrighi, L., Fazio, G., Selli, D., & Di Valentin, C. (2017). π magnetism of carbon monovacancy in graphene by hybrid density functional calculations. The Journal of Physical Chemistry C, 121(15), 8653-8661.
3. Ferrighi, L., Perilli, D., Selli, D., & Di Valentin, C. (2017). Water at the interface between defective graphene and Cu or Pt (111) surfaces. ACS Applied Materials & Interfaces, 9(35), 29932-29941.
4. Perilli, D., Selli, D., Liu, H., Bianchetti, E., & Di Valentin, C. (2018). h-BN Defective Layers as Giant N-Donor Macrocycles for Cu Adatom Trapping from the Underlying Metal Substrate. The Journal of Physical Chemistry C, 122(41), 23610-23622. (**Chapter 3**)
5. Nguyen, T. H., Perilli, D., Cattelan, M., Liu, H., Sedona, F., Fox, N. A., ... & Agnoli, S. (2019). Microscopic insight into the single step growth of in-plane heterostructures between graphene and hexagonal boron nitride. Nano Research, 12(3), 675-682.
6. Perilli, D., Selli, D., Liu, H., & Di Valentin, C. (2019). Computational Electrochemistry of Water Oxidation on Metal-Doped and Metal-Supported Defective h-BN. ChemSusChem, 12(9), 1995-2007. (**Chapter 4**)
7. Liu, H., Perilli, D., Dolce, M., & Di Valentin, C. (2020). Insight into the Na adsorption on $WSe_2xS_{2(1-x)}$ monolayers: a hybrid functional investigation. Journal of Physics: Condensed Matter, 32, 395001.
8. Fiori, S., Perilli, D., Panighel, M., Cepek, C., Ugolotti, A., Sala, A., ... & Africh, C. (2020). “Inside out” growth method for high-quality nitrogen-doped graphene. Carbon, 171, 704-710. (**Chapter 6**)
9. Perilli, D., Fiori, S., Panighel, M., Liu, H., Cepek, C., Peressi, M., ... & Di Valentin, C. (2020). Mechanism of CO Intercalation Through the graphene/Ni (111) Interface and Effect of Doping. The Journal of Physical Chemistry Letters, 11(20), 8887-8892. (**Chapter 7**)

---

10. Perilli, D., Di Valentin, C., & Studt, F. (2020). Can Single Metal Atoms Trapped in Defective h-BN/Cu (111) Improve Electrocatalysis of the H_2 Evolution Reaction?. The Journal of Physical Chemistry C, 124(43), 23690-23698. (**Chapter 5**)